Preprocessing Issues in High Resolution Radar Target Classification

by

Anthony Zyweck, B.E. (Hons.), B.Sc.

Thesis submitted for the degree of

Doctor of Philosophy

The University of Adelaide
Faculty of Engineering
Department of Electrical and Electronic Engineering

March, 1995

This thesis is dedicated to

my Parents, Heinz and Ursula

and

the memory of my late Grandfather, Anton Holstein.

TABLE OF CONTENTS

ABSTRACT

Research in the area of radar target classification has been active for at least 30 years. The bulk of the research effort has been directed at aspect-independent techniques which classify a target according to its resonant response. Recently there has been a renewed interest in radar target classification, particularly in techniques which provide target classification from high resolution radar imagery. This dissertation addresses preprocessing issues for radar target classification from high resolution radar imagery.

This thesis begins by examining radar backscatter from full-scale aircraft targets. High resolution radar imagery of real aircraft in flight and of a MIRAGE aircraft on a turntable is examined. Several important backscatter characteristics such as engine cavity backscatter and jet engine modulation (JEM) are highlighted. The observed radar backscatter phenomena are discussed in the context of preprocessing for radar target classification. A high resolution radar data simulator called ISARLAB (ISAR LABoratory) is created to produce data for target classification studies. The design of ISARLAB is based upon well established radar backscatter theory and the examination of radar backscatter from real full-scale aircraft. ISARLAB only models the essential target attributes which are likely to be useful for radar target classification.

Radar target classification from a high resolution range profile (HRRP) is required when other techniques such as inverse synthetic aperture radar (ISAR) are unavailable. This dissertation discusses the important preprocessing issues for HRRP target classification. In particular the issues of: aspect independent classification; target localisation; HRRP averaging and HRRP thresholding are highlighted. A classification experiment, using real data of fullscale aircraft, is conducted to further illustrate the preprocessing issues for radar target classification.

An algorithm to coherently average HRRPs is proposed. The algorithm is applicable when the target is at medium to long range or when the target rotation rate is small. The coherent averaging algorithm provides the best possible averaged HRRP, in terms of target scatterer detectability, for a given number of HRRPs averaged. The algorithm coherently processes a sequence of HRRPs and the target return is separated from the noise on the basis of Doppler frequency. The target return, which is localised in Doppler, is extracted to give a coherently averaged HRRP. The averaged HRRP is thresholded using constant false alarm rate (CFAR) processing.

DECLARATION

This thesis contains no material which has been accepted for the award of any other degree or diploma in any University or other tertiary institution, and to the best of the author's knowledge and belief contains no material previously published or written by another person, except where due reference has been made in the text.

Should the thesis be accepted for the award of the Degree, the author hereby consents to this copy, when deposited in the University Library, being made available for loan and photocopying.

Signature _____

Date March, 1995

ACKNOWLEDGMENTS

I have had the support and encouragement of many people. The people who immediately come to mind are:

Bob Bogner
My supervisor, Bob, has provided steady support and encouragement throughout my candidature. Bob has been particularly helpful in improving my technical writing style.

Brett Haywood and Ross Kyprianou
I'd like to thank Brett for the initial idea of ISARLAB. Working with Brett was very easy and he provided many useful comments on my work. I'd also like to thank Ross, our MATLAB guru who faithfully brought ISARLAB to life.

Graeme Nash
Graeme "The Wizard" Nash has been a consistent sounding board on which I could constantly refine new ideas. I thank him for many hours of fruitful discussion.

David Heilbronn
Through many changes of supervisor at MRD, David has been the only consistent factor.

John Cashen
John proved to have an infinite depth of knowledge in the area of radar backscatter phenomenology.

Kenneth Pope
Kenneth reviewed my thesis drafts and provided many useful comments.

Paul Dansie and Mark Ingham
My thanks go to Paul and Mark for collecting the radar data used in this thesis.

Grant Ward
Grant kept the computers running and configured special purpose computers which I could "hammer" with large simulations.

Microwave Radar Division, DSTO
I thank MRD for allowing me to complete a PhD whilst being employed as an Engineer. MRD provided not only financial support but also a focus for my studies and researchers with a wealth of knowledge that I could draw upon.

The Centre for Sensor Signal and Information Processing
I spent the latter part of my candidature at CSSIP. CSSIP is an excellent environment for research, with computer facilities second to none.

Finally I would like to thank my parents whose continuous support made everything possible.

A.Z.

LIST OF FIGURES

LIST OF TABLES

GLOSSARY

R	range to the target
Δr_s	slant-range resolution
Δr_c	cross-range resolution
w_s	slant-range ambiguity window
w_c	cross-range ambiguity window
l_c, w_c	cross-range length of target
β	radar waveform bandwidth
c	speed of light
β_D	target Doppler bandwidth with respect to cross-range
$\frac{\partial \beta_D}{\partial d_c}$	target Doppler gradient
$\bar{f}$	centre frequency of a radar waveform
Δf_D	Doppler frequency resolution
λ	wavelength (usually centre wavelength)
$\phi_{3\text{dB}}$	antenna half-power beamwidth
ω	target rotation rate seen by the radar
T	coherent integration time
$\Delta\theta$	target aspect change seen by the radar
Δt	sampling time interval
Δf	frequency step
n	number of frequency steps or range bins, as appropriate
N	number of sweeps or HRRPs, as appropriate
T_{pri}	pulse repetition interval
T_p	time length of transmitted pulse
$\theta_{\text{per sweep}}$	target aspect change per sweep
θ_0	target aspect at the beginning of a data record
θ	target aspect angle
v_T	target velocity perpendicular to the radar line of sight
v	target velocity
μ_{window}	mean amplitude of range window
μ_{target}	mean amplitude of target in range window
μ_{noise}	mean amplitude of noise in range window
σ	radar cross section or standard deviation, as appropriate
μ	mean

σ^2	variance
Σ	covariance matrix
$\boldsymbol{w}_i$	linear discriminant function
W	dimensionality reduction matrix
$g_i(\boldsymbol{x})$	Bayes discriminant function
$J(W)$	criterion function for linear discriminant analysis
S_B	between class scatter matrix
S_W	within class scatter matrix
P_{fa}	probability of false alarm
P_{d}	probability of detection
H_0	null hypothesis
H_a	alternative hypothesis
z	Gaussian test statistic
z_c	critical value for Gaussian test statistic
$E[\,]$	the expectation operator
DFT[ ]	the discrete Fourier transform operator
IDFT[ ]	the inverse discrete Fourier transform operator
z_i^{c}	signal received by coherent receiver at time t_i
z_i^{nc}	signal received by non-coherent receiver at time t_i
v^{c}	the coherent average of N samples
v^{nc}	the non-coherent average of N samples
$\mathcal{X}_t$	the threshold used for target detection
I_0	zero-order modified Bessel function of the first kind
I_1	first-order modified Bessel function of the first kind
L_i	integration loss
PRF	pulse repetition frequency

ABBREVIATIONS

ADC	Analogue to Digital Converter
AGC	Automatic Gain Control
ATR	Automatic Target Recognition
CAD	Computer Aided Design
CFAR	Constant False Alarm Rate
COTS	Commercial Off The Shelf
DFT	Discrete Fourier Transform
DPI	Dots Per Inch
DSA	Dominant Scatterer Algorithm
DSTO	Defence Science and Technology Organisation
FFT	Fast Fourier Transform
FLIR	Forward Looking Infra-Red
FM	Frequency Modulation
GUI	Graphical User Interface
HF	High Frequency
H–H	Horizontal–Horizontal polarisation
HRRP	High Resolution Range Profile or Profiling as appropriate
H–V	Horizontal–Vertical polarisation
I	In-phase signal component
IDFT	Inverse Discrete Fourier Transform
IR	Infra-Red
ISAR	Inverse Synthetic Aperture Radar
ISARLAB	ISAR LABoratory
ISLR	Integrated Sidelobe Level Ratio
JEM	Jet Engine Modulation
LFM	Linear Frequency Modulation
MRD	Microwave Radar Division
MSA	Multiple Scatterer Algorithm
NOSC	Naval Ocean Systems Centre
OCR	Optical Character Recognition
OSU	Ohio State University
PDF	Probability Density Function
PRF	Pulse Repetition Frequency

PRI	Pulse Repetition Interval
PSLR	Peak Sidelobe Level Ratio
Q	Quadrature-phase signal component
RAM	Radar Absorbent Material
RCS	Radar Cross Section
RF	Radio Frequency
RLOS	Radar Line Of Sight
RMO	Radar Master Oscillator
SAR	Synthetic Aperture Radar
SAW	Surface Acoustic Wave
SNR	Signal to Noise Ratio
TOT	Time On Target
V–H	Vertical–Horizontal polarisation
V–V	Vertical–Vertical polarisation
XYZ	ISARLAB global coordinate frame
xyz	ISARLAB local coordinate frame

PUBLICATIONS

A. Zyweck and R. E. Bogner,
"Radar target recognition using range profiles",
in *Proceedings of ICASSP 94, Adelaide, Australia*,
pp. V–177–180, April 1994.

A. Zyweck, B. Haywood, and R. Kyprianou,
"ISARLAB: A radar signal processing tool",
in *Proceedings of ICASSP 94, Adelaide, Australia*,
pp. II–373–376, April 1994.

A. Zyweck and R. E. Bogner,
"High-resolution radar imagery of the Mirage III aircraft",
IEEE Transactions on Antennas and Propagation,
vol. 42(9), pp. 1356-1360, September 1994.

A. Zyweck and R. E. Bogner,
"Coherent averaging of range profiles",
IEEE International Radar Conference RADAR95, Washington D.C. USA, May 8-11th 1995.

A. Zyweck and R. E. Bogner,
"Radar target classification of commercial aircraft",
to appear in *IEEE Transactions on Aerospace and Electronic Systems*,
vol. 31(4), October 1995.

Chapter I

INTRODUCTION

1.1 Motivation

Research in the area of radar target classification has been active for at least 30 years. The bulk of the research effort has been directed at aspect-independent techniques which classify a target according to its resonant response. Resonance techniques have not yet been fielded in an operational radar system.

Recently there has been a renewed interest in radar target classification, particularly in target classification from high resolution radar imagery. The primary driving force behind this resurgence in radar target classification research is the commercial availability of coherent high resolution radars. These high resolution radars resolve individual target scatterers in slant-range by employing a high bandwidth waveform. By using phase coherency and synthetic aperture processing these radars can also resolve scatterers in cross-range. Radars are now becoming equipped with modes which produce high resolution radar imagery for target classification. Unfortunately these high resolution radars only provide *operator based* target classification. Automatic classification of the high resolution radar imagery is desirable. It is the purpose of this dissertation to provide an insight into the issues of automatic radar target classification from high resolution radar imagery.

1.2 Dissertation overview and organisation

Chapter 2 begins by reviewing previous work on radar target classification. Each radar classification technique is reviewed with particular emphasis on the practical applicability of the technique in an operational context. The promising techniques of high resolution range profiling (HRRP), inverse synthetic aperture radar (ISAR) and jet engine modulation (JEM) are singled out and their suitability for radar target classification is discussed in detail. It is found that whilst ISAR and JEM may provide good signatures for target classification, their availability in an operational scenario cannot be guaranteed. In contrast, HRRPs have a high availability in all operational scenarios but they present a more difficult signature for target classification. Target classification from HRRPs is given particular emphasis in this thesis.

Chapter 3 provides an introduction to high resolution radar concepts. In Section 3.2

the concepts of slant-range resolution, cross-range resolution, coherency and synthetic aperture processing are reviewed. Section 3.3 reviews the commonly used high resolution radar waveforms and Sections 3.4 and 3.5 introduce HRRP processing and ISAR processing respectively.

Before designing any target classification system which uses sensor imagery as a basis for classification, it is important to understand the link between the physical attributes of the target and the corresponding features in the observed target imagery. An understanding of this nature (*domain knowledge*) enables the identification of the image features which provide target discrimination. A knowledge of the important features in the target imagery drives the design of feature extraction and preprocessing algorithms. Chapter 4 begins by summarising some of the theoretical aspects of radar backscatter from complex targets. In Sections 4.3 and 4.4 two experiments in which real radar data were collected from full-scale aircraft targets are described. High resolution radar imagery collected from real aircraft in flight and from a Mirage III aircraft on a turntable is displayed. The experiments were carefully chosen to highlight the important characteristics of radar backscatter and provide an introduction to radar backscatter phenomenology. Section 4.5 examines the results of the experimental investigation into radar backscatter phenomenology and discusses them in the context of radar target classification. Several important backscatter characteristics such as engine cavity backscatter and jet engine modulation (JEM) are highlighted. The phenomenological knowledge of radar backscatter gained in this chapter provides the basis for further direction in the remainder of this dissertation.

Even though high resolution radars are becoming more common there still is a fundamental lack of access to real high resolution radar data. Not everyone has access to an experimental radar and those who have are often involved in classified radar cross section (RCS) studies. The problem with collecting real data in the field is that it costs time and money. For the thorough study of high resolution radar target classification a huge amount of data is needed. Chapter 5 presents a high resolution radar simulator called ISARLAB which was specifically designed to meet the needs of target classification studies. The design of ISARLAB was based upon well established radar backscatter theory and the observations of radar backscatter from real full-scale aircraft made in Chapter 4. ISARLAB does not attempt to model all electromagnetic phenomena, but rather ISARLAB models to a level which satisfies the objective of producing realistic radar imagery for target classification studies. ISARLAB only models the essential target attributes which are likely to be useful for target classification. ISARLAB is validated by comparing the imagery produced from its simulated data to imagery produced from corresponding real data.

Chapter 6 addresses radar target classification from HRRPs. The chapter begins with Section 6.2 discussing HRRP preprocessing issues in detail. In particular, the issues

of: aspect independent classification; target localisation; HRRP averaging; and HRRP thresholding are highlighted. Much of the discussion and insight of this section is based upon the observations of Chapter 4. The remainder of Chapter 6 presents an experiment where real HRRPs are preprocessed and classified. Real data were collected from a local airport and the experimental objective was to differentiate Boeing 727 aircraft from Boeing 737 aircraft over a limited range of aspect angles. The techniques used for preprocessing and classification are not, by any means, the best way to achieve target classification but they are only intended to further illustrate the issues which were discussed in Section 6.2. Section 6.7 provides an overview of the target classification processing used in the chapter and the results of the target classification experiment are discussed in Section 6.8.

Chapter 7 presents a coherent averaging algorithm which produces the best possible averaged HRRP, in terms of target scatterer detectability, for a given number of HRRPs averaged. The algorithm is applicable when the target rotation rate is small. A small target rotation rate is most commonly seen when the target is at medium to long range. The chapter begins by reviewing the principles of non-coherent and coherent integration. Several well known results are derived and used later in the chapter. Section 7.4.1 outlines the operational context in which the coherent averaging of HRRPs is used. An overview of the coherent averaging algorithm is given in Section 7.4.2. The coherent processing used is essentially ISAR processing, but there is only a poor cross-range resolution obtained in the range-Doppler image. Tracking information is used to estimate the target Doppler bandwidth which in turn is used to determine the radar parameters for data collection. The required number of HRRPs are collected and coherent processing is performed on the collected sequence of HRRPs. A statistical test is evaluated to determine whether the coherent processing has been successful. If the target energy has been successfully separated from the majority of the noise on the basis of Doppler frequency, the target Doppler bin is extracted to give a coherently averaged HRRP. A CFAR based technique is used to threshold the range bins in the coherently averaged HRRP. A simulation comparing the coherent and the non-coherent averaging of HRRPs is presented in Section 7.5. The results from this simulation confirm that coherent averaging provides better averaged HRRPs than non-coherent averaging.

Chapter 8 summarises the important results of this dissertation and also outlines future research that is needed.

1.3 Original contributions

There has been a lack[1] of published work which has addressed the practical issues of radar target classification. Chapter 2 reviews potential radar target classification techniques and assesses the practical applicability of each technique. The promising techniques of high resolution range profiling (HRRP), inverse synthetic aperture radar (ISAR) and jet engine modulation (JEM) are singled out and their suitability for radar target classification is discussed in detail.

The majority of data which have appeared in the open literature have either been simulated or they have been collected from model targets in an anechoic chamber. Whilst the study of such data is undoubtedly useful, this data often lacks some important characteristics which are found in real data. Chapter 4 presents real radar imagery of commercial aircraft in flight and of a Mirage aircraft on a turntable. The radar imagery is examined and specific characteristics which have important implications for radar target classification are highlighted. In particular, the important radar backscatter phenomena of engine cavity backscatter and JEM are discussed.

Previously developed high resolution radar simulators have been complex and cumbersome to use or they have lacked the flexibility required for a radar target classification testbed. Chapter 5 presents a high resolution radar data simulator called ISARLAB which represents a practical way to generate the huge amounts of data required for the study of radar target classification. The simulated data produced by ISARLAB are used to generate radar imagery which is very similar in appearance to real radar imagery. ISARLAB was developed at the Microwave Radar Division, DSTO as part of a larger project. The author of this thesis had the major input into the specification and conceptual design of ISARLAB. The majority of the implementation (coding) of ISARLAB was carried out by Ross Kyprianou of MRD.

Chapter 6 discusses the important preprocessing issues for radar target classification from HRRPs. In particular, the issues of: aspect independent classification; target localisation; HRRP averaging; and HRRP thresholding are highlighted. Several solutions to each preprocessing issue are reviewed. Previous work which has not been based on real data has often ignored these fundamental preprocessing issues. The second half of the chapter presents a novel method for classifying aircraft HRRPs from a limited range of viewing aspects. Real radar data are collected from aircraft in flight and a target classification experiment is performed. The SNR of the HRRPs is increased by non-coherently averaging consecutive HRRPs. The target localisation problem is avoided by using the magnitude of the FFT as a shift-invariant transform. Dimensionality reduction based upon a generalised linear discriminant is used prior to final target classification. Final

[1] Cohen [1] has published a paper which has accurately reviewed radar target classification from a practical rather than an academic viewpoint.

classification of the test HRRPs is achieved using a Bayes classifier. The experiment presented in Chapter 6 does not provide the "final solution" to radar target classification from HRRPs but rather it provides a valuable insight on the subject.

Chapter 7 presents a coherent averaging algorithm which produces, in terms target scatterer detectability, the best possible averaged HRRP for a given number of HRRPs averaged. The algorithm is applicable when the target is at medium to long range or when the target rotation rate is small. The fact that ISAR imaging is not always possible, establishes a need for HRRP averaging. The principles of coherent and non-coherent integration are reviewed in the beginning of the chapter and an algorithm for coherently averaging HRRPs is proposed. The basic principle of coherent averaging is to oversample the target returns in Doppler and then separate the target from the noise according to Doppler frequency. The radar parameters are chosen according to an estimate of the target Doppler bandwidth. A sequence of HRRPs is collected and it is coherently processed to produce a range-Doppler image. A statistical test is proposed to determine whether the coherent processing is successful or not. If the coherent processing has been successful, the target Doppler bin is extracted from the range-Doppler image to give a coherently averaged HRRP. The coherently averaged HRRP is thresholded using a CFAR technique.

A series of five HRRP averaging simulations are presented to demonstrate the advantages of the proposed coherent averaging algorithm. The first three simulations show how the target scatterer detectability improves linearly with the number N of HRRPs averaged. The results from the simulations also confirm that coherent averaging produces better averaged HRRPs, in terms of target scatterer detectability, than non-coherent averaging. The performance gap (integration loss) between non-coherent averaging and coherent averaging is seen to increase as the SNR becomes smaller. Simulations 4 and 5 show the degraded performance of coherent averaging when the Doppler resolution Δf_D is set to values other than the ideal value of $\Delta f_D \approx \beta_D$. The reasons for the degraded performance when $\Delta f_D \neq \beta_D$ are detailed.

Chapter II

SURVEY OF RADAR TARGET CLASSIFICATION

2.1 Introduction

This chapter surveys previous research in the area of radar target classification. Each radar target classification technique is assessed in the context of operational radar target classification. Section 2.1.1 introduces the concept of radar cross section (RCS) and also introduces the three broad scattering regions corresponding to Rayleigh, resonance and optical radar backscatter. A taxonomy of radar target classification techniques is given in Section 2.1.2. A variety of radar target classification techniques are discussed in Sections 2.2, 2.3 and 2.4. The three most promising radar target classification techniques are singled out for discussion in Section 2.5.

2.1.1 Radar cross section

A simple characterisation of a target's scattering properties is given by its RCS. Knott [2, 3] formally defines radar cross section as

$$\sigma = \lim_{R \to \infty} 4\pi R^2 \frac{|E_s|^2}{|E_i|^2} \tag{2.1}$$

where R is the distance between the radar and target, E_s is the field strength at the radar receiver due to the target reflection or scattering, and E_i is the incident field strength at the target.

The RCS of a target is affected by the following factors:

- radar frequency;
- radar polarisation;
- target aspect;
- target size and shape;
- target composition.

The RCS of a target is usually parameterised by frequency, polarisation and viewing aspect. Frequency and polarisation can be controlled by the radar operator. Viewing

aspect can be controlled in cooperative data collection and it can be estimated in non-cooperative data collection.

The physics of radar backscatter from a target depends on the relationship between the wavelength of the electromagnetic illumination and the target size. Three broad scattering regions exist [3]:

The Rayleigh region *Wavelength is greater than target size.*

In this region there is little variation in the phase of the incident field over the target body. The gross target shape and size determines the radar backscatter and details of the exact target shape are not relevant.

The resonance region *Wavelength is approximately the same as target size.*

In this region the phase of the incident field changes significantly over the body of the target. In this region there are physical mechanisms by which electromagnetic energy becomes attached to one point on the target body and is reradiated from a different point on the target body. The target RCS varies slowly with aspect in the resonance region. The resonance region corresponds roughly to the high frequency (HF) band for typical target sizes.

The optical region *Wavelength is smaller than target size.*

In the optical[1] region the interactions between the different regions on the target body are very weak. The target is considered to be a collection of discrete scattering centres and the overall return from the target is the complex phasor sum of the individual scatterer returns. For typical target sizes the optical region corresponds to microwave frequencies or higher.

The majority of previous radar target classification research has been directed at the identification of radar target backscatter from the resonance region. This thesis addresses radar target classification in the optical backscatter region. The optical region is where the majority of radars operate and it is the favoured region for the implementation of an operational radar target classification system.

2.1.2 Radar target classification

It is the goal of a radar target classification system to classify a target from its radar return. Radar target classification research commenced at least 30 years ago. The bulk of the research effort has been directed at aspect-independent techniques which classify a target according to its return in the resonance scattering region. Classification techniques using target resonant responses have not yet been fielded in an operational radar system. Recently there has been a renewed interest in radar target classification,

[1] The optical region is also referred to as the *Fresnel* region.

particularly in techniques which provide target classification from high resolution radar imagery. Radar target classification is on the verge of becoming a standard function for new multi-mode radars. A number of radars already provide high resolution modes for target classification. Currently, the classification of high resolution radar imagery is done by the radar operator but automated classification is desired.

Non-cooperative radar target classification techniques can be subdivided into three broad categories:

Resonance techniques

Resonance techniques identify a target from its radar backscatter in the resonance region;

Structural techniques

Structural techniques identify a target by inferring the target's *physical structure* from its radar backscatter;

Dynamic techniques

Dynamic techniques identify a target by using *dynamic features* from the target's radar backscatter. An example is the modulation of radar signals caused by the rotating machinery of a target.

Target classification using radar is still very immature compared to target classification using other sensors such as forward looking infra-red (FLIR). Most general articles on automatic target recognition (ATR) [4, 5, 6] deal only briefly with radar sensors. Cohen [1] provides a good overview article on radar ATR and he mentions many important radar system design issues. The subject of radar ATR is also addressed in [7, 8].

2.2 Target classification using resonance techniques

The bulk of the previous literature on radar target classification has focussed on identifying targets from their radar backscatter in the resonance region. The resonance region has the major advantage that the target backscatter is approximately independent of aspect. While resonance region radar target classification is appealing from a theoretical viewpoint, there are major obstacles preventing its practical application. The particular obstacles which make the collection of target resonant responses difficult are:

A high power requirement

Very high power radars are required to excite the resonant modes of a target. The technology does not currently exist to produce the required power at a useful range from the radar.

A large antenna aperture requirement

For typical targets, the frequencies corresponding to the resonant responses lie in

the HF band. At these frequencies very large antenna apertures are required to achieve a narrow antenna beam with reasonable angular resolution.

The received signal has a low SNR

Not only are the resonant modes of a target difficult to excite but the energy reradiated from these resonant modes is very small. Consequently it is difficult for the radar receiver to detect the return from these resonant modes at a useful range from the illuminated target.

Research into the classification of target resonant responses has slowed considerably with the advent of high resolution radars.

2.2.1 The E–pulse technique

The extinction–pulse (E–pulse) technique has been the subject of much academic research [9, 10, 11]. The basis of this technique is to transmit a tailored waveform for each potential target type. The tailored waveform is designed to produce a zero or single resonant response from the target. The technique has the advantage of aspect-independence but it suffers from the practical obstacles common to resonance techniques. In [10] Chen *et al.* report that research in the laboratory for the E–pulse technique is essentially complete and that future work will be directed at system development issues. It will be interesting to see if an operational system eventuates.

2.2.2 Ohio State University

A particularly large radar research group exists at Ohio State University (OSU). OSU has strong contacts with local defence laboratories and its research is focussed on radar ATR in the HF or resonance frequency band. The research group publishes profusely e.g. [12, 13, 14, 15, 16, 17, 18, 19, 20, 21]. OSU has a microwave anechoic chamber [12] which has been used to establish a database of radar backscatter from model aircraft.

The early work at OSU [22, 23, 24, 25, 15] considered discrete frequency measurements in the HF band for target classification. More recently OSU researchers have examined parametric methods for spectral estimation which may improve the quality of the resonant response used for target classification [20, 17]. There has also been significant research in applying syntactic classification techniques to radar target classification [19, 14].

2.3 Target classification using structural features

The three–dimensional physical structure of a target can be inferred from its radar backscatter if a radar waveform with a suitable bandwidth is used. High resolution

radar, which is discussed in Chapter 3, can be used to differentiate between different target types.

2.3.1 *High resolution range profiling*

High Resolution Range Profiling (HRRP)[2] generates a one–dimensional projection of the target scattering centres onto the radar line of sight (RLOS). The target structure can be inferred, although not necessarily unambiguously, from a High Resolution Range Profile (HRRP). An introduction to HRRPs is given in Section 3.4 and previous research on radar target classification from HRRPs is discussed in Section 6.2. A discussion of target classification from HRRPs is given in Section 2.5.1.

2.3.2 *Inverse synthetic aperture radar imaging*

Inverse synthetic aperture radar (ISAR) is a technique which is used to image targets such as ships and aircraft. An ISAR image is a two–dimensional projection of a target's scattering centres onto an imaging plane. The imaging plane is normally range versus angle. An introduction to ISAR is given in Section 3.5. A discussion of target classification from ISAR imagery is given in Section 2.5.3.

Systems which classify ISAR ship imagery are discussed in [26, 27]. Both systems apply significant image preprocessing before classification. The actual preprocessing used is similar to that used for preprocessing IR images. A detailed discussion of both of these systems is beyond the scope of this thesis and it suffices to say that traditional image processing and pattern recognition techniques can be used to classify good quality ISAR imagery. Neither of these papers address how often good quality ISAR imagery is available. The availability of good quality ISAR imagery is discussed in Sections 3.5.3 and 3.5.4.

2.4 Target classification using dynamic features

Almost all airborne targets contain some form of rotating machinery, which causes the frequency modulation of incident radar signals. This modulation can be very prominent and hence it can used as a basis for target classification. Techniques which exploit modulation effects are commonly referred to as *Doppler* techniques. Radar returns from helicopters exhibit significant modulation due to the exposed main and tail rotors of a helicopter [28, 29]. Jet engines also impart significant jet engine modulation (JEM) [30, 31, 32] on the incident radar signal.

---

[2] The abbreviation HRRP is used in this thesis to represent High Resolution Range Profiling which is a target classification technique or High Resolution Range Profile which is the resultant one–dimensional projection of the target scattering centres onto the RLOS.

Doppler techniques are probably the most researched technique for radar target classification but there is a lack of open literature references on the subject because of national security interests. Nevertheless, some excellent papers such as [30] have appeared recently. A discussion on target classification from JEM is given in Section 2.5.2.

2.5 A comparison of promising radar ATR techniques

For practical radar target classification there are only three techniques which are likely to be implemented in a operational radar. These techniques are HRRP, ISAR and JEM. The majority of research work undertaken in defence research laboratories has been focussed on these three techniques whereas the majority of work at universities has been focussed on resonance techniques. In Sections 2.5.1, 2.5.2 and 2.5.3 the merits of HRRP, JEM and ISAR are discussed.

2.5.1 HRRP

HRRP offers the possibility of target classification at all viewing aspects. The only prerequisite for collecting HRRPs is a radar waveform with a large enough bandwidth. The collection of HRRPs requires only a short radar dwell time on target (TOT) since no coherent integration is required. A short TOT is important if the radar has other surveillance functions to perform or if it is important to minimise the emissions of the radar. A HRRP can always be collected whereas ISAR or JEM require special conditions for data collection. HRRPs are not inherently suitable for radar operator interpretation and hence automated classification is desired. Since HRRPs are a one–dimensional projection of the target scatterers onto the RLOS, there may be situations where the unambiguous interpretation of a HRRP is not possible. In general HRRPs may not provide the best signature for target classification, but their guaranteed availability makes them very useful when other techniques such as ISAR or JEM are not available.

2.5.2 JEM

Doppler techniques classify targets from modulation effects caused by rotating machinery. Doppler techniques are most useful for target types where modulation effects are significant. Target types which exhibit significant modulation effects include helicopters and jet aircraft. Doppler techniques require a radar mode with a very high pulse repetition frequency (PRF) to unambiguously sample the Doppler frequencies produced by the target. Maintaining a high PRF when the target is at a long range is a considerable challenge for the radar system designer. A long TOT is required to achieve a suitable

Doppler frequency resolution[3], although it may be possible to reduce the TOT requirement by employing parametric spectral estimation. For jet aircraft JEM is only seen at aspects within ± 70° of head-on[4]. JEM information can be obtained at all aspects for helicopters.

2.5.3 *ISAR*

ISAR techniques offer the greatest potential for target classification. The images produced have a high SNR due to the coherent processing used and they have the potential to be recognised by a trained radar operator. The main drawback with ISAR is that good ISAR images are not always obtainable within a reasonable TOT. To obtain a good ISAR image there must be suitable relative motion between the target and the radar. The required relative motion cannot be guaranteed in all target classification scenarios[5]. The necessary preconditions for ISAR imaging are discussed in Sections 3.5.3 and 3.5.4. In summary, a good ISAR image provides excellent target information, but unfortunately a good ISAR image is not available all of the time.

The *projection plane* of an ISAR image refers to the plane onto which the target's scattering centres are projected. The orientation of the projection plane depends on the target's rotational motion. The RLOS lies in the projection plane and the target's rotation vector is normal to the projection plane. Since the target motion is unknown it is often difficult to deduce the projection plane of an ISAR image and this makes feature extraction and subsequent classification difficult.

2.5.4 *Discussion*

Table 2.1 compares the three techniques of HRRP, ISAR and JEM. Figure 2.1 shows the angular viewing sectors over which each of the three techniques are applicable. It is evident that neither of the three techniques of HRRP, ISAR and JEM suffices in its own right for complete target classification. A comprehensive radar target classification system should include all three techniques to achieve the best performance in all scenarios. The best performance in all scenarios could be achieved by providing three different radar modes for HRRP, ISAR and JEM. When the preconditions for ISAR or JEM exist, these modes are used, but when all else fails the HRRP mode is used as a fall back. HRRPs represent a broadly applicable technique from which reasonable results may be possible. ISAR and JEM offer better performance if the conditions are appropriate.

---

[3] For Discrete Fourier Transform (DFT) based spectral estimation, a longer observation time gives a better frequency resolution.

[4] A head-on aspect is the situation when the target is travelling directly towards the radar.

[5] ISAR is not possible for the particularly important case of the target heading directly towards the radar.

For the particular application of aircraft classification at long range, HRRP is an important technique. ISAR is inappropriate because of the long time on target required to form an image. JEM only provides target classification at close to head-on aspects. This thesis suggests that HRRP is a promising technique for long-range aircraft target classification.

A comparison between various radar target classification techniques

Feature	HRRP	ISAR	JEM
Signature variability	The shape of HRRPs vary with aspect. The amplitude levels in a HRRP can vary drastically with small changes in aspect.	ISAR images vary according to the relative motion between the target and the radar. The image projection plane is often difficult to determine.	JEM varies according to the engine rotation rate but this dependency can be removed. JEM characteristics do not vary with aspect but the strength of the JEM return does vary with aspect.
Radar mode requirements	A high bandwidth radar mode is required.	A coherent high bandwidth radar mode is required.	A coherent, high PRF radar mode is required.
Cost of radar system	A HRRP mode is relatively inexpensive.	An ISAR mode is relatively expensive due to the coherent processing required.	A JEM mode is relatively expensive due to the coherent processing required.
Time on target required	A very short time on target is required.	The target is required to undergo a certain aspect change for imaging. If the target is at long-range this TOT may be significant. If the image is produced from target-induced motion then only a small TOT is required.	The TOT determines the Doppler resolution achievable. A longer TOT gives a better Doppler resolution. A good Doppler resolution is important for JEM target classification.
Operator interpretability	It is very difficult for an operator to visually interpret a HRRP. Automated classification is essential.	The contrast of an ISAR image is usually high due to the coherent processing gain. ISAR images may be suitable for operator interpretation although automated classification is still desired.	Operator interpretation of JEM is difficult and automated classification is essential.
Processing required	The generation of HRRPs requires minimal processing.	The generation of an ISAR image requires a large amount of processing.	The generation of JEM information requires minimal processing.
Aspect	HRRPs can be obtained at all aspects, although broadside HRRPs may be of limited use.	ISAR images require the target to undergo a certain aspect change. It is not always possible to utilise the induced motion of a target to form an ISAR image. For example, in low sea states the ISAR imaging of ships is not possible.	JEM signatures can only be obtained at aspects within 70 degrees of head-on.

Table 2.1: A comparison of the merits of using HRRP, ISAR and JEM for radar target classification.

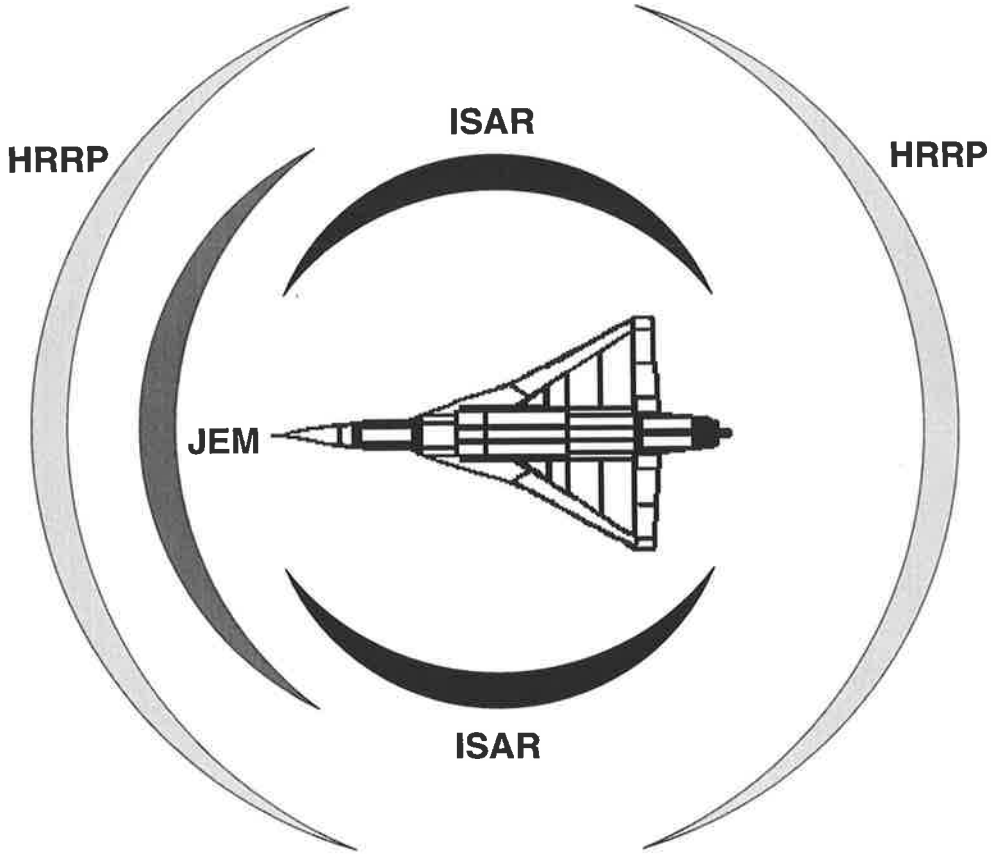

Figure 2.1: The angular sectors in which the radar ATR techniques of HRRP, ISAR and JEM are applicable.

2.6 Summary

Section 2.1.1 reviewed the concept of radar cross section. It was noted that for a given target, RCS is parameterised in terms of frequency, polarisation and viewing angle. The three regions of Rayleigh, resonance and optical radar backscatter were reviewed. Section 2.1.2 categorised radar target classification techniques as either:

- Resonance techniques;
- Structural techniques;
- Dynamic techniques.

It was found that the majority of previous research work was directed at target classification using resonant responses. Resonance techniques are conceptually appealing but there are several serious problems with their practical implementation. Large powers, large antenna apertures, and high receiver sensitivities are required for the implementation of target classification from resonant responses.

The three techniques of HRRP, ISAR and JEM were identified as being the most promising radar target classification techniques. These three techniques were discussed in Section 2.5 and it was found that each technique had particular drawbacks. It was concluded that a radar should be equipped with a number of classification modes with each mode corresponding to a particular target classification technique. The appropriate radar mode can then be chosen according to the target encounter scenario.

Chapter III

INTRODUCTION TO HIGH RESOLUTION RADAR

3.1 Introduction

3.1.1 Chapter purpose

This chapter introduces some of the concepts associated with high resolution radar and provides a background for the material presented in later chapters. The discussion of high resolution radar is not intended to be complete or detailed. Some of the introductory material in this chapter is based upon the excellent book by Wehner [33]. This book should be used by the reader as a primary reference. Mensa [34], Knott [2], and Rihaczek [35] are also good high resolution radar references.

3.1.2 Chapter overview

Section 3.2 introduces the high resolution radar concepts of slant-range resolution, cross-range resolution and coherency. The three commonly-used high resolution radar waveforms are discussed in Section 3.3. Section 3.4 provides a short introduction to high resolution range profiles (HRRP). A brief introduction to inverse synthetic aperture radar (ISAR) is given in Section 3.5. Section 3.5 does not provide a complete treatment of ISAR but rather it emphasises the aspects of ISAR processing which are important for this thesis.

3.2 High resolution radar concepts

3.2.1 What is high resolution?

In [33] Wehner provides the following explanation of radar range resolution:

> *The range resolution of a radar can be defined in terms of its ability to resolve point targets that are separated in range to the radar.*

High resolution is typically used to denote the ability to resolve individual scattering centres on a target. High resolution is a generic term which is not linked to any particular absolute resolution. Nevertheless, for typical targets, the term high range resolution is generally used when the target body is divided up into 10 or more resolution bins. For

a target of range length 50 metres a range resolution of greater than 5 metres could be called "high resolution".

Not only is it possible to achieve high resolution in slant-range[1] , but it is also possible to achieve high resolution in cross-range. For high resolution in slant-range a *large bandwidth* is needed. To achieve high resolution in cross-range, a very narrow beam antenna or *synthetic aperture* processing is needed. The concepts of slant-range resolution and cross-range resolution are discussed in Sections 3.2.2 and 3.2.4 respectively.

3.2.2 High resolution in slant-range

High resolution in slant-range corresponds to high resolution in time. A high bandwidth waveform is required to achieve high resolution in time. Slant-range resolution Δr_s is related to the radar waveform bandwidth by

$$\Delta r_s = \frac{c}{2\beta} \tag{3.1}$$

where c is the speed of propagation and β is the bandwidth of the waveform. A high bandwidth can be achieved with a number of different waveforms. Some of the more common waveforms are:

- Short pulse waveforms, which are discussed in Section 3.3.1;
- Pulse–compression waveforms, which are discussed in Section 3.3.2;
- Stepped frequency waveforms, which are discussed in Section 3.3.3.

The bandwidth of a radar waveform is real in the case of a pulse–compression or a short pulse waveform and it is synthesised in the case of a stepped frequency waveform. Other methods used to achieve a high bandwidth are described in [33].

3.2.3 Coherency

Coherency is necessary if cross-range resolution is required. There are two forms of coherence which are needed depending on the type of waveform being used. For a pulse–compression waveform, *intrapulse* coherence is required. Wehner [33] describes intrapulse coherence as:

> *Intrapulse coherence means that the waveform phase is preserved through the transmitter. In this way, signals for each echo pulse can be compressed on the basis of the known phase characteristics of the transmitted pulse.*

---

[1] *Slant-range* refers to range measured along the radar line of sight RLOS. The term *down-range* is sometimes used interchangeably. *Cross-range* is a direction orthogonal to the RLOS. This direction is usually in azimuth but the actual cross-range direction depends on the relative motion between the target and the radar.

Pulse–compression is not possible without intrapulse coherence through the transmitter. For a stepped frequency waveform another type of coherence is required. This second form of coherence is called *interpulse* coherence. As the name suggests interpulse coherence means that the relative phase differences between the successive transmitted pulses are known. Wehner comments:

> *A radar with interpulse coherence defined in this manner can measure*[2] *the RF phase difference between the transmitted and echo pulses.*

3.2.4 High resolution in cross-range

Radar resolution in azimuth depends upon the beamwidth of the antenna being used. The 3 dB beamwidth $\phi_{3\text{dB}}$ is a convenient measure of beamwidth and it is determined by

$$\phi_{3\text{dB}} \approx \frac{\lambda}{d} \tag{3.2}$$

where λ is the wavelength and d is the antenna size. The resolution in cross-range Δr_c depends directly upon the resolution in azimuth and the range to the target R. For small beamwidths[3]

$$\Delta r_c = R\phi_{3\text{dB}} \tag{3.3}$$

From Equations 3.2 and 3.3 it can be seen that there are two ways to increase cross-range resolution:

1. Reduce the wavelength being used;
2. Increase the size of the antenna or aperture.

While it may seem simple to reduce the wavelength to increase the resolution, such a wavelength reduction does affect other aspects of the radar system. Reducing the wavelength affects atmospheric propagation losses and the radar system size and cost. Increasing the antenna size increases the cross-range resolution, but physical limitations dictate an upper bound on the size of the antenna that can be used. Mobile platforms also place harsh constraints on the physical size of an antenna. In summary, the limitations on antenna size and wavelength determine an upper bound on the cross-range resolution that can be achieved using a real aperture antenna.

---

[2] The phase is usually measured relative to a radar master oscillator (RMO). Wehner mentions that if the transmitter is intrapulse coherent, then the relative phase can be conveniently measured relative to the RF signal *input* to the transmitter.

[3] Where $\sin\theta \approx \theta$.

Synthetic aperture radar (SAR)

It is possible to create a *synthetic aperture* if there is a relative aspect change between the target and the radar. This is the principle used for Synthetic Aperture Radar (SAR) and ISAR imaging. Since SAR processing is not directly relevant to this thesis, a detailed discussion is not included here, but instead the reader is directed to [33]. An important equation which comes from synthetic aperture radar theory is

$$\begin{aligned} \Delta r_c &= \frac{\lambda}{2\omega T} \\ &= \frac{\lambda}{2\Delta\theta} \end{aligned} \tag{3.4}$$

where λ is the wavelength, T is the coherent integration time, $\Delta\theta$ is the aspect change seen by the radar and ω is the relative rotation rate between the radar and the target. It can be seen from Equation 3.4 that the cross-range resolution achievable depends on the absolute amount of aspect change between the radar and the target.

3.3 High resolution radar waveforms

3.3.1 Short pulse waveforms

High resolution in the time domain corresponds directly to high resolution in slant-range. A resolution of Δt in the time domain corresponds to a slant-range resolution of $\Delta r_s = \frac{c\Delta t}{2}$ where the factor of two appears because of the travel of energy to and from the target. Decreasing the pulse width was the first approach which was used by radar designers to increase range resolution. This approach worked to an extent but as the pulse width was decreased, certain practical problems which limited the usefulness of the technique were encountered. The two main problems with very short pulse widths are:

High sampling rates

A very short pulse width, or more correctly the corresponding high bandwidth, means that a very high Analogue to Digital Converter (ADC) sampling rate is required. A 1 μs pulse means that a minimum sampling rate of 2 MHz is required to satisfy the Nyquist criterion. It is difficult and costly to simultaneously achieve a high sampling rate and a large number of digitised bits in an ADC.

Low average power

A very short duration pulse has a very small average power. A large average power is desired since it is this waveform characteristic that determines the detectable range [36] of a target . The ratio of peak power to average power is very large for a short pulse waveform. A high peak power requirement imposes high stresses on the radar system components and it makes a short pulse system very expensive to build.

To achieve a high slant-range resolution without using short pulses, it is necessary to spread the radar waveform energy over time whilst still maintaining a high bandwidth. Two different techniques which achieve this are discussed in Sections 3.3.2 and 3.3.3.

3.3.2 *Pulse–compression waveforms*

A block diagram of a pulse–compression system is shown in Figure 3.1. The key to a pulse–compression system is the transmission of an *expanded* high bandwidth waveform. Expanded means that the waveform energy is spread over time. On reception this waveform is *compressed* to give a high resolution in time. The expansion and compression operations can be done in hardware (passive pulse–compression) or in software (active pulse–compression). A surface acoustic wave (SAW) device is often used for passive pulse–compression since it is a frequency-dispersive device.

Analogue to digital conversion can be accomplished before or after pulse–compression but it is usually done before compression to limit the ADC dynamic range needed. Note that in this case the signal bandwidth is the same before and after compression, but the dynamic range of the signal is significantly higher after compression.

The expansion of a narrow pulse is not necessary if a suitable expanded waveform is produced by another means. The *chirp* waveform, shown in Figure 3.2, is an example of such an expanded waveform. It is produced by linearly increasing the frequency of an oscillator. With fast inexpensive digital synthesisers now available this is becoming a common and economical way to produce a high bandwidth waveform. The increasing use of digital components is bringing down the cost of radar systems and it is also increasing radar system flexibility. For more information on chirp and related pulse–compression techniques see [37, 38].

Why chirp instead of other pulse–compression waveforms?

The chirp waveform is a type of pulse–compression waveform which has several advantages over other non-linear frequency modulated (FM) waveforms [37]. The advantages which have led to the popularity of linear FM (LFM) are:

- The pulse shape and SNR of a chirp waveform are fairly insensitive to Doppler frequency shifts. This means that the same matched filter can be used to process incoming chirp pulses with different Doppler shifts. Other non-linear FM waveforms require different matched filters when the returned signal is Doppler shifted.

- The linear chirp waveform is easy to generate using either active or passive techniques.

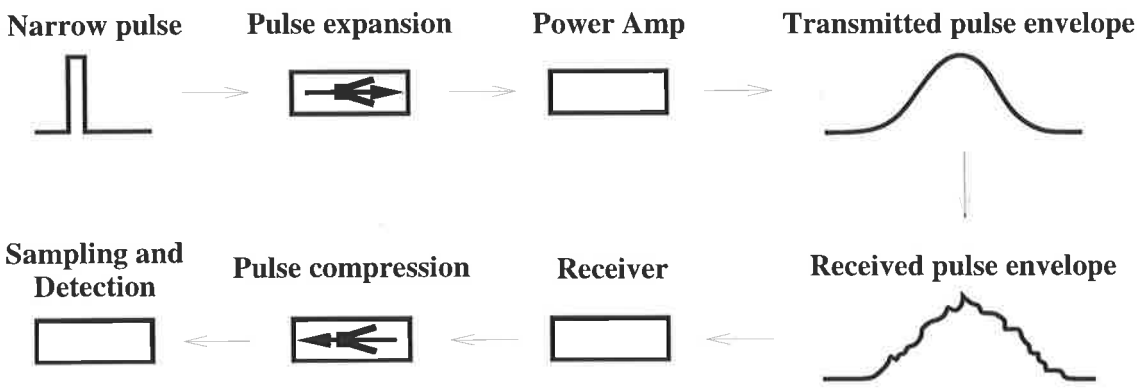

Figure 3.1: A simple illustration of pulse–compression.

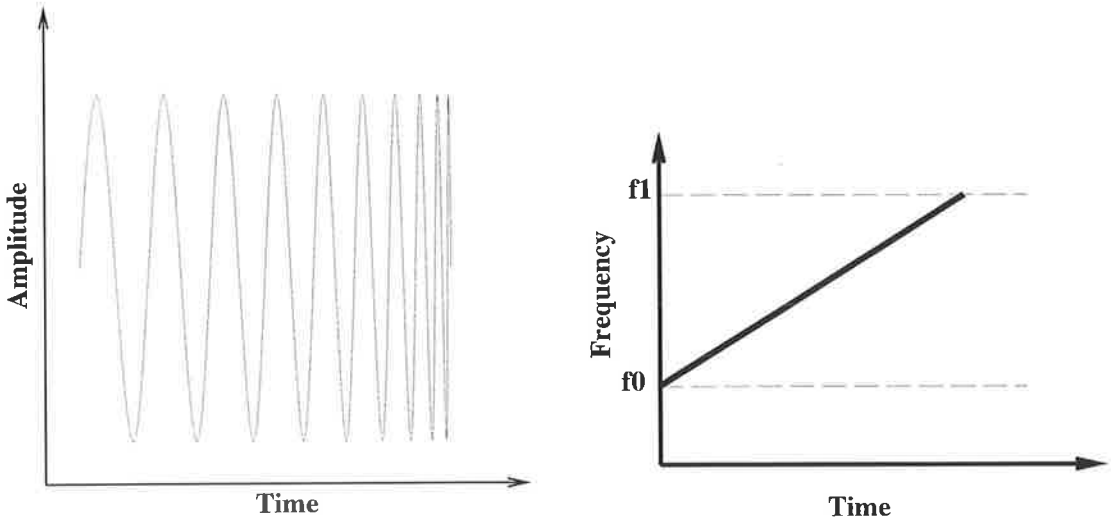

(a) The linear chirp waveform.

(b) The frequency versus time characteristic for the linear chirp waveform.

Figure 3.2: The linear chirp waveform.

Sidelobe reduction

The frequency envelope of a chirp is approximately rectangular. On transmission the frequency envelope (or conversely the time envelope) is not usually modified since this enables the maximum possible average power to be transmitted. If the frequency envelope of the receiving filter is also rectangular (the *matched* condition), then the result of the matched filter exhibits large sidelobes in time. The sidelobes in time (range) are undesirable since they can obscure other targets. To reduce these range sidelobes the receiver filter is usually mismatched [37]. A small penalty in SNR (1-3 dB) is paid for the mismatched filter. The filter is mismatched by windowing (weighting) the rectangular frequency envelope of the matched filter. The windowing broadens the impulse response of the matched filter and reduces the range sidelobes. For a good discussion on windowing issues see [39].

3.3.3 *Stepped frequency waveforms*

High resolution in slant-range corresponds to high resolution in time which in turn is achieved by using a wide bandwidth waveform. Instead of collecting the target scattering information in the time domain, a *stepped frequency* waveform collects the information in the frequency domain. Once the information has been collected in the frequency domain it is transformed into an equivalent representation in the time domain. This transformation is normally achieved using the inverse discrete Fourier transform (IDFT). HRRPs collected using a stepped frequency waveform are referred to as *synthetic* HRRPs.

Figure 3.3 illustrates a stepped frequency waveform. A *sweep* (or burst) of n pulses is transmitted and the in-phase (I) and quadrature (Q) receiver samples are stored for each pulse. The frequency of each pulse differs from the previous pulse by Δf. The effective bandwidth of the sweep is $\beta = n\Delta f$. Note that the bandwidth is called *effective* because it is synthesised from a number of discrete frequencies. The time between pulses, pulse repetition interval (PRI) is T_{pri} and each pulse has a length of T_p. A HRRP is formed by transforming a sweep, via the IDFT, into the time domain. In an imaging scenario, the radar transmits N sweeps to achieve an appropriate synthetic aperture for cross-range processing.

Practical considerations

Using a stepped frequency waveform to achieve a high resolution in range requires a careful choice of the radar waveform parameters. The parameters to be decided upon and the significance of each are listed in Table 3.1. An example of choosing these stepped frequency waveform parameters is given in Appendix B. Appendix B covers the stepped frequency waveform which was used to collect ISAR images of aircraft at a local airport. For more information on the data collection at a local airport, see Section 4.4.

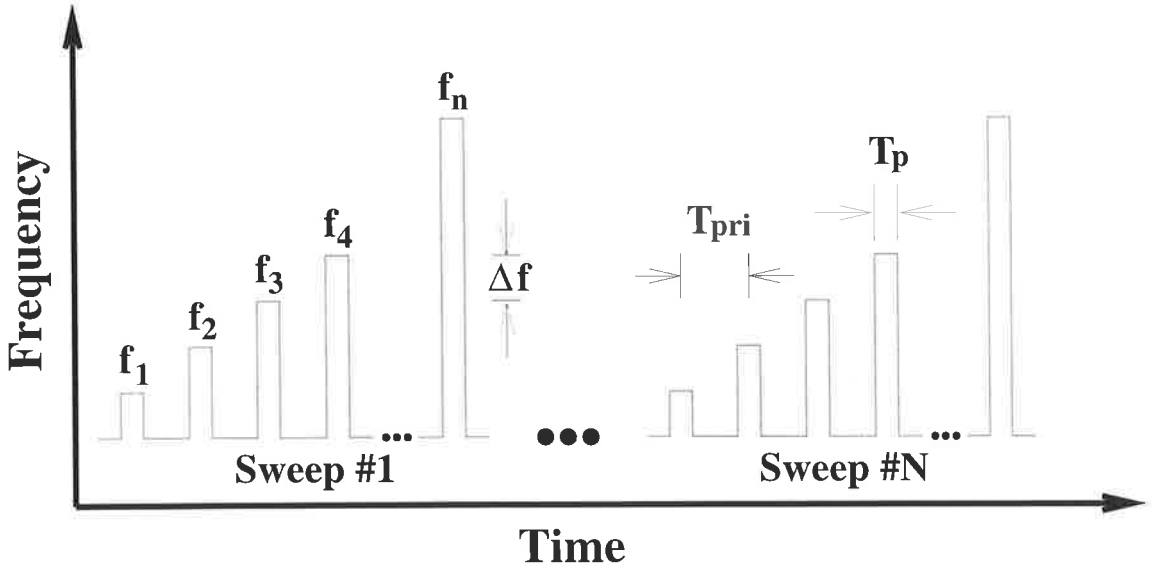

Figure 3.3: The stepped frequency waveform. T_p is the pulse width and T_{pri} is the PRI. In this particular waveform there are n frequency steps of Δf and a total of N sweeps.

Waveform parameter.	Meaning and significance.
Δf	The frequency increment between successive pulses in a sweep.
n	The number of discrete pulses per sweep.
N	The number of sweeps coherently processed to form an ISAR image.
β	The effective bandwidth of a sweep $\beta = n\Delta f$. β determines the slant-range resolution according to Equation 3.1.
T_p	The pulse width. This must be large enough (in range) to envelop the entire target.
T_{pri}	The pulse repetition interval (PRI). This must be large enough to prevent Doppler ambiguities and also be small enough to prevent range ambiguities.

Derived quantities.	Meaning and significance.
Δr_s	The slant-range resolution which is determined by Equation 3.1.
Δr_c	The cross-range resolution which is determined by Equation 3.4.
w_s	The size of the slant-range ambiguity window which is calculated from $w_s = n\Delta r_s$.
w_c	The size of the cross-range ambiguity window which is calculated from $w_c = N\Delta r_c$.

Table 3.1: The parameters of a stepped frequency waveform and the quantities which can be derived from the waveform parameters.

3.3.4 *Pulse–compression versus stepped frequency*

Operational radars normally employ pulse–compression waveforms. Stepped frequency waveforms are used by research radars and RCS instrumentation radars. The major limitation of a stepped frequency waveform is that it takes too long to collect the data from the target. This limitation is a consequence of having to transmit n pulses to get a single HRRP. For a radar required to operate with a high PRF, a stepped frequency waveform is not feasible. Table 3.2 compares pulse–compression and stepped frequency waveforms. With the advent of high speed digital waveform synthesis, future radars may employ a combination of a chirp and stepped frequency waveform called a *stepped chirp* waveform [33]. The extra processing required by this type of waveform is offset by the extra flexibility it provides.

A comparison of the pulse–compression and stepped frequency waveforms

	Pulse–compression	Stepped frequency
Cost	Pulse–compression devices are normally expensive. High speed, high dynamic range ADC's are expensive. The front end of the radar must be designed to cope with a high instantaneous bandwidth.	With the advent of relatively inexpensive digital frequency synthesisers stepped frequency radar is a very affordable technology. The front end of the radar need only cope with a narrow instantaneous bandwidth.
Time on target	A pulse–compression radar minimises the time on target. A single pulse returns a single HRRP.	A stepped frequency radar needs a lot of time on target to collect target scattering information. This is a critical issue if radar emissions need to be minimised. When processing stepped frequency data it is normally assumed that the target motion is not significant during a sweep. This assumption holds only if the effective PRI of the sweeps is fast enough to oversample the target's Doppler bandwidth.
Flexibility	A passive pulse–compression radar is not very flexible in the waveforms it can transmit. An active pulse–compression radar provides more flexibility.	A stepped frequency radar provides a lot of flexibility in collecting target scattering information.
Resolution	The best possible resolution is usually limited by the maximum ADC sampling rate available.	Since the effective bandwidth of a stepped frequency waveform can be very large, the resolution obtainable can be extremely high.
Processing	A pulse–compression waveform generally requires less processing than a stepped frequency waveform. This may not be true if active pulse–compression is used.	A stepped frequency waveform generally requires more processing than a pulse–compression waveform.

Table 3.2: A comparison of the merits of using pulse–compression and stepped frequency waveforms for collecting HRRPs. The short pulse waveform has not been included in this comparison because it is the least suitable waveform for collecting HRRPs.

3.4 High resolution range profiles (HRRP)

A high resolution range profile (HRRP) represents a one–dimensional range projection of a target's complex[4] return onto the RLOS. Figure 3.4 illustrates how a HRRP is formed. Examples of HRRPs collected from fullscale aircraft targets are shown in Figure 3.5.

A HRRP separates the scatterers on a target in slant-range. A *range bin* is the minimum resolution element which is resolved in a HRRP. If a number of target scatterers exist in a particular range bin then their backscatter returns are combined coherently at the radar receiver. It is not possible to identify the individual scatterer returns. An example of this problem is shown in Figure 3.6.

A pulse–compression waveform produces a HRRP for every pulse transmitted. A stepped frequency waveform produces enough data for a single HRRP every n pulses, where n is the number of discrete frequency steps used in the waveform. An IDFT transforms the discrete frequency samples into a synthetic HRRP.

[4] When (complex) HRRPs from a coherent radar are viewed, only the *amplitude* information is displayed. A non-coherent radar only produces the amplitudes of target returns.

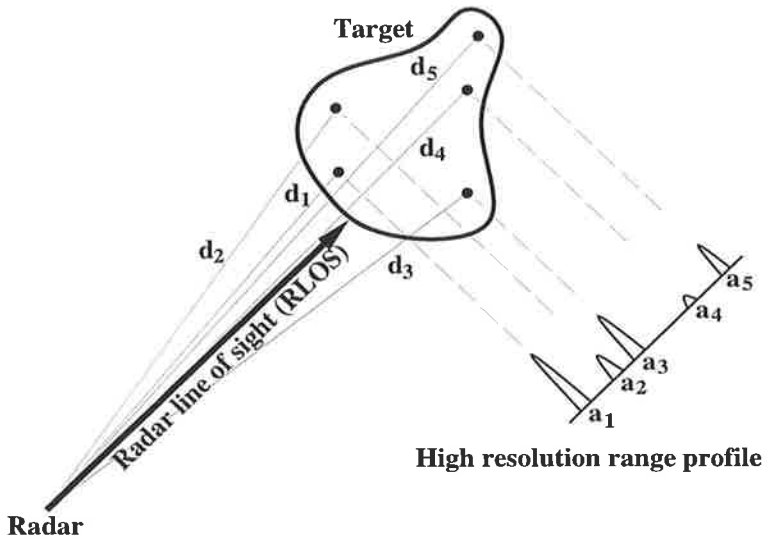

Figure 3.4: The relationship between a HRRP, the radar and the target. Note how the target positions (in range) are projected onto the RLOS. $d_1 \ldots d_5$ represent the distances from the radar to the individual scattering centres. $a_1 \ldots a_5$ represent the amplitudes of the backscatter from the discrete scattering centres.

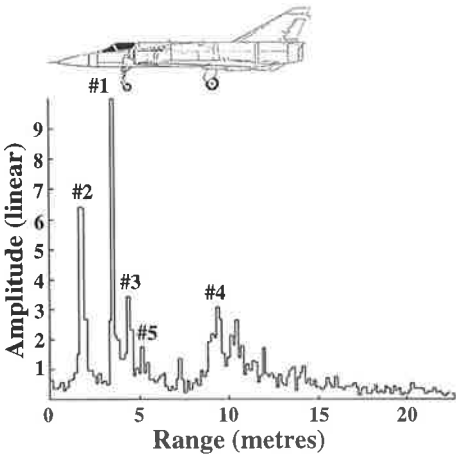

(a) A HRRP of the Mirage aircraft taken from a head-on aspect. The prominent backscatter features are #1 cockpit canopy; #2 radar dish; #3 front undercarriage; #4 rear undercarriage; #5 engine intake.

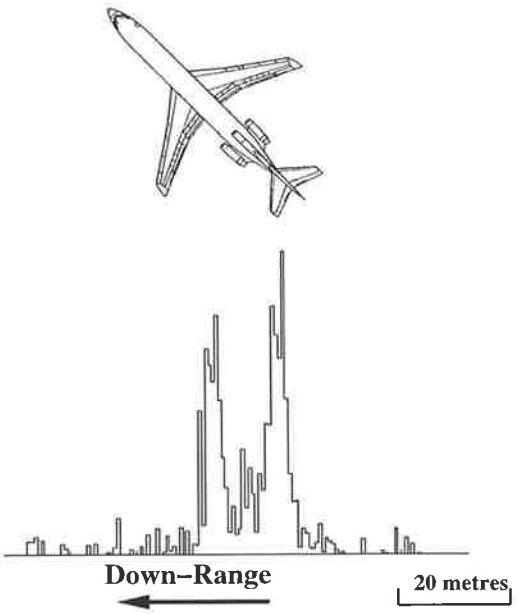

(b) A typical HRRP of the Boeing 727 aircraft. The aspect is 135° from head-on.

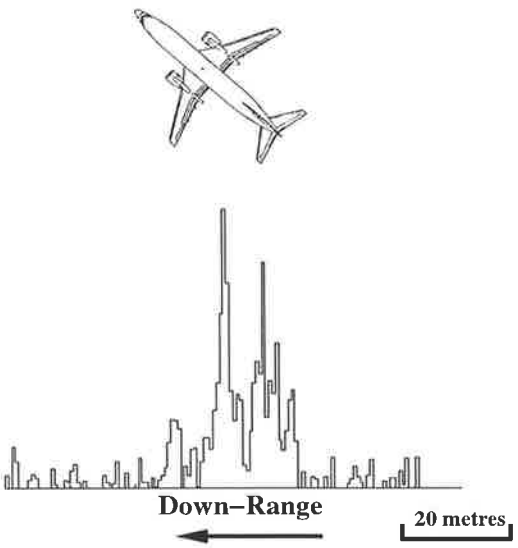

(c) A typical HRRP of the Boeing 737 aircraft. The aspect is 140° from head-on.

Figure 3.5: Three examples of HRRPs collected from real fullscale targets. The Mirage data were collected from a turntable whereas the data from the in-flight Boeing 727 and Boeing 737 aircraft were collected at a local airport.

3.5 Inverse synthetic aperture radar (ISAR)

3.5.1 Overview of ISAR

Inverse synthetic aperture radar (ISAR) is a technique which is used to image targets such as ships and aircraft. An ISAR image is a two–dimensional projection of the target scattering centres onto an imaging plane. The imaging plane is normally range versus angle. ISAR resolves target scatterers in two orthogonal directions; slant-range and cross-range. A HRRP only resolves scatterers in the slant-range direction. The relationship between a HRRP and an ISAR image is shown in Figure 3.6. ISAR achieves slant-range resolution with a wide bandwidth waveform and cross-range resolution with a synthetic aperture. To create a synthetic aperture, relative (rotational) motion between the radar and target is needed. In ISAR the target normally contributes the main component of the rotational motion, whereas in SAR the radar normally contributes the main component of the rotational motion. The basic theory of ISAR in the context of turntable imaging is covered by Mensa [34] and by Chen and Andrews [40, 41]. Other excellent introductory references to ISAR include [33, 42]. For a tomographic interpretation of ISAR, see [43].

Examples of ISAR images collected with the Microwave Radar Division (MRD) radar van are shown in Figure 3.7. The raw data were processed with Haywood's algorithm [44] which is summarised in Appendix A. The intermediate results generated from the ISAR processing are shown in Figure 3.8. For more details on the radar data collection procedure and the subsequent processing, see Section 4.4.

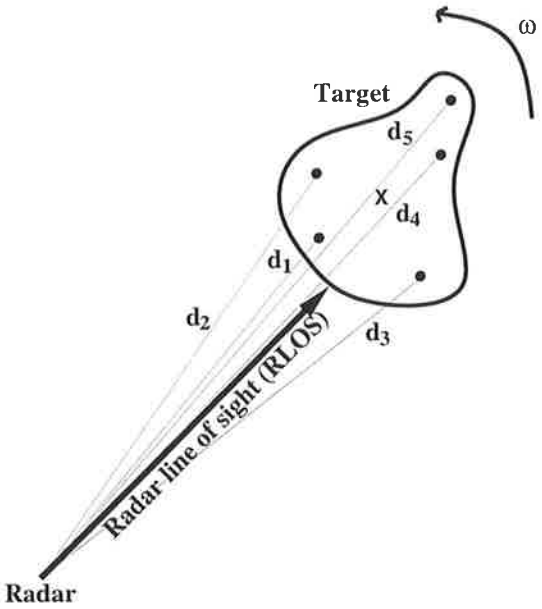

(a) A particular scenario geometry for ISAR image collection. The radar position, RLOS, and the individual scatterer positions on the target determine the image projection plane. The target has an angular rotation velocity of ω, and the centre of the rotation is denoted by an "X". $d_1 \ldots d_5$ represent the distances from the radar to the individual scatterers. $a_1 \ldots a_5$ represent the amplitudes of the backscatter from the discrete scattering centres.

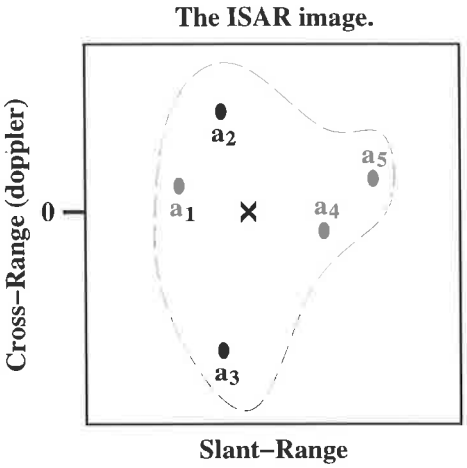

(b) The ISAR image obtained from the scenario geometry depicted in subfigure (a). Note how scatterers 2 and 3 are separated in cross-range. The slant-range resolution is independent of the target motion whereas the cross-range resolution depends on the angular rotation rate ω.

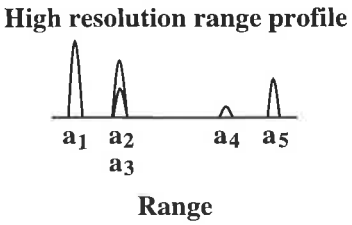

(c) The HRRP obtained from the scenario geometry depicted in subfigure (a). The difference in the positions of scatterers 2 and 3 cannot be resolved since $d_2 = d_3$.

Figure 3.6: A particular scenario geometry for ISAR image collection. Note how the scatterers are resolved in cross-range in the ISAR image and how certain scatterers cannot be resolved in the HRRP.

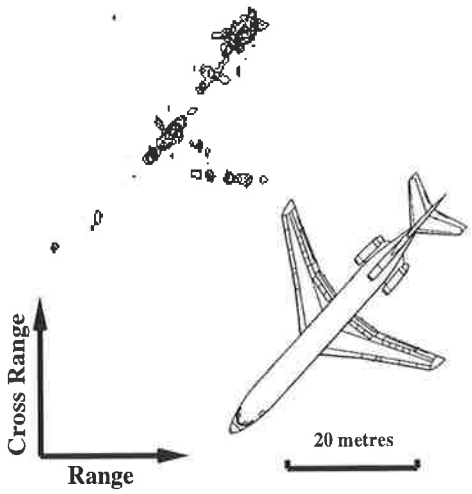

(a) A typical ISAR image of the Boeing 727 aircraft shown with a dynamic range of 25 dB. The average aspect was 135° from head-on. The processing used was standard range-Doppler processing with single hot spot focussing [44].

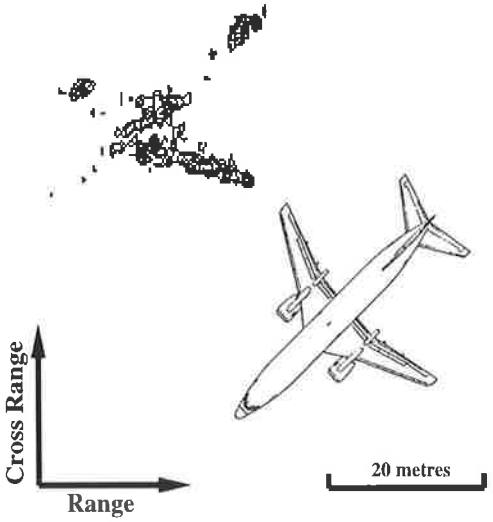

(b) A typical ISAR image of the Boeing 737 aircraft shown with a dynamic range of 25 dB. The average aspect was 140° from head-on. The processing used was standard range-Doppler processing with single hot spot focussing [44].

Figure 3.7: Two examples of ISAR images which were obtained from noncooperative aircraft in flight.

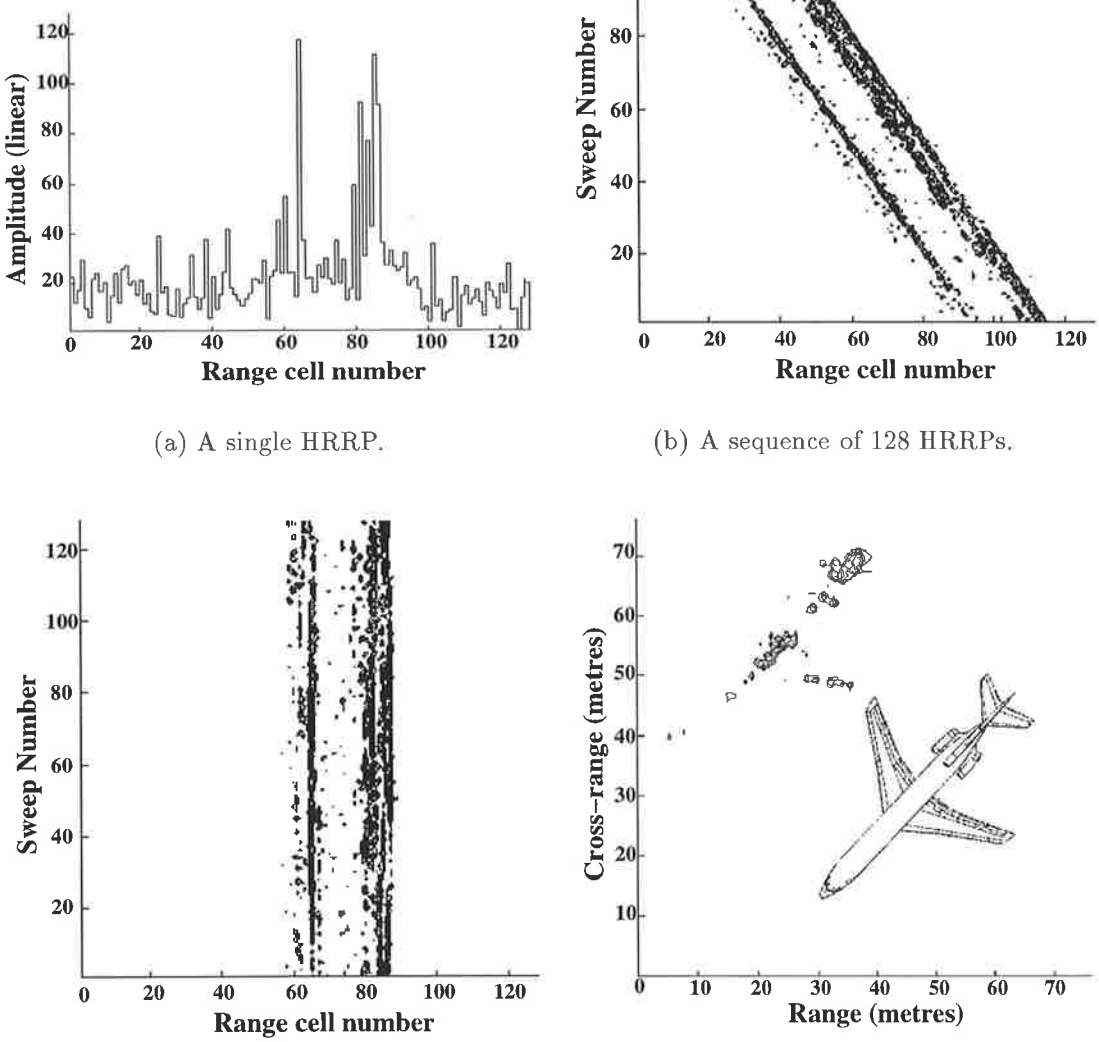

(a) A single HRRP.

(b) A sequence of 128 HRRPs.

(c) The 128 HRRPs from subfigure (b) after range alignment.

(d) The resultant ISAR image shown with a dynamic range of 25 dB. A scaled schematic of the target is shown for comparison.

Figure 3.8: The intermediate results produced by ISAR processing with Haywood's algorithm [44].

3.5.2 Motion compensation

Pure rotation of the target about the radar does not occur in a real imaging scenario. The relative motion between the radar and the target is normally composed of both radial and rotational components. Radial motion complicates the imaging process and it must be removed. The term *motion compensation* refers to the estimation and subsequent removal of unwanted motion components to achieve a pure rotational motion suitable for synthetic aperture processing. Undesirable motion components include the target radial motion and the undesirable motion of the radar platform. Motion compensation is a complex issue which is only briefly dealt with in this section. The interested reader is directed to [44, 45], both of which contain good descriptions of motion compensation issues and techniques. Research into motion compensation algorithms is still an ongoing activity.

The objective of radial motion compensation is to remove the effects of radial motion from the collected data. There are two sources of distortion that occur due to radial motion [33]. *Range walk* refers to the migration of scatterers between range bins because the target is moving in range. Range walk is illustrated in Figure 3.8(b). *Range offset* results from the range-Doppler coupling inherent in a frequency-dispersive waveform. A number of researchers have suggested methods for radial motion compensation. The Phase Method [33] was developed by Hughes Aircraft Company for the Naval Ocean Systems Centre (NOSC) of San Diego. Chen and Andrews [41] have also proposed a number of algorithms for range alignment.

In this thesis a motion compensation algorithm developed by Haywood [44] is used. It is basically a three-stage algorithm; range alignment followed by adaptive beamforming and Doppler processing. The algorithm is briefly described in Appendix A. The reader should become familiar with the motion compensation algorithm of Appendix A because the problems with the algorithm are discussed in the next section.

3.5.3 Difficulties with ISAR processing

ISAR processing is not guaranteed to be successful. Successful processing means that the energy in each range bin has been correctly separated according to Doppler frequency and a focussed image is the result. A focussed image may have a good or poor cross-range resolution. If the cross-range resolution is good then the image may be used for target classification.

The main difficulty with ISAR processing is that the motion of the target is unknown. It is the goal of *motion compensation* to estimate and correct for any unknown and undesired target motion. Motion compensation is not always successful and problems can occur in any of the motion compensation steps.

Range alignment

Range alignment is the removal of the radial motion of the target. Cross-correlation is often used for radial motion compensation. Range alignment using cross-correlation is described in Appendix A. There are two main reasons why the range alignment of HRRPs may not be successful. Firstly, there is normally noise present in the HRRPs which affects the cross-correlation process and can cause HRRP misalignment. Secondly, depending on the scenario and the radar PRI, the target aspect may change significantly over the HRRP alignment interval. If the structure of the HRRPs has varied significantly over the alignment interval, then range alignment may fail.

Adaptive beamforming

Adaptive beamforming is an integral part of the motion compensation algorithm described in Appendix A. Adaptive beamforming was first proposed by Steinberg [46]. Adaptive beamforming follows range alignment. If range alignment has not been successful then there is no chance that adaptive beamforming will work. If range alignment has been successful, then adaptive beamforming may still fail if a suitable phase synchronising source is not available. As Steinberg states in [46], for adaptive beamforming to succeed:

> *There must exist at least one range bin on the airplane in which the backscattered field from one scatterer is larger than the sum of all the echoes from the remaining scatterers in that range bin.*

If this condition is not met then adaptive beamforming will fail. Steinberg also points out that the higher the slant-range resolution, the larger the probability that a range bin, containing a single dominant scatterer, will exist. If the dominant scatterer algorithm (DSA) fails then the multiple scatterer algorithm (MSA) [47] may still be successful. The MSA uses a weighted sum of returns from different range bins as a phase synchronising source.

ISAR imaging at broadside aspects

The DSA requires the return of a dominant scatterer to exceed the combined sum of all other scatterers in the same range bin by at least 4 dB. If this criterion is not met then poor image focussing results. It is most difficult to satisfy this criterion when there are many scatterers in a single range bin. This geometrical situation corresponds to a broadside aspect where the major aircraft scattering centres, (cockpit, radar dish, fuselage, tail *etc.*), are all at approximately the same range. If the engines are also at the same range (*e.g.* Boeing 727) then the problem is made worse since there are more scatterers which are in the same range bin. In Section 4.4 data from a local airport were

collected and it was noted that poor focussing occured regularly at broadside aspects. The focussing problem at broadside aspects can be overcome by:

- Increasing the slant-range resolution to better resolve scatterers;
- Using adaptive beamforming algorithms other than the DSA or MSA. Bocker [48] has suggested an entropy based measure for image focussing.

3.5.4 The unavailability of ISAR

It has been suggested [46, 49, 27] that ISAR images can be used for radar target classification. Even though ISAR images may provide a good basis for target classification, the preconditions for ISAR imaging are not always available. The fundamental prerequisite for ISAR imaging is a relative aspect change between the target and radar. In an operational scenario this aspect change must occur within a reasonable time period. There are many situations in which this aspect change is not available:

Allocation of the radar resource
: If the radar's primary function is surveillance, there may not be sufficient free radar time available to schedule the time on target (TOT) necessary for ISAR imaging;

Rotating antenna
: If the radar has a rotating antenna then it may be physically impossible to provide a long enough coherent integration time for ISAR imaging;

Long-range geometry
: When the target is at long-range or moving towards the radar, it becomes unlikely that the necessary aspect change for imaging will be available within a reasonable time period;

Lack of induced motion
: In the case of ISAR ship imaging at long range from an aircraft, it is the induced motion of the ship which provides the aspect change necessary for imaging. Consequently, in low sea states it is not possible to obtain a good ISAR image.

In the situations where ISAR imaging is not possible, a HRRP must be used for classification.

Appendix C presents an example of a possible aircraft target classification scenario. The calculations to determine the required ISAR imaging time are included in the appendix. The example given in Appendix C should help to illustrate how difficult it may be to obtain the required aspect change for ISAR imaging.

3.6 Summary

A high resolution radar can resolve point scatterers which are separated in range. The slant-range resolution achievable with a particular waveform is determined by its bandwidth according to Equation 3.1. A coherent radar is required to separate point scatterers in cross-range, and the cross-range resolution is achieved through synthetic aperture processing. The achievable cross-range resolution is determined by the rotation of the target as seen by the radar according to Equation 3.4.

There are three waveform types commonly used to achieve a suitable bandwidth for high resolution imaging:

- Short pulse waveforms;
- Pulse–compression waveforms;
- Stepped frequency waveforms.

Pulse–compression waveforms are usually used in operational radar systems. Stepped frequency waveforms are popular for inexpensive experimental radars or for RCS instrumentation radars.

A HRRP represents a one–dimensional projection in range of a target's complex return onto the RLOS. ISAR is a technique which is used to image targets such as ships and aircraft. ISAR resolves target scatterers in two orthogonal directions; slant-range and cross-range, whereas a HRRP only resolves scatterers in the slant-range direction.

Motion compensation is an important issue for ISAR. Motion compensation is not always successful and even when it is successful, the resulting ISAR image may have a poor cross-range resolution. In certain operational scenarios the prerequisites for ISAR imaging may not be available. In these operational scenarios it is necessary to use HRRPs for target classification.

Chapter IV

RADAR BACKSCATTER PHENOMENOLOGY

4.1 Introduction

4.1.1 Chapter purpose

Before designing any target classification system which uses sensor imagery as a basis for classification, it is important to understand the link between the physical attributes of the target and the corresponding features in the observed target imagery. An understanding of this nature (*domain knowledge*) enables the identification of the image features which provide target discrimination. A knowledge of the important features in the target imagery drives the design of feature extraction and preprocessing algorithms.

This chapter was designed to give an phenomenological introduction to radar backscatter from aircraft targets, rather than to collect a comprehensive target database. To collect a complete data set of many target types over 360° of aspect is a formidable and thankless task. Some of the work in this chapter has been published by the author in [50] and similar material has appeared recently in the excellent book by Knott [2] which can be used as a primary reference for this chapter. Related material can also be found in [34].

4.1.2 Chapter overview

This chapter begins by summarising some of the theoretical aspects of radar backscatter from complex targets. In Sections 4.3 and 4.4 a number of experiments which provided real radar data of full-scale aircraft targets are described. The experiments were carefully chosen to highlight the important characteristics of radar backscatter and provide a background on radar backscatter phenomenology. Section 4.5 examines the results of the experiments in radar backscatter phenomenology and discusses them in the context of radar target classification. The phenomenological knowledge of radar backscatter gained in this chapter provides the basis for further direction in the remainder of this dissertation.

4.1.3 *Drowning in data*

The amount of raw experimental data collected for this chapter exceeded 300 megabytes. The data were processed using MATLAB on a workstation specially configured with a large amount of memory and disk space. Whilst the amount of data processed was huge, the actual processing required to produce the radar imagery was quite straightforward. Due to the large amount of data collected, all of the imagery[1] produced cannot be shown in this thesis. Rather, specific images are chosen to illustrate the important phenomenological principles of radar backscatter from real aircraft targets. Several complex phenomena, such as cavity scattering and Doppler modulation, are highlighted since they are likely to have a major influence on the design of a radar target classification system.

4.1.4 *Techniques for RCS measurement*

The variable factors which dramatically affect radar imagery for a given radar signal are:

- Target type;
- Target aspect.

RCS measurement techniques usually parameterise RCS in terms of aspect, frequency and polarisation for a given target type. RCS measurement techniques are discussed in detail in [2], but a short overview can be found in [51]. There are two main methods for collecting radar data from full-size targets. The first method, known as a *static RCS range,* involves placing the target on a rotating turntable or other support structure and illuminating it with a radar. The second method, known as a *dynamic RCS range,* is where the target moves through free space under its own power, whilst being illuminated by a radar. A static RCS range can provide 360° aspect coverage but it is normally limited in the target types that can be placed on the turntable. A dynamic RCS range offers more flexibility in target types but it is often limited by the range of target aspects that can be achieved. For this chapter, data were collected from both a static RCS range (Section 4.3) and from a dynamic RCS range (Section 4.4).

4.2 Radar backscatter from complex targets

In this section a brief theoretical introduction to radar backscatter from complex objects is given. This introduction is a summary of an excellent discussion which appears in [2]. Radar backscatter from complex objects is characterised by seven mechanisms. For the consideration of radar backscatter from aircraft, these seven mechanisms can be combined into four broader mechanisms:

[1] Imagery is used here in a general sense to refer to both HRRPs and ISAR images.

1. Direct illumination specular scattering normal to surfaces or edges;
2. Diffractive scattering from edges and surface discontinuities;
3. Indirect (multiple) specular scattering from structures or cavities;
4. Travelling wave scattering along edges.

These mechanisms are illustrated in Figure 4.1. A similar grouping of these scattering mechanisms has been made by Smith [7]. Normally mechanisms 1 and 2 account for the majority of radar backscatter from aircraft[2]. Specular backscatter is much larger in amplitude than its diffractive counterpart. Specular backscatter normally occurs from the following aircraft features:

- Radar dish;
- Cockpit bulkhead;
- Fuselage (when the incidence is normal).

Diffractive backscatter can occur from:

- Externally mounted antennas;
- Control surfaces and actuators;
- Wing and tail tips;
- Wing and tail edges (with normal incidence);
- Surface discontinuities in the aircraft structure. *e.g.* gaps, steps *etc.*

Travelling waves are important only when the wavelength is similar to the target size. For the microwave frequencies considered in this thesis, travelling wave backscatter is not significant. Backscatter due to multiple specular reflections from structures is normally an infrequent occurrence with aircraft. On the other hand, multiple reflections from cavities are quite common with fighter aircraft. These cavity reflections occur when radar energy is captured and then reradiated by the cavities on the aircraft. The electromagnetic energy can traverse much or all of the cavity length. The most common cavities on a fighter aircraft are the engine intake and the engine duct. Section 4.5.2 discusses engine cavity backscatter and Appendix D contains excellent examples of imagery with engine cavity backscatter.

[2] Engine cavity backscatter is a notable exception to this general rule.

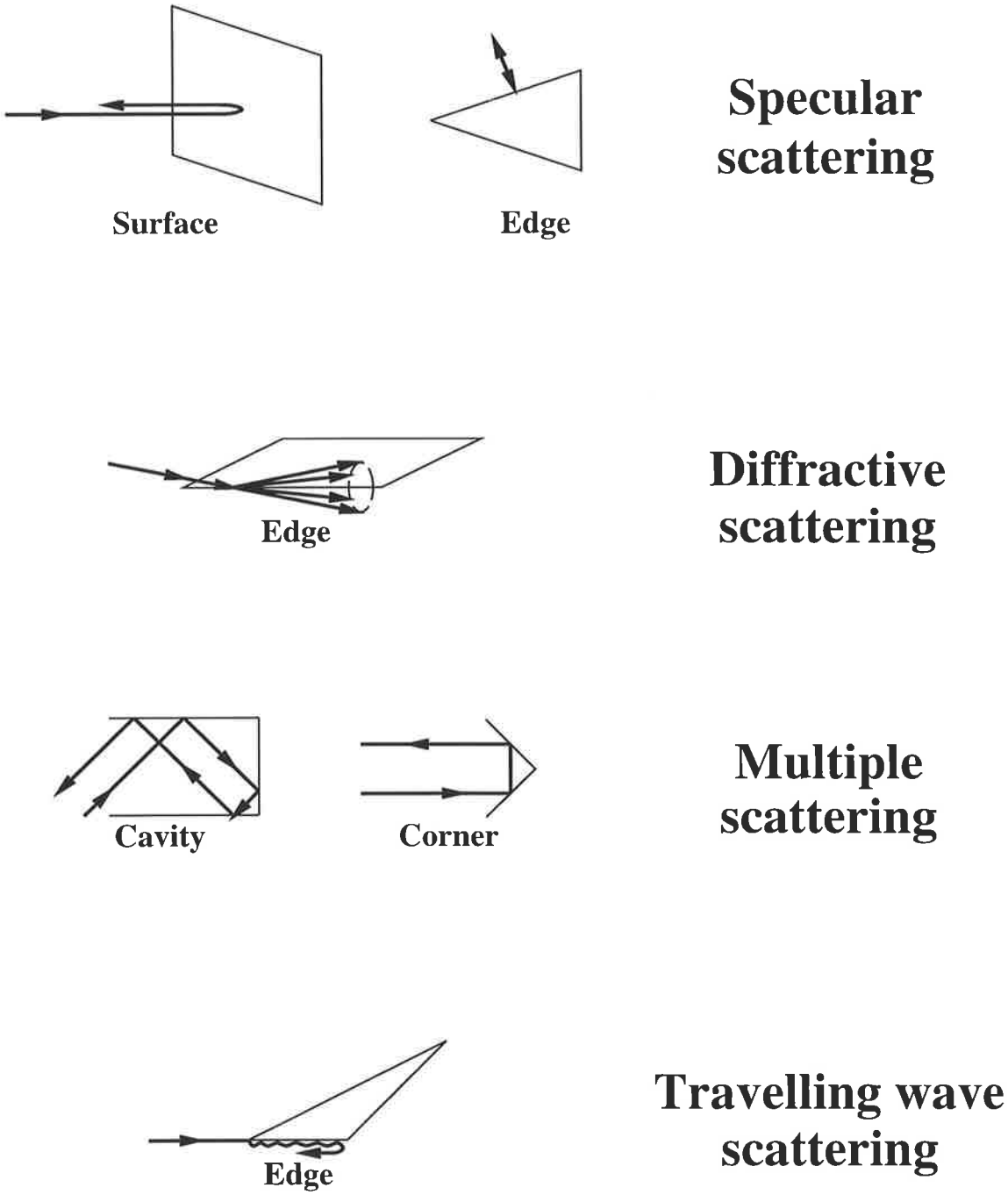

Figure 4.1: The different mechanisms for radar backscatter from aircraft.

4.3 Radar imagery of the Mirage aircraft

This section is intended to highlight the important features of radar backscatter, as a function of aspect angle, for a typical fighter aircraft. The results of this section are not intended to be exact numerical measurements of the Mirage RCS, but rather a phenomenological introduction to radar backscatter from a typical fighter aircraft.

4.3.1 Data collection

Microwave Radar Division (MRD) of the Defence Science and Technology Organisation (DSTO), Australia, operates a turntable facility which is used for RCS measurements [52]. In the experiment described in this chapter, an actual Mirage aircraft was placed on a turntable and radar data were collected using a portable radar housed in a van. Three separate sets of measurements of the Mirage were made. In the first set of measurements, the engine intakes were plugged with radar absorbent material (RAM) to eliminate engine cavity backscatter. For the second set of measurements, the engine intakes were left in their normal state. For the final set of measurements, the engine intake compressors were electrically rotated at operating speed to observe the effects of JEM.

For each measurement set, the aircraft was rotated through 360° at a constant rate of approximately 2° per second and a stepped frequency waveform, starting at 8.96 GHz and stepping over a 960 MHz band in 256 steps of 3.75 MHz, was used to collect the data. The stepped frequency waveform which was used to collect the data of the Mirage aircraft is illustrated in Figure 4.2. Data were collected for H–H, V–V, H–V and V–H polarisations[3]. In all experiments the undercarriage of the aircraft was screened with RAM to reduce the returns from this part of the aircraft. Four calibration reflectors were placed at a known distance in front of the aircraft. These calibration reflectors, which are seen in some of the radar imagery, served two purposes:

1. They provided a range reference so that the position of the aircraft could be calculated;

2. They allowed the vertical beam pattern of the incident radar illumination to be measured. The antenna height was then adjusted so that the maximum of the vertical beam pattern occured at the height of the aircraft fuselage.

The instrumentation in the radar van has been described in [52], but it is briefly summarised here. The radar is built from commercial off-the-shelf (COTS) equipment and the heart of the radar is a Comstron digital frequency synthesiser. The radar transmits a stepped frequency waveform with no coherent integration of individual pulses.

[3] H–V represents the transmission of a horizontally polarised signal and the reception of a vertically polarised signal. H–H, V–V and V–H have similarly defined meanings.

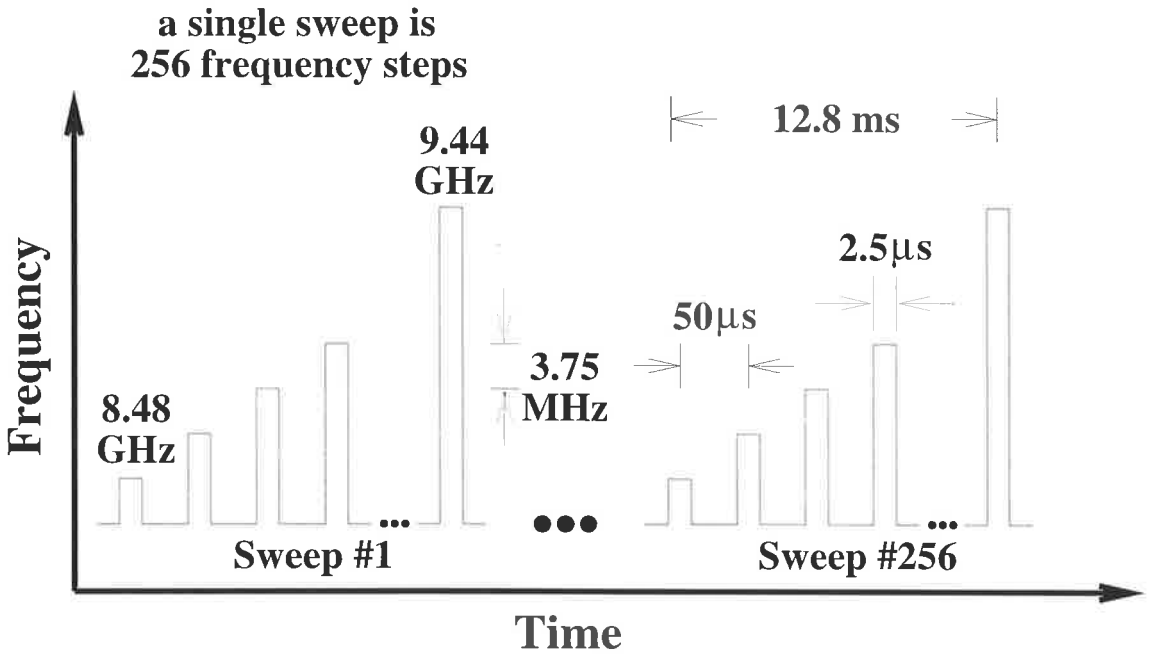

(a) The stepped frequency waveform which was used to collect data of the Mirage aircraft.

Waveform parameter	Value
Start frequency	8.48 GHz
Centre frequency	8.96 GHz
End frequency	9.44 GHz
Frequency step	3.75 MHz
Bandwidth	960 MHz
Pulse width	2.5 μs
Effective PRF	78 Hz
Pulses per frequency sweep	256
Sweeps per image	256

(b) The parameters of the stepped frequency waveform which was used to collect data of the Mirage aircraft.

Figure 4.2: The stepped frequency waveform which was used to collect data of the Mirage aircraft.

The radar receiver contains a digitally controlled attenuation setting which performs automatic gain control (AGC). The attenuation setting, along with the other radar parameters, was stored with the raw data. After a set of measurements was taken the raw data was processed to compensate for changes in the receiver attenuation setting.

A *record* of data refers to a complete set of measurements over 360° of aspect with a particular polarisation and aircraft engine state. The polarisations used were H–H, V–V, H–V, V–H, and the aircraft engine states were:

Normal
: The engine intakes were clear and the engine compressors were not rotating;

Rammed
: The engine intakes were filled with RAM;

Rotating
: The engine intakes were clear and the engine compressors were rotating at operating speed.

Each record of raw data was approximately 16 megabytes in size and data were collected over all combinations of the above parameters.

4.3.2 *Difficulties with the data collection*

Compared with the US, Australia has a very small defence budget and a fledgling defence and aerospace industry. Consequently the DSTO static RCS measurement facility cannot ever compete with the sophisticated facilities that exist in the US today. A particular problem that exists with the DSTO RCS range is a lack of proper far-field (plane-wave) illumination for large targets. With the data collected for this thesis this is not a serious problem, as the following quotation from Knott [2] illustrates:

> *Moreover, high accuracy in RCS measurements is often unnecessary unless the data are to be used as the basis for detailed analytical work or the development of scattering predictions.*
>
> *Therefore, when determining how important the nearfield effects may be, the end use of the data should be considered.*

In following Knott's advice, no apologies are made for the quality of the data, but instead the known problems with the data are clearly stated. It should soon be seen that the data quality from the DSTO RCS range is more than adequate for a phenomenological investigation of radar backscatter from full-scale aircraft.

The far-field requirement

To check whether a target is in the far-field of an illuminating radar the following formula [2] is often used

$$R \geq 2\left(\frac{l_c^2}{\lambda}\right) \tag{4.1}$$

where R is the distance from the radar to the target, l_c is the transverse (cross-range) length of the target and λ is the wavelength of the illumination used. For the DSTO turntable with $R = 400$ m and a mean λ of 0.03 m (10 GHz) the maximum transverse target size that meets far-field requirements is

$$\begin{aligned} l_c &\leq \sqrt{\frac{R\lambda}{2}} \\ &\leq 2.45 \text{ m} \end{aligned}$$

Hence for the Mirage aircraft which is approximately 15 m in length, the far-field approximation does not hold. To collect data from this aircraft in the far-field, a range of greater than 15 km is needed! This is obviously impractical for a static RCS range. Since the data collected in this chapter are only used to highlight important aircraft backscatter features relevant to target classification, the lack of a proper far-field illumination does not affect the conclusions made later in this chapter.

Ground returns

Static RCS ranges tend to produce radar imagery which is contaminated by ground returns [2]. This ground contamination appears in the imagery as backscatter characterised by a fixed position in range and a zero Doppler (cross-range) position. Careful examination of the Mirage imagery reveals a number of ground scatterers which are independent of the turntable aspect. It is very difficult to prevent this ground contamination.

Undercarriage screening

When the data from the Mirage aircraft were collected, the undercarriage was screened with RAM. Even though the RAM significantly reduced the return from this part of the aircraft, it could not completely eliminate the return. During the measurements with the engine intakes open, all of the available RAM was used to shield the undercarriage. In the measurements with the engine intakes RAM plugged, there was less RAM available to shield the undercarriage. This explains why the undercarriage is more prominent in the engine-rammed measurements.

Limited radar PRF

The rotating engine compressors of the Mirage produce a characteristic Doppler modulation known as JEM. To collect high resolution imagery with the JEM information intact,

it is necessary to sample at greater than the Nyquist rate for the highest frequency JEM component. The sampling frequency for the Doppler information is the PRF of the radar. The effective PRF of the stepped frequency waveform which was used for data collection was 78 Hz. A chirp waveform would have to be used to achieve a higher PRF whilst still maintaining a high bandwidth. Unfortunately DSTO does not have access to a radar with a chirp waveform. Hence a stepped frequency waveform was used for data collection and this has meant that the Doppler frequencies above 78 Hz were aliased and consequently the JEM phenomenon cannot be properly studied for this particular set of data.

4.3.3 *Processing*

Calculating the aspect of the aircraft

The turntable aspect was calculated by knowing the constant rotation rate ω and the aspect θ_0 at the beginning of a record. The turntable aspect at the beginning of each record was recorded along with the raw data. The rotation rate was set to be $\omega = 2°$ per second and the PRI between successive frequency pulses was 50 μs. Hence

$$\Delta\theta_{\text{per sweep}} = 2 \times 256 \times 50 \times 10^{-6} = 0.0256°$$

where 256 discrete frequency pulses were used for each sweep. To calculate the aspect[4] of the aircraft for any particular frequency sweep, the following formula was used

$$\theta = \theta_0 + (0.0256 \times \texttt{sweep\_number}) \tag{4.2}$$

where `sweep_number` is the number of the sweep relative to the beginning of the data record.

HRRP processing

Since the radar was using a stepped frequency waveform, the frequency samples that were collected need to be converted into synthetic range (time) data. To begin with, 256 in-phase (I) and quadrature (Q) frequency samples corresponding to a particular target aspect are chosen. A complex HRRP is produced by weighting these samples using a Hann window and then performing a 256 point IDFT. The magnitude of the resultant complex vector is a HRRP.

ISAR processing

The processing used in this chapter to produce an ISAR image is outlined in Appendix A. The steps are as follows:

[4] 0° and 360° represent a head-on aspect of the aircraft.

1. The change in aspect required, to achieve a cross-range resolution which is equivalent to the range resolution (0.15 m), can be calculated from Equation 3.4

$$\Delta\theta = \frac{\lambda}{2\Delta\theta} = \frac{3.35 \times 10^{-2}}{2 \times 0.15} = 0.1 \text{ radians} \approx 6^\circ$$

   Hence a complex data block, of size (256 sweeps)x(256 frequency steps), spanning 6.6°, is chosen to give a cross-range resolution which approximately matches the range resolution. The data block is chosen so that the 128^{th} sweep corresponds to the aspect of interest.

2. 256 HRRPs are formed in the manner previously outlined.

3. Range alignment corrections using cross-correlation are calculated and these corrections are applied to the HRRP data.

4. The data are phase compensated using the dominant scatterer algorithm [46].

5. Doppler processing is performed by Hann windowing and then using a 256 point DFT on each range bin. This gives the cross-range profile for each range bin.

Removing the contribution of the calibration scatterers

To produce the frequency-azimuth RCS plots, the contributions from the calibration scatterers need to be removed. This is done by transforming the frequency data into the time domain via the IDFT, gating out the time segment which contains the calibration scatterers, and finally returning to the frequency domain via the DFT. The contributions from the calibration scatterers were not removed in the range-azimuth RCS plots since they are visually separated in range from the target returns.

Data display techniques

In [2] different techniques for displaying RCS data are discussed in detail. Some of the conventional RCS display techniques which are used in Section 4.3.4 are:

- HRRP plots at specified aspects;
- ISAR image plots at specified aspects;
- Frequency-azimuth RCS plots over 360° of aspect;
- Range-azimuth RCS plots over 360° of aspect.

Averaging of displayed RCS data

Frequency sweeps were generated for every 0.0256° of turntable rotation. This mean that approximately 14000 sweeps were generated for a full 360° of aspect. Plotting 14000 sweeps, each with 256 frequency samples, is both difficult[5] and unnecessary. Plots of 360° of coverage are displayed to highlight the gross features of the radar backscatter with respect to aspect rather than to observe fine angular detail. Data reduction for display is achieved by plotting suitable statistical averages of the RCS data. If a detailed examination of the data is required at a particular aspect, then the data can be plotted over an appropriately small aspect interval.

Plotting RCS data averaged over small aspect intervals is a popular way to reduce the amount of data that is displayed [2]. Averaging smoothes the RCS variations with aspect. The size of the aspect *averaging window* used determines the amount of fine detail that is seen in the final RCS plot. Averaging windows can be *overlapped* to provide additional smoothing. In this chapter, the frequency-azimuth RCS plots and the range-azimuth RCS plots show measurement data averaged over 0.5° aspect intervals. Each averaged frequency sweep or averaged HRRP was generated from 20 consecutive raw measurements.

4.3.4 Discussion

Frequency-azimuth RCS plots

Figures 4.3, 4.4 and 4.5 show averaged frequency-azimuth RCS plots of the Mirage with the engines normal, rammed and rotating. The contrast between Figure 4.3 (normal engines) and Figure 4.4 (rammed engines) is quite apparent. In Figure 4.4, the prominent engine intake and cavity returns at 30° and 330° are missing. There is still a strong return from 0° since ramming the engine intakes has no effect on the radar dish and cockpit bulkhead returns. There are also differences between Figures 4.3 and 4.4 because the rammed measurements are made with a V–V polarisation[6] whereas the normal measurements are made with H–H polarisation. In Figure 4.4, the specular returns from the rear edge of the delta wing are exaggerated compared to Figure 4.3. In both figures the specular backscatter from the forward delta wing edges is clearly seen at 60° and 300°.

There is little observable difference between Figure 4.3 (normal engines) and Figure 4.5 (rotating engines). The differences between the radar returns from these two engine states are better illustrated in the range-azimuth RCS plots shown in Figures 4.6 and 4.8.

The general conclusions which can be made from the frequency-azimuth RCS plots

[5] Due to the large amount of data involved.

[6] A V–V polarisation produces stronger specular horizontal edge returns than a H–H polarisation. A V–V polarisation was chosen for the rammed measurements so that the horizontal aircraft edges would be prominent.

are:

- Broadside aspects (90° and 270°) produce very strong specular returns;
- Engine cavities and tailpipe cavities produce complex backscatter over a wide range of aspects;
- Specular returns from wing edges are visible particularly with a V–V polarisation.

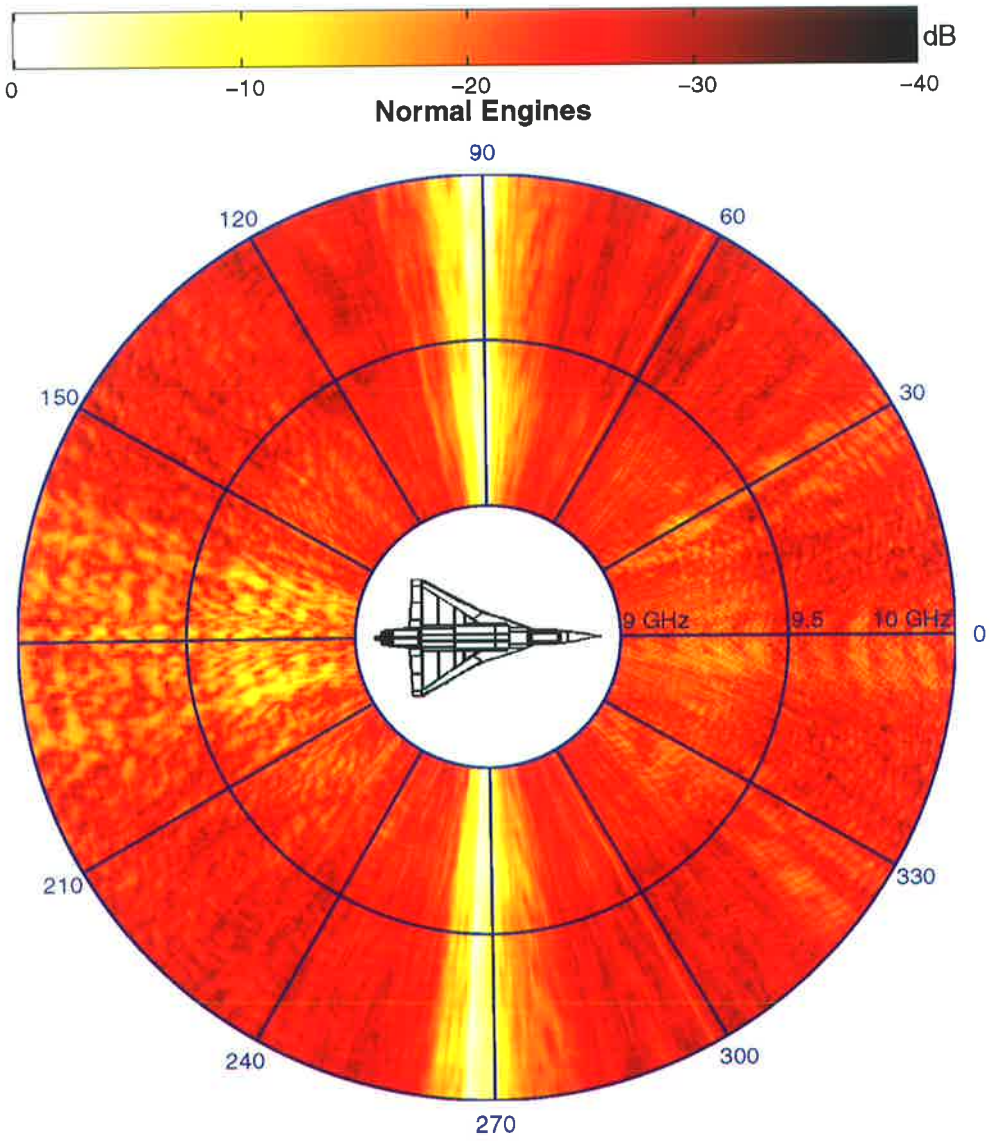

Figure 4.3: A frequency-azimuth RCS plot of the Mirage aircraft with normal engines and a H–H polarisation.

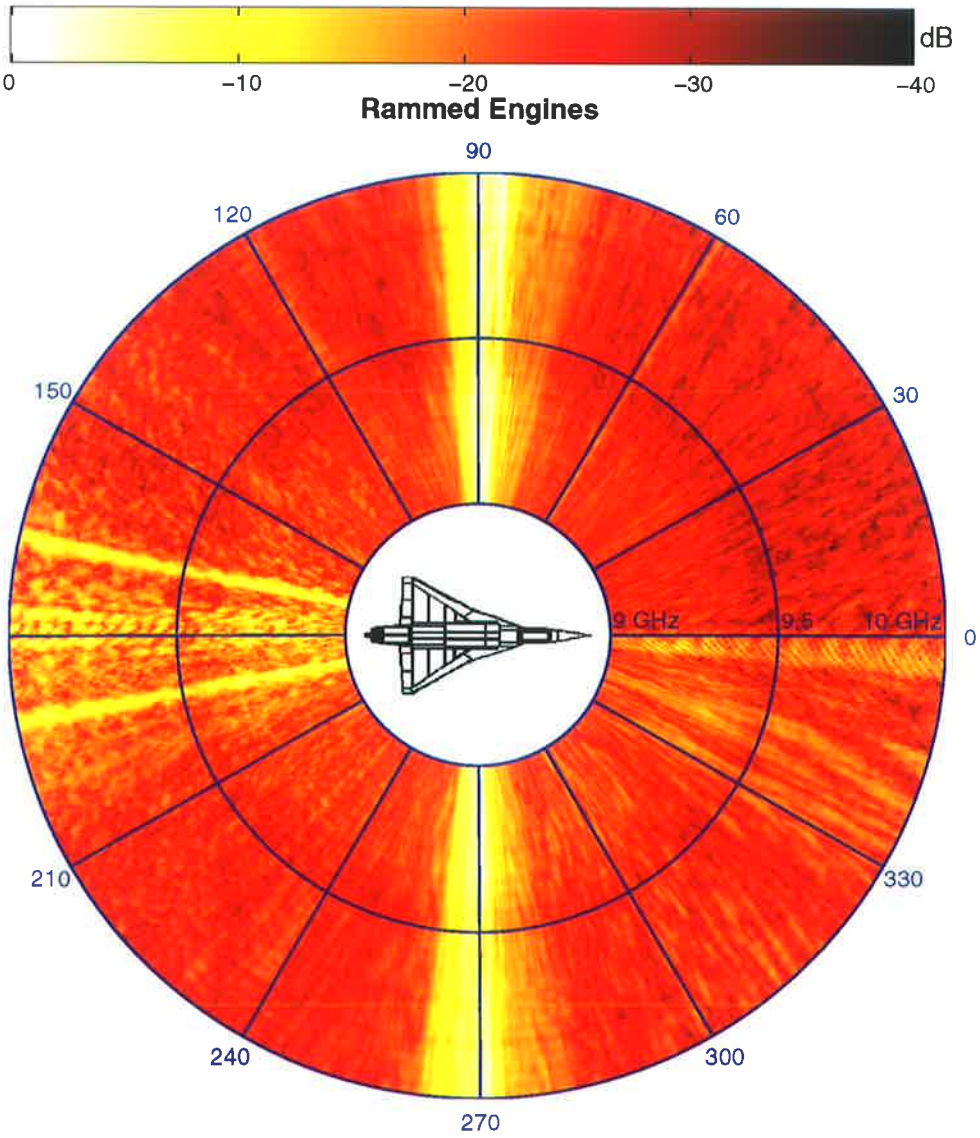

Figure 4.4: A frequency-azimuth RCS plot of the Mirage aircraft with rammed engines and a V–V polarisation.

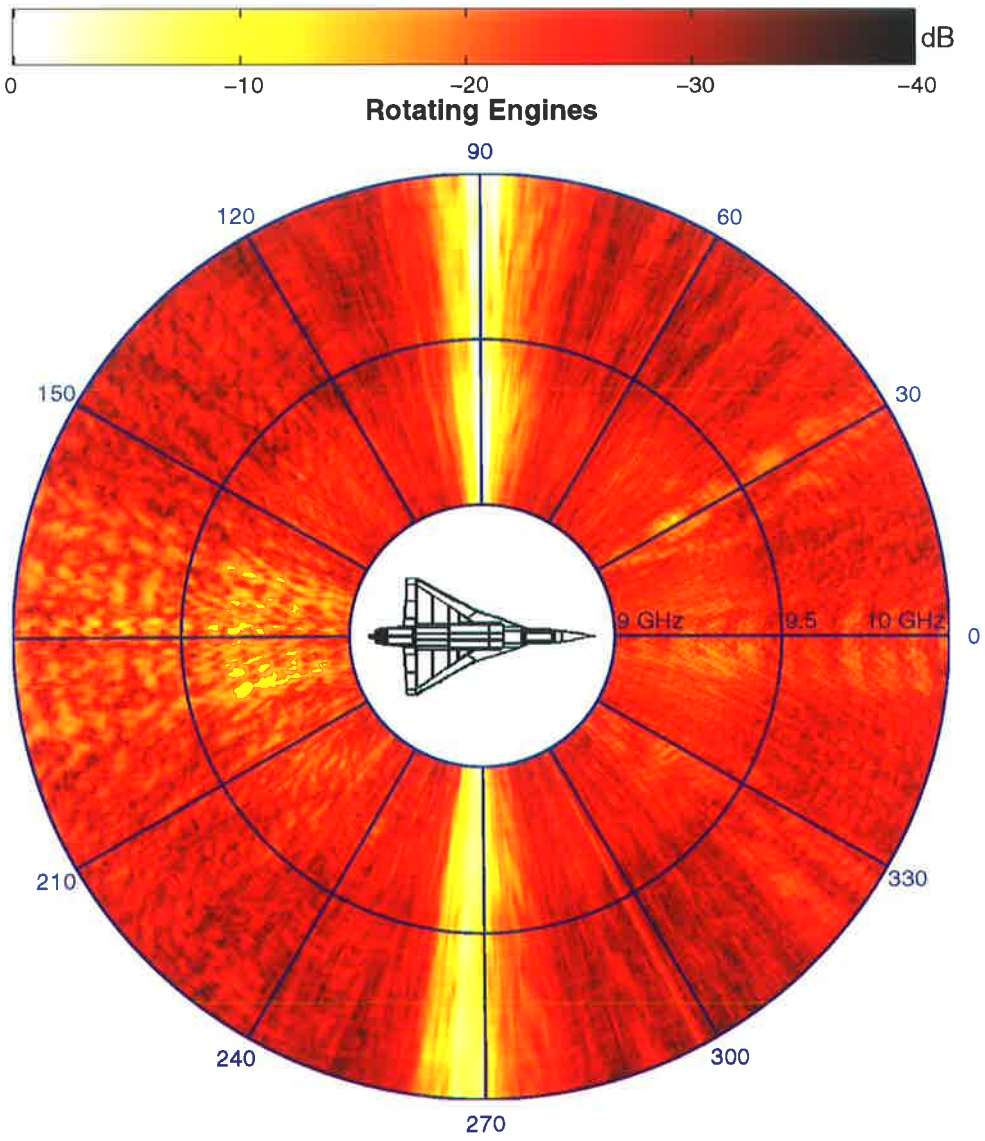

Figure 4.5: A frequency-azimuth RCS plot of the Mirage aircraft with rotating engine compressors and a H–H polarisation.

Range-azimuth plots

Figures 4.6, 4.7 and 4.8 show averaged range-azimuth plots of the Mirage RCS with the engines normal, rammed and rotating. Very strong broadside returns, (labelled B), at 90° and 270° are evident in all three figures. The sidelobes from these bright returns (labelled C) are also evident. In the experiment with the engines rammed (Figure 4.7), RAM was removed from the undercarriage shield to plug the engine intakes. Unfortunately this has resulted in the undercarriage backscatter (labelled I) being very prominent in this particular range-azimuth RCS plot.

In each figure the returns from the radar dish and the cockpit bulkhead, (labelled E and F respectively), are clearly evident. These features are strongly visible over a broad range of forward aspects and are still visible, albeit with a greatly reduced amplitude, from rearward aspects. The radar dish provides a stronger return than the cockpit bulkhead for frontal aspects and vice-versa for rearward aspects.

The initial tailpipe returns (labelled D) are clearly visible in each plot. It is interesting to note that there are a number of returns from the tailpipe cavity which probably correspond to different structures inside the rear section of the aircraft engine. The extended tailpipe cavity returns (labelled H) are also visible in every figure and are, as expected, unaffected by the ramming of the engine intakes.

The initial returns from the engine intake (labelled G) and the extended engine cavity returns (labelled H) are visible in Figures 4.6 and 4.8. They are not present in Figure 4.7 because the engine intakes have been plugged with RAM. Note that there is a difference between the engine cavity returns in the normal and rotating engine states. More data with a very high Doppler sampling rate would be needed to investigate this difference which is due to JEM.

The extended engine cavity returns have a definite gross structure with respect to viewing aspect. As the aspect moves away from end-on, the extended cavity return shortens proportionately. This is easy to understand because as the viewing aspect moves away from end-on, the capture area[7] of the cavity decreases. This means that less energy enters the cavity and consequently there is less energy in the extended cavity returns.

The general conclusions which can be made from the range-azimuth RCS plots are:

- Broadside aspects (90° and 270°) produce very strong returns;
- Engine cavity and tailpipe cavity returns extend well beyond the physical length of the aircraft;
- The radar dish and cockpit bulkhead are dominant backscatter features in frontal aspects.

[7] The capture area of the cavity is its apparent area as seen by the radar.

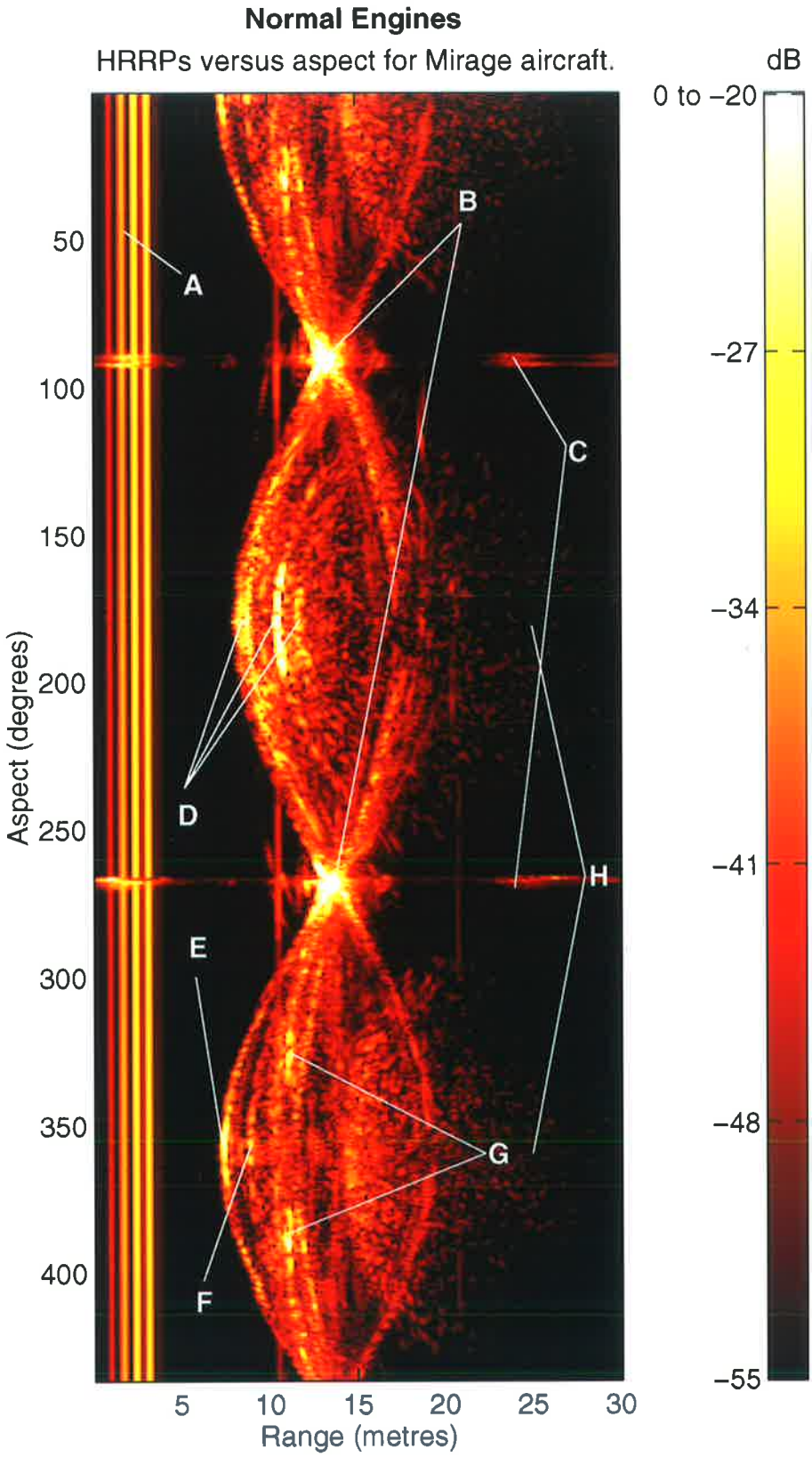

Figure 4.6: A range-azimuth RCS plot of the Mirage aircraft with normal engines and a H–H polarisation. The interesting features include: (A) The four calibration scatterer returns; (B) The broadside returns; (C) The sidelobes of the broadside returns; (D) The tailpipe return; (E) The radar dish return; (F) The cockpit return; (G) The engine intake returns; (H) The tailpipe cavity returns and the engine cavity returns.

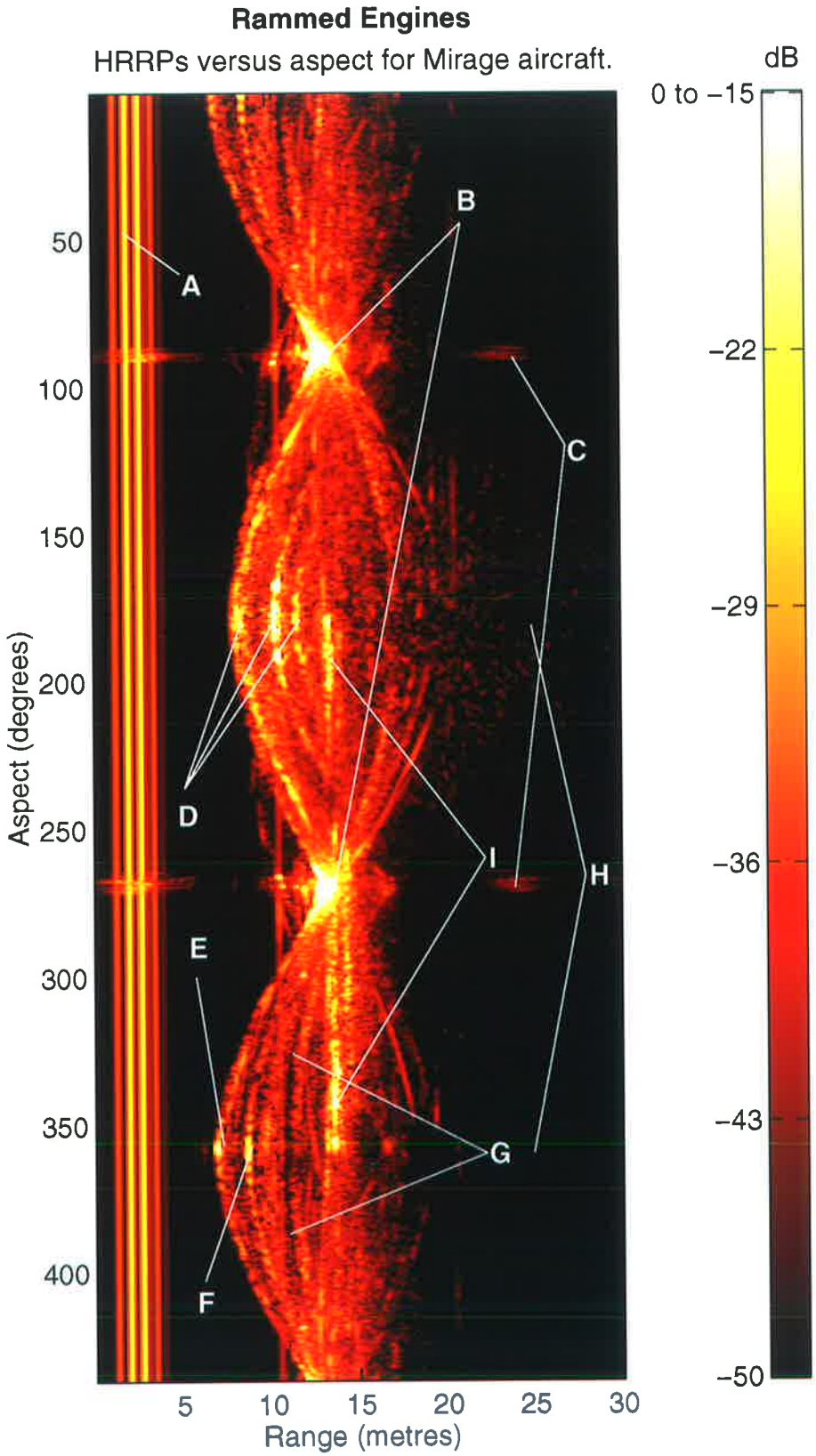

Figure 4.7: A range-azimuth RCS plot of the Mirage aircraft with rammed engines and a V–V polarisation. The interesting features include: (A) The four calibration scatterer returns; (B) The broadside returns; (C) The sidelobes of the broadside returns; (D) The tailpipe returns; (E) The radar dish return; (F) The cockpit return; (G) The absent engine intake returns; (H) The tailpipe cavity returns and the (absent) engine cavity returns; (I) The undercarriage return.

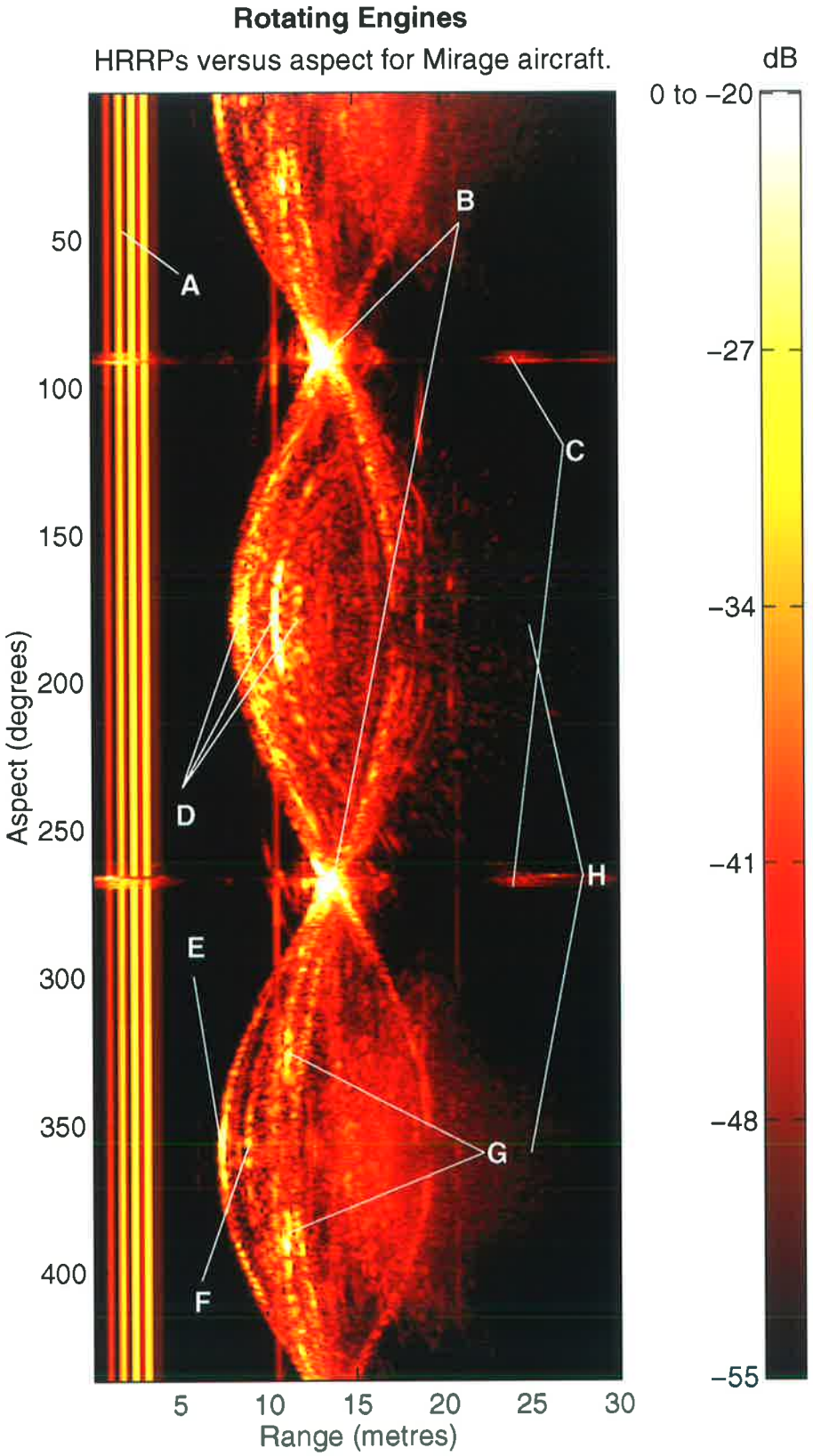

Figure 4.8: A range-azimuth RCS plot of the Mirage aircraft with engine compressors rotating and a H–H polarisation. The interesting features include: (A) The four calibration scatterer returns; (B) The broadside returns; (C) The sidelobes of the broadside returns; (D) The tailpipe returns; (E) The radar dish return; (F) The cockpit return; (G) The engine intake returns; (H) The tailpipe cavity returns and the engine cavity returns.

ISAR and HRRP plots

The results of HRRP and ISAR processing of three particular records are shown in Appendix D. The three data records chosen for display are:

1. Normal engines with H–H polarisation shown in Figures D.1 to D.12;
2. Rammed engines with V–V polarisation shown in Figures D.13 to D.24;
3. Rotating engine compressors with H–H polarisation shown in Figures D.25 to D.36.

A V–V (rather than H–H) polarisation was chosen for the engine rammed data because the V–V polarisation highlights[8] the backscatter from horizontal edges hence providing a better "outline" of the aircraft. Plots are shown for every 30° of aspect and each plot was normalised separately so that the direct comparison of amplitudes between plots is not possible. Every plot is not discussed in detail, but Table 4.1 summarises which backscatter features can be seen in which plots. This does not mean that a particular backscatter feature does not appear in other plots, but rather the recommended plots show a particular backscatter feature most clearly.

[8] A vertical orientation of the electric field vector is compatible, in terms of boundary conditions, with the horizontal orientation of a flat plate conductor. A horizontal flat plate conductor cannot support a horizontal electric field vector.

The backscatter features of the Mirage aircraft

Backscatter feature of interest	Recommended figures		
	Normal	Rammed	Rotating
Very large amplitude broadside returns.	D.4 D.10	D.16 D.22	D.28 D.34
Extended engine cavity returns.	D.2 D.3 D.11 D.12		D.26 D.27 D.35 D.36
Extended tailpipe cavity returns.	D.5 D.6 D.8 D.9	D.17 D.18 D.20 D.21	D.29 D.30 D.32 D.33
JEM returns.			D.25 D.26 D.36
Radar dish and cockpit bulkhead returns.	D.1 D.2 D.3 D.11 D.12	D.13 D.14 D.15 D.23 D.24	D.25 D.26 D.27 D.35 D.36
Diffractive returns from wing tips.	D.1 D.11 D.12	D.14 D.15 D.18 D.20 D.24	D.36
Specular returns from wing edges.	D.3 D.7 D.11	D.15 D.17 D.18 D.20 D.23	D.27 D.35

Table 4.1: The interesting backscatter features which can be seen in the high resolution radar imagery of the Mirage aircraft. For each backscatter feature there are a number of figures listed in which the feature of interest can be clearly seen. The figures appear in Appendix D.

4.4 Radar imagery of commercial aircraft

Section 4.3 described a controlled turntable experiment where radar data from the Mirage aircraft were collected. This section describes an experiment where radar data were collected from real aircraft in flight at a local airport.

4.4.1 Collecting the data

Microwave Radar Division (MRD) of the Defence Science and Technology Organisation (DSTO), Australia, has a mobile radar van which is used to collect high resolution radar data [52]. The radar is routinely used to collect data from commercial aircraft using Adelaide airport. The X-band radar has an effective range of only 4 kilometres for medium-sized commercial aircraft. Tracking of an aircraft is achieved by manually steering the antenna dish as the aircraft is viewed through a telescopic sight which is rigidly attached to the antenna mount. Nevertheless, even with this limited facility, it has been possible to obtain excellent HRRPs and ISAR images of non-cooperative aircraft in flight.

For the experiment described in this section a stepped frequency waveform, starting at 8.96 GHz and stepping over a 256 MHz band in 128 steps of 2.0 MHz, was used to achieve a large bandwidth, and hence a high resolution in range. The time taken for one complete frequency sweep was 6.4 ms, and the sweeps were continuously taken during the aircraft's flight. The stepped frequency waveform which was used to collect the data is shown in Figure 4.9. A data *record* consists of the data collected from a single aircraft over the range of aspects available. Each data record was collected from a physically different aircraft. The necessary calculations for stepped frequency ISAR imaging at the airport are given in Appendix B.

4.4.2 Difficulties with the data collection

The major limitations of the Mirage experiment (Section 4.3) are those common to static RCS ranges:

- Difficulty in eliminating ground returns;
- Difficulty in shielding the aircraft support structure.

A dynamic RCS range, where the target moves under its own power in free space, eliminates both of these problems. MRD does not operate a dynamic RCS range, but instead MRD collects such data at the local airport. One limitation of collecting data at the local airport is that the data collection is restricted to targets which frequently use the airport. Another limitation is that data can only be collected from limited aspects. The available data collection aspects at this particular airport are 110° to 160° for outgoing

aircraft and 20° to 80° for incoming aircraft[9]. The geometry which was used to collect data at Adelaide airport is shown in Figure 4.10. The choice of the data collection site was determined by the limited radar range ($\approx$ 4 km) and the necessity of being outside the prohibited area of the airport.

For outgoing aircraft, data collection began after the aircraft had retracted its landing gear. For incoming aircraft, data collection with the aircraft landing gear lowered was unavoidable, due to the limited range of the radar.

[9] 0° represents a head-on aspect of the aircraft.

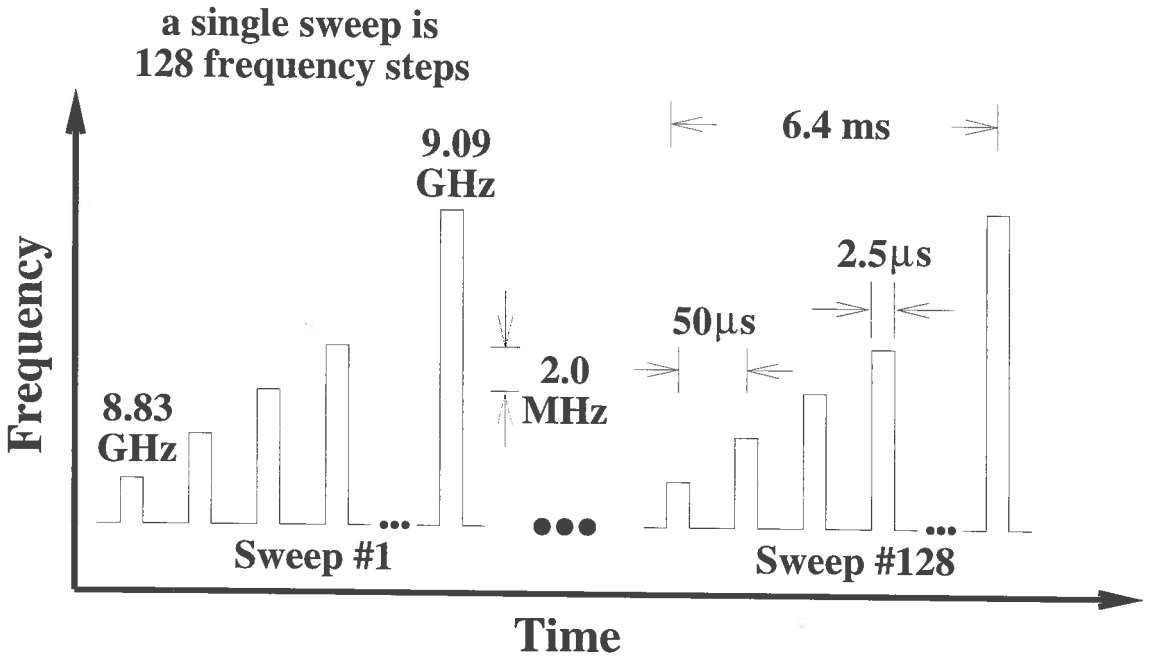

(a) The stepped frequency waveform which was used to collect data at Adelaide airport.

Waveform parameter	Value
Start frequency	8.83 GHz
Centre frequency	8.96 GHz
End frequency	9.09 GHz
Frequency step	2.0 MHz
Bandwidth	256 MHz
Pulse width	2.5 μs
Effective PRF	156 Hz
Pulses per frequency sweep	128
Sweeps per image	128

(b) The parameters of the stepped frequency waveform which was used to collect data at Adelaide airport.

Figure 4.9: The stepped frequency waveform which was used to collect data at Adelaide airport.

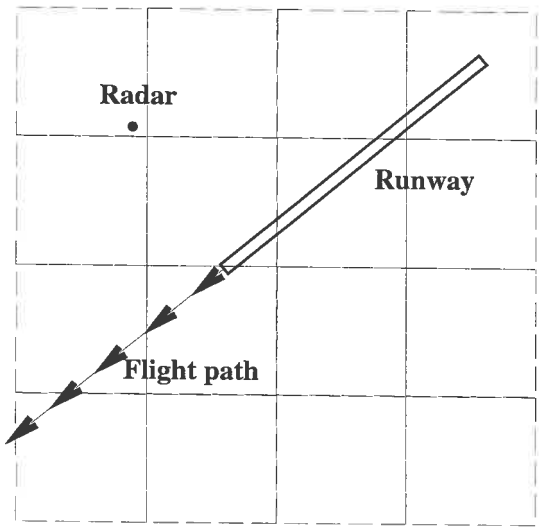

Figure 4.10: The site near Adelaide airport which was used for collecting commercial aircraft data. Data were collected after the aircraft had retracted their landing gear. The grid size is one kilometre.

4.4.3 *Processing*

128 complex frequency samples were processed with a Hann window and an IDFT to produce a HRRP with a resolution of approximately 1.0 metre. The ISAR processing used is described in Appendix A.

4.4.4 *Discussion*

Figures 4.11, 4.12 and 4.13 show ISAR images of the Boeing 727 and 747 aircraft at various aspects. These images have been chosen for display because their cross-range resolution corresponds closely to their range resolution thus giving the images a square aspect ratio. It can be seen that in each case the ISAR image corresponds closely to the accompanying aircraft schematic. The sources of backscatter that can be identified are very similar to those found on the Mirage aircraft, with the exception that the extended engine cavity returns are absent. Several reasons for the absence of engine cavity backscatter are given in Section 4.5.2. Even though extended engine cavity returns are absent, the backscatter from the engine support structures is still clearly evident.

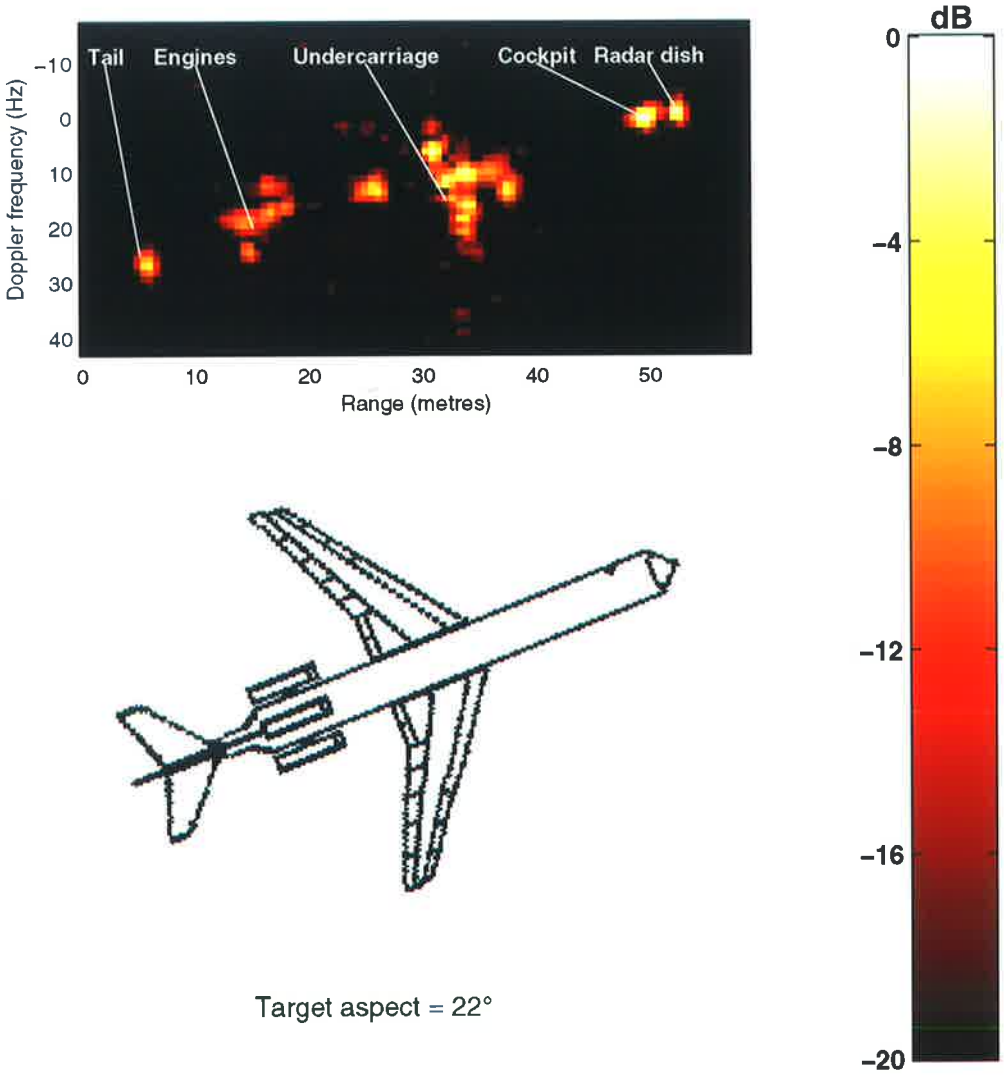

Figure 4.11: An ISAR image of an incoming Boeing 727 aircraft viewed from an aspect of 22°. The image was generated from real data collected at Adelaide airport. The prominent visible scatterers include: the radar dish; the cockpit canopy; the main undercarriage; the trailing edge of the wing; the engine intakes; the engine support structure and the tail tip.

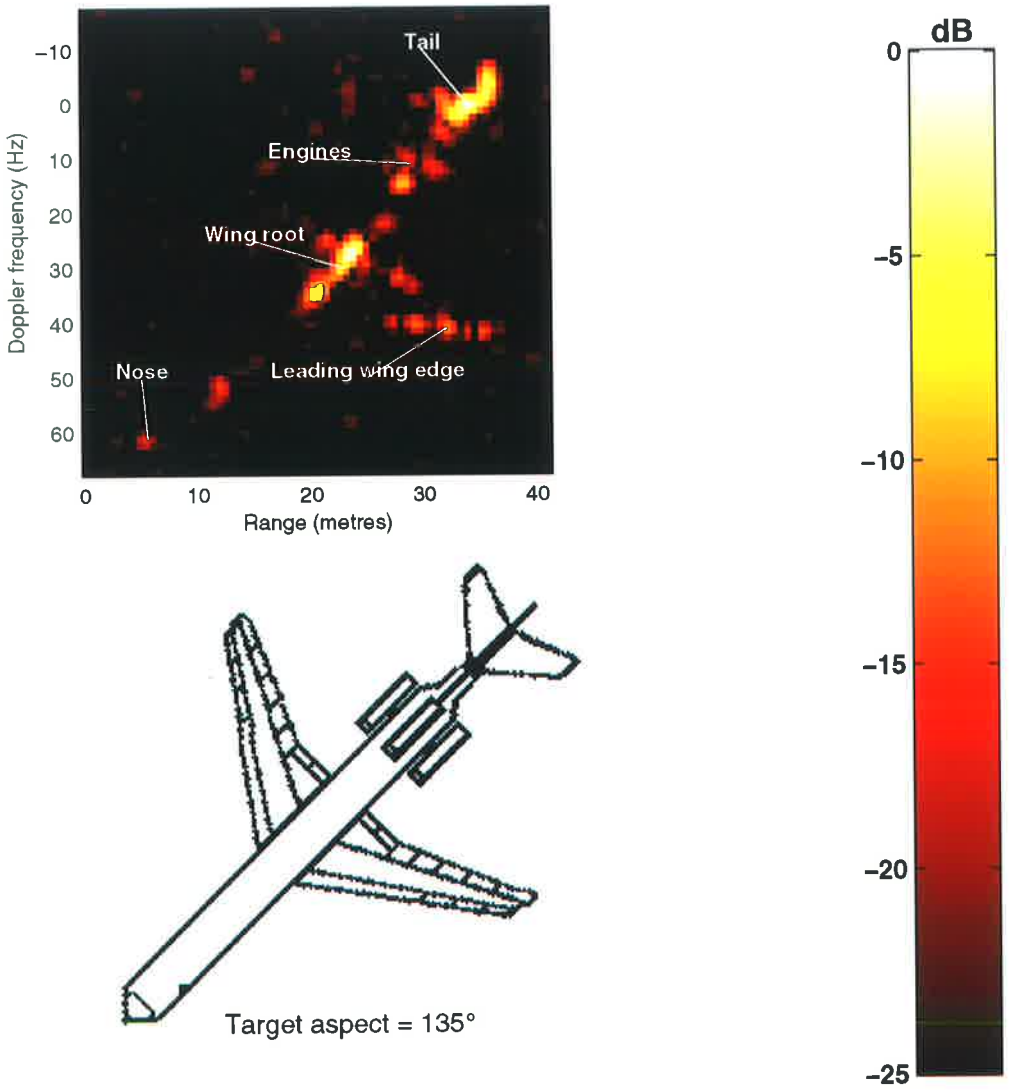

Figure 4.12: An ISAR image of an outgoing Boeing 727 aircraft viewed from an aspect of 135°. The image was generated from real data collected at Adelaide airport. The prominent visible scatterers include: the nose tip; the wing root; the leading and trailing edges of the wing; the engine support structures and the tail tip.

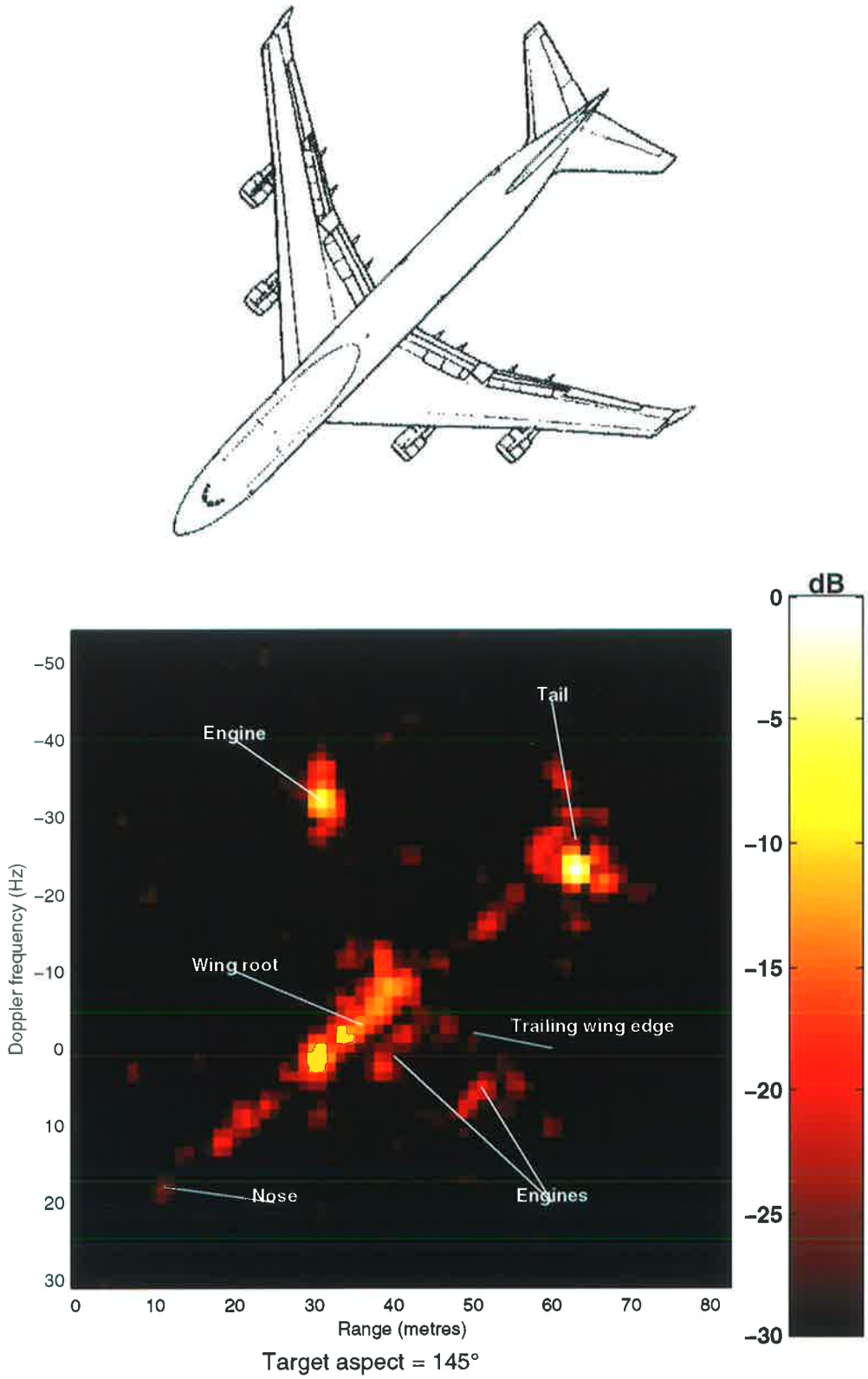

Figure 4.13: An ISAR image of an outgoing Boeing 747 aircraft viewed from an aspect of 145°. The image was generated from real data collected at Adelaide airport. The prominent visible scatterers include: the nose tip; the wing root; the engine support structures; the tail tip and the trailing wing edge.

RCS variation with aspect

The amplitude of the return in a range bin of a HRRP or a range-Doppler bin of an ISAR image varies with small changes in aspect. This amplitude variation is due to the single bin return being the coherent sum of a number of scattering features on the target. The exact imaging geometry determines the way in which the returns from the target coherently sum. The variation in amplitude, for a given aspect change and resolution bin, is likely to be larger for HRRP range bins than ISAR range-Doppler bins. This is because the "bins" in an ISAR image are smaller than the corresponding range bins in a HRRP. Sections 3.4 and 3.5 provided an introduction to HRRPs and ISAR respectively.

Figures 4.14, 4.15 and 4.16 illustrate how backscatter amplitude changes with aspect. Figure 4.14 shows a sequence of consecutive HRRPs of the Boeing 737 aircraft. The change in aspect between each HRRP is approximately 0.03°. The SNR for each HRRP is very low but it can be seen that there are four combined[10] scattering centres on the Boeing 737 aircraft at this particular aspect. Note that even though there are significant amplitude variations for each "scattering centre", the change in position of each scatterer, over the 10 HRRPs, is negligible.

Figure 4.15 shows a longer sequence of HRRPs of a Boeing 737 aircraft. Figure 4.16 shows a sequence of ISAR images generated from the same sequence of data. The data cover a time period of 3.3 seconds and a change in aspect of approximately 8°. Note that even though the positions of the scattering centres remain reasonably constant over the 8° data sequence, the amplitudes of the scattering centres fluctuate. The variation in scatterer amplitudes is especially evident in Figure 4.15 and less evident[11] in Figure 4.16. Note that the variation in scatterer positions with respect to aspect is much less than the corresponding variation in scatterer amplitudes. Consequently it is the relationship between the scattering centre positions which should be the primary clue to target identity.

[10] The scattering centres are called *combined* because they probably do not correspond to single scattering features on the aircraft.

[11] The smaller the resolution bin the smaller the fluctuations in RCS for a given aspect change. Hence there is less fluctuation in a sequence of ISAR images.

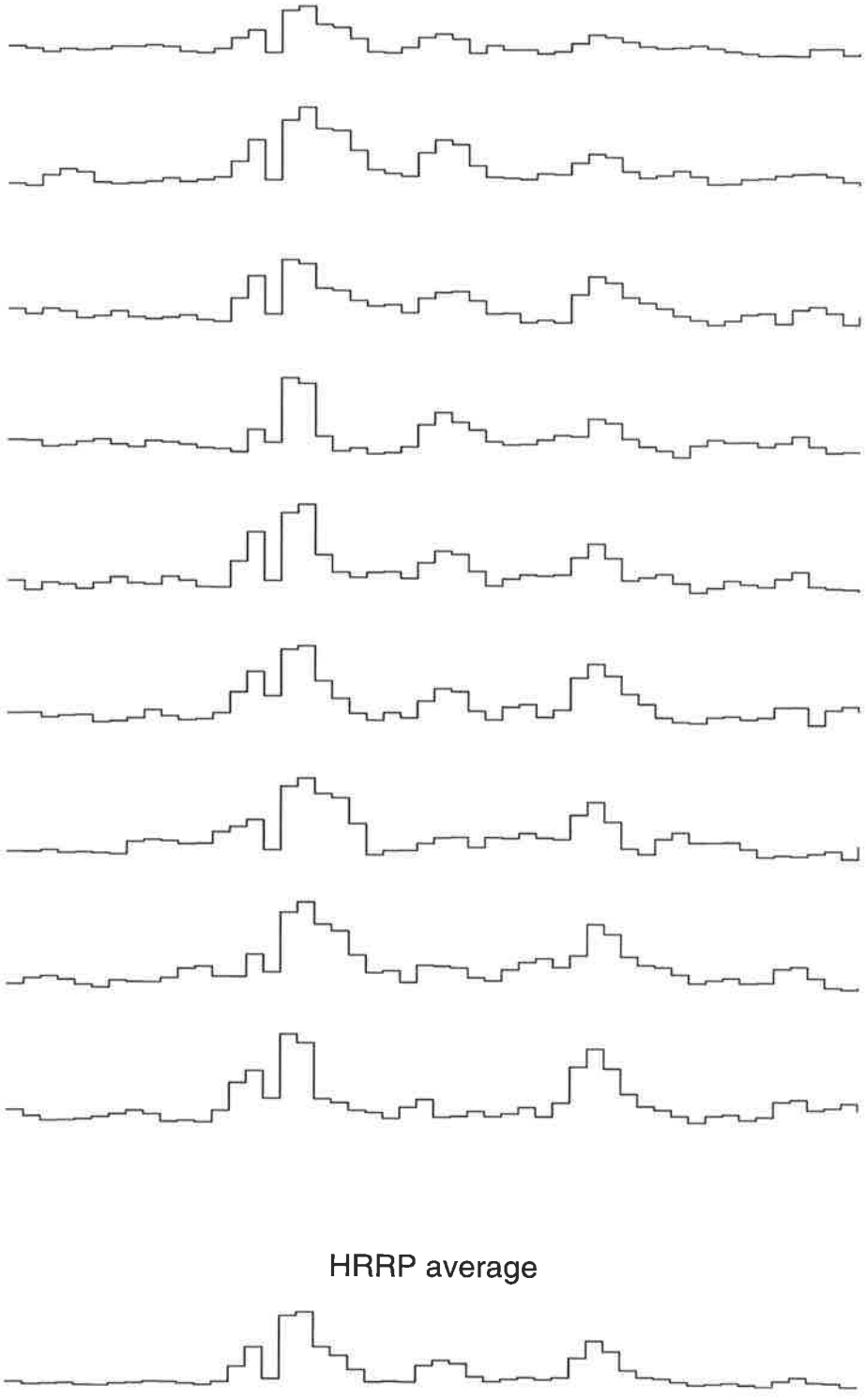

Figure 4.14: A sequence of HRRPs from a Boeing 737 aircraft. The change in aspect between each HRRP is approximately 0.03°. It can be seen that there are four scattering centres for the Boeing 737 aircraft at this particular aspect. Note that the positions of the scattering centres remain constant whereas the amplitudes of the scattering centres fluctuate.

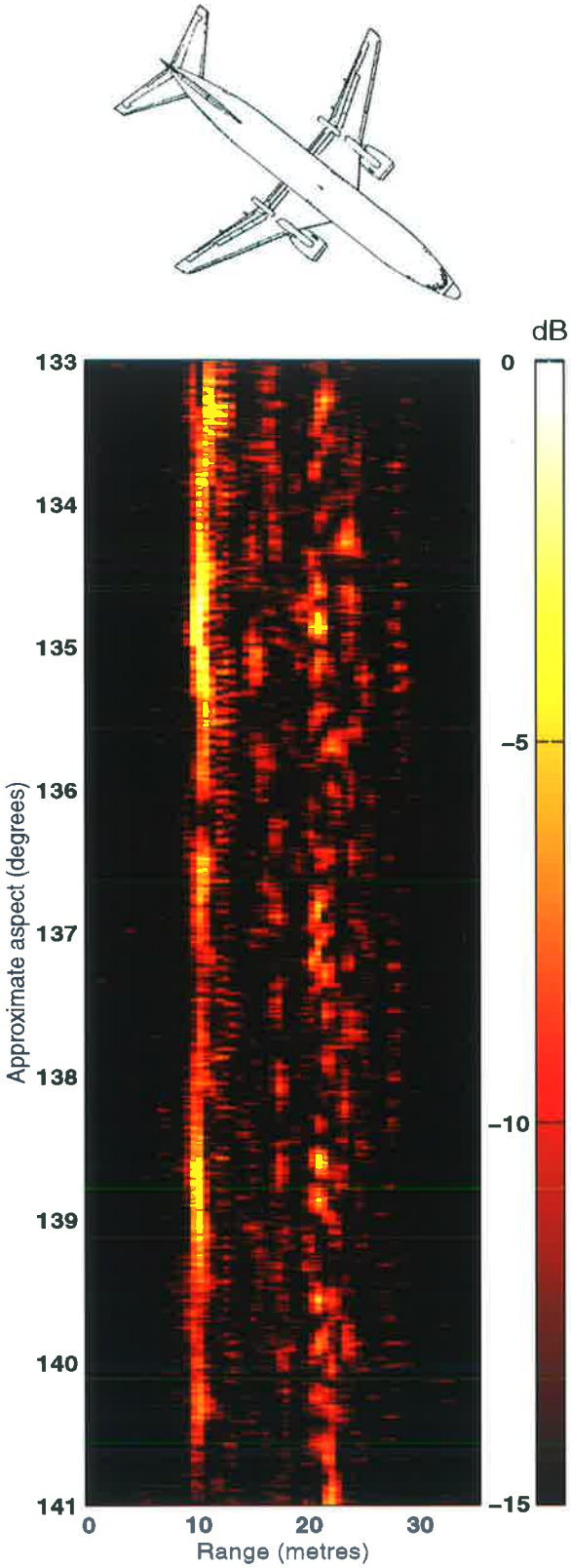

Figure 4.15: A sequence of HRRPs from a Boeing 737 aircraft. Radial motion compensation has been applied to align the HRRPs. The HRRPs cover a time period of 3.3 seconds and a change in aspect of approximately 8°. Note that the positions of the scattering centres remain constant over the HRRP sequence whereas the amplitudes of the scattering centres fluctuate.

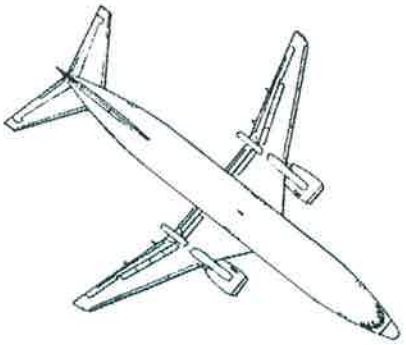

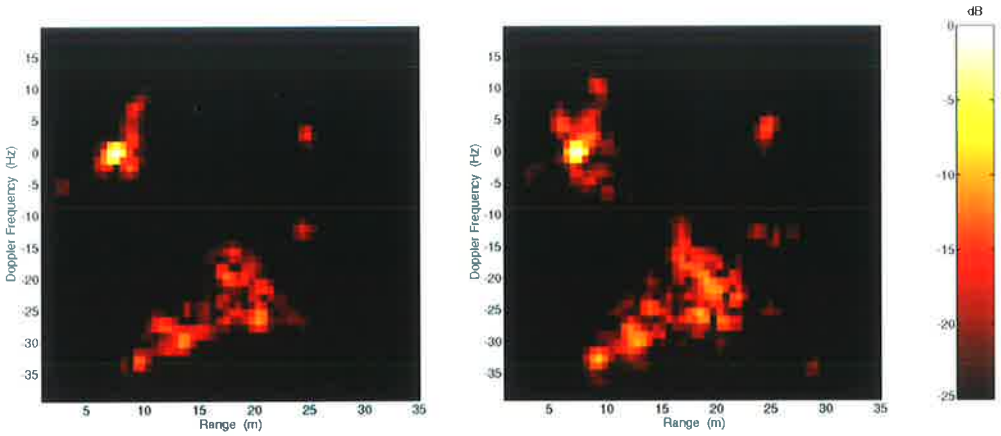

(a) Time 0.0 s. Aspect is 133°. (b) Time 0.8 s. Aspect is 135°.

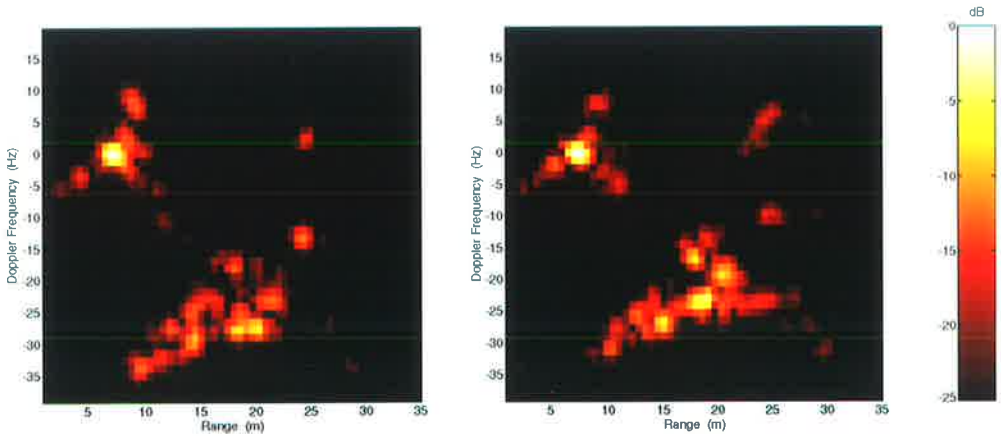

(c) Time 1.7 s. Aspect is 137°. (d) Time 2.5 s. Aspect is 139°.

Figure 4.16: A sequence of ISAR images from a Boeing 737 aircraft. The images cover a time period of 3.3 seconds and a change in aspect of approximately 8°. Note that the positions of the scattering centres remain constant over the image sequence whereas the amplitudes of the scattering centres fluctuate.

4.5 Discussion

4.5.1 Broadside aspects

Section 4.3 has shown that broadside aspects of the Mirage aircraft produce very large radar returns. The HRRPs at broadside aspects provide very little information about the target structure or target identity. The same is true for broadside aspects of commercial aircraft. Typical examples of broadside HRRPs are shown in Figure 4.17. Note how the Boeing 737 HRRP is similar to the Boeing 727 HRRP. In general broadside HRRPs of most aircraft appear similar.

There are two main reasons why it is difficult to classify HRRPs from broadside aspects. Broadside is the worst aspect angle for the slant-range separation of the prominent scatterers which are located on the fuselage of an aircraft. These prominent scatterers include the radar dish, cockpit canopy, engine intakes and the engine support structure. A small separation in range for a large number of important scatterers suggests that target classification would be difficult from a broadside aspect.

The second reason why target classification using HRRPs is difficult from broadside aspects is related to a practical issue. The aircraft fuselage produces a very large specular return at broadside aspects. Since the radar receiver has a limited dynamic range, many small scattering features (*e.g.* wing tips) on the aircraft are not seen in the HRRP. The smaller scattering features are either lost in the noise floor or obscured by the sidelobes of the large fuselage return.

Another problem that has been found at broadside aspects is that ISAR focussing is generally more difficult to achieve at broadside aspects. Broadside aspects accounted for the majority of the aircraft data which could not be satisfactorily focussed using Haywood's algorithm. A discussion on why focussing is more difficult at broadside aspects was given in Section 3.5.3.

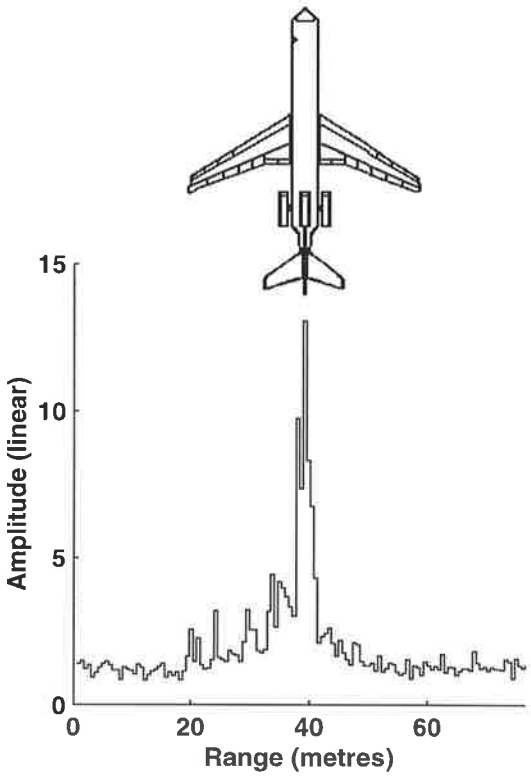

(a) A typical broadside HRRP of the Boeing 727 aircraft.

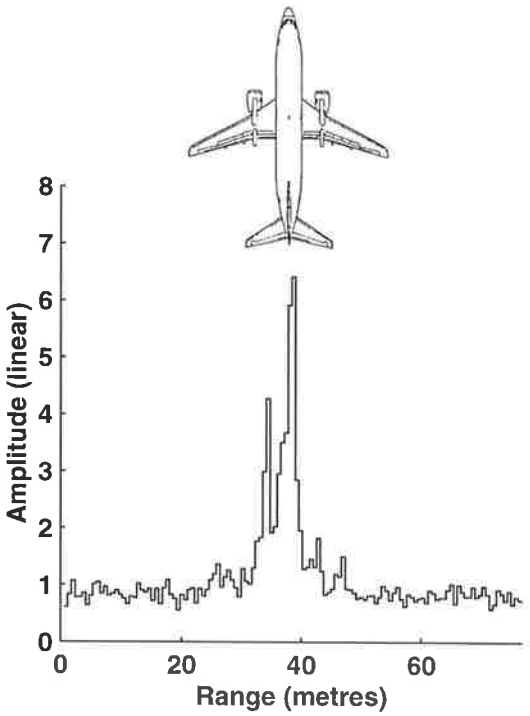

(b) A typical broadside HRRP of the Boeing 737 aircraft.

Figure 4.17: Typical broadside HRRPs of the Boeing 727 aircraft and the Boeing 737 aircraft. Note that the broadside HRRPs are very similar even though the aircraft are quite different.

4.5.2 *Engine cavity scattering*

The HRRPs and ISAR images of the Mirage aircraft indicate that the dominant contributions to overall RCS are made by direct and indirect (cavity) specular reflections. The engine cavity returns are seen at aspects up to 70° from head-on. From rearward aspects the tailpipe cavity scattering is very significant. Figures 4.18 and 4.19 dramatically illustrate the importance of engine cavity backscatter.

Figure 4.18 shows two HRRPs of the Mirage along with a scaled side-view schematic. Both HRRPs are at head-on (0°) aspects but the upper HRRP has normal engine cavities whereas the lower HRRP has rammed engine cavities. The labelled backscatter features are:

1. cockpit bulkhead;
2. radar dish;
3. front undercarriage;
4. rear undercarriage;
5. engine intake;
6. trailing wing edge;
7. trailing edge of fuselage.

The most compelling evidence of engine cavity backscatter is the severe reduction in the returns of the rammed HRRP after 10 metres. The reduction in returns is due to the engine cavities being rammed. The absence of the engine cavity returns means that smaller backscatter features on the aircraft become "visible" since they are not obscured by the engine cavity return. In particular the returns from the trailing wing edge and the trailing fuselage edge can be clearly seen in the rammed HRRP of Figure 4.18.

Figure 4.19 illustrates the effect of each engine state (normal, rammed and rotating) on the generated ISAR imagery. The labelled backscatter features are:

1. engine cavity;
2. radar dish;
3. wing tip;
4. tailpipe cavity;
5. modulated compressor returns;
6. ground returns.

In these ISAR images, the engine cavity backscatter appears at a cross-range position of approximately 2 metres. These engine cavity returns should not be confused with the spurious ground returns which appear at a cross-range position of 0 metres.

Ramming the engine intakes has eliminated the extended engine cavity returns. The effect of the rotating compressors on the ISAR image is more complex. Since the rotating compressor blades modulate the incident radar signal, the returns from the compressor blades are offset in cross-range. The actual cross-range offset for each blade return is meaningless because the sampling rate of the data is not high enough to avoid aliasing. The returns from the compressor blades are discussed further in Section 4.5.3.

Extended engine cavity returns are not evident in the radar imagery of the commercial aircraft. Nevertheless, returns from the engine intakes and the engine support structures are still clearly visible (see Figures 4.11 and 4.12). The lack of extended cavity returns from commercial aircraft is understood when the physical engine geometry of a commercial aircraft is compared to that of a typical fighter aircraft. A fighter aircraft is built around its engine whereas a commercial aircraft is built around its passenger carrying fuselage. The fighter aircraft has a long slender engine cavity which has a length comparable to the aircraft size. The commercial aircraft has a short stubby engine cavity which has a length which is a small fraction of the aircraft size. This suggests that the engine length to width ratio influences the significance of engine cavity backscatter and that the backscatter from a long slender cavity is more pronounced than the backscatter from a short stubby cavity. A detailed discussion of engine cavity backscatter is beyond the scope of this thesis and the reader is referred to [2] for further discussion. Note that Knott's discussion may not satisfy the inquisitive reader, but it must be remembered that much of the work on engine cavity backscatter is classified due to national security interests.

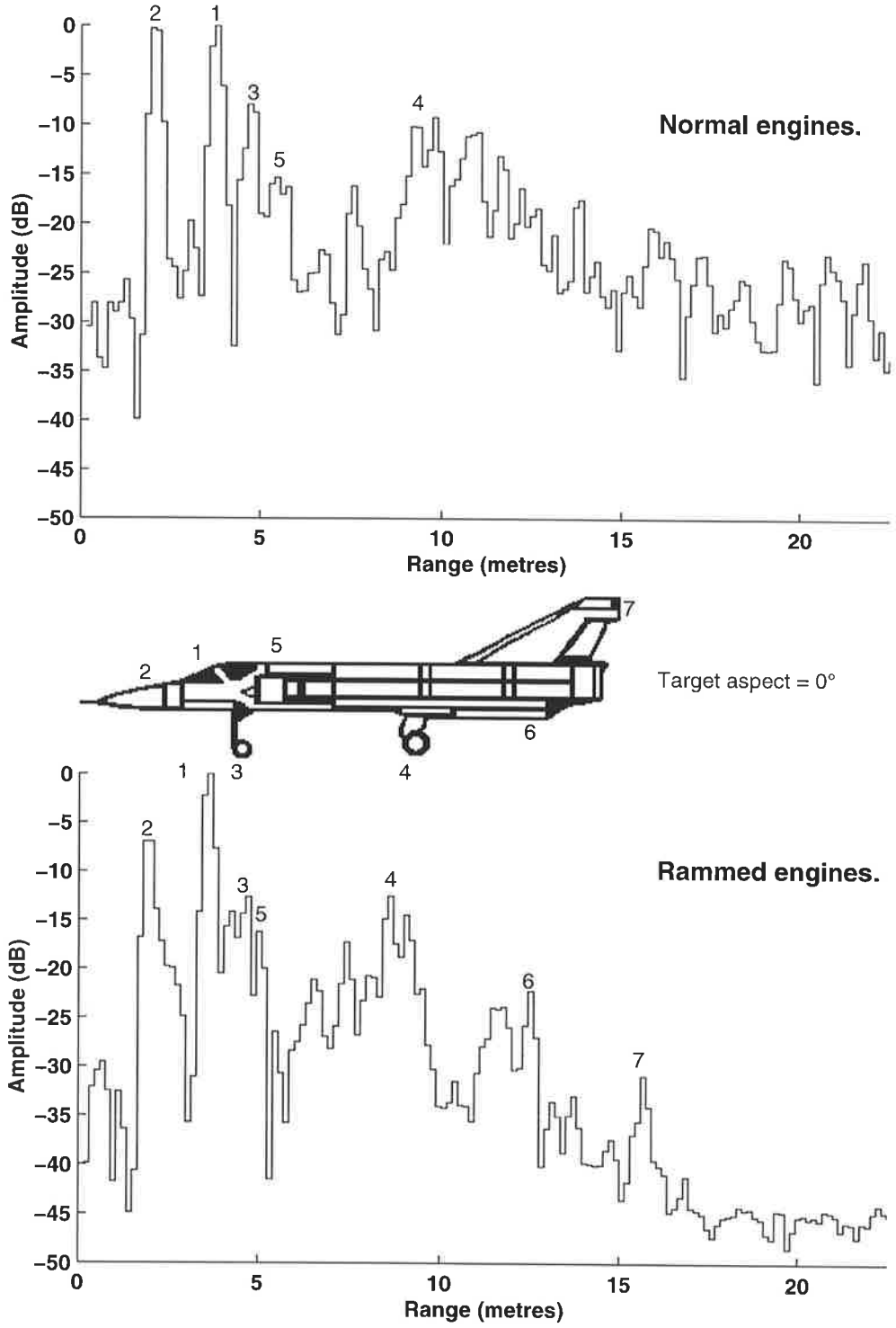

Figure 4.18: Head-on HRRPs of the Mirage aircraft. The polarisation is V–V. The top HRRP is of the Mirage with the engine intakes clear, and the bottom HRRP is the same aircraft with the engine intakes rammed. The prominent radar scatterers are: (1) The cockpit bulkhead; (2) The radar dish; (3) The front undercarriage; (4) The rear undercarriage; (5) The engine intake; (6) The trailing edge of the wing; (7) The trailing edge of the fuselage.

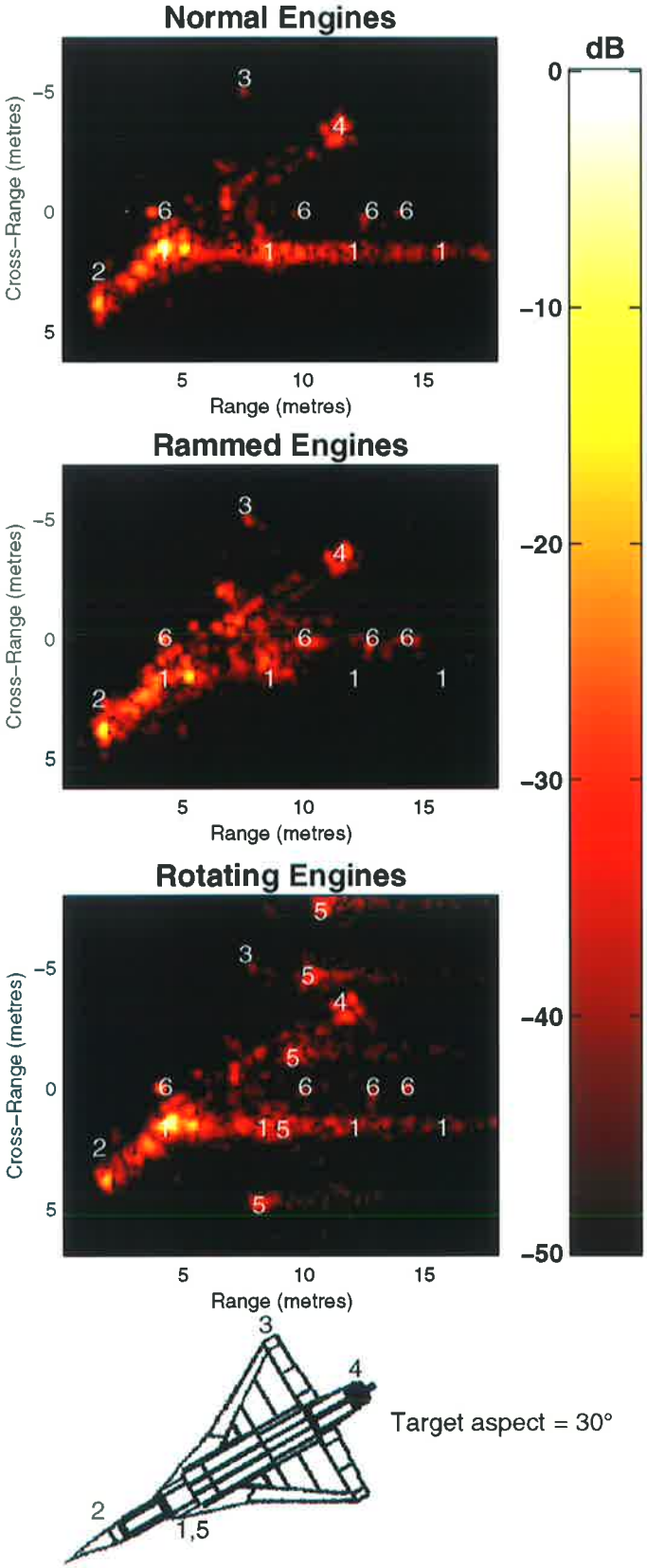

Figure 4.19: ISAR images of the Mirage aircraft with the engines in three different states. The polarisation is H–H. The prominent radar scatterers are: (1) The engine cavity; (2) The radar dish; (3) The wing tip; (4) The tailpipe cavity; (5) The engine compressor which modulates the radar returns; (6) The ground returns.

4.5.3 *Doppler modulation*

Almost all airborne targets are equipped with some form of rotating machinery which modulates incoming radar signals [30]. Radar imagery of helicopters displays significant modulation effects due to the exposed main and tail rotors of a helicopter [28]. Aircraft jet engines cause JEM due to the rotating engine compressor blades. Radar returns from the Mirage aircraft exhibit significant JEM. Unfortunately the sampling rate of the data collected in this chapter was limited to 78 Hz, thus precluding the further study of the Mirage JEM.

4.5.4 *Target classification using high resolution data*

In this section some comments are made regarding target classification from high resolution radar imagery:

Broadside aspects

It has been seen that broadside aspects of targets produce very large radar returns with very little target identification information. This suggests that target classification at broadside aspects is especially difficult.

Large dynamic range

Radar imagery is very different to infrared or visual imagery. Radar imagery has a very large dynamic range and special preprocessing techniques are needed to extract the relevant features for high resolution radar target classification.

Variation of RCS with aspect

The amplitude of the radar return for a particular target scatterer can change significantly over a very small aspect range whereas the position of the scatterer remains consistent. Hence the knowledge of scatterer positions is very important for target classification whereas the relative scatterer amplitudes are less important.

Engine cavity backscatter

It has been shown that engine cavity backscatter is a very important backscatter feature for the Mirage aircraft. Engine cavity backscatter is not a dominant feature in the commercial aircraft imagery, but it is likely to be a dominant feature in imagery of other fighter aircraft. Engine cavity backscatter complicates target classification because it is a distributed (multiple scattering) backscatter phenomenon.

Jet engine modulation

A JEM phenomenon has been observed in the radar imagery of the Mirage aircraft. A detailed investigation of JEM was not possible because the sampling rate (PRF) of the radar was not high enough. Nevertheless, [30, 53] suggest that target classification can be based upon JEM.

4.6 Summary

Section 4.2 reviewed the theory of radar backscatter from complex objects. The review was based upon material covered in [2]. It was found that there was a good agreement between the theoretical predictions of radar backscatter and the experimental observations made later in the chapter.

This chapter has examined experimental RCS data of a Mirage aircraft and several commercial aircraft. The Mirage data were collected from a turntable facility whereas the commercial aircraft data were collected at a local airport. The objective of this chapter was to provide a phenomenological introduction to radar backscatter from aircraft. The objective of this chapter was successfully accomplished by processing experimental data and comparing the imagery with theoretical predictions of radar backscatter.

Three separate sets of measurements of the Mirage aircraft were made. In the first set of measurements, the engine intakes were plugged with RAM to eliminate engine cavity backscatter. For the second set of measurements, the engine intakes were left in their normal state. For the final set of measurements, the engine intake compressors of the aircraft were electrically rotated at operating speed to observe the effects of JEM. The RCS data of the Mirage aircraft were displayed in the following formats:

- HRRP plots at specified aspects;
- ISAR image plots at specified aspects;
- Frequency-azimuth RCS plots over 360° of aspect;
- Range-azimuth RCS plots over 360° of aspect.

Data were collected of incoming and outgoing commercial aircraft at a local airport. These non-cooperative data of real aircraft in flight, were intended to supplement the turntable controlled Mirage data. Sections of the commercial aircraft data were processed to give ISAR imagery and range-azimuth RCS plots. In Section 4.5, the phenomena of engine cavity scattering and JEM were discussed. Finally, the chapter concluded with a brief discussion of the issues relevant to target classification using high resolution radar.

Chapter V

ISARLAB: A SIMULATOR FOR HIGH RESOLUTION RADAR DATA

5.1 Introduction

5.1.1 Chapter purpose and motivation

Even though high resolution radars are becoming more common there is still a fundamental lack of access to real high resolution radar data. Not everyone has access to an experimental radar and those who do have access are often involved in classified RCS measurement. Target classification research demands a variety of target types viewed from many different aspects but collecting data in the field costs time and money. Chapter 4 collected radar backscatter data from a few full-scale aircraft targets. Even though a huge amount of real radar data was collected, these data do not suffice for the development of a target classification system. The only way to provide the diversity of scenarios required for developing a target classification system is by simulating high resolution radar data.

High resolution radar simulators are scarce and building a new one from scratch is a formidable task. This chapter presents a radar simulator called ISARLAB (ISAR LABoratory) which has been specifically designed to meet the needs of high resolution target classification studies. The design of ISARLAB was based upon well established radar backscatter theory and the study of radar backscatter from full-scale aircraft made in Chapter 4. ISARLAB was designed to generate high resolution radar data which can be used for *target classification studies* . ISARLAB was *not* intended for detailed RCS modelling or for studying radar backscatter from targets. Consequently, the measure for success for ISARLAB is whether it can produce radar imagery with the same general characteristics that were seen in Chapter 4.

ISARLAB is used to serve a number of functions:

Data browser

ISARLAB is used to process real data collected from experimental facilities.

Target classification studies

ISARLAB is used to generate simulated data over a wide variety of scenarios. These data are then used to test target classification algorithms.

Algorithm testbed

ISARLAB is used as a convenient environment for testing new high resolution radar processing algorithms.

5.1.2 *Chapter overview*

ISARLAB is a very comprehensive software suite which has taken approximately 2 man-years to develop. Consequently, all of the design and implementation details for ISARLAB cannot be given in this chapter. This chapter gives an overview of ISARLAB along with some of the key design decisions which have made ISARLAB the readily usable system that it is. Some of the work in this chapter has been published by the author in [58]. The further development of ISARLAB is continuing at Microwave Radar Division, DSTO.

Section 5.2 provides an overview of the ISARLAB system. The system is divided into functional subsystems which are discussed in subsequent sections. Sections 5.3, 5.4 and 5.5 discuss radar backscatter modelling, motion modelling and radar waveform modelling respectively. Section 5.6 gives a brief summary of some of the processing algorithms that ISARLAB supports. Section 5.7 discusses some of the implementation issues associated with the development of ISARLAB. To demonstrate the utility of ISARLAB the radar data collection trial described in Section 4.4 is simulated in Section 5.8. The results show that ISARLAB produces ISAR images comparable in appearance to those produced from real data. Finally, Section 5.9 discusses some of the ongoing work which is increasing the functionality of ISARLAB.

5.1.3 *Modelling in ISARLAB*

Choosing the modelling complexity of a radar simulator is a key decision which depends upon the final application for the generated data. For target detection simulations a Swerling model may suffice. For target RCS modelling more detailed models are required and it it is always necessary to collect some real data to verify even the most detailed simulation. Simulators [54, 55, 56] which perform RCS calculation or prediction are computationally expensive and cumbersome to use. Other simulators [49, 57] which use simpler scattering models have been geared towards very specific problems and lack the flexibility and extensibility required for different target types and target classification scenarios.

Knott [2] points out that there can be many reasons for RCS measurement:

> *There are five basic reasons for conducting RCS measurements, and each has a different influence on the way the measurements are carried out. The five reasons are:*

- *Acquire understanding of basic scattering phenomena;*
- *Acquire diagnostic data;*
- *Verify system performance;*
- *Build a database;*
- *Satisfy a contractual requirement.*

Similarly, there are many reasons for simulating radar data. The reason for simulating the data does influence the way in which the simulation is carried out. RCS simulations require a simulator with a detailed electromagnetic approach because the amplitude of the simulated returns must correspond very closely to the amplitude of the real (measured) returns.

ISARLAB does not attempt to completely model all electromagnetic phenomena, but rather ISARLAB models to a depth which satisfies the objective of producing realistic radar imagery for target classification studies. ISARLAB models the essential target attributes which are likely to be used for target classification.

5.2 ISARLAB system overview

ISARLAB consists of five main simulation subsystems:

Radar backscatter modelling
The mapping from a target's physical attributes to a radar backscatter model is discussed in Section 5.3.

Scenario specification and update
The incremental update of target and radar positions is discussed in Section 5.4.

Radar waveform modelling
The provision for different radar waveform types is discussed in Section 5.5.

Radar signal processing
The radar signal processing provided by ISARLAB is discussed in Section 5.6.

Display processing
The data visualisation capabilities of ISARLAB are discussed in Section 5.7.

Figure 5.1 provides a system overview of ISARLAB. Note that the system is partitioned into naturally distinct subsystems. The main advantage of this partitioning is that each subsystem can be implemented and maintained separately as long as the interfaces between subsystems are well defined. The subsystem interfaces are listed in Table 5.1.

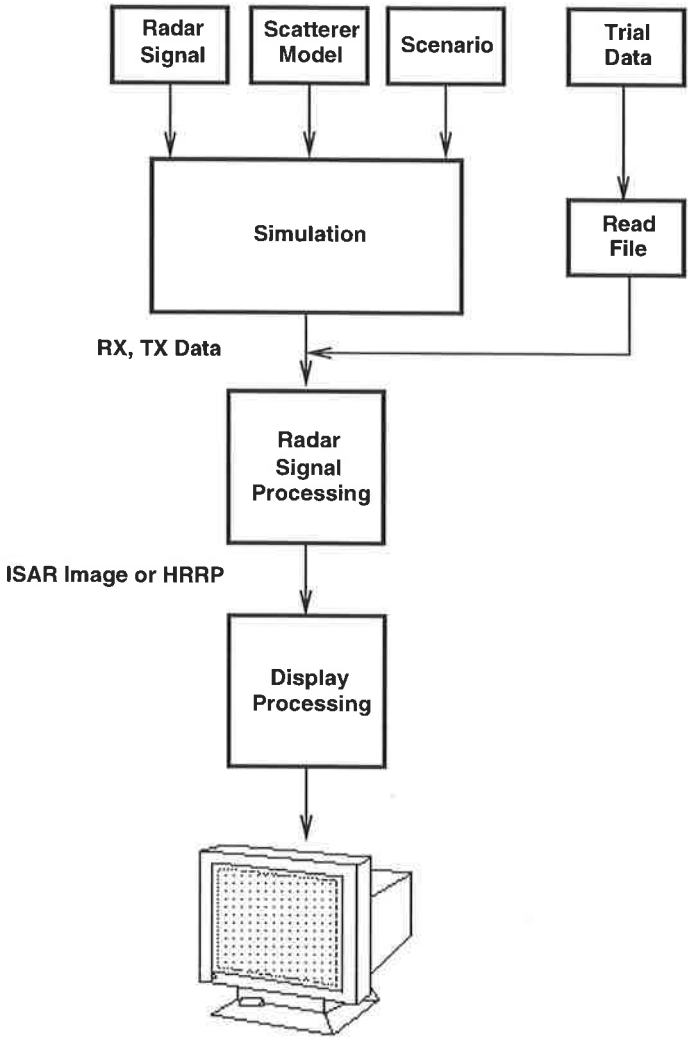

Figure 5.1: An overview of the processing hierarchy in ISARLAB. Note that the radar signal, scatterer model and scenario need to be defined in order to run a simulation and that the radar and display processing can be applied to real data.

Input	Subsystem	Output
A list of scatterers with: • occlusion pattern; • radiation pattern; • three–dimensional position; • amplitude; for each scatterer.	Radar backscatter	For a given viewing angle, the list of *visible* scatterers with: • three–dimensional position; • amplitude and phase; information provided.
A specification of the radar and target trajectories in three–dimensional space.	Scenario update	At each simulated time instant this subsystem provides the current three–dimensional positions and orientations of the radar and the target.
A choice of the radar waveform and any associated parameters.	Radar waveform	The waveform specification is used to generate the radar return from each target scatterer.
A choice of various processing algorithms, parameters and output formats.	Radar signal processing	The output can be raw data, HRRPs or ISAR images.
User defined display parameters, *e.g.* dynamic range, colormap, zoom *etc.*	Display processing	The data are displayed in various formats, *e.g.* image, waterfall plot, mesh plot *etc.*

Table 5.1: Subsystem interfaces for ISARLAB.

5.3 Radar backscatter modelling

A summary of the theory of radar backscatter from complex objects in the optical scattering region was given in Section 4.2. The major point of interest was that a complex target can be characterised as a set of discrete scattering centres. Chapter 4 showed that this approximation is essentially true except for a number of distributed backscatter phenomena such as engine cavity backscatter. ISARLAB models a complex target as a set of discrete point scatterers. ISARLAB does not model any distributed scattering phenomena.

5.3.1 Scattering assumptions

The assumptions on which the ISARLAB target scattering model is based are:

1. It is assumed that the target is a rigid body with no rotating parts or engine cavities.

2. Since ISARLAB is modelling in the optical (Fresnel) region, it is assumed that the target is composed of a finite number of discrete scatterers each with a particular radiation pattern. The effects of occlusion are incorporated along with the scatterer's radiation pattern.

3. It is assumed that the scatterer locations on the target provide more important clues to target identity than the respective scatterer amplitudes. This assumption does not mean that the relative amplitude differences between the scatterers are not modelled, but rather that the *exact level of the backscatter amplitude for each scatterer is not critical.*

4. It is assumed that any target classification decision is made on the basis of the major[1] target scatterers. Hence the modelling of minor target features is a lower priority.

Assumption 1 was made to minimise the complexity of ISARLAB. It was seen in Chapter 4 that engine cavity scattering and JEM are complex phenomena. These phenomena only occur for certain target types and their modelling is beyond the scope of this thesis.

Assumption 2 was justified from well established radar backscatter theory [2] and from the experimental data examined in Chapter 4. A scatterer radiation pattern is used to model the aspect dependence of the return from each point scatterer. An occlusion pattern is used to model the line-of-sight occlusion to the scatterer.

Assumption 3 may seem like common sense, but it is difficult to formally justify. Some of the arguments which support the assumption that *the location of a backscatter centre is more important than its exact amplitude,* are as follows:

[1] A *major* target scatterer is a scatterer which consistently has a large amplitude.

- The set of target scatterer locations gives important clues about the target's physical geometry. The set of target scatterer amplitudes does not provide these clues.
- The position of a particular scatterer changes only slightly with small changes in aspect. The amplitude of a particular scatterer can change dramatically with a small change in aspect, due to the coherent summation in a particular resolution bin.

Assumption 4 is also a common sense assumption. It is justified from practical considerations. The dynamic range of a radar receiver is limited which means that smaller scatterers are not consistently seen. Smaller scatterers are also obscured by the sidelobes of larger scatterers. To obtain accurate, consistent, target classification it is important to base decisions on the consistently appearing, larger, target scatterers.

5.3.2 The single scatterer model

The important characteristics which need to be modelled for a single scatterer are:

1. The location of the scatterer;
2. The maximum reflectivity of the scatterer;
3. The radiation pattern of the scatterer;
4. The radiation pattern orientation;
5. The occlusion pattern of the scatterer.

Characteristics 1 and 2 are simple to model, whereas characteristics 3, 4 and 5 are more complicated to model. The single scatterer model used in ISARLAB has the following parameters:

- x position of the scatterer;
- y position of the scatterer;
- z position of the scatterer;
- Maximum complex amplitude return from the scatterer;
- A function which calculates the scatterer radiation pattern as a function of aspect;
- A function which calculates occlusion information as a function of aspect.

It should be noted that the x, y and z coordinates of the scatterer position are measured relative to a local coordinate frame which is introduced in Section 5.4.2. Ideally the *target origin* should correspond to the centre of effective rotation of the target

with respect to the radar. The scatterer radiation and occlusion functions take a single argument which represents the viewing aspect of the target from the radar. The current version of ISARLAB supports two–dimensional radiation and occlusion functions although an upgrade to three–dimensional functions is currently being considered. For a given viewing aspect the occlusion function returns 0 if the scatterer is occluded and 1 if it is not. The radiation pattern function returns a real number between 0 and 1. By having the occlusion and radiation pattern information modelled and implemented separately as functions, a single scatterer behaviour of arbitrary complexity can be generated. Some of the occlusion and radiation functions used in ISARLAB are shown in Tables 5.2 and 5.3 respectively.

The contribution of a single scatterer to the total target return is given by the following pseudo code

```
single_return = occlusion(aspect)*radiation(aspect)*max_amplitude
```

where `single_return` is the return from a single scatterer, `occlusion()` is the occlusion function, `radiation()` is the radiation pattern function, `aspect` is the radar viewing aspect and `max_amplitude` is the maximum possible reflectivity of the scatterer.

The contribution from each scatterer is delayed according to its distance from the radar and the total target return is calculated by coherently summing these delayed returns. The following pseudo code shows how the total target return is calculated

```
total_return = 0;
for i = 1 to number_of_scatterers
total_return = total_return + delay(single_return(i),distance(i))
endfor
```

where `delay()` is a function which delays the radar waveform according to the scatterer's distance and `distance(i)` is the distance from the radar to scatterer `i`.

Functions which are used to simulate occlusion patterns in ISARLAB

Function	Description	Illustration
`occ_none(aspect)`	The `occ_none` function is used to simulate scatterers which are not occluded for any aspects. `occ_none` returns zero for all values of `aspect`.	
`occ_wedge(aspect,`θ_0`,`θ`)`	The `occ_wedge` function defines an angular segment where the scatterer is not visible. `occ_wedge` returns one for $(\theta_0 - \frac{\theta}{2}) \leq$ `aspect` $\leq (\theta_0 + \frac{\theta}{2})$ and zero elsewhere.	

Table 5.2: Functions which are used to simulate single scatterer occlusion patterns in ISARLAB. Each function takes an input argument `aspect` and produces an output of zero if the scatterer is visible or an output of one if the scatterer is occluded. Some of the functions also take other input arguments which specify the shape of the single scatterer occlusion pattern. All angles (*e.g.* boresight direction) are defined with respect to the target local coordinate frame xyz.

Functions which are used to simulate radiation patterns in ISARLAB

Function	Description	Illustration
`scat_isotropic(aspect)`	The `scat_isotropic` function is used to simulate diffractive backscatter which is aspect independent. `scat_isotropic` returns one for all values of `aspect`.	
`scat_cos2x(aspect,`θ_0`,`θ`)`	The `scat_cos2x` function is used to simulate specular backscatter without sidelobes. θ_0 represents the boresight direction of the specular backscatter and θ represents the 3 dB beamwidth of the specular backscatter.	
`scat_cos2x_x2(aspect,`θ_0`,`θ`,`α`)`	The `scat_cos2x_x2` function is used to simulate specular backscatter with sidelobes. θ_0 represents the boresight direction of the specular backscatter and θ represents the 3 dB beamwidth of the specular backscatter. The input parameter α specifies the level of the first specular sidelobes. The sidelobe level is measured relative to the main specular beam. *e.g.* $\alpha = 10$ specifies that the first specular sidelobes are 10 dB below the main specular backscatter.	

Table 5.3: Functions which are used to simulate single scatterer radiation patterns in ISARLAB. Each function takes an input argument `aspect` and produces an output real number between zero and one. Some of the functions also take other input arguments which specify the shape of the single scatterer radiation pattern. All angles (*e.g.* boresight direction) are defined with respect to the target local coordinate frame xyz.

5.4 Radar and target motion modelling

The simulated motion of the target or radar is subdivided into two components, gross motion and induced motion. Gross motion is where the distributed target is represented by a single point moving with respect to a global reference frame XYZ. Induced motion is measured with respect to a local reference frame xyz. Induced motion refers to the motion induced on the target by the medium it is travelling through. Induced motion is discussed further in Section 5.4.2.

5.4.1 The global coordinate frame

Gross target or radar platform movement is specified in the global coordinate frame. Movement trajectories are specified in one of three ways; a *linear* trajectory, a *circular* trajectory or a *stationary* trajectory. The parameters required for linear and circular trajectories are listed in Table 5.4. In the future, more complicated trajectory specifications may be included in ISARLAB.

The target scatterer positions are measured relative to a local coordinate frame. The origin of this local coordinate frame xyz is the target's position in the global reference frame XYZ. The relationship between the global and local reference frames is shown in Figure 5.2. The local reference frame xyz assumes that the target scatterers are defined in such a way that the target *forward direction* [2] is along the x-axis and the target is *level* in the xy plane.

5.4.2 The local coordinate frame

Target alignment

It is important that the target orientation is maintained in both the local and global coordinate frames for each time step of the simulation. To ensure this, the target is rotated (after induced motion is calculated), so that its *forward direction* (local x axis) corresponds with its global velocity vector.

Induced motion

Induced motion [59] commonly occurs when ships are travelling through water. The water waves induce motion on the ship which can significantly affect any radar imagery taken of the ship. The types of motion induced by the water waves include: roll; pitch; yaw; surge; heave and sway, but it is only the rotational motion components which affect the imaging process. Even though a detailed discussion of induced motion is beyond the

[2] The target *forward direction* is the direction in which the target normally moves.

scope of this thesis, the way in which ISARLAB models this type of motion is briefly mentioned.

Induced motion is very complicated to model since it depends on parameters such as sea state, wave direction, ship mass and ship hull shape. ISARLAB accommodates induced motion in two ways:

1. Precalculated induced motion;

2. Simple modelling of induced motion.

Programs which model the induced hull motion for ships under a variety of conditions already exist. The output from these programs is usually a set of three–dimensional ship displacements versus time. It makes sense to isolate the complexities of induced motion modelling from the core of ISARLAB. Hence rather than ISARLAB duplicating the induced modelling, it is easier and more appropriate for precalculated induced motion displacements to be used by ISARLAB.

If precalculated values are not available, then the induced motion is crudely modelled by specifying the following parameters:

- Amplitude, period and initial phase for the roll angle;
- Amplitude, period and initial phase for the pitch angle;
- Amplitude, period and initial phase for the yaw angle;

where roll is rotation about the x axis, pitch is rotation about the y axis and yaw is rotation about the z axis. The induced motion can then be modelled as sinusoidal oscillations about the three local axes. Figure 5.3 shows how the induced motion components of roll, pitch and yaw are measured relative to the local coordinate system.

The parameters for a linear trajectory	The parameters for a circular trajectory
Initial X position	Initial X position
Initial Y position	Initial Y position
Initial Z position (altitude)	Initial Z position (altitude)
Heading	X position of centre of rotation
Velocity	Y position of centre of rotation
Acceleration	Speed
Climb rate	

Table 5.4: The parameters which are used to describe target or radar motion trajectories.

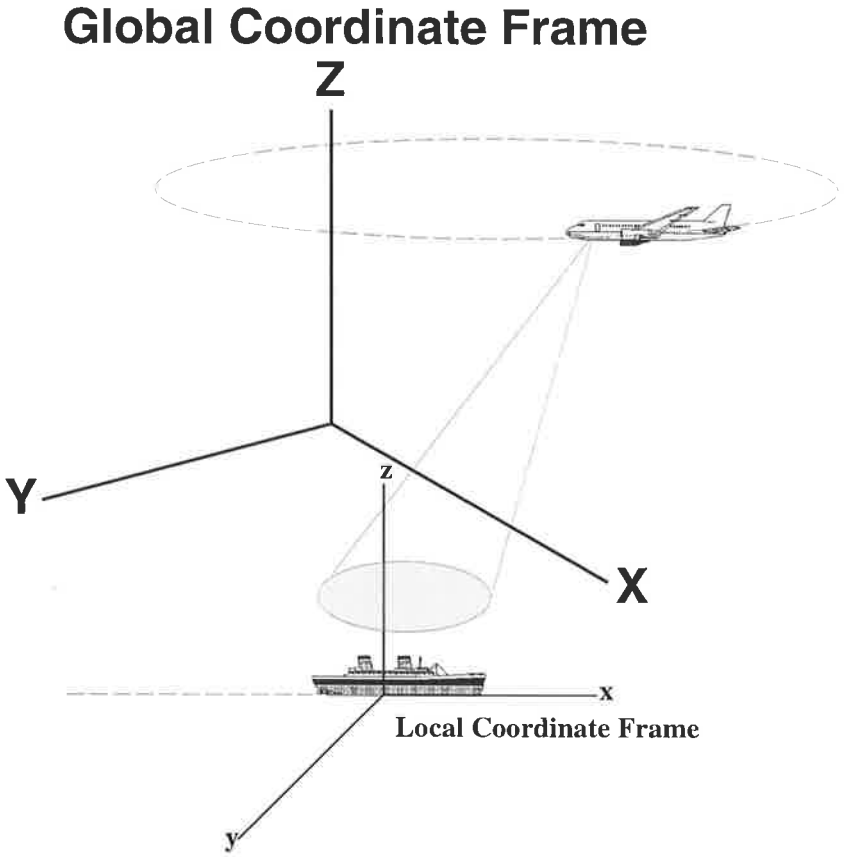

Figure 5.2: The global and local coordinate frames used for motion modelling. In this particular example, the ship (target) is following a linear trajectory and the aircraft (radar) is following a circular trajectory. Both of these motion trajectories are measured relative to the global reference frame XYZ. Note that the two coordinate frames are linked so that the local origin coincides with the target position in the global coordinate frame and the x axis of the local coordinate frame is aligned with the velocity vector of the target in the global coordinate frame.

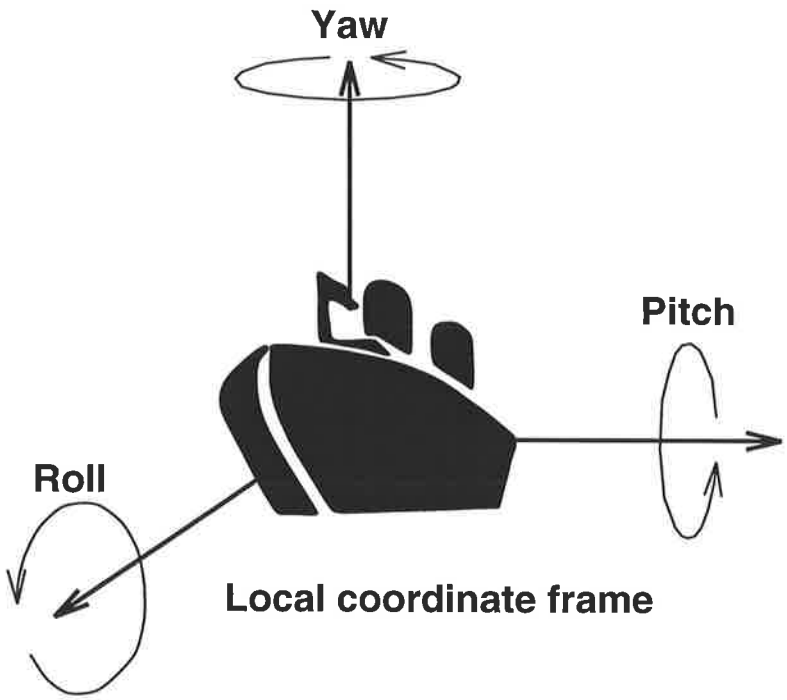

Figure 5.3: Induced motion and the target's local coordinate frame. Roll, pitch and yaw are the major components of induced motion on a ship. The rotations are measured relative to the local coordinate frame xyz.

5.5 Radar waveform modelling

The two most common high bandwidth waveforms used in high resolution radars are the stepped frequency and the linear frequency modulation (chirp) waveforms. An introduction to these waveforms was given in Sections 3.3.3 and 3.3.2 respectively. ISARLAB accommodates both of these waveforms and the parameters required for each waveform type are listed in Table 5.5.

5.5.1 Level of simulation

The calculations which simulate the generation of the raw radar signals proceed on a single HRRP basis. It is assumed that there is no relative motion between the radar and the target during the collection of the data required to form a single HRRP. This is not consistent with reality but it is a close approximation[3] for typical radar data collection scenarios. A chirp waveform only requires a single pulse to form a HRRP, so the target and radar positions are updated after every pulse. A stepped frequency waveform requires a sweep of pulses to form a HRRP and hence the target and radar positions are updated after each frequency sweep.

[3] The approximation may be invalid if the target velocity is very high and the radar is using a stepped frequency waveform.

The stepped frequency waveform	The chirp waveform
Centre frequency	Centre frequency
Effective bandwidth	Chirp bandwidth
Pulse width	Pulse width
Effective pulse repetition frequency	Pulse repetition frequency
Sampling frequency	ADC sampling frequency
Number of frequency samples per sweep	Number of ADC samples per pulse
Number of sweeps per ISAR image	Number of pulses per ISAR image
Signal to noise ratio	Signal to noise ratio

Table 5.5: The parameters which are used to describe the stepped frequency and the chirp radar waveforms.

5.6 Radar signal processing

ISARLAB performs various types of radar signal processing. The processing is broken into modular sections so that new processing algorithms can be easily incorporated. The processing is divided into two main sections. The first section is the generation of the radar signal returned from the target model and the second is the processing of this returned signal to produce HRRPs or ISAR images. Division of the processing in this way allows ISARLAB to process experimentally collected radar data.

The generation of the radar return signal involves a convolution of the target scatterer model and the transmitted radar signal. ISARLAB caters for the two most commonly used wideband radar signals, namely stepped frequency and linear FM (chirp). It is easy to incorporate other waveforms.

ISARLAB allows the selection of a number of different radar signal processing algorithms to produce HRRPs and ISAR images. Some algorithms that are included in ISARLAB are:

- Various radial motion compensation algorithms;
- Various phase compensation algorithms, including the DSA and MSA algorithms;
- Various windows for spectral estimation.

5.7 Implementation of ISARLAB

ISARLAB is layered upon the MATLAB$^{(tm)}$ 4.2 numerical computation software. The main features of the ISARLAB implementation are:

Modularity

All the functional features and interfaces of ISARLAB are well defined. This functional subdivision means it is very easy to add new algorithms or features to ISARLAB.

Portability

Since ISARLAB is built on top of MATLAB, it can be run on many computer platforms.

GUI interface

ISARLAB is built with a graphical user interface (GUI) to make it user friendly.

Visualisation

ISARLAB uses MATLAB's data visualisation capabilities. Hence the processed data are very easy to manipulate and display.

The GUI for ISARLAB is shown in Figure 5.4.

5.7.1 Display of results

ISARLAB can display the results of the radar signal processing in a number of ways. Some of the display features which ISARLAB supports are:

- A choice of the image dynamic range displayed;
- A zoom facility to examine the finer details of plots;
- A choice of colormaps for image display;
- A choice of display format. *e.g.* image plot, waterfall plot, mesh plot[4] *etc.*

[4] Image, mesh and waterfall are different types of plots that are provided by MATLAB.

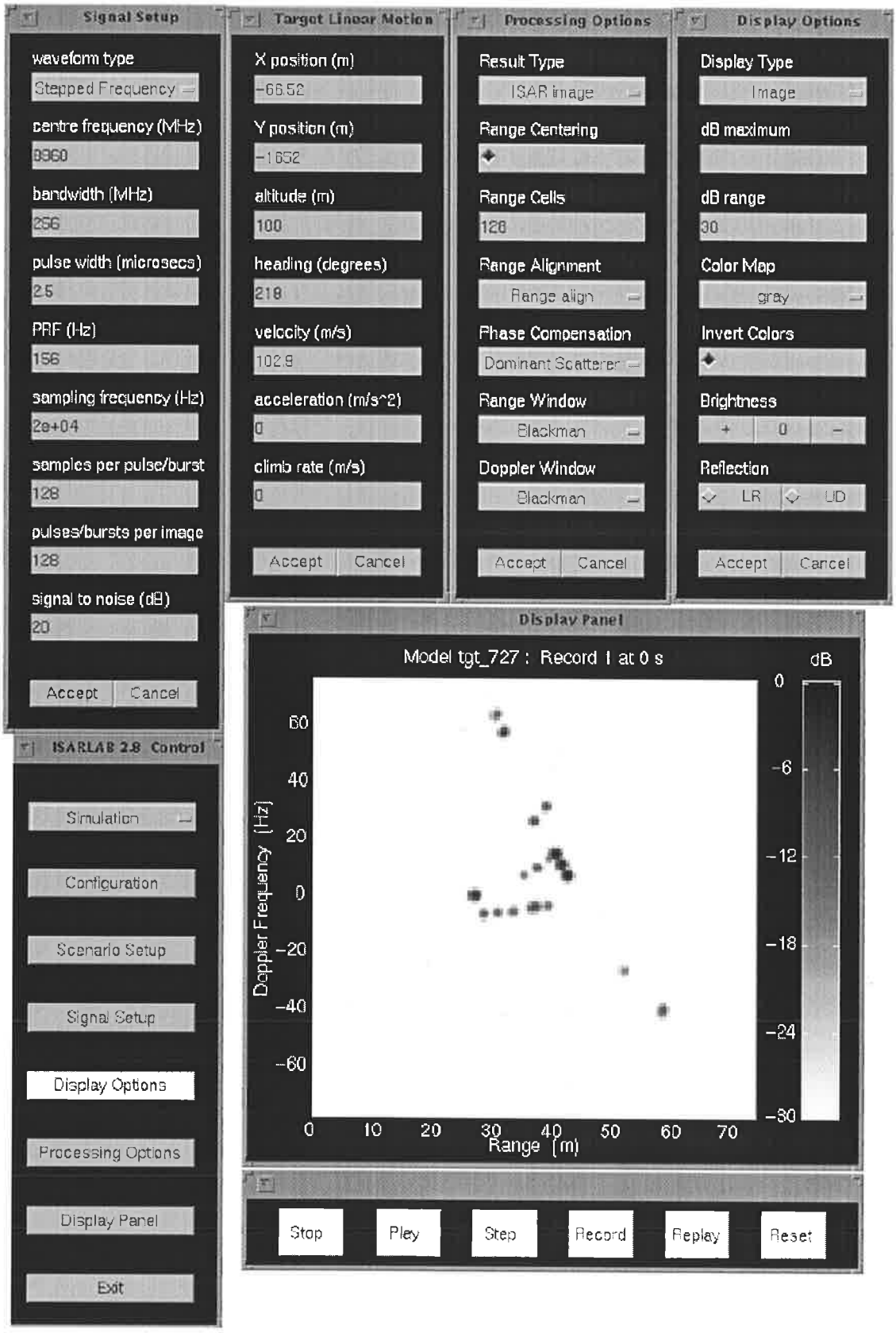

Figure 5.4: The ISARLAB user interface. A number of subwindows are shown. These subwindows show the scenario, the radar parameters and the radar processing used for a particular simulation.

5.8 ISARLAB demonstrations

This section contains three examples which illustrate how ISARLAB is being used to generate high resolution radar data. The first two examples simulate the data collection experiments described in Section 4.4.1. Both the real data and the simulated data were processed in the same way. The processing is described in Section 4.4.3. The third example shows some imagery of a bulk carrier ship which was generated from simulated data.

5.8.1 A simulation example with ISARLAB

The objective of this ISARLAB simulation was to simulate the non-cooperative target imaging experiment conducted at Adelaide airport (see Section 4.4). The scenario and radar parameters used for the airport experiment are summarised in Table 5.6. A Boeing 727 target model, a scenario, and a set of radar parameters were used by ISARLAB to simulate raw radar returns. Two instances of the Adelaide airport experiment were simulated. The first involved an incoming aircraft and the second involved an outgoing aircraft. Comparisons of the ISAR images generated from the real and the simulated data are shown in Figures 5.5 and 5.6.

5.8.2 The Boeing 727 scatterer model

The scattering model for the Boeing 727 aircraft was created according to the radar backscatter theory discussed in Section 4.2 and the experimental observations of Chapter 4. The scattering model shown in Figure 5.7 was created in just over an hour. The modelled scattering centres of the Boeing 727 aircraft are listed in Table 5.7 and the occlusion and scattering functions are described in Tables 5.2 and 5.3 respectively.

5.8.3 Discussion

It can be seen from Figures 5.5 and 5.6 that the ISAR images from the simulated data represent good approximations to the ISAR images obtained from the real data. Some problems that are evident with the simulated data are:

- The engine intake returns appear offset (about 3 m in down-range) in the real images compared to the simulated images. This offset is particularly noticeable in the ISAR images of the incoming aircraft (see Figure 5.6).
- The undercarriage of the incoming aircraft (at a range of 22 m) was not modelled in the simulated data. It is difficult and not necessarily desirable to model this complicated aircraft undercarriage structure. It is unfortunate that the real data analysed was of an incoming aircraft with the landing gear down.

- The noise levels in the simulated data do not correspond exactly with the noise levels in the real data.
- The images from the simulated data have a more "discrete" appearance than the images from the real data.

The offset engine intake returns in the real data probably corresponds to the radar signal being reflected from an internal engine structure. Since the engine "pods" are 6 m long an offset of 3 m is not entirely unreasonable. A revised Boeing 727 model could probably account for this engine scattering behaviour. A more detailed model with a greater number of smaller scatterers would give the imagery from the simulated data an appearance which is closer to that of the real imagery.

The scenario for an incoming aircraft	
Radar initial position	[0, 0, 0] (Stationary)
Aircraft initial position	[-800, -2100, 100]
Aircraft speed	100 ms^{-1}
Aircraft heading	45°

The scenario for an outgoing aircraft	
Radar initial position	[0, 0, 0] (Stationary)
Aircraft initial position	[0, -1600, 100]
Aircraft speed	100 ms^{-1}
Aircraft heading	218°

The radar parameters	
Radar waveform	Stepped frequency
Centre frequency	8.96 GHz
Bandwidth	256 MHz
Pulse width	2.5 μs
Effective PRF	156 Hz
Sampling frequency	20000 Hz
Samples per sweep	128
Sweeps per image	128
Signal to noise ratio	15 dB

Table 5.6: The parameters used for simulating the Adelaide airport non-cooperative target imaging experiment from Chapter 4. See Figure 4.10 for an illustration of the data collection geometry.

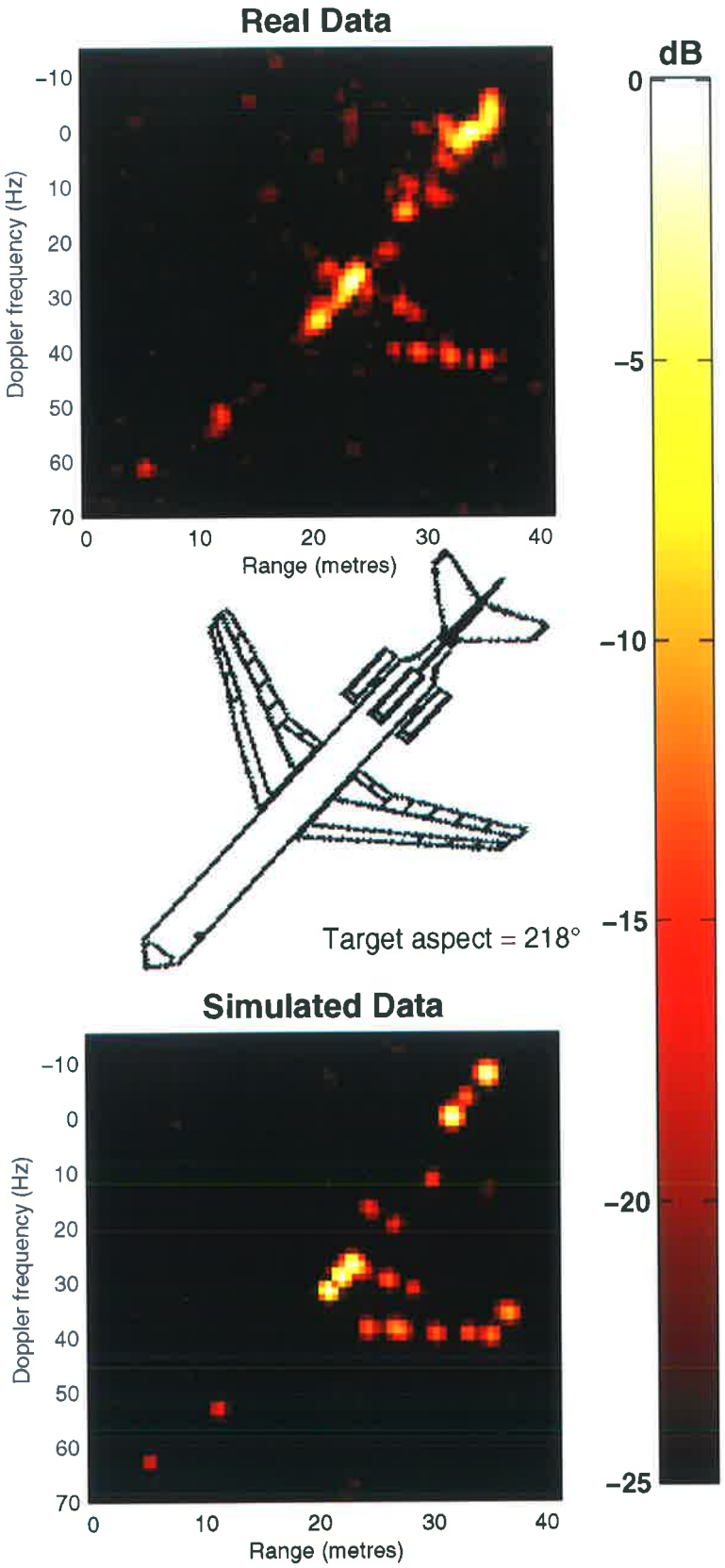

Figure 5.5: A comparison of Boeing 727 ISAR images generated from both real and simulated data. The viewing aspect for the outgoing aircraft is 135°.

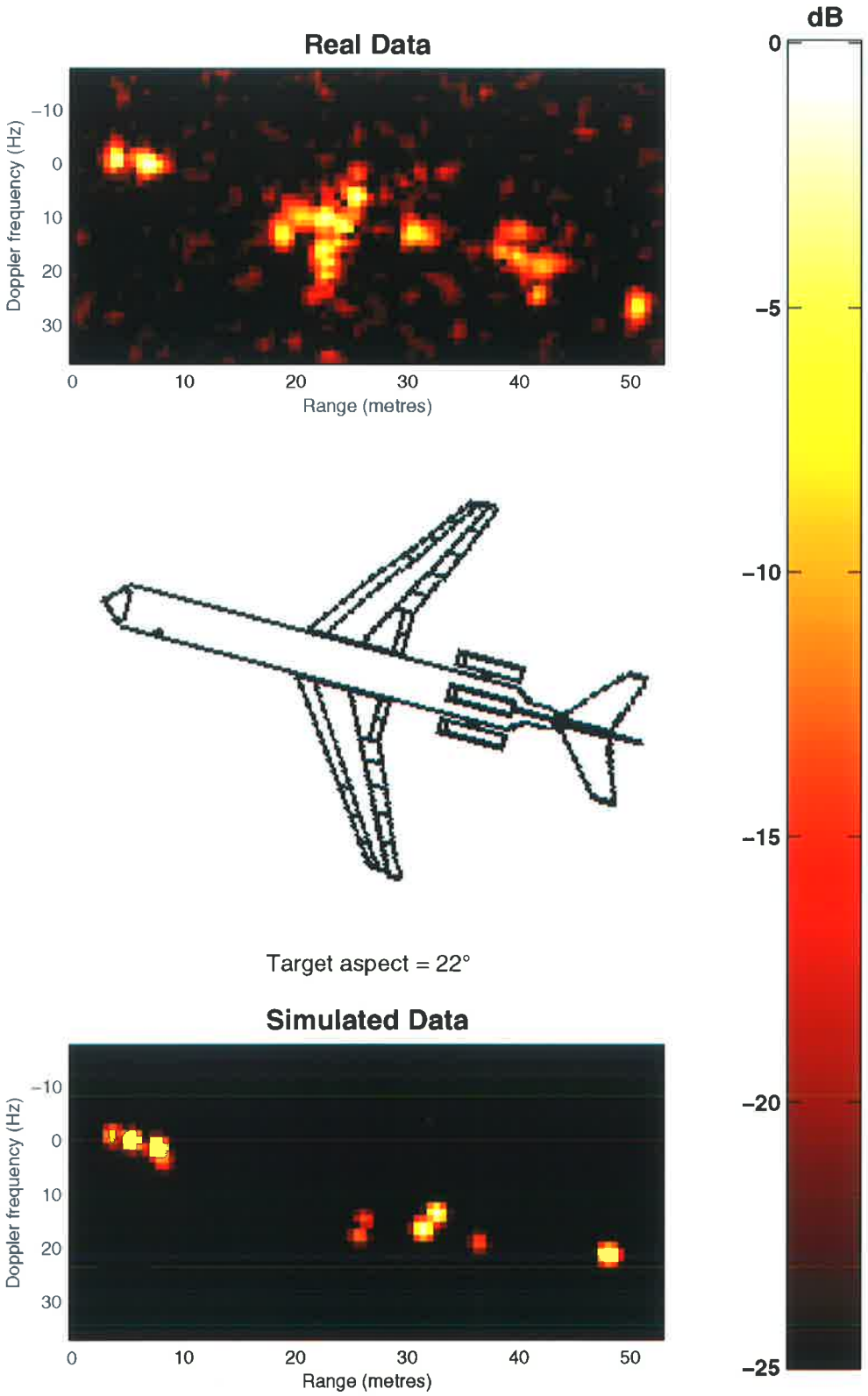

Figure 5.6: A comparison of Boeing 727 ISAR images generated from both real and simulated data. The viewing aspect for the incoming aircraft is 22°. Note the absence of the aircraft landing gear in the image produced from the simulated data.

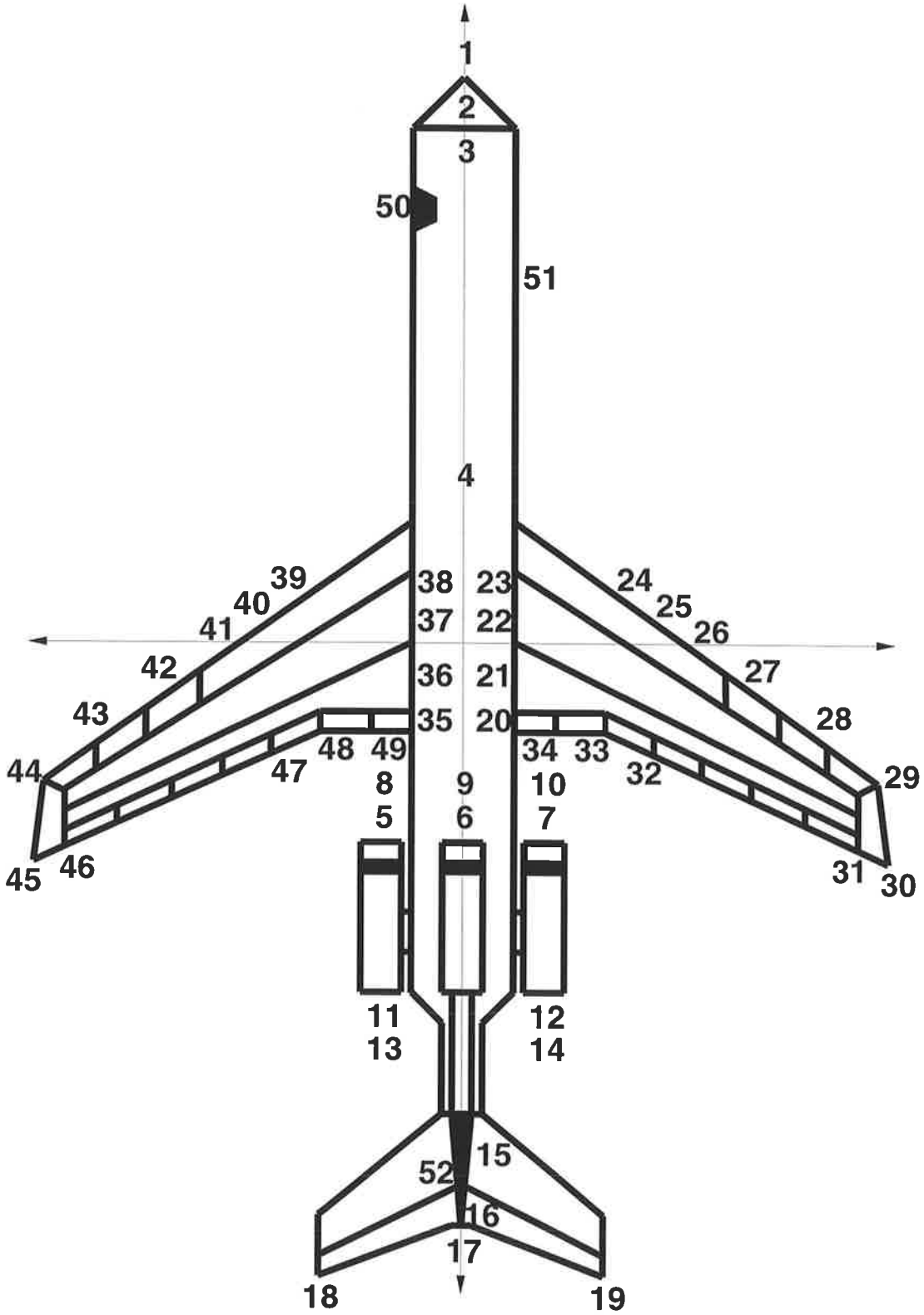

Figure 5.7: Scattering centres on a schematic of the Boeing 727 aircraft. An explanation of the scattering centres is given in Table 5.7.

Aircraft feature	Scatterer number	Position (metres)			Relative amplitude	Occlusion function	Scattering function
		X	Y	Z			
Nose tip	1	22.8	0	0	2	wedge(180,20)	isotropic
Radar dish	2	21.0	0	0	100	wedge(180,110)	cos2x_x2(0,10,10)
Cockpit bulkhead	3	18.5	0	0	100	wedge(180,110)	cos2x_x2(0,10,10)
Antenna (top)	4	7.4	0	2.8	0.2	none	isotropic
Portside engine intake	5	-8.6	2.6	2	100	wedge(-140,130)	cos2x_x2(0,10,10)
Central engine intake	6	-8.6	0	3.6	100	wedge(180,90)	cos2x_x2(0,10,10)
Starboard engine intake	7	-8.6	-2.6	2	100	wedge(140,130)	cos2x_x2(0,10,10)
Portside engine intake	8	-8.6	2.6	2	2	wedge(-45,135)	isotropic
Central engine intake	9	-8.6	0	3.6	2	wedge(0,90)	isotropic
Starboard engine intake	10	-8.6	-2.6	2	2	wedge(45,135)	isotropic
Portside engine exhaust	11	-14	2.6	2	4	wedge(-45,135)	cos2x_x2(180,10,15)
Starboard engine exhaust	12	-14	-2.6	2	4	wedge(45,135)	cos2x_x2(180,10,15)
Portside engine exhaust	13	-14	2.6	2	1	wedge(-135,135)	isotropic
Starboard engine exhaust	14	-14	-2.6	2	1	wedge(135,135)	isotropic
Main engine exhaust	15	-20	0	1	7	wedge(0,90)	cos2x(180,45)
Tail tip	16	-22.4	0	5.6	1.5	wedge(0,110)	isotropic
Tail tip	17	-25.4	0	6.6	5	wedge(25,45)	isotropic
Port tail tip	18	-24.4	5.6	6.6	0.2	wedge(25,45)	isotropic
Starboard tail tip	19	-24.4	-5.6	6.6	0.2	wedge(25,45)	isotropic
Wing root	20	-3.2	-2.0	-1.6	5	wedge(75,115)	isotropic
Wing root	21	-1.6	-2.0	-1.6	5	wedge(75,115)	isotropic
Wing root	22	0	-2.0	-1.6	100	wedge(75,115)	isotropic
Fuselage (specular)	23	1.5	-2.0	-1.6	5	wedge(90,160)	cos2x_x2(270,5,15)
Control surface gap	24	0.8	-7.0	0	1.5	wedge(75,105)	isotropic
Antenna	25	-0.4	-8.6	0	1.5	wedge(65,95)	isotropic
Control surface gap	26	-0.8	-9.4	0	1.5	wedge(70,100)	isotropic
Control surface gap	27	-2.4	-12.0	0	1.5	wedge(65,95)	isotropic
Control surface gap	28	-4.0	-14.2	0	1.5	wedge(60,90)	isotropic
Control surface gap	29	-5.2	-16.0	0	1.5	wedge(50,80)	isotropic
Antenna	30	-8.0	-16.0	0	2	wedge(10,125)	isotropic
Antenna	31	-7.8	-15.6	0	2	wedge(10,125)	isotropic
Antenna	32	-4.6	-7.8	0	1	wedge(35,125)	isotropic
Wing fairing	33	-3.8	-5.4	-1.4	1.5	wedge(90,100)	isotropic
Wing fairing	34	-3.4	-3.2	-1.4	1	wedge(90,110)	isotropic
Wing root	35	-3.2	2.0	-1.6	5	wedge(-75,115)	isotropic
Wing root	36	-1.6	2.0	-1.6	5	wedge(-75,115)	isotropic
Wing root	37	0	2.0	-1.6	5	wedge(-75,115)	isotropic
Fuselage (specular)	38	1.5	2.0	-1.6	100	wedge(-90,160)	cos2x_x2(90,5,15)
Control surface gap	39	0.8	7.0	0	1.5	wedge(-75,105)	isotropic
Antenna	40	-0.4	8.6	0	1.5	wedge(-65,95)	isotropic
Control surface gap	41	-0.8	9.4	0	1.5	wedge(-70,100)	isotropic
Control surface gap	42	-2.4	12.0	0	1.5	wedge(-65,95)	isotropic
Control surface gap	43	-4.0	14.2	0	1.5	wedge(-60,90)	isotropic
Control surface gap	44	-5.2	16.0	0	1.5	wedge(-50,80)	isotropic
Antenna	45	-8.0	16.0	0	2	wedge(-10,125)	isotropic
Antenna	46	-7.8	15.6	0	2	wedge(-10,125)	isotropic
Antenna	47	-4.6	7.8	0	1	wedge(-35,125)	isotropic
Wing fairing	48	-3.8	5.4	-1.4	1.5	wedge(-90,100)	isotropic
Wing fairing	49	-3.4	3.2	-1.4	1	wedge(-90,110)	isotropic
Passenger door (port)	50	17.0	2	1	1	wedge(270,100)	isotropic
Passenger door (starboard)	51	15.0	-2	1	1	wedge(90,100)	isotropic
Main engine exhaust	52	-20	0	1	2	wedge(0,180)	isotropic

Table 5.7: Scattering centres of the ISARLAB Boeing 727 aircraft model. A plan view of the Boeing 727 aircraft, with the scattering centres shown, can be seen in Figure 5.7. The occlusion and scattering functions used in the model are described in Tables 5.2 and 5.3 respectively.

5.8.4 *ISARLAB modelling of ship imagery*

Microwave Radar Division collects high resolution radar data of ships at sea [52]. The MRD radar van is normally placed in the open cargo bay of a Hercules aircraft and the target ship is imaged through the open cargo bay door. Radar imagery of ship targets is routinely collected in this way.

In this section, an ISARLAB simulation is conducted to simulate the real data collection. The parameters for the simulation are given in Table 5.8. An illustration of the scattering model of the target is not shown due to it's complexity. The target-induced motion (roll, pitch, yaw) is simulated in ISARLAB rather than generated from a hull motion modelling package. Note that it is inherently more difficult to simulate data collection of ship targets than data collection of aircraft targets. There are two reasons for this:

1. Ship motion, especially the induced motion, is more difficult to model than aircraft motion;

2. Ships are complex physical structures which provide many opportunities for multi-bounce backscatter.

Figure 5.8 shows imagery of a bulk carrier produced from both real and simulated data. The image produced from simulated data represents a reasonable approximation to the real image. The real and simulated images are at different orientations because of the unknown induced motion experienced by the real ship.

The radar and bulk carrier scenario	
Target initial position	[0, 0, 0] (Stationary)
Radar aircraft initial position	[-1414, 1414, 300]
Radar aircraft speed	72 ms^{-1}
Radar aircraft heading	315°

The radar parameters	
Radar waveform	Stepped frequency
Centre frequency	8.96 GHz
Bandwidth	153.6 MHz
Pulse width	3.5 μs
Effective PRF	78 Hz
Sampling frequency	20000 Hz
Samples per sweep	256
Sweeps per image	256
Signal to noise ratio	15 dB

Table 5.8: The parameters used for simulating the bulk carrier non-cooperative target imaging trial.

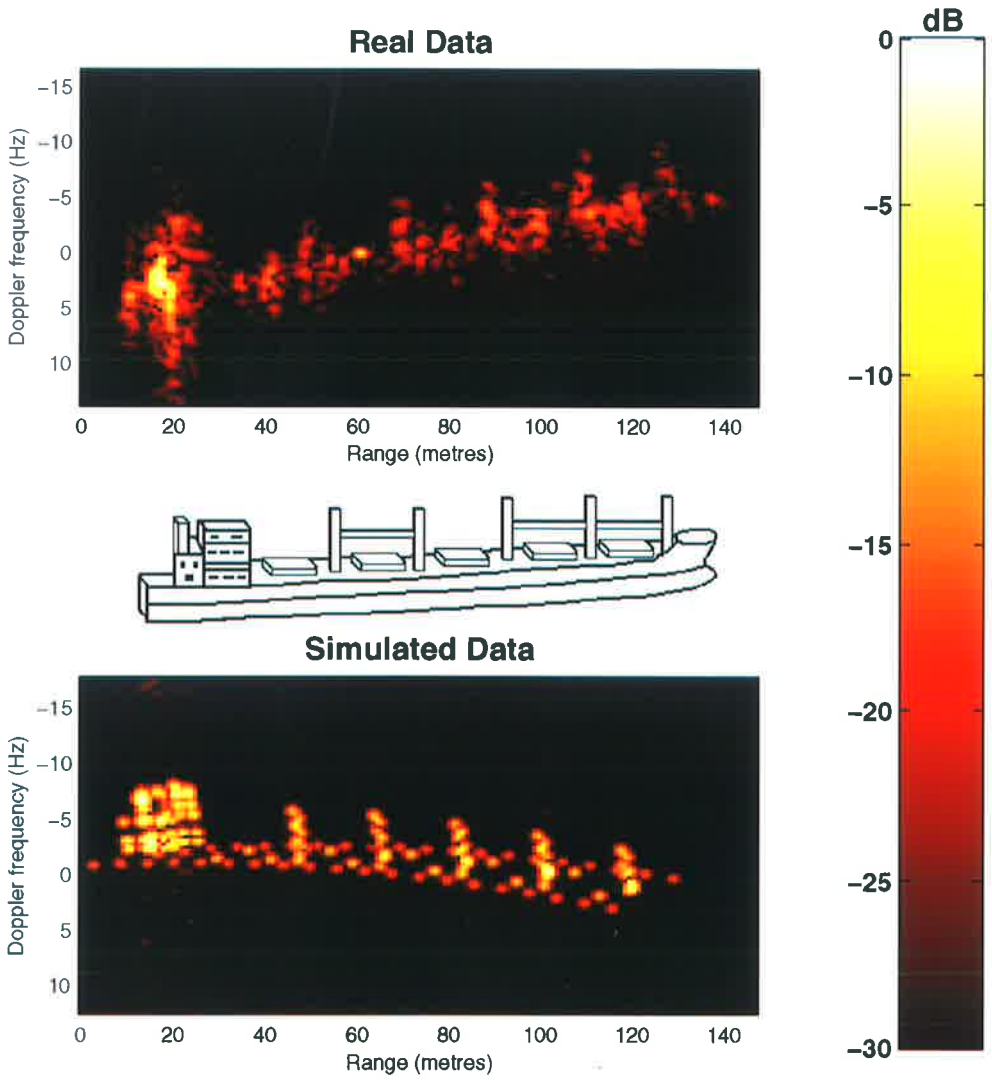

Figure 5.8: A comparison of ISAR images of a bulk carrier ship generated from both real and simulated data.

5.9 ISARLAB extensions

ISARLAB is undergoing continuous development at Microwave Radar Division, DSTO. Since ISARLAB is structured as a collection of modules with well defined interfaces, the upgrading of a particular module does not affect the entire system. The areas in which the further development of ISARLAB is proceeding are:

Induced motion modelling

Induced motion modelling is very important if the accurate modelling of ship imagery is required. An existing ship hull motion modelling package is being modified and incorporated into ISARLAB.

Automatic generation of target models

Currently target models for ISARLAB are manually generated. It is desirable to automatically generate target models from computer aided design (CAD) information. This automatic generation of target models will be done in two stages. First the CAD models will be converted into a set of primitive shapes (dihedrals, trihedrals, flat plates *etc.*) and then an ISARLAB scattering model will be generated from the set of primitive shapes.

New radar processing algorithms

New ISAR algorithms are being added to ISARLAB.

5.10 Summary

High resolution radar target classification research requires large amounts of data over many viewing aspects and target types. The purpose of ISARLAB is to generate high resolution radar data which can be used for *target classification studies*. ISARLAB is *not* intended for detailed RCS modelling or for the study of radar backscatter from targets. ISARLAB was designed to generate high resolution radar data of aircraft and ships, process real data and test new radar signal processing algorithms.

The ISARLAB target model was based upon discrete scattering centres. This type of model is well supported by established radar backscatter theory and the experimental observations of Chapter 4. The key to ISARLAB was the management of modelling complexity. Everything was modelled to a depth which satisfied the end goal of producing realistic radar imagery. Complexity was managed in ISARLAB by:

- Not modelling the exact amplitude of scatterer returns;
- Not modelling complex multi-bounce phenomena;
- Dividing the system into well defined functional modules.

Three examples of the use of ISARLAB have been given. Two of these examples simulated the data collection experiments which were described in Chapter 4. The third example simulated the ISAR imaging of a ship at sea. The use of ISARLAB has been very successful. The development of ISARLAB is continuing with particular emphasis on the automatic generation of target scattering models and the development of better target induced motion models.

Chapter VI

TARGET CLASSIFICATION USING HRRPS

6.1 Introduction

Chapter 2 showed that previous research in the area of radar target classification had mainly used approaches which were based upon the target resonant response. Chapter 2 concluded that the three techniques of HRRP, ISAR and JEM offered the greatest potential for an operational radar target classification system. This chapter addresses preprocessing for radar target classification from HRRPs. Some of the work presented in this chapter has been published by the author in [60] and a comprehensive description of the work has been accepted for publication and is due to appear in [61].

6.1.1 Chapter purpose

Section 2.5.1 concluded that radar target classification from HRRPs is necessary when target classification from ISAR or JEM is not possible. The merits of HRRP compared to ISAR and JEM were summarised in Table 2.1. The purpose of this chapter is to investigate the issues surrounding aircraft target classification from HRRPs. This chapter provides an informed discussion on the important issues in HRRP radar target classification rather than attempting to provide the best HRRP preprocessing or classification algorithm. The emphasis and contribution of this chapter is on HRRP preprocessing issues and potential preprocessing techniques.

6.1.2 Chapter overview

An introduction to HRRPs was given in Section 3.4 and a general discussion of radar target classification from HRRPs was given in Section 2.5.1. Research addressing radar target classification from HRRPs [62, 63, 64] has only appeared recently in the open literature. The importance of HRRP preprocessing has been ignored by much of the previously published work. Consequently, this chapter begins with Section 6.2 discussing HRRP preprocessing issues.

The remainder of this chapter presents an experiment in which real HRRPs are preprocessed and classified. The experiment provides a start-to-finish example of two-target classification from HRRPs and the experiment serves to reinforce the discussion of HRRP preprocessing issues which is given in Section 6.2. The techniques used for the HRRP

preprocessing and classification experiment are applicable to multi-target multi-aspect data.

Section 6.3 describes how real data were collected for the target classification experiment. In Section 6.4 a simple solution is proposed for each preprocessing issue raised in Section 6.2. Section 6.5 presents a technique, based upon a generalised linear discriminant, to reduce the dimensionality of the HRRP data before classification. Section 6.6 presents a Bayes classifier which is used to classify the preprocessed data. Section 6.7 provides a summary of the target classification processing which was described in the previous four sections. Section 6.8 presents and discusses the results of the target classification experiment.

6.2 HRRP preprocessing issues

6.2.1 The quality of a HRRP

This section introduces the three characteristics of a HRRP which determine its quality in the context of target classification. These three characteristics are shown in Figure 6.1 and a discussion of each is given below:

Slant-range resolution

In order to resolve adjacent target scattering centres, high resolution in slant-range is necessary[1]. Unfortunately, practical considerations dictate a limit on the slant-range resolution that can be achieved. Currently, there is no definitive answer on how much slant-range resolution is needed for reliable target classification. Informed opinion [65] suggests that a slant-range resolution of approximately 0.5 m should be sufficient for aircraft target classification. For the classification of smaller fighter aircraft a higher resolution may be needed and for ship classification a resolution of 1-2 m may be sufficient. Further research is still required to determine the slant-range resolution required for reliable target classification.

Sidelobe levels

A high slant-range resolution is of limited value if there is significant sidelobe leakage from the largest scatterer returns in the HRRP. High sidelobes can easily obscure the small scattering centres of the target or the high sidelobes can easily be interpreted as additional target scattering centres. Sidelobe reduction is discussed in Section 6.2.9.

Noise level

If clutter is absent, the noise statistics are the same in each range bin of a HRRP.

[1] High resolution in slant-range is less important for ISAR images than for HRRPs because ISAR images benefit from having a resolution in the cross-range direction. HRRPs are only one-dimensional and hence the target scatterers are not resolved in cross-range.

The target signal strength varies between range bins depending upon the strength of the target scatterer return (if any) in the range bin. Consequently it is difficult to define a quantity which can be associated with the term "HRRP SNR". Since the scatterer distribution of the target is not known a priori, an average SNR over the HRRP is not necessarily a useful quantity to define. Nevertheless, the SNR for a particular range bin m can be defined by

$$\text{SNR}_{(\text{range bin } m)} = \frac{E\left[(s_m(t))^2\right]}{2\sigma_m^2} \tag{6.1}$$

where $s_m(t)$ is the target signal in range bin m and σ_m^2 is the variance of the noise in range bin m. When the expression "HRRP SNR" or "SNR of a HRRP" is used in this thesis, it is intended that the SNR is measured in the range bin with the largest target return.

It is the SNR in a range bin which determines whether a scatterer return is visible (detectable) above the HRRP noise floor. The SNR of a HRRP can be increased by *averaging* which is discussed in Section 6.2.6 and Chapter 7. Currently there is no clear understanding of how much SNR is required for reliable target classification but Cohen [66] has suggested that an additional 10-20 dB of SNR over the required detection SNR may be required.

The relative importance of the characteristics which determine HRRP quality is unknown and the area requires further research. Nevertheless, these general comments can be made:

- High slant-range resolution gives good target scatterer separation, but further research is still required to determine the degree of slant-range resolution required for reliable target classification;
- Low sidelobe levels are necessary for a high quality HRRP;
- A high SNR is necessary for a high quality HRRP.

6.2.2 *The need for HRRP preprocessing*

Previous work on radar target classification has not given HRRP preprocessing the attention that it deserves. To illustrate the importance of preprocessing in a classification system, the well established field of optical character recognition (OCR) is considered. Excellent reviews of OCR work can be found in [67, 68]. Without initiating a detailed discussion of OCR, it suffices to say that preprocessing is a very important step in an OCR system. The typical preprocessing steps required in an OCR system are detailed in Table 6.1. Just as preprocessing is very important for OCR systems, preprocessing is very important for target classification from HRRPs. The majority of the HRRP data

used in the open literature are taken from turntables or are simulated. Such data often obscures some fundamental preprocessing issues. The preprocessing steps required for target classification from HRRPs are detailed in Table 6.2. The preprocessing steps detailed in Table 6.2 are discussed in the remainder of this section. The reader is directed to [69, 70] which discuss some of these important HRRP preprocessing issues.

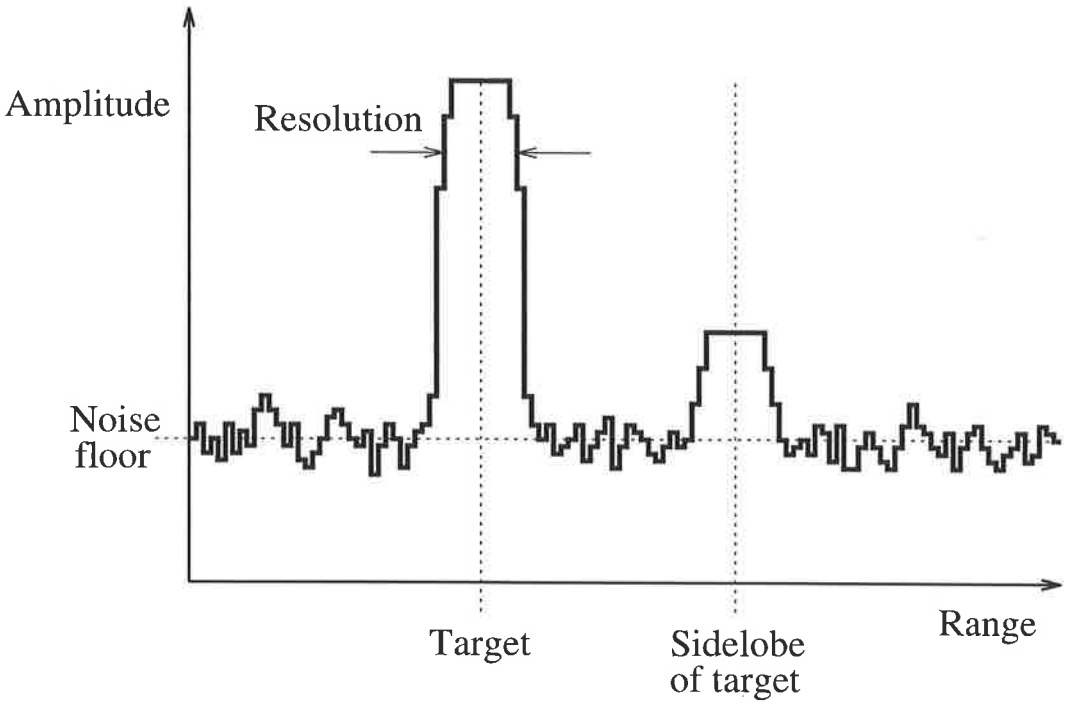

Figure 6.1: The three characteristics of: resolution; noise floor amplitude; and HRRP sidelobes, which determine the quality of a HRRP.

The preprocessing steps required for OCR

OCR preprocessing step	Description
Segmentation	Segmentation is the separation of individual characters from a page of optically scanned text. Once the characters have been extracted from the scanned text, they are processed individually. The majority of errors made by state-of-the-art OCR systems are usually made in the segmentation processing step.
Thinning	Printed text can be scanned at many resolutions. "Thinning" refers to the thinning of scanned lines so that they become a standard minimum pixel thickness. *e.g.* the numeral "1" may have a thickness of 2 pixels when scanned at 100 dots per inch (DPI) but it may have a thickness of 4 pixels when it is scanned at 200 DPI. Thinning is used to deal with the variation in scanned line thickness.
Thresholding	An ideal scanned image of printed text has only two intensities which are normally black and white. An optical scanner may produce an image with grey-scale intensities. The conversion of a grey-scale image into a binary image is called *binarisation* or *thresholding*. The choice of the grey-scale threshold can dramatically affect the appearance of the resulting binary image.
Registration	Registration refers to the alignment of a scanned character with respect to a particular reference position. Registration is necessary for classification systems which employ template matching and it is also necessary for many types of feature extraction.

Table 6.1: The preprocessing steps required for OCR.

The preprocessing steps required for HRRP classification

HRRP preprocessing step	OCR equivalent	Description
Target localisation	Segmentation	Target localisation refers to *locating* the target in the range window. Target localisation is discussed in Section 6.2.3.
HRRP alignment	Registration	HRRP alignment refers to aligning a HRRP with a particular reference position. HRRP alignment is discussed in Section 6.2.4.
HRRP aspect compensation	N/A	The appearance of a HRRP varies depending upon the aspect from which the target is viewed. The variation of target HRRPs with viewing aspect is discussed in Section 6.2.5.
HRRP averaging	N/A	The SNR of a HRRP can be increased by averaging consecutive HRRPs. An averaged HRRP with an improved SNR should lead to an improved classification performance. HRRP averaging is discussed in Section 6.2.6 and a novel coherent averaging algorithm is presented in Chapter 7.
HRRP thresholding	Thresholding	HRRPs are thresholded to reduce the data rate for subsequent processing steps. HRRP thresholding is discussed in Section 6.2.7.
HRRP normalisation	N/A	The term HRRP *normalisation* describes how a HRRP is processed to reduce its dependence on the absolute amplitude variations found in HRRPs. HRRP normalisation is discussed in Section 6.2.8.
Sidelobe reduction	N/A	High sidelobes can easily obscure the small scattering centres of a target or the high sidelobes can easily be interpreted as additional target scattering centres. The reduction of sidelobes can be achieved with windowing. The reduction of sidelobes is briefly discussed in Section 6.2.9.

Table 6.2: The preprocessing steps required for HRRP classification.

6.2.3 *Target localisation*

Target localisation refers to *locating* a target in the range window. Target localisation is important because it influences the quality and consistency of subsequent target feature extraction. If a target cannot be localised accurately then feature extraction and ultimately classification performance will suffer. Williams [70] has noted the importance of target localisation for target classification from HRRPs.

Target localisation is needed regardless of the type of radar waveform used for HRRP collection. For a stepped frequency waveform, the unambiguous range window length w_s is related to the number of range bins n and the size of each range bin Δr_s, by $w_s = n\Delta r_s$. The radar parameters are normally chosen so that w_s is bigger than the largest possible target. Since the target is moving in range its position in the range window is not necessarily consistent from HRRP to HRRP. Hence for each HRRP the target location in the range window needs to be determined. For a pulse or chirp waveform, an explicit range window doesn't exist since the received echo is continuously sampled in time. Nevertheless, some type of target localisation or target cueing is still needed because the start of the received waveform sampling cannot be accurately controlled with respect to the unknown beginning of the target return.

Two hypothetical HRRPs are shown in Figure 6.2. These HRRPs illustrate how the location of a target can vary in the range window. In Figure 6.2(a) the target is located near the centre of the range window. In Figure 6.2(b) the target is split on either side of the range window. The target is split across the range window due to the synthetic generation of the HRRP. The split target situation in Figure 6.2(b) can only occur when a stepped frequency waveform is used to collect the HRRP data.

Target localisation can be handled in a number of ways:

Correlation-based classification

A correlation-based classification scheme is a popular solution to the target localisation problem. Correlation-based classification is appealing since there is no explicit target localisation step. Correlation-based classification has been suggested in [70, 63, 71, 62]. For a test HRRP with a length of n range bins and a given range shift j, the correlation coefficient is given by

$$C(\boldsymbol{t}, \boldsymbol{r}, j) = \sum_{i=1}^{n} (t(i)r(i-j)) \qquad \forall\ 1 \leq j \leq n \tag{6.2}$$

where $\boldsymbol{t}$ is the HRRP to be classified and $\boldsymbol{r}$ is an appropriate reference HRRP. The peak value of the correlation coefficient $C(\boldsymbol{t}, \boldsymbol{r})$ with respect to j occurs when the test HRRP is correctly aligned with the reference HRRP.

Although correlation-based classification is simple, it is not very robust because the correlation process is easily affected by the variations in HRRP backscatter amplitude. Variations in HRRP amplitude occur when HRRPs are collected from

slightly different viewing aspects. Several researchers [70, 63, 71, 62] have suggested a normalised correlation coefficient to provide increased robustness to the amplitude variations found in a sequence of HRRPs. The normalised correlation coefficient is given by

$$C_n(\boldsymbol{t}, \boldsymbol{r}, j) = \frac{\sum_{i=1}^{n} (t(i)r(i-j))}{|\boldsymbol{t}||\boldsymbol{r}|} \qquad \forall\ 1 \leq j \leq n \tag{6.3}$$

where $|\boldsymbol{t}|$ and $|\boldsymbol{r}|$ are the root mean square lengths of $\boldsymbol{t}$ and $\boldsymbol{r}$ respectively. Even the normalised correlation coefficient is dominated by the largest backscatter return in the HRRP. This would not be a problem if, for a given aircraft, the largest backscatter peak in the HRRP always originated from the same feature of the aircraft.

Shift-invariant transforms

Another popular way to deal with target localisation is to use a shift-invariant transform on the collected HRRP to produce a shift-invariant feature vector for classification. Zwicke [72] has used the magnitude of the FFT of a HRRP as a shift-invariant transform. HRRP shift-invariance is achieved in the same way in Section 6.4.3. The auto-correlation function of the HRRP magnitude is an equivalent shift-invariant function [73].

The magnitude of the FFT of a HRRP is invariant to shifts in the target position within the range window. Unfortunately the same FFT magnitude can correspond to different HRRPs. Hence there is the potential for misclassification if two different HRRPs produce the same FFT magnitude. Oppenheim [74] has shown that the majority of the information which affects the "shape" of a signal is contained in the phase of the signal. Oppenheim has presented several fascinating experiments where a signal is reconstructed from only its magnitude or only its phase information. The results suggest that the loss of phase information may increase the difficulty of discrimination between different signals.

Centroid location

Various methods using moments can be used to localise the target return in a range window. Li and Chiou [71] have proposed a centroid alignment scheme to localise the target return in a range window. The centroid of a HRRP is defined by

$$C = \frac{\sum_{i=1}^{n} (i \times t(i))}{\sum_{i=1}^{n} t(i)} \tag{6.4}$$

where $t(i)$ is the amplitude of range bin i in the HRRP $\boldsymbol{t}$ which has a total of n range bins. Even if the centroid of a target has been located in a HRRP the edges of the target return still need to be located. Hence the location of the target centroid only provides an "alignment" function. Furthermore, the calculation of the target centroid is usually very sensitive to noise or amplitude variations in the HRRP. The alignment of HRRPs is discussed in Section 6.2.4.

Locating the "start" of the target

The naive reader may suggest that target localisation is not a problem since only the beginning and the end of the target return in the range window need to be located. The location of the "ends" of the target return would not be a problem in an ideal world of no receiver noise or clutter. In practice however, locating the ends of the target return can be very difficult. In a HRRP with noise and clutter, locating the ends of the target return implies using some sort of threshold to determine where the target return ends. HRRP thresholding is discussed in Section 6.2.7.

Songhua [64] describes a very primitive method to extract the target return from a HRRP. The notation used by Songhau is confusing so his method is described below in a modified notation:

> Consider a range profile consisting of L range bins. Let the amplitude of a given range bin i be $X(i)$ with $i = 1, L$. A subset of the range profile is then extracted such that
>
> $$g_i = X(i) \qquad \forall\, i = i_0, (i_0 + T_0)$$
>
> where T_0 is selected to ensure that "there is no scattering component in the region $X(j)$ with $j = (i_0 + T_0), L$".

Songhua fails to mention of how the first range cell i_0 of the target is detected or of how the length T_0 is chosen and consequently the robustness of the algorithm is unlikely to be good.

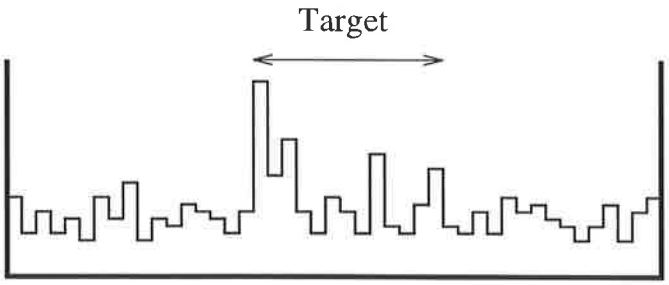

(a) A hypothetical HRRP with the target located near the centre of the range window.

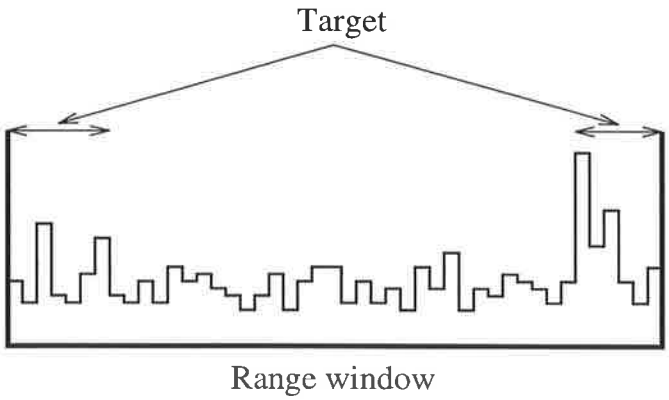

(b) A hypothetical HRRP with the target split on either side of the range window.

Figure 6.2: Two hypothetical HRRPs which illustrate how the location of a target can vary in the range window. It is the aim of target localisation to locate the target in the range window. In (a) the target is located near the centre of the range window but in (b) the target is split on either side of the range window. The situation shown in (b) can only occur when the HRRP is synthetically generated using a stepped frequency waveform.

6.2.4 *HRRP alignment*

HRRP alignment refers to aligning a HRRP with a particular reference position. There are three main reasons why HRRP alignment may be necessary:

Alignment for HRRP averaging

Consider the situation when a number of HRRPs are being collected sequentially in time from a target. These HRRPs need to be range aligned if averaging is to take place. HRRP averaging is discussed in Section 6.2.6.

Alignment for ISAR processing

ISAR processing requires that the radial motion component of the target motion is removed since only the rotational target motion contributes constructively to the ISAR image. The alignment of a sequence of HRRPs is equivalent to radial motion compensation.

Alignment for classification

Some classification techniques require that the target return is always in a fixed position relative to the boundaries of the range window. For example, Li and Chiou [71] describe a neural network method for classifying HRRPs. The neural network used is a multi-layer perceptron trained with backpropagation. A single HRRP is applied to the input layer of the neural network for classification. Since the neural network cannot recognise range-shifted HRRPs an alignment scheme is necessary. Li and Chiou use a centroid based scheme for HRRP alignment before classification by the neural network.

There are two main ways in which HRRP alignment can be achieved:

Correlation alignment

Cross-correlation [44] is the most popular method used to achieve HRRP alignment. A reference HRRP is chosen and all other HRRPs are correlated with it. The maximum correlation peak of a particular HRRP with the reference HRRP, indicates how much this HRRP must be shifted to be range aligned with the reference. Alignment using correlation works well in the case where all of the HRRPs are from the same target and the relative aspect change between the consecutive HRRPs is small. In the case of HRRP averaging or ISAR processing, all of the HRRPs to be aligned are from the same target. Alignment using correlation does not work as well when the HRRPs to be aligned are from different targets. The HRRPs to be aligned can be from different targets if one HRRP is from an unknown target and it is being aligned with a known reference HRRP from a library of previously stored HRRPs.

Centroid alignment

Another method to achieve HRRP alignment is to calculate the centroid of each

HRRP and then range shift each HRRP so that the centroids of the HRRPs are aligned. The HRRP centroid is calculated according to Equation 6.4. Note that the calculation of the target return centroid is sensitive to noise or amplitude variation in the HRRP.

6.2.5 HRRP variation with aspect

Section 4.4.4 has shown that HRRPs vary according to the aspect from which the target is viewed. The are two ways in which HRRPs vary as the viewing aspect changes:

HRRP amplitude variation

For small[2] changes in viewing aspect, the amplitude of the radar return in a single range bin changes due to the coherent summation of the multiple returns contributing to the amplitude of that particular range bin. This type of amplitude variation in a single range bin is known as *speckle*.

HRRP "shape" variation

The "shape" of a HRRP is determined by the orientation of the target and the aspect from which the target is viewed. The shape of a HRRP only changes for large variations in viewing aspect. The variation of HRRP shape with large changes in viewing aspect is a more serious problem than HRRP variation due to speckle which occurs over small changes in viewing aspect.

Consider a sequence of HRRPs collected from a target. The coherent nature of HRRP formation means that the amplitude of the return in a particular range bin will fluctuate (speckle) from HRRP to HRRP. Conversely, for a given aspect, the position of a scatterer return will remain fixed[3] in range regardless of any fluctuations in its amplitude. Hence as a discriminating feature, the scatterer amplitude information assumes secondary importance to the scatterer position information. This point was made in Chapter 4 and it is important that any HRRP preprocessing scheme should be designed to reflect this observation.

Figures 4.14, 4.15 and 4.6 illustrate how HRRPs vary with three scales of viewing aspect change:

A small change in viewing aspect

Figure 4.14 shows the variation in a Boeing 737 HRRP over a change in viewing aspect of approximately 0.3°. Note that although there are significant amplitude

[2] A change in aspect of 5° or less is considered to be a small variation in viewing aspect and a change in viewing aspect greater than 5° is considered to be a large change in viewing aspect.

[3] The scatterer position remains "fixed" in range if radial motion compensation is performed on the sequence of HRRPs under consideration.

variations over the sequence of HRRPs, the overall HRRP shape does not vary much.

A medium change in viewing aspect

Figure 4.15 shows the variation in a Boeing 737 HRRP over a change in viewing aspect of 8°. Once again there are significant amplitude variations over the sequence of HRRPs but the basic shape of the HRRP remains unchanged.

A large change in viewing aspect

Figure 4.6 is a range-azimuth RCS plot of a Mirage aircraft on a turntable. The change in viewing aspect is approximately 440°. Note how the shape of the Mirage HRRP changes significantly over such a large change in viewing aspect. The sinusoidal variation in the projected[4] length of the aircraft is quite evident from Figure 4.6. The range-azimuth RCS plot of Figure 4.6 is commonly referred to as an *hourglass* plot due to the sinusoidal variation in the projected target length.

There are several ways to deal with HRRP dependence on viewing aspect:

Subdivision of aspect

It is reasonable to assume that a radar would have an estimate of the aspect from which HRRPs of a target are being collected. An estimate of the target viewing aspect can be used to index a database of previously stored HRRPs. For example, HRRPs could be stored at azimuth increments of 5°. If a HRRP to be classified is collected at 37°, then the HRRP could be compared to a previously stored HRRP from an aspect of say, 35°.

The choice of the angular segment size is an important decision that must be made in designing a target classification system. A very small angular segmentation ($< 5°$) is not practical for two reasons:

- The angular segment size should not be smaller than the accuracy of the target viewing aspect estimate. An estimate of the target aspect to within 5° seems reasonable considering current radar capabilities.
- A small angular segment size implies that a large number[5] of HRRPs must be stored in a target classification database. Limitations on the HRRP storage capacity available, especially in airborne platforms, means that it is preferable to use larger angular segment sizes.

---

[4] The scatterers on the aircraft are projected onto the RLOS to produce a HRRP.

[5] Smith [7] suggests that 10^5 signatures are required per target for an uniform aspect segmentation of 0.2°.

If the angular segment size is too large then the discrimination between different sized targets will become difficult. For example, a large ship viewed from a side-on aspect has a similar projected length to a small ship viewed from an end-on aspect.

Both Li [62, 71] and Hudson [63] have correctly noted that the maximum aspect change over which two HRRPs can be considered to be the same projection of an aircraft is

$$\Delta\theta_{\max} = \frac{\Delta r_s}{D} \tag{6.5}$$

where the radar has a slant-range resolution of Δr_s and the aircraft has a maximum span between scatterers of D. If the aspect change of $\Delta\theta_{\max}$ is exceeded then two scatterers on the aircraft, separated by a distance D, will appear in two different range bins when they were originally in the same range bin. Even though two HRRPs separated by an aspect of $\Delta\theta_{\max}$ will be different, they may still be similar enough to be regarded as the same target by a classification system. Hence an aspect subdivision into segments larger than $\Delta\theta_{\max}$ should not be precluded in the design of a target classification system. In [63] the azimuthal aspect was divided into equal 20° angular segments and reasonable classification results were obtained.

A possible subdivision of azimuthal aspect is shown in Figure 6.3. In Figure 6.3 the 360° of azimuthal aspect has been subdivided non-uniformly. Chapter 4 showed that target classification from HRRPs is very difficult from broadside aspects. Consequently, for a fixed number of aspect segments, it makes sense to increase the aspect subdivision in the azimuth region where target classification is more likely to be accurate. Increasing the aspect subdivision for broadside aspects would not overcome the fundamental problems which exist at broadside aspects, but instead it would only leave less space for the other HRRPs which need to be stored in the fixed-size database.

In the target classification experiment which is discussed later in this chapter, all broadside aspect data are discarded and all of the aircraft HRRPs from a non-broadside aspect segment are processed by the same classifier. The best way in which to subdivide aspect for a particular target classification system requires further research.

A scale-invariant transform

Consider a HRRP obtained from a target viewed at a head-on aspect. If the target's length is greater than its width then the target HRRP will have a maximum length at a head-on aspect. As the viewing aspect rotates from head-on, the shape of the target HRRP changes due to two effects [72]:

HRRP compression

The HRRP length is compressed due to the rotation in viewing aspect;

Scatterer occlusion

The shape of the target HRRP changes due to the occlusion or appearance of various scattering centres on the target.

If it is assumed[6] that the first effect due to viewing aspect rotation dominates, then the Mellin transform [75] can be used to compensate for the target HRRP compression. The Mellin transform is a scale-invariant transform which is used in pattern classification. The reader is directed to [72, 76, 64, 77], all of which use the Mellin transform for aspect normalisation.

HRRP length normalisation

Mohamed [78] has described a very simple technique for dealing with HRRP variation with aspect. Mohamed normalises the target HRRP length according to the viewing aspect. This technique relies on the same assumption as the scale invariant Mellin transform. The assumption is that the HRRP compression effect dominates all other effects which occur due to target rotation.

Classification of multiple HRRPs

A method for dealing with HRRP variation with aspect has been described by Farhat [79, 80, 81]. The technique uses a *sinogram* as the basic target signature which is classified. Sinograms are object representations encountered in tomography [82]. The sinogram of a target is a Cartesian plot of the positions of the target scatterers in coordinates of measured relative range or differential range versus aspect angle. The range-azimuth RCS plots shown in Figures 4.6, 4.7 and 4.8 are good examples of sinograms. The classification of sinograms offers several advantages over the classification of a single HRRP:

- More data are used for the classification decision and so there is a greater potential for reliable classification;
- Sinograms characterise the target by its dominant scatterers that are visible over an extended range of aspect angles whereas a HRRP only characterises a target at a single aspect angle;

The disadvantages of sinograms include:

- The aspect angle spanned by a sinogram, used for target classification, must still be chosen;
- The entire azimuthal aspect range of 360° must still be divided into regions over which a single sinogram can operate.

[6] The validity of this assumption depends upon the ratio of the target's length to its width. If the target's length is large compared to its width, the effect of compression will be dominant over scatterer occlusion. Hence compression is more likely to dominate for ship targets rather than aircraft targets.

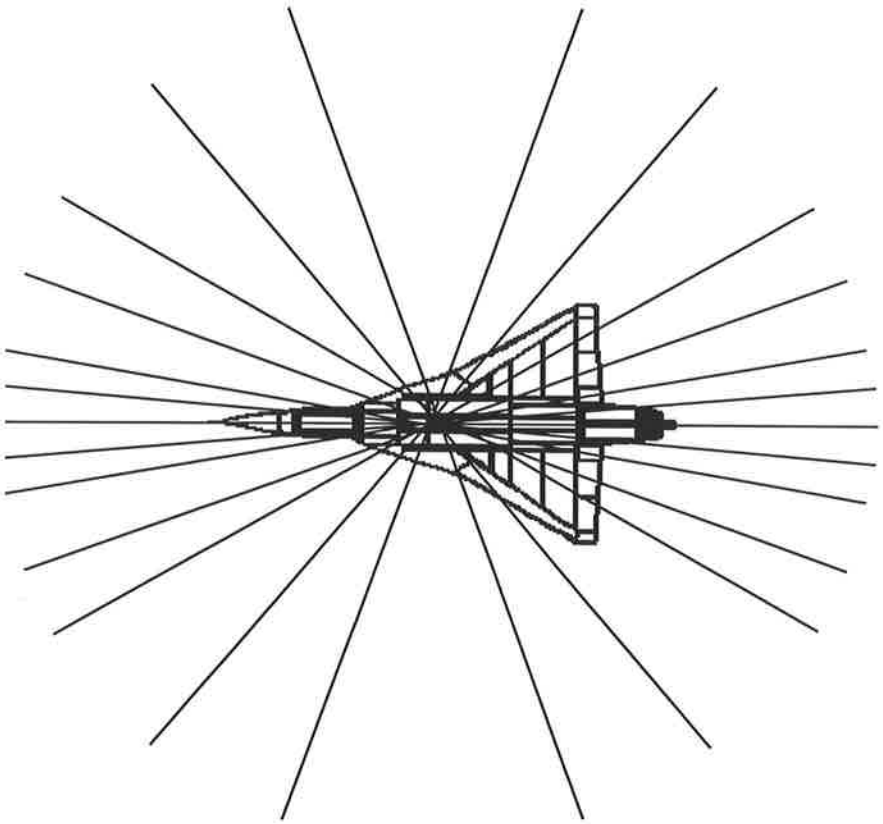

Figure 6.3: A possible subdivision of azimuthal aspect for HRRP target classification. The azimuthal aspect has been divided into small angular segments at head-on and tail-on aspects and into larger angular segments at aspects closer to broadside. Larger angular segments have been used at broadside since classification from HRRPs is very difficult at broadside aspects. The larger angular segments do not make the classification task easier but they ensure that less storage space is devoted to the aspect segments where target classification is unlikely to be accurate.

6.2.6 *Averaging*

A single HRRP can have a low SNR. Figure 6.4 is an example of a HRRP with a low SNR. A low SNR can be improved by using non-coherent averaging over a sequence of HRRPs. If N HRRPs are averaged then the increase in SNR is between $\sqrt{N}$ and N [36]. The benefits of non-coherent averaging can be seen by comparing Figures 6.4 and 6.6. Non-coherent averaging is discussed in greater detail in Chapter 7. Chapter 7 also presents another averaging technique called *coherent averaging* which provides an increase in SNR of N when N HRRPs are averaged.

Figure 6.7 shows averaged HRRPs from an in-flight Boeing 727 aircraft. The HRRPs were collected at an average aspect of 22°. There are four features on the Boeing 727 aircraft which make major contributions to the Boeing 727 HRRP from this aspect. At approximately 15 m the return from the aircraft nose can be seen. The three returns between 27 m and 40 m are from the lowered undercarriage of the aircraft. The two returns at approximately 50 m are from the engines or their associated support structure. The return at 60 m is from the tail of the aircraft. Figure 4.11 shows an ISAR image generated from the same sequence of HRRP data. The accompanying aircraft schematic shown in Figure 4.11 should help to illustrate the origin of the scattering centres seen in Figure 6.7.

Figure 6.7(a) shows a HRRP in which only two returns from the aircraft can be seen. Figure 6.7(b) shows an averaged HRRP produced from 32 HRRPs. Note that all of the major returns from the aircraft are now clearly visible. Figures 6.7(c), 6.7(d) and 6.7(e) show averaged HRRPs produced from 64, 96 and 128 HRRPs respectively. There does not seem to be a visible improvement in the appearance of the averaged HRRPs when greater than 32 HRRPs are averaged even though the noise floor appears to be flatter. Figures 6.7(a), 6.7(b) and 6.7(c) indicate that the undercarriage return at approximately 35 m is a bimodal return. In Figure 6.7(e) the bimodal return at 35 m has been lost in the averaging process. This loss could be due to bad alignment of the HRRPs before averaging or it could be due the change in viewing aspect over the 128 HRRPs. Either way, Figure 6.7 illustrates that increasing the number of HRRPs that are averaged does not necessarily increase the quality of the resulting averaged HRRP.

The number of HRRPs over which to average is a parameter which must be chosen. If too many HRRPs are averaged there may be a significant change in aspect angle over the set of HRRPs which are averaged and averaging will not be useful since the features of the HRRP will be smeared in range. On the other hand, enough HRRPs need to be averaged to produce an averaged HRRP with a suitable SNR. The amount of averaging used in a particular application, depends upon the required HRRP SNR, the rate of change of the target aircraft aspect, and the HRRP collection rate. The averaging of the HRRP data can be overlapped to give more, albeit correlated, averaged data. Some examples of overlapping to get averaged data are shown in Figure 6.8. The amount of

overlapping that is used is a tradeoff. If more overlapping is used, more averaged data are generated but the caveat is that the averaged data are more correlated.

Unfortunately little is known about the required SNR for HRRP target classification. Cohen [66] has suggested that an additional 10-20 dB of SNR over the required detection SNR would be required for target classification. A greater SNR means more target scatterers are visible, but further research is needed to determine the HRRP dynamic range required for reliable target classification. Chapter 4 has indicated that the positions of the target scattering centres provide the major clues to target identity. Consequently it is reasonable to suggest that target classification should be based upon the relative distances between the major scatterers on the target. A major scatterer is loosely defined in this thesis as one whose return amplitude is within 25 dB of the largest return in the target HRRP.

6.2.7 Thresholding

Binary[7] thresholding or detection has traditionally been used in radar applications for target detection [36]. Thresholding can be used in HRRP preprocessing to reduce the amount of data to be classified or it can be used as part of a target localisation scheme[8]. Unfortunately the issue of HRRP thresholding has been ignored by most of the previous work on target classification from HRRPs. Previous work has used unthresholded HRRPs for classification. It is best if the level of the HRRP threshold is determined from the HRRP data. The noise level of the HRRP is estimated and the threshold can be set accordingly. A novel technique for HRRP thresholding is discussed in Section 7.4.7.

[7] Thresholding of a HRRP does not necessarily result in a HRRP with two intensity levels. The range bins which are below the threshold can be set to zero and the other range bins can retain their original amplitudes.

[8] Given an appropriate threshold, the location of the target return in the range window may become obvious.

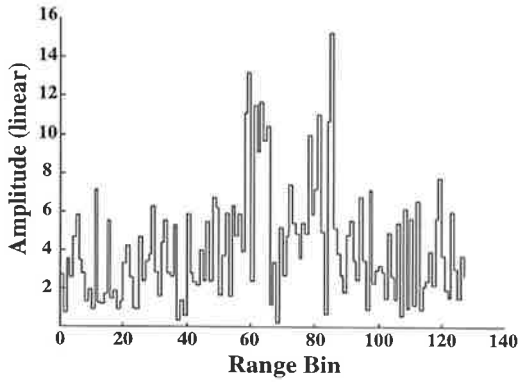

Figure 6.4: A HRRP produced from 128 complex frequency samples. The SNR in the range bin containing the largest target scatterer is approximately 18.3 dB. Note that the target is not clearly visible in the range window. The same HRRP with the target position shifted appears in Figure 6.5.

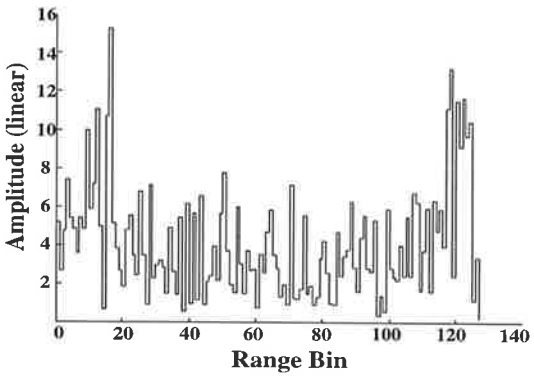

Figure 6.5: The same HRRP as shown in Figure 6.4. Here the target position has shifted in the range window which makes the target more difficult to locate. The type of target shift shown in this figure can only occur when a stepped frequency waveform is used to collect the HRRP data.

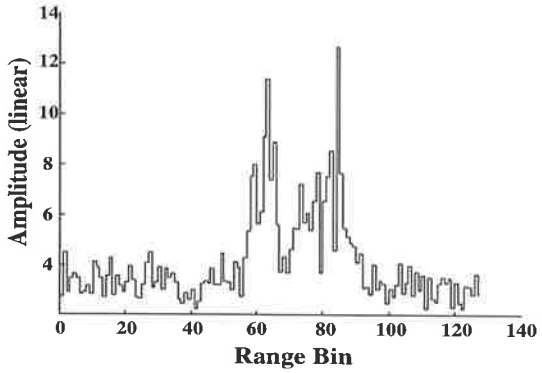

Figure 6.6: An averaged HRRP produced from 30 HRRPs. The SNR in the range bin containing the largest target scatterer is approximately 26 dB. Note how the target is now clearly visible in the range window, whereas in Figure 6.4 it is more difficult to see the target.

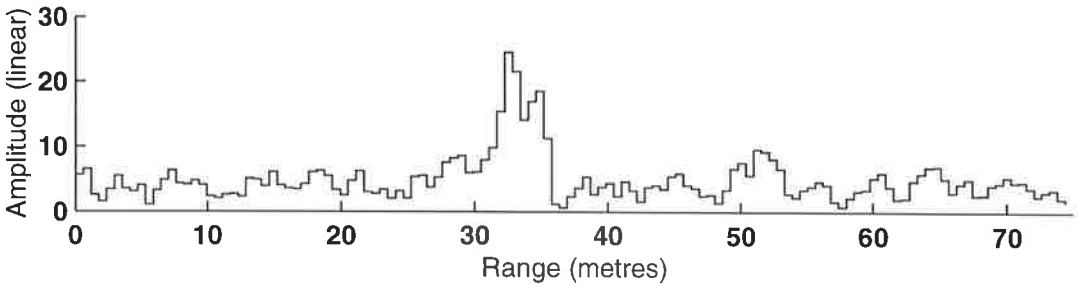

(a) A single HRRP.

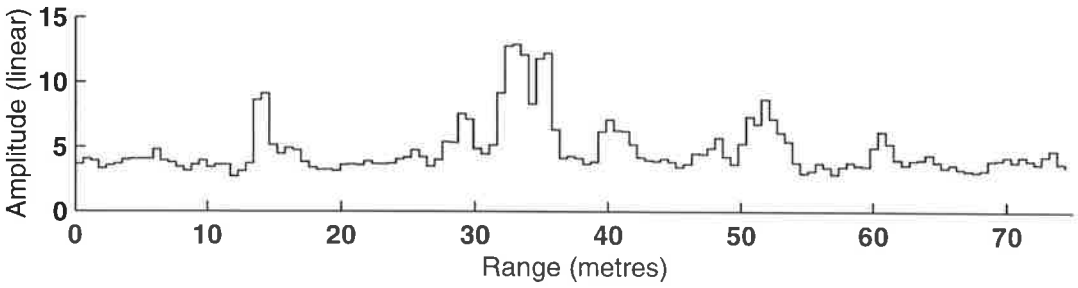

(b) An averaged HRRP produced from 32 HRRPs using non-coherent averaging.

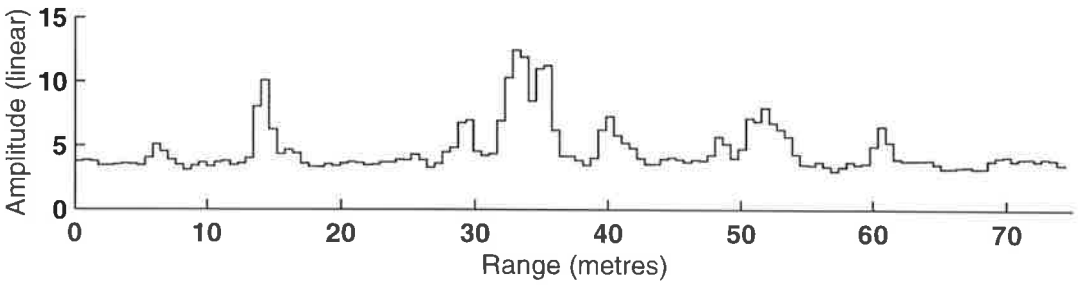

(c) An averaged HRRP produced from 64 HRRPs using non-coherent averaging.

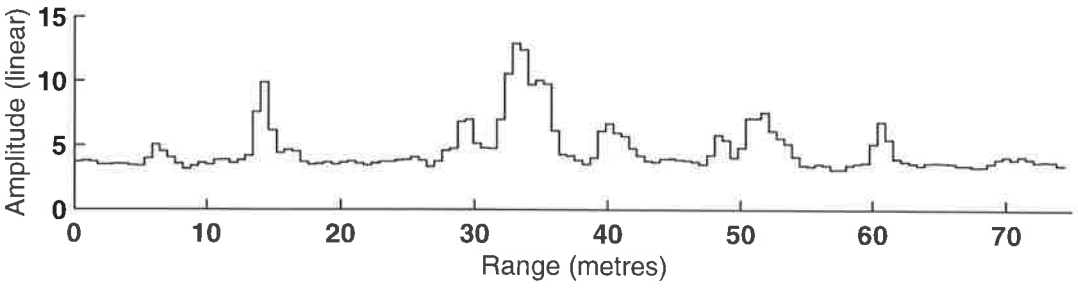

(d) An averaged HRRP produced from 96 HRRPs using non-coherent averaging.

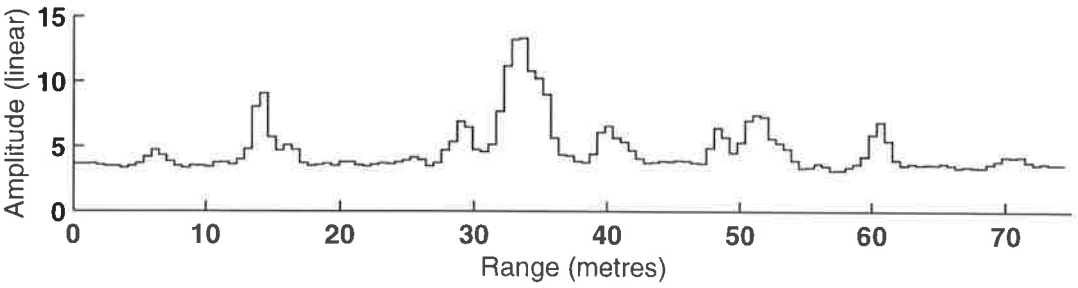

(e) An averaged HRRP produced from 128 HRRPs using non-coherent averaging.

Figure 6.7: Averaged HRRPs of a Boeing 727 aircraft. The HRRPs were collected at an average aspect of 22°. See Figure 4.11 for an ISAR image produced from the same sequence of HRRP data.

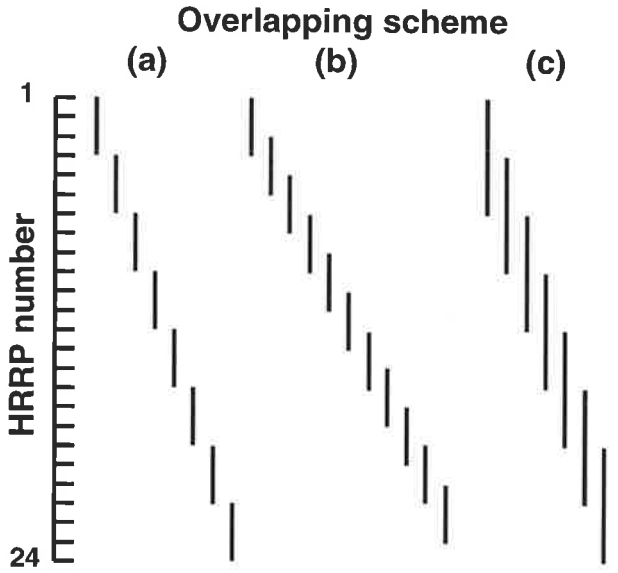

Figure 6.8: The different ways in which overlapping and averaging can be applied to HRRP data. (a) shows 8 averaged HRRPs produced from 24 HRRPs by using non-overlapping averaging of 3 HRRPs. (b) shows 11 averaged HRRPs produced from 24 HRRPs by using overlapping averaging. The amount of overlapping shown in (b) is 66%. (c) shows 7 averaged HRRPs produced from 24 HRRPs by using overlapping averaging. The amount of overlapping shown in (c) is 100%.

6.2.8 Normalisation

Modern radars usually have front-end automatic gain control (AGC) which ensures that the received radar signals are kept under the receiver saturation level but over the receiver noise floor. Unless radar backscatter data are fully calibrated, the absolute signal strength of a target with respect to the receiver noise floor cannot be guaranteed to be consistent. If a target classification system bases its decision on the relative positions of the major scatterers on the target, as is suggested in this thesis, then it is questionable whether amplitude calibration information would significantly improve target classification performance. If fully calibrated radar data cannot be expected, any form of preprocessing which reduces the dependence of the target HRRP on the overall radar signal levels would very useful. The term *target normalisation* is coined in this chapter to describe how a HRRP is processed to reduce its dependence on absolute backscatter amplitude.

Most researchers, working in the area of target classification from HRRPs, have recognised the need for HRRP normalisation. Both Williams [70] and Cohen [69] suggest that the normalisation of energy in a HRRP may provide increased classification robustness for small changes in viewing aspect. Hudson [63] and Zwicke [72] normalised the HRRP energy as a preprocessing step. A heuristic approach to HRRP normalisation is given in Section 6.4.2.

6.2.9 Sidelobe reduction

Since the radar backscatter from a target can extend over a large dynamic range, it is very important to keep the sidelobe levels in a HRRP low. There are two common ways to measure sidelobe levels: the peak sidelobe level ratio (PSLR); and the integrated sidelobe level ratio (ISLR). The PSLR is the ratio of the largest sidelobe peak power to the mainlobe peak power and the ISLR is the ratio of the integrated sidelobe power to the peak mainlobe power. High peak sidelobes can easily obscure the small scattering centres in a HRRP, or they can easily be interpreted as additional target scattering centres. Windowing [39] is normally used to reduce sidelobe levels. The use of windowing imposes a trade-off between resolution and sidelobe levels. Resolution is normally sacrificed in order to reduce the sidelobes to an acceptable level. The level of sidelobes which is deemed acceptable depends upon the dynamic range of the data. Chapter 4 has shown that radar imagery can easily have a dynamic range in excess of 40 dB. For such imagery it is prudent to use a window which reduces the peak sidelobe levels to at least 40 dB below the main response. Alternatively, if target classification is possible from only the largest target scattering centres, as is suggested in this thesis, a peak sidelobe level of 30 dB may be acceptable. The ultimate level to which the HRRP sidelobes can be reduced depends upon the radar hardware used for HRRP collection.

6.3 Data collection

The data collection procedure for the aircraft classification experiment was described in Section 4.4.1. The data records which were collected are listed in Table 6.3. The collected data have three main limitations:

Limited viewing aspects

The site geometry for the data collection at Adelaide airport is shown in Figure 4.10. As the aircraft took-off they were at a roughly broadside aspect and as the aircraft ascended, the aspect became closer to end-on.

Limited radar range

The radar has an effective range of approximately 3 km for medium-sized commercial aircraft. Beyond this range the signal to noise ratio becomes very low and the range gate tracker in the radar receiver loses the aircraft in the noise floor.

Limited target types

The collection of data was limited to aircraft which frequently use Adelaide airport. The Boeing 727 and Boeing 737 aircraft make up the bulk of the air traffic at Adelaide airport. Single data records of other aircraft types were collected but they were not used in the aircraft classification experiment.

There are a number of data records which were collected from a predominately broadside[9] aspect. Section 4.5.1 has already indicated that it is very difficult to discriminate between different targets at broadside aspects. Consequently, broadside aspect records were not used for the target classification experiment. Records 13b and 20b were also omitted from the target classification experiment because they are only half-length records. The data records deemed suitable for the target classification experiment are listed in Table 6.4.

6.3.1 Subdividing the data into training and testing sets

Subdividing data into training and testing sets is always a difficult task. With too much training data there may not be enough data left to properly evaluate the resulting classifier. With too little training data the classifier may not have a fair chance of learning the data characteristics. The subdivision into training and testing sets becomes more difficult when there is a lack of data. Data are normally scarce when they are difficult or costly to obtain.

In the following subdivision of the available data it was ensured that more data were used for testing than for training. All available aspects of both aircraft types were

[9] Broadside is used loosely here to refer to aspects within ± 20° of actual broadside.

represented in both the training and testing sets. An entire[10] record of a particular aircraft was allocated into either the training or the testing set. The data listed in Table 6.4 consists of 7 aircraft records and the subdivision into training and test data is shown in Table 6.5. The proportion of data used for training and testing was chosen heuristically. Note that 60% of the data have been reserved for testing. The training set contained one example of the Boeing 727 aircraft and two examples of the Boeing 737 aircraft. The testing set consisted of two previously unseen Boeing 727 aircraft and two unseen Boeing 737 aircraft.

[10] Note that each aircraft record is not subdivided with respect to aspect and that a particular aircraft record may span an aspect segment of up to 30°.

Record number	Target type	Number of HRRPs in record	Number of preprocessed feature vectors	Approximate aspect
5	727	512	48	broadside
6	727	512	48	non-broadside
8	737	512	48	broadside
10	737	512	48	non-broadside
11	737	340	33	non-broadside
13a	737	256	24	broadside
13b	737	256	24	non-broadside
14	737	340	33	non-broadside
15	727	512	48	broadside
16	727	512	48	non-broadside
20a	737	256	24	broadside
20b	737	256	24	non-broadside
22	727	512	48	non-broadside
23	737	512	48	non-broadside
24	737	512	48	non-broadside

Table 6.3: The data records which were collected at Adelaide airport for the aircraft classification experiment. The omitted records (1, 2, 3, 4, 7 ... *etc.*) are of aircraft other than Boeing 727s or Boeing 737s.

Record number	Aircraft class	Number of feature vectors	Allocation	Initial aspect
6	727	48	testing	130°
10	737	48	testing	122°
11	737	33	training	139°
14	737	33	training	140°
16	727	48	training	135°
22	727	48	testing	134°
24	737	48	testing	136°

Table 6.4: The aircraft data which were used in the target classification experiment.

Aircraft type	Number of training vectors	Number of testing vectors	Total number of aircraft
727	48	96	3
737	66	96	4

Table 6.5: The subdivision of the preprocessed data into training and testing sets. Note that over 60% of the data were reserved for testing.

6.4 HRRP preprocessing

The issues of HRRP preprocessing were discussed in Section 6.2. This section aims to reinforce the understanding of these issues by providing an example of a HRRP preprocessing scheme. The HRRP preprocessing scheme described in this section is used as a part of the target classification experiment described in this chapter. The preprocessing techniques used are not necessarily the best possible preprocessing techniques but they serve the purpose of demonstrating what is needed for a complete target classification system.

6.4.1 HRRP averaging

For this particular target classification experiment, HRRPs with a SNR of at least 25 dB were desired. The choice of a SNR of 25 dB was somewhat arbitrary since there is no established guide for what HRRP SNR is required for target classification. Nevertheless, a SNR of 25 dB should ensure that the major scatterers on the target are visible. An examination of the HRRP data showed that the SNR of a HRRP was typically between 18 and 20 dB. HRRP averaging was required to increase this SNR to the desired 25 dB. HRRP averaging was discussed in Section 6.2.6. For this target classification experiment non-coherent averaging was used. An averaging gain of 7 dB was needed and this corresponded to non-coherently averaging 30 HRRPs[11]. The averaged HRRPs were produced by stepping in increments of 10 HRRPs along a data record. This gave a 66% overlap between the consecutive averaged HRRPs. The overlap of 10 HRRPs was empirically chosen.

6.4.2 HRRP normalisation

The target classification philosophy of this thesis emphasises the target scatterer location information and deemphasises the scatterer amplitude information. Section 6.2.8 discussed HRRP normalisation and the preprocessing described in this section is a simple attempt at HRRP normalisation.

For a HRRP consisting of n range bins, the range window mean μ_{window} is defined as

$$\mu_{\text{window}} = \frac{1}{n}\sum_{i=1}^{n} A_i \tag{6.6}$$

where A_i is the amplitude of the return in range bin i. Since any HRRP preprocessing needs to be independent of the target type, the removal of the range window mean μ_{window} after AGC and averaging does not suffice for preprocessing since μ_{window} depends on the target size. For a fixed range window size a larger target occupies more of the range

[11] Since the minimum SNR gain for non-coherent averaging is $\sqrt{N}$ and $10\log_{10}(\sqrt{30}) \approx 7$.

window than a smaller target. This leads to an increase in μ_{window}. Hence μ_{window} is related to the target size and it should not be indiscriminately removed.

The range window mean μ_{window} depends upon both the mean target amplitude μ_{target} and the mean noise amplitude μ_{noise}. The target mean is defined by

$$\mu_{\text{target}} = \frac{1}{t} \sum_{i \in \mathcal{T}} A_i \tag{6.7}$$

where $\mathcal{T}$ is the set of t range bins which contain target energy. The mean noise amplitude is defined by

$$\mu_{\text{noise}} = \frac{1}{(n-t)} \sum_{i \notin \mathcal{T}} A_i \tag{6.8}$$

The normalisation preprocessing described in this section removes the average amplitude of the noise floor without affecting the target mean. The normalisation preprocessing is illustrated in Figure 6.9. In order that the target mean μ_{target} is not affected by the normalisation preprocessing, some *estimate* of the target position in the range window is needed. The signal amplitude excursions above μ_{window} are used to construct a *target mask*. Once a target mask has been constructed, the non-target returns are averaged to get a measure of the average noise floor amplitude μ_{noise}. The mean noise amplitude is subtracted from the non-target areas in the range window. The removal of the average noise floor amplitude makes the target more prominent in the range window. A before and after comparison showing the results of this normalisation preprocessing technique can be seen in Figures 6.6 and 6.10.

6.4.3 *A position-invariant transform*

The subject of target localisation was discussed in Section 6.2.3. Using a position-invariant transform was a technique which dealt with target localisation. Position-invariance means that a target can be correctly identified independently of its position with respect to some reference[12]. In the context of this chapter the target position varies relative to the boundaries of the HRRP range window. Position-invariance is very useful for target localisation because it means that *the target location in the range window does not need to be identified.*

The magnitude of the discrete Fourier transform (DFT), which is invariant to linear shifts of its input vector, is commonly used to provide position invariance [83]. The DFT is usually implemented via the fast Fourier transform (FFT). In this target classification experiment the magnitude of the fast Fourier transform of a preprocessed HRRP is used as a real feature vector. The FFT of the preprocessed HRRP magnitude has a length of 128 samples[13], and since the HRRP magnitude is real the magnitude of its FFT is

[12] The reference in range in usually implicit. It is either the boundary of the range window or the range position where the sampling for the HRRP begins.

[13] The complex HRRP is formed from 128 complex frequency samples.

symmetrical about zero frequency. Hence only half of the FFT magnitude (64 real values) is needed for the feature vector. The feature vector is passed onto the dimensionality reduction stage which is described in Section 6.5.

A shift-invariant feature vector has two appealing qualities. Firstly, the feature vector is the same regardless of the target position in the HRRP range window. Secondly, for a fixed HRRP range window size, the feature vector always has the same dimensionality regardless of the actual target size. The fixed feature vector dimensionality enables targets of different lengths to be compared easily by a classification algorithm. Even though it is easy for the human eye to compare target sizes in the range (time) domain it is not simple to do a comparison automatically with a computer. If the target classification processing is done exclusively in the time domain, a decision has to be made on where the target begins in range and where it ends in range[14]. This enables the target length to be measured. Locating the "ends" of a target is not easy since the "end" scatterers seen in a HRRP do not always originate from the same target feature. Even if a target could be successfully extracted from the range window by locating its "end" points, the resulting feature vector is of a different dimensionality for each target. This makes the classification task difficult for a classification algorithm. If the HRRPs are examined in the frequency domain *the localisation problem is avoided* and the feature vector dimensionality is constant regardless of the actual target size. It isn't easier in a theoretical sense to classify a target in the frequency domain, but from a practical point of view, the target localisation problem is avoided. Figure 6.11 shows the preprocessed feature vector which results from applying the shift-invariant DFT to the HRRPs shown in Figures 6.4 and 6.5.

[14] This is the *target localisation* problem.

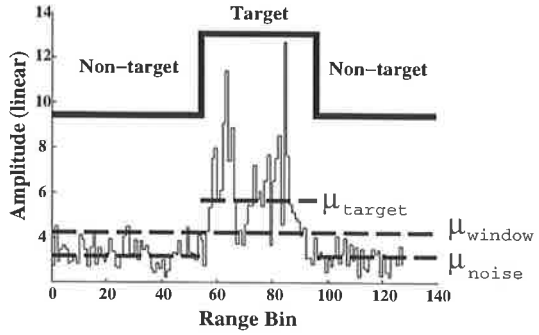

Figure 6.9: A crude *target mask* in a range window. The mean target amplitude μ_{target} is indicated by the upper dashed line. The mean amplitude over the range window μ_{window} is indicated by the middle dashed line. The mean noise amplitude μ_{noise} is indicated by the lower dashed line.

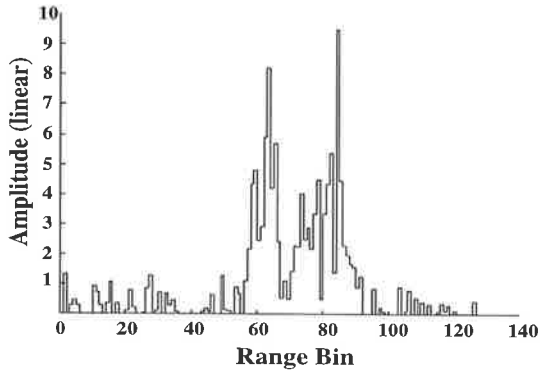

Figure 6.10: The HRRP of Figure 6.6 with the mean amplitude of the noise floor removed. Note how the target is now more prominent in the range window.

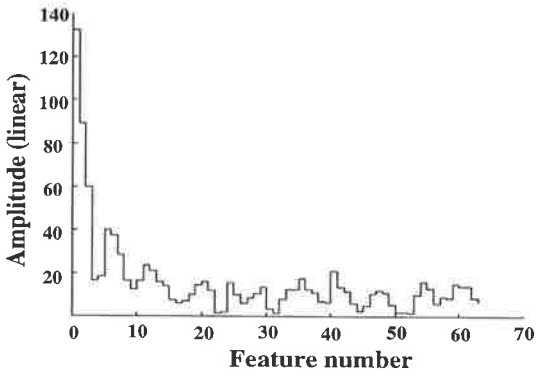

Figure 6.11: The FFT of the preprocessed HRRP from Figure 6.10. The Fourier spectral components are used as a feature vector for classification. The feature vector is invariant with respect to the target position within the range window. Both of the HRRPs shown in Figures 6.4 and 6.5 produce the feature vector shown here.

6.5 Dimensionality reduction

In general as the dimensionality of data increases it becomes more difficult to implement a successful classification scheme. The difficulty of dealing with high–dimensional data is referred to as *the curse of increasing dimensionality* [84]. A problem which is intractable[15] in a high–dimensional space may become tractable when it is transformed to a low–dimensional space [84]. The transformation from a high–dimensional space to a low–dimensional space is called dimensionality reduction. Even though dimensionality reduction may degrade the achievable final classification performance, it is often used because having a tractable non-optimal classification solution is better than having no solution. Feature extraction usually involves dimensionality reduction. Just as the choice of features is very important for a classification system, the choice of how to reduce the dimensionality of the incoming data is an important preprocessing decision.

6.5.1 The generalised linear discriminant

The generalised linear discriminant function (LDF) [84] is a well known statistical analysis technique. A LDF can be used to project high–dimensional data onto a low–dimensional space and hence LDFs are often used for dimensionality reduction. Consider a d–dimensional column vector

$$\boldsymbol{x} = \begin{bmatrix} x_1 \\ \vdots \\ x_i \\ \vdots \\ x_d \end{bmatrix}$$

for which dimensionality reduction is required. For a c class classification task the d–dimensional vector $\boldsymbol{x}$ is transformed to a $(c-1)$–dimensional column vector

$$\boldsymbol{y} = \begin{bmatrix} y_1 \\ \vdots \\ y_i \\ \vdots \\ y_{(c-1)} \end{bmatrix}$$

via $(c-1)$ d–dimensional linear discriminant functions $\boldsymbol{w}_1 \ldots \boldsymbol{w}_{c-1}$. The transformation can be expressed as

$$y_i = \boldsymbol{w}_i^t \boldsymbol{x} \qquad \forall\ i = 1 \ldots c-1 \tag{6.9}$$

[15] From a practical point of view.

If the weight vectors $\boldsymbol{w}_i$ are viewed as the columns of a $d \times (c-1)$ matrix W, then the linear transformation for dimensionality reduction can be written as a single matrix equation

$$\boldsymbol{y} = W^t \boldsymbol{x} \tag{6.10}$$

where $\boldsymbol{x}$ is the original d–dimensional column vector, $\boldsymbol{y}$ is the reduced $(c-1)$–dimensional column vector and the $(c-1)$–dimensional subspace is spanned by $\boldsymbol{w}_1 \ldots \boldsymbol{w}_{c-1}$.

The generalised linear discriminant method finds the matrix W which maximises the criterion function $J(W)$ given by

$$J(W) = \frac{|W^t S_B W|}{|W^t S_W W|} \tag{6.11}$$

S_W, defined below, is called the within-class scatter matrix and it represents how tightly each class is clustered. S_B, defined below, is called the between-class scatter matrix and it represents the relative separation between classes. Maximising the criterion $J(W)$ can be interpreted as finding the linear transformation which maximises the ratio of inter-class distances to intra-class distances. The within-class scatter matrix S_W is given by

$$S_W = \sum_{i=1}^{c} S_i \tag{6.12}$$

with

$$S_i = \sum_{\boldsymbol{x} \in \mathcal{X}_i} (\boldsymbol{x} - \boldsymbol{\mu}_i)(\boldsymbol{x} - \boldsymbol{\mu}_i)^t \tag{6.13}$$

where $\mathcal{X}_i$ is the set of vectors in class i. The mean vector $\boldsymbol{\mu}_i$ of each class $\mathcal{X}_i$ is given by

$$\boldsymbol{\mu}_i = \frac{1}{n_i} \sum_{\boldsymbol{x} \in \mathcal{X}_i} \boldsymbol{x} \tag{6.14}$$

where n_i is the number of vectors in the class $\mathcal{X}_i$. The between-class scatter matrix S_B is given by

$$S_B = \sum_{i=1}^{c} n_i (\boldsymbol{\mu}_i - \boldsymbol{\mu})(\boldsymbol{\mu}_i - \boldsymbol{\mu})^t \tag{6.15}$$

with

$$\boldsymbol{\mu} = \frac{1}{n} \sum_{i=1}^{c} n_i \boldsymbol{\mu}_i \tag{6.16}$$

where n is the total number of vectors across all classes. The columns of W which maximise $J(W)$ are the generalised eigenvectors that correspond to the eigenvalues of

$$S_B \boldsymbol{w}_i = \lambda_i S_W \boldsymbol{w}_i \tag{6.17}$$

If S_W is non-singular then the problem is reduced to a conventional eigenvalue problem by premultiplying both sides by ${S_W}^{-1}$. For more details on the derivation of generalised linear discriminant functions see [84].

6.6 Classification

The emphasis of this chapter is on the preprocessing of HRRPs. It is the goal of preprocessing to ensure that the target classes are as distinguishable as possible. If the preprocessing of the HRRPs has been adequately done, then the final classification step should be quite simple. Consequently, a simple Bayes classifier was used for the final classification step of this target classification experiment. The generalised linear discriminant functions which were described in Section 6.5.1 were used to reduce the dimensionality of the feature vectors. The generalised linear discriminant transformation matrix W was calculated from the training data and it was applied to feature vectors from the test data.

In this target classification experiment there were two aircraft classes; the Boeing 727 aircraft and the Boeing 737 aircraft. All Boeing 727 HRRPs were bundled into the Boeing 727 class regardless of aspect. A similar grouping was made for the Boeing 737 HRRPs. A total of two aircraft classes ($c = 2$) meant that the reduced feature vector for each aircraft was of length 1 (*i.e.* a scalar).

6.6.1 The Bayes classifier

After preprocessing and dimensionality reduction each aircraft feature vector was reduced to a single scalar. The objective of the classification step was to determine, from the single scalar, whether the aircraft was a Boeing 727 or a Boeing 737. For simplicity, it was assumed that the final distributions of the preprocessed Boeing 727 and Boeing 737 classes were normal. Examination of the distributions for each class (see Figure 6.13) showed that the assumption was justified for these particular data. It was assumed that the a priori probabilities of the two aircraft classes are the same. A simple maximum likelihood Bayes classifier [84] was used to make the final classification decision. The Bayes quadratic discriminant function $g_i(\boldsymbol{y})$ for class i was derived from the training data according to

$$g_i(\boldsymbol{y}) = \boldsymbol{y}^t C_i \boldsymbol{y} + \boldsymbol{c}_i^t \boldsymbol{y} + c_{i0} \tag{6.18}$$

with

$$C_i = -\tfrac{1}{2}\Sigma_i^{-1} \tag{6.19}$$

$$\boldsymbol{c}_i = \Sigma_i^{-1}\boldsymbol{\mu}_i \tag{6.20}$$

$$c_{i0} = -\tfrac{1}{2}\boldsymbol{\mu}_i^t\Sigma_i^{-1}\boldsymbol{\mu}_i - \tfrac{1}{2}\log|\Sigma_i| \tag{6.21}$$

where $\boldsymbol{y}$ is the column vector to be classified and $\boldsymbol{\mu}_i$ and Σ_i are the mean and covariance of class i respectively. For a test vector $\boldsymbol{y}$ the discriminant functions $g_i(\boldsymbol{y})$ are evaluated and the largest result indicates the most likely class for the test vector.

6.7 Summary of processing for the classification experiment

A summary of the target classification experiment processing is given in this section. The details of each processing technique are contained in previous sections.

6.7.1 HRRP preprocessing

The following steps[16] were used to produce a preprocessed HRRP *feature vector*:

1. The complex frequency profile (raw data) was Hann windowed and then an IDFT was performed to give a complex HRRP. The magnitude of the complex HRRP was taken to produce a HRRP. A HRRP is shown in Figure 6.4.

2. 30 consecutive HRRPs were aligned by correlation and then non-coherently averaged to produce a single averaged HRRP. The non-coherent averaging used was described in Section 6.4.1 and an averaged HRRP is shown in Figure 6.6.

3. The average value of the HRRP noise floor was removed from the averaged HRRP. This procedure is described in Section 6.4.2. The result of this procedure is shown in Figure 6.10.

4. A DFT of the HRRP produced in step 3 was taken to give a shift-invariant feature vector. This procedure is described in Section 6.4.3 and an example of a shift-invariant feature vector is shown in Figure 6.11.

6.7.2 Offline processing

Offline processing was performed on the training data. The steps were:

1. The HRRPs were preprocessed according to Section 6.7.1;

2. The linear discriminant functions $\boldsymbol{w}_i$ were calculated from Equations 6.12 to 6.17;

3. Dimensionality reduction was applied by premultiplying the training vectors by the matrix $W = [\boldsymbol{w}_1 \ldots \boldsymbol{w}_{c-1}]$;

4. The means μ_1, μ_2 and covariances Σ_1, Σ_2 of the two aircraft classes were calculated;

5. The parameters C_1, C_2, $\boldsymbol{c}_1$, $\boldsymbol{c}_2$, c_{10} and c_{20} of the Bayes discriminant functions $g_1(\boldsymbol{y})$ and $g_2(\boldsymbol{y})$ were calculated according to Equations 6.18 to 6.21.

---

[16] The preprocessing steps were the same for both the training and test data.

6.7.3 *Online processing*

Online processing was performed on the test data. A flow chart summarising the steps required to get a classification decision from a test HRRP is shown in Figure 6.12. The steps required to reach a classification decision from a single HRRP were:

1. The HRRP was preprocessed according to Section 6.7.1;

2. Dimensionality reduction was performed on the preprocessed HRRP by premultiplying by the matrix W. This gave a test vector $\boldsymbol{y}$;

3. The Bayes quadratic discriminant functions $g_1(\boldsymbol{y})$ and $g_2(\boldsymbol{y})$ were evaluated for the test vector $\boldsymbol{y}$. The largest result indicated the most likely class for the aircraft HRRP.

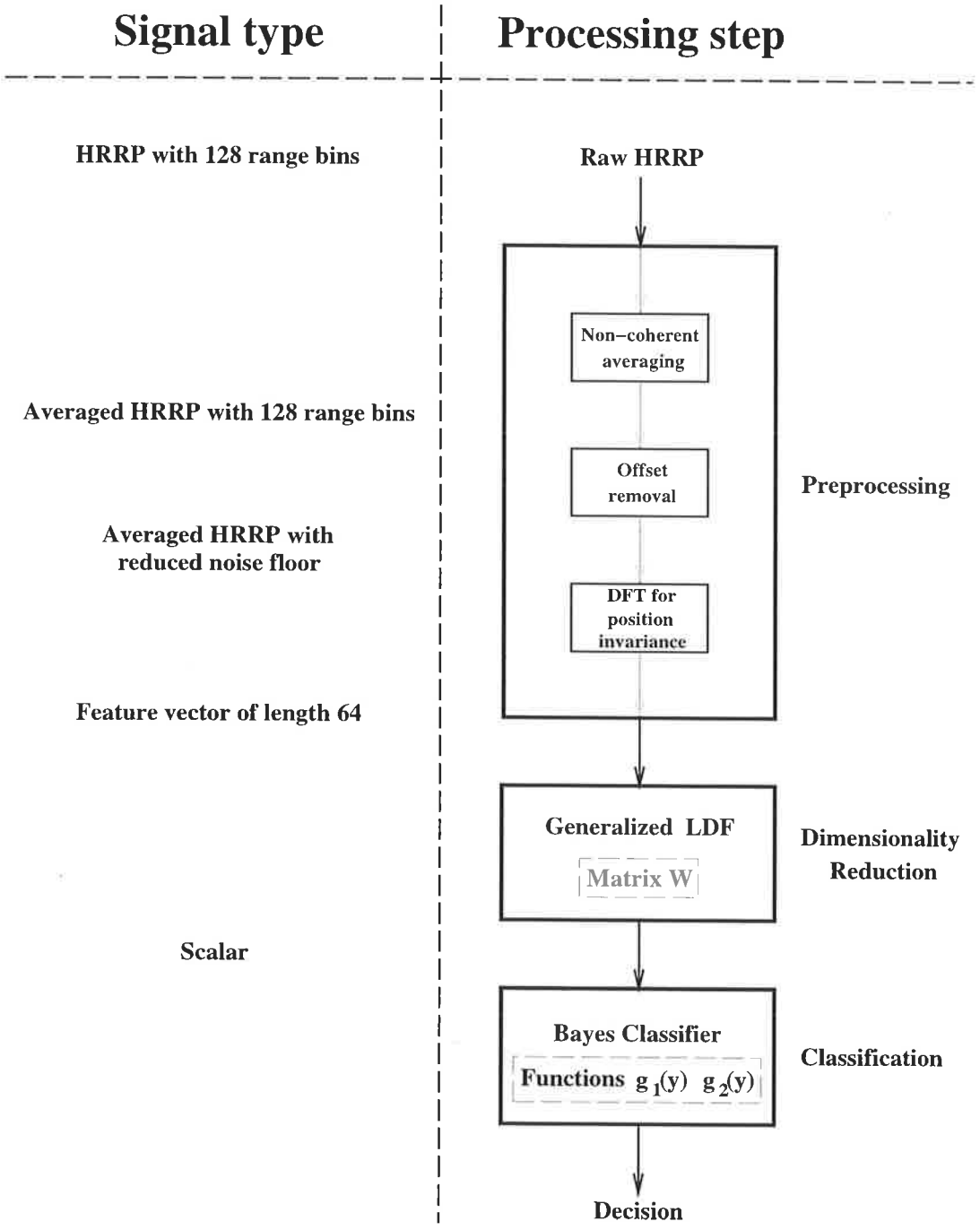

Figure 6.12: The steps required to classify a HRRP. The dimensionality reduction matrix W and the parameters of the Bayes decision functions $g_1(\boldsymbol{y})$ and $g_2(\boldsymbol{y})$ were calculated from the training data.

6.8 Results and discussion

The results of the aircraft target classification from HRRPs are shown in Table 6.6. Since the testing set size was relatively small the estimate of the correct classification rate may be optimistic, but nevertheless the results are good and they auger well for aircraft target classification from HRRPs. The results indicate that it was in fact not very difficult to obtain a high rate of correct target classification after suitable preprocessing.

In this two class experiment, dimensionality reduction has yielded a one–dimensional (scalar) feature vector $\boldsymbol{y}$. The distributions of the Boeing 727 and Boeing 737 classes after preprocessing and dimensionality reduction ($\boldsymbol{y}$) are shown in Figure 6.13. Figure 6.13 shows there is only a slight overlap between the two class distributions and this good class separation accounts for the high correct classification rate. The good class separation can be attributed to the preprocessing of the data and the dissimilarity of the targets being classified.

From a HRRP perspective, the Boeing 727 and Boeing 737 are quite disimiliar aircraft. Not only are the Boeing 727 and Boeing 737 quite different[17] in size, the locations of their engines are also quite different. The Boeing 727 has three engines mounted near the tail of the aircraft and the Boeing 737 has two engines mounted on the wings of the aircraft. Engines and their associated support structures are major sources of backscatter and their locations on an aircraft have a significant impact on HRRPs obtained from the aircraft.

Even though this aircraft classification experiment may now seem quite simple, the results obtained are still very promising for the following reasons:

- The data were collected with a real radar using manual visual tracking of the aircraft;
- The HRRPs cover viewing aspects which vary from 110° to 160° and the HRRPs were not sorted according to aspect for the classification experiment;
- Only 40% of the data were used for training. The classifier was tested using the remaining 60% of the data;
- Testing was performed on different physical aircraft to those used for training;
- The correct classification rate for the experiment was high using only a very simple classifier;
- All the HRRP preprocessing techniques proposed are applicable to multi-aspect, multi-target data.

[17] The Boeing 727 aircraft has a length of 47 m and the Boeing 737 aircraft has a length of 37 m.

More research is needed to make further statements on the correct target classification rates achievable in a real environment of many targets over a wide range of viewing aspects.

Number (percentage) of correct classifications		Classified class	
		727	737
Actual class	727	94 (98%)	2 (2%)
	737	4 (4%)	92 (96%)

Table 6.6: The confusion matrix showing the classification results from the test data.

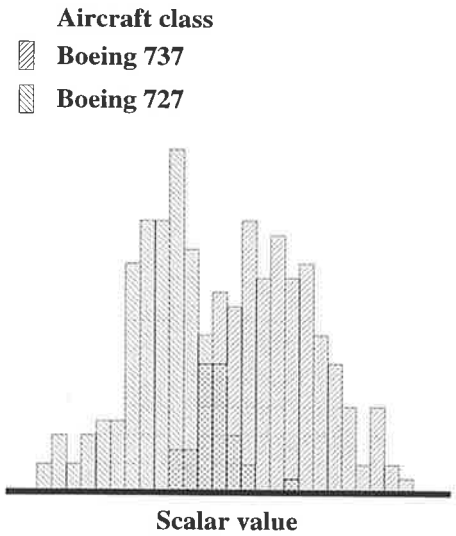

Figure 6.13: The distributions of the Boeing 727 and Boeing 737 classes after preprocessing and dimensionality reduction. Each aircraft HRRP was reduced to single scalar.

6.9 Summary

The first half of this chapter discussed preprocessing issues for radar target classification from HRRPs. The important preprocessing issues of aspect-independent classification, target localisation, HRRP averaging and HRRP thresholding were discussed and previous work addressing these issues was reviewed. Several solutions to each preprocessing issue were presented.

The second half of this chapter presented a target classification experiment where real HRRPs were preprocessed and classified. Real data were collected at a local airport in order to differentiate Boeing 727 aircraft from Boeing 737 aircraft over a limited range of viewing aspects. The SNR of the collected HRRPs was increased by non-coherently averaging consecutive HRRPs. The target localisation problem was avoided by using the magnitude of the FFT as a shift-invariant transform. Dimensionality reduction based upon a generalised linear discriminant was used prior to final target classification. For the two-class classification experiment discussed in this chapter, the test HRRPs were reduced to single scalar number before final classification. Final classification of the test scalar was achieved using a Bayes classifier. The correct classification rates achieved were very good and the results of the experiment auger well for aircraft target classification from HRRPs.

Chapter VII

COHERENT AVERAGING OF HRRPS

7.1 Introduction

7.1.1 Chapter purpose

This chapter presents a coherent averaging algorithm to average a sequence of HRRPs. This algorithm enables the averaged HRRP to be thresholded without localising the target in range. Coherent averaging produces an averaged HRRP with a better target scatterer detectability than that which is achievable with non-coherent averaging. In essence, this chapter provides a more fundamental approach to HRRP averaging and thresholding than that which was presented in Chapter 6.

7.1.2 Chapter overview

This chapter presents a coherent averaging algorithm which produces the best possible[1] averaged HRRP, in terms of target scatterer detectability, for a given number of HRRPs to be averaged. Section 7.2 reviews the principles of both coherent and non-coherent integration. Several results which are derived in this section are summarised in Table 7.1 for easy reference. The non-coherent averaging of HRRPs is discussed in Section 7.3. An algorithm for the coherent averaging of HRRPs is presented in Section 7.4. Section 7.4.1 outlines the operational context in which the coherent averaging of HRRPs is used and Section 7.4.2 provides an overview of the coherent averaging algorithm. Section 7.4.3 presents the way in which the radar parameters are chosen according to the estimated target Doppler bandwidth. Section 7.4.4 outlines the way in which an averaged HRRP is extracted from the range-Doppler image and Section 7.4.5 presents a technique for reliably estimating the noise level in the coherently averaged HRRP. Section 7.4.6 describes a statistical test that is used to determine whether the coherent processing has been successful and Section 7.4.7 describes how a coherently averaged HRRP is thresholded without localising the target in range.

A series of five simulations is presented in Section 7.5 to compare the performance of the non-coherent and coherent averaging algorithms. The results from these simulations confirm that coherent averaging provides better averaged HRRPs, in terms of target

[1] Given that no a priori information about the target scatterer distribution is available.

scatterer detectability, than non-coherent averaging. Some of the work presented in this chapter has been accepted for publication and it is due to appear in [85].

7.2 Coherent and non-coherent integration

This section presents a review of coherent and non-coherent integration. The principles of coherent and non-coherent integration were originally investigated in pioneering work by Rice and Marcum.

Consider a sampled complex signal

$$s_i = Ae^{(j\omega_0 t_i + j\phi_0)} \tag{7.1}$$

where ω_0 is the frequency of the signal, ϕ_0 is the initial phase of the signal, A is the amplitude of the signal and $\boldsymbol{t} = [t_1 \ldots t_i \ldots t_N]$ represents the N time instants when the signal is sampled. A coherent receiver maintains the phase relationship between successive samples of the signal whereas a non-coherent receiver does not maintain the phase relationship. The received signal from noiseless coherent receiver is

$$s_i^{\mathrm{c}} = Ae^{(j\omega_0 t_i + j\phi_0)} \tag{7.2}$$

If the coherent receiver is not noiseless the received signal is

$$\begin{aligned} z_i^{\mathrm{c}} &= s_i^{\mathrm{c}} + n_i \\ &= Ae^{(j\omega_0 t_i + j\phi_0)} + n_i \end{aligned} \tag{7.3}$$

with

$$n_i = I_i + jQ_i \tag{7.4}$$

where I and Q are jointly independent, real, Gaussian random variables with zero mean and variance σ_0^2. The received signal from a noiseless non-coherent receiver is

$$s_i^{\mathrm{nc}} = Ae^{(j\omega_0 t_i + j\phi_i)} \tag{7.5}$$

where ϕ_i is a random variable uniformly distributed over $[0, 2\pi)$. If the non-coherent receiver is not noiseless the received signal is

$$\begin{aligned} z_i^{\mathrm{nc}} &= s_i^{\mathrm{nc}} + n_i \\ &= Ae^{(j\omega_0 t_i + j\phi_i)} + n_i \end{aligned} \tag{7.6}$$

Coherent and non-coherent reception are illustrated in Figure 7.1.

The non-coherent integration v^{nc} of N samples is defined by

$$v^{\mathrm{nc}} = \sum_{i=1}^{N} |z_i^{\mathrm{nc}}| \tag{7.7}$$

and the coherent integration v^c of N samples is defined by

$$v^c = \left| \sum_{i=1}^{N} z_i^c e^{-j\omega_0 t_i} \right| \tag{7.8}$$

Coherent and non-coherent integration of the signals in Figure 7.1 is illustrated in Figure 7.2.

Non-coherent integration is relatively simple to achieve. At each time step the magnitude of the signal is calculated and the non-coherent integration of the signal is defined as the sum of these magnitudes. Coherent integration is more difficult to achieve. To ensure that the signal samples add constructively, a phase adjustment of $e^{-j\omega_0 t_i}$ is applied to each z_i^c. When the phase adjustment has been applied, the phase adjusted samples can be added coherently in the complex domain. The coherent integration of the N samples is the magnitude of the coherent (phasor) sum.

Often the signal frequency ω_0 is unknown. The DFT can be used to coherently integrate a signal when ω_0 is unknown. The DFT for a signal $x(1) \ldots x(N)$ is defined by

$$X(m) = \sum_{l=0}^{N-1} x(l) e^{-j\left(\frac{2\pi}{N}\right) lm} \tag{7.9}$$

It can be seen that $X(m)$ is the coherent sum for a signal of normalised[2] frequency $\omega_m = \frac{2\pi m}{N}$.

[2] The actual frequency of the signal is $\omega = \omega_m f_s$ where f_s is the sampling frequency.

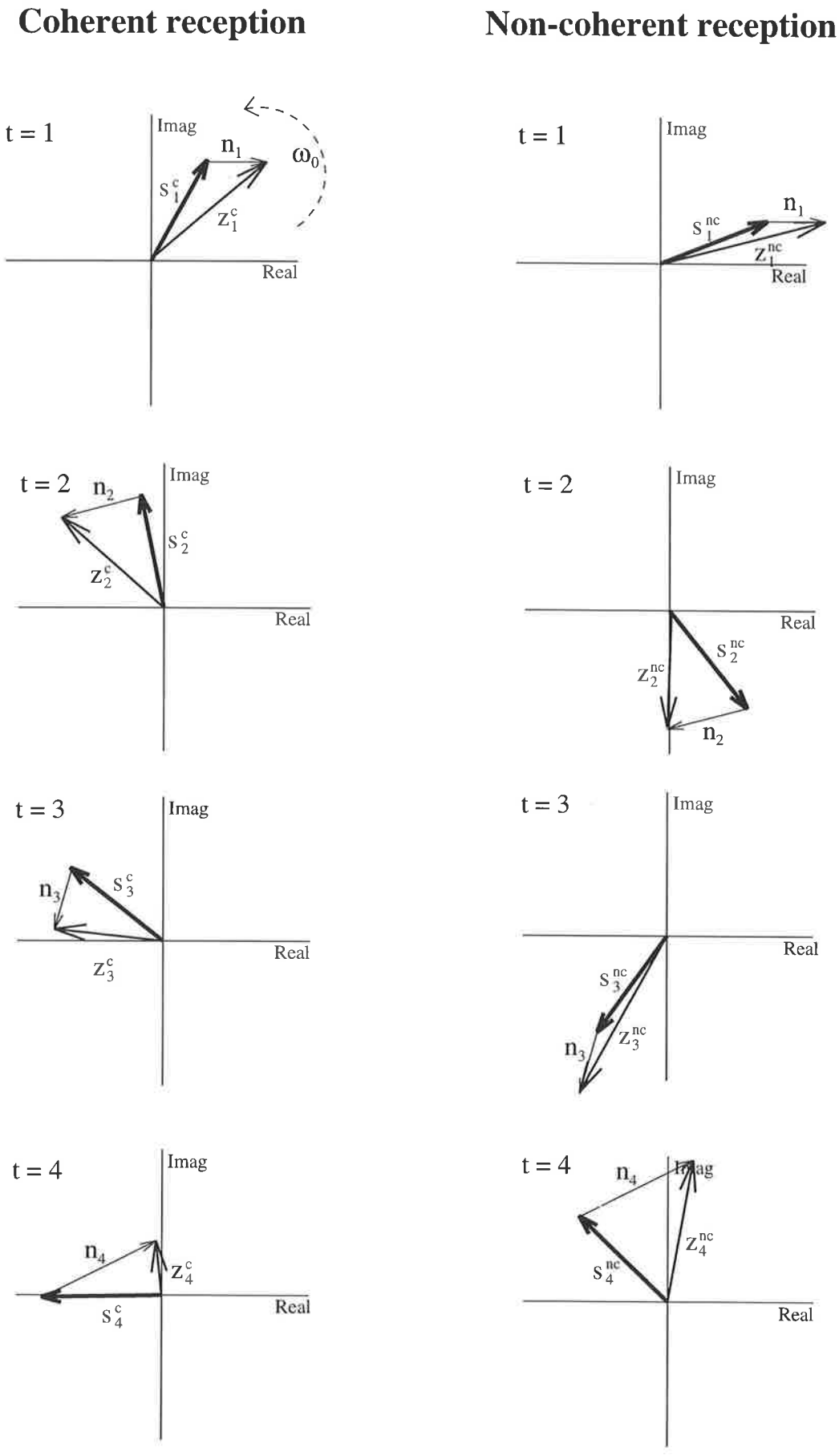

Figure 7.1: Coherent and non-coherent reception of $s_i = Ae^{(j\omega_0 t_i + j\phi_0)}$.

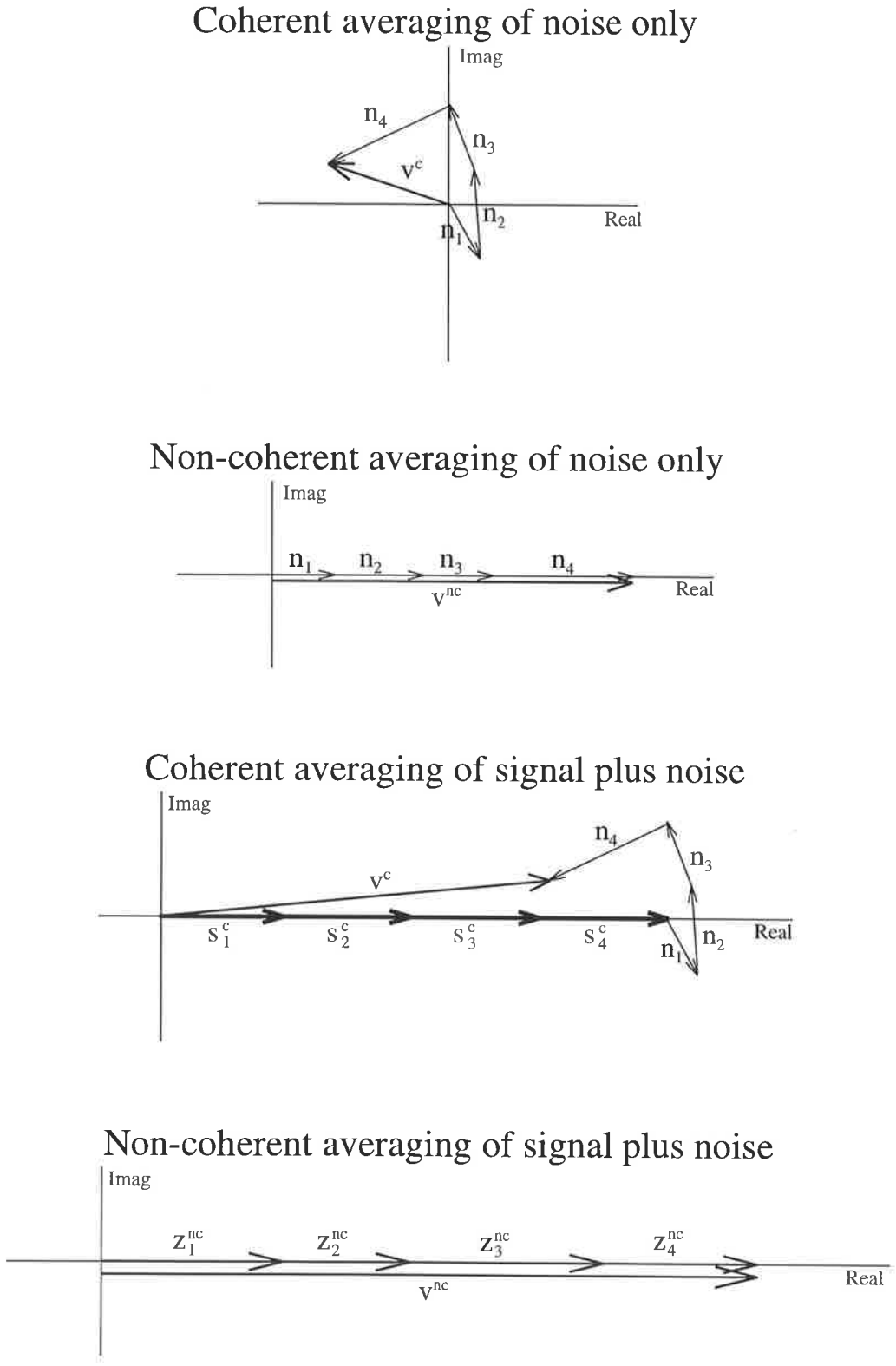

Figure 7.2: Coherent and non-coherent integration of the signals in Figure 7.1.

7.2.1 Comparing coherent and non-coherent integration

If v is a received signal which may consist of noise only or signal plus noise, then the probability of false alarm can be defined as

$$P_{\text{fa}} = \int_{\mathcal{X}_t}^{\infty} p_{\text{noise\_only}}(v)\text{d}v \tag{7.10}$$

where $p_{\text{noise\_only}}(v)$ is the probability density function (PDF) of the noise and $\mathcal{X}_t$ is the threshold used for detection. The probability of detection can be defined by

$$P_{\text{d}} = \int_{\mathcal{X}_t}^{\infty} p_{\text{signal\_plus\_noise}}(v)\text{d}v \tag{7.11}$$

where $p_{\text{signal\_plus\_noise}}(v)$ is the PDF of the signal plus noise.

In order to determine whether coherent or non-coherent integration is better in terms of target detectability for a given false alarm rate, it is necessary to calculate the probability density functions of v^{nc} and v^{c} for the following cases:

1. Non-coherent integration with only noise present ($A = 0$);
2. Coherent integration with only noise present ($A = 0$);
3. Non-coherent integration with signal plus noise present;
4. Coherent integration with signal plus noise present.

Previous work by Rice

Rice [86, 87, 88] has analysed the signal $s_i = A + n_i$ where A is a real constant and n_i is defined by Equation 7.4. Rice has shown that the magnitude $|s_i|$ has a PDF given by

$$p(|s_i|) = \frac{|s_i|}{\sigma_0^2} e^{-\left(\frac{|s_i|^2 + A^2}{2\sigma_0^2}\right)} I_0\left(\frac{|s_i|A}{\sigma_0^2}\right) \tag{7.12}$$

where I_0 is a zero-order modified[3] Bessel function of the first kind. The type of PDF described by Equation 7.12 is often referred to as a Ricean probability density function. The mean of this probability density function is

$$E\left[|s_i|\right] = \sqrt{\frac{\pi}{2}}\sigma_0 e^{-\frac{P}{2}}\left((1+P)I_0\left(\frac{P}{2}\right) + PI_1\left(\frac{P}{2}\right)\right) \tag{7.13}$$

where

$$P = \frac{A^2}{2\sigma_0^2} \tag{7.14}$$

is the mean signal power to noise ratio commonly seen in the radar literature. The variance of the probability density function is

$$E\left[|s_i|^2\right] - E\left[|s_i|\right]^2 = 2(1+P)\sigma_0^2 - E\left[|s_i|\right]^2 \tag{7.15}$$

Equations 7.12, 7.13, 7.14 and 7.15 are results which are used in the following analysis of non-coherent and coherent integration.

---

[3] A modified Bessel function is a Bessel function of an imaginary argument.

Non-coherent integration with no signal present

If $A = 0$ (no signal present) then $P^{\mathrm{nc}} = \frac{A^2}{2\sigma_0^2} = 0$. The probability density function of the real variate $|z_i^{\mathrm{nc}}|$ is derived from Equation 7.12

$$p(|z_i^{\mathrm{nc}}|) = \frac{|z_i^{\mathrm{nc}}|}{\sigma_0^2} e^{-\left(\frac{|z_i^{\mathrm{nc}}|^2}{2\sigma_0^2}\right)} \tag{7.16}$$

since $I_0(0) = 1$. It can be seen that $|z_i^{\mathrm{nc}}|$ is Rayleigh distributed. The mean of $|z_i^{\mathrm{nc}}|$ is derived from Equation 7.13

$$E\left[|z_i^{\mathrm{nc}}|\right] = \sqrt{\frac{\pi}{2}}\sigma_0 \tag{7.17}$$

since $I_0(0) = 1$ and $I_1(0) = 0$. The variance of $|z_i^{\mathrm{nc}}|$ is derived from Equation 7.15

$$\begin{aligned} E\left[|z_i^{\mathrm{nc}}|^2\right] - E\left[|z_i^{\mathrm{nc}}|\right]^2 &= 2\sigma_0^2 - \frac{\pi}{2}\sigma_0^2 \\ &= \left(2 - \frac{\pi}{2}\right)\sigma_0^2 \end{aligned} \tag{7.18}$$

The non-coherent integration v^{nc} of N samples is defined by Equation 7.7. The Central Limit Theorem [92] implies that, for large N, the mean and variance of v^{nc} are approximately

$$E\left[v^{\mathrm{nc}}\right] = N\sqrt{\frac{\pi}{2}}\sigma_0 \tag{7.19}$$

and

$$E\left[(v^{\mathrm{nc}})^2\right] - E\left[v^{\mathrm{nc}}\right]^2 = N\left(2 - \frac{\pi}{2}\right)\sigma_0^2 \tag{7.20}$$

For large N the PDF of v^{nc} tends to a Gaussian PDF

$$p(v^{\mathrm{nc}}) = \frac{1}{\sqrt{2\pi N\left(2 - \frac{\pi}{2}\right)}\sigma_0} e^{-\left(\frac{\left(v^{\mathrm{nc}} - N\sqrt{\frac{\pi}{2}}\sigma_0\right)^2}{2N\left(2-\frac{\pi}{2}\right)\sigma_0^2}\right)} \tag{7.21}$$

Coherent integration with no signal present

If $A = 0$ (no signal present) then $P^{\mathrm{c}} = \frac{A^2}{2\sigma_0^2} = 0$. The probability density function of the complex variate $z_i^{\mathrm{c}} e^{-j\omega_0 t_i}$ is Gaussian with zero mean and variance σ_0^2. The sum of N such complex variates has a Gaussian probability density function with zero mean and variance $N\sigma_0^2$. The coherent integration of N samples is defined by Equation 7.8 and the probability density function of v^{c} is derived from Equation 7.12

$$p(v^{\mathrm{c}}) = \frac{v^{\mathrm{c}}}{N\sigma_0^2} e^{-\left(\frac{(v^{\mathrm{c}})^2}{2N\sigma_0^2}\right)} \tag{7.22}$$

since $I_0(0) = 1$. It can be seen that v^{c} is Rayleigh distributed. The mean of v^{c} is derived from Equation 7.13

$$E\left[v^{\mathrm{c}}\right] = \sqrt{\frac{\pi}{2}}\sqrt{N}\sigma_0 \tag{7.23}$$

since $I_0(0) = 1$ and $I_1(0) = 0$. The variance of v^c is derived from Equation 7.15

$$\begin{aligned} E\left[(v^c)^2\right] - E\left[v^c\right]^2 &= 2N\sigma_0^2 - \frac{\pi}{2}N\sigma_0^2 \\ &= \left(2 - \frac{\pi}{2}\right)N\sigma_0^2 \end{aligned} \tag{7.24}$$

Non-coherent integration with a signal present

With a signal present the probability density function of the real variate $|z_i^{nc}|$ is Ricean as in Equation 7.12

$$p(|z_i^{nc}|) = \frac{|z_i^{nc}|}{\sigma_0^2} e^{-\left(\frac{|z_i^{nc}|^2 + A^2}{2\sigma_0^2}\right)} I_0\left(\frac{|z_i^{nc}|A}{\sigma_0^2}\right) \tag{7.25}$$

From Equation 7.13 the mean of $|z_i^{nc}|$ is

$$E\left[|z_i^{nc}|\right] = \sqrt{\frac{\pi}{2}}\sigma_0 e^{-\frac{P^{nc}}{2}}\left((1 + P^{nc})I_0\left(\frac{P^{nc}}{2}\right) + P^{nc}I_1\left(\frac{P^{nc}}{2}\right)\right) \tag{7.26}$$

where

$$P^{nc} = \frac{A^2}{2\sigma_0^2} \tag{7.27}$$

The variance of $|z_i^{nc}|$ is derived from Equation 7.15

$$E\left[|z_i^{nc}|^2\right] - E\left[|z_i^{nc}|\right]^2 = 2(1 + P^{nc})\sigma_0^2 - E\left[|z_i^{nc}|\right]^2 \tag{7.28}$$

The non-coherent integration of N samples is defined by Equation 7.7. The Central Limit Theorem [92] implies that, for large N, the mean and variance of v^{nc} are approximately

$$E\left[v^{nc}\right] = N\sqrt{\frac{\pi}{2}}\sigma_0 e^{-\frac{P^{nc}}{2}}\left((1 + P^{nc})I_0\left(\frac{P^{nc}}{2}\right) + P^{nc}I_1\left(\frac{P^{nc}}{2}\right)\right) \tag{7.29}$$

and

$$E\left[(v^{nc})^2\right] - E\left[v^{nc}\right]^2 = N\left(2(1 + P^{nc})\sigma_0^2 - E\left[|z_i^{nc}|\right]^2\right) \tag{7.30}$$

For large N the PDF of v^{nc} tends to a Gaussian PDF.

Coherent integration with a signal present

With a signal present the probability density function of the complex variate $z_i^c e^{-j\omega_0 t_i}$ is Gaussian with mean A and variance σ_0^2. The sum of N such complex variates has a Gaussian probability density function with mean NA and variance $N\sigma_0^2$. The coherent integration of N samples is defined by Equation 7.8 and the probability density function of v^c is derived from Equation 7.12

$$p(v^c) = \frac{v^c}{N\sigma_0^2} e^{-\left(\frac{(v^c)^2 + (NA)^2}{2N\sigma_0^2}\right)} I_0\left(\frac{v^c A}{\sigma_0^2}\right) \tag{7.31}$$

It can be seen that the distribution of v^c is Ricean. The mean of v^c is derived from Equation 7.13

$$E\left[v^c\right] = \sqrt{\frac{\pi}{2}}\sqrt{N}\sigma_0 e^{-\frac{P^c}{2}}\left((1 + P^c)I_0\left(\frac{P^c}{2}\right) + P^c I_1\left(\frac{P^c}{2}\right)\right) \tag{7.32}$$

where

$$P^c = \frac{(NA)^2}{2N\sigma_0^2} = \frac{NA^2}{2\sigma_0^2} \tag{7.33}$$

The variance of v^c is derived from Equation 7.15

$$E\left[(v^c)^2\right] - E\left[v^c\right]^2 = 2(1+P^c)N\sigma_0^2 - E\left[v^c\right]^2 \tag{7.34}$$

Non-coherent integration (noise only)
PDF type: **Gaussian**
$E\left[v^{\mathrm{nc}}\right] = N\sqrt{\frac{\pi}{2}}\sigma_0 \quad (7.19)$
$E\left[\left(v^{\mathrm{nc}}\right)^2\right] - E\left[v^{\mathrm{nc}}\right]^2 = N\left(2 - \frac{\pi}{2}\right)\sigma_0^2 \quad (7.20)$

Coherent integration (noise only)
PDF type: **Rayleigh**
$E\left[v^{\mathrm{c}}\right] = \sqrt{N}\sqrt{\frac{\pi}{2}}\sigma_0 \quad (7.23)$
$E\left[\left(v^{\mathrm{c}}\right)^2\right] - E\left[v^{\mathrm{c}}\right]^2 = N\left(2 - \frac{\pi}{2}\right)\sigma_0^2 \quad (7.24)$

Non-coherent integration (signal plus noise)
PDF type: **Gaussian**
$E\left[v^{\mathrm{nc}}\right] = N\sqrt{\frac{\pi}{2}}\sigma_0 e^{-\frac{P^{\mathrm{nc}}}{2}}\left((1+P^{\mathrm{nc}})I_0\left(\frac{P^{\mathrm{nc}}}{2}\right) + P^{\mathrm{nc}}I_1\left(\frac{P^{\mathrm{nc}}}{2}\right)\right) \quad (7.29)$
$E\left[\left(v^{\mathrm{nc}}\right)^2\right] - E\left[v^{\mathrm{nc}}\right]^2 = N\left(2(1+P^{\mathrm{nc}})\sigma_0^2 - E\left[\lvert z_i^{\mathrm{nc}}\rvert\right]^2\right) \quad (7.30)$
$P^{\mathrm{nc}} = \frac{A^2}{2\sigma_0^2} \quad (7.27)$

Coherent integration (signal plus noise)
PDF type: **Ricean**
$E\left[v^{\mathrm{c}}\right] = \sqrt{\frac{\pi}{2}}\sqrt{N}\sigma_0 e^{-\frac{P^{\mathrm{c}}}{2}}\left((1+P^{\mathrm{c}})I_0\left(\frac{P^{\mathrm{c}}}{2}\right) + P^{\mathrm{c}}I_1\left(\frac{P^{\mathrm{c}}}{2}\right)\right) \quad (7.32)$
$E\left[\left(v^{\mathrm{c}}\right)^2\right] - E\left[v^{\mathrm{c}}\right]^2 = 2(1+P^{\mathrm{c}})N\sigma_0^2 - E\left[v^{\mathrm{c}}\right]^2 \quad (7.34)$
$P^{\mathrm{c}} = \frac{NA^2}{2\sigma_0^2} \quad (7.33)$

Table 7.1: A summary of the probability density functions for the results of coherent and non-coherent integration.

7.2.2 *Interpretation of coherent and non-coherent integration*

The probability density functions for v^{nc} and v^{c} are summarised in Table 7.1. These PDFs are somewhat tedious to manipulate. This section provides a general discussion of coherent and non-coherent integration rather than duplicating the rigourous mathematical analysis [86, 87, 88, 89, 90] which has been previously published. Blake [91, pp 41-42] provides a good intuitive explanation of non-coherent integration:

> *Non-coherent integration can be thought of as a variation reducing process. If N independent noise pulses are summed to give $V = \sum_{i=1}^{N} V_i$ then the variation (standard-deviation-to-mean ratio) of V is reduced relative to the variation of the V_i's. The smoothing of the output noise samples allows improved signal detectability. Specifically, once the noise variation has been reduced, it is possible to reduce the threshold-to-mean ratio while still maintaining the same false alarm probability. But now with a smaller threshold-to-mean ratio, a smaller signal can produce a threshold crossing; thus the sensitivity of the system to small signals is improved. The ability of non-coherent integration to provide improved detectability is primarily dependent on the variation reduction of the noise rather than on the signal characteristics. Non-coherent integration provides a processing gain even when the signal has a random phase or is rapidly fluctuating.*

For a single $|z_i^{nc}|$ variate the noise variation is

$$\frac{\sqrt{E\left[|z_i^{nc}|^2\right] - E\left[|z_i^{nc}|\right]^2}}{E\left[|z_i^{nc}|\right]} = \frac{\left(\sqrt{2-\frac{\pi}{2}}\right)\sigma_0}{\sqrt{\frac{\pi}{2}}\sigma_0} = \sqrt{\frac{4-\pi}{\pi}} \tag{7.35}$$

For the sum of N $|z_i^{nc}|$ variates, the noise variation is

$$\frac{\sqrt{E\left[(v^{nc})^2\right] - E\left[v^{nc}\right]^2}}{E\left[v^{nc}\right]} = \frac{\sqrt{N}\left(\sqrt{2-\frac{\pi}{2}}\right)\sigma_0}{N\sqrt{\frac{\pi}{2}}\sigma_0} = \sqrt{\frac{4-\pi}{N\pi}} \tag{7.36}$$

Hence non-coherent integration reduces the noise variation by a factor of $\sqrt{N}$.

Coherent integration can be viewed as a technique which improves the SNR. Coherent integration depends upon the signal having a predictable phase behaviour and the noise having a random behaviour. Coherent integration does not reduce the noise variation since both the mean noise amplitude and the standard deviation of the noise increase by the same factor $\sqrt{N}$.

$$\frac{\sqrt{E\left[(v^{c})^2\right] - E\left[v^{c}\right]^2}}{E\left[v^{c}\right]} = \frac{\sqrt{N}\left(\sqrt{2-\frac{\pi}{2}}\right)\sigma_0}{\sqrt{N}\sqrt{\frac{\pi}{2}}\sigma_0} = \sqrt{\frac{4-\pi}{\pi}} = \frac{\sqrt{E\left[|z_i^{c}|^2\right] - E\left[|z_i^{c}|\right]^2}}{E\left[|z_i^{c}|\right]} \tag{7.37}$$

Whilst the noise power increases by a factor of N the signal power increases by a larger factor. The signal phasors add head to tail so that the amplitude of the resultant phasor

is N times the amplitude of a single phasor. Hence the signal power increases by a factor of N^2 and the SNR is

$$P^{\mathrm{c}} = NP_1 \tag{7.38}$$

where

$$P_1 = \frac{A^2}{2\sigma_0^2} \tag{7.39}$$

is the SNR of a single sample.

7.2.3 *Integration loss*

Marcum [89, 90] defined an *integration loss* L_{i} for the non-coherent integration of N samples compared to the coherent integration of N samples

$$L_{\mathrm{i}} = 10\log_{10}\left(\frac{P_1}{\left(\frac{P_N}{N}\right)}\right) \tag{7.40}$$

where P_1 is the SNR of a single sample required to achieve a specified P_{fa} and P_{d}, and P_N is the SNR of N integrated samples. For coherent integration $P_N = P^{\mathrm{c}} = NP_1$ and hence the integration loss is

$$L_{\mathrm{i}}^{\mathrm{c}} = 0 \tag{7.41}$$

For non-coherent integration $\sqrt{N}P_1 \leq P^{\mathrm{nc}} \leq NP_1$ and the integration loss is

$$L_{\mathrm{i}}^{\mathrm{nc}} = 10\log_{10}\left(N\frac{P_1}{P^{\mathrm{nc}}}\right) \tag{7.42}$$

Marcum has calculated and plotted the non-coherent integration loss versus the number N of samples integrated for a given P_{fa} and P_{d}. It was found that the integration loss was remarkably insensitive to P_{fa} and P_{d}. For $N \gg 1$ the integration loss in dB is approximately equal to

$$L_{\mathrm{i}}^{\mathrm{nc}} = (10\log_{10}\sqrt{N} - 5.5)\ \mathrm{dB} \qquad N \gg 1 \tag{7.43}$$

In practice it is found that coherent integration is seldom used instead of non-coherent integration for a single sample SNR of $P_1 \geq 20$ dB since the integration loss is negligible. As the single sample SNR drops below 20 dB, the performance difference (integration loss) between coherent and non-coherent integration becomes significantly larger.

7.3 Non-coherent averaging of HRRPs

A simple way to improve the SNR of a HRRP, is to apply non-coherent averaging to the magnitudes of a sequence of aligned HRRPs. Non-coherent averaging of HRRPs was discussed in Section 6.2.6. The HRRPs were aligned using cross-correlation [44] and averaging of the HRRP magnitudes took place over a number of consecutive HRRPs. If N HRRPs are averaged then the increase in SNR is between $\sqrt{N}$ and N [36].

The analysis of non-coherent integration presented in Section 7.2 corresponds to non-coherent averaging in a single range bin. The signal in a particular range bin m is $z_m(t_i) = z_i^{\text{nc}}$ where HRRP number i is collected at time t_i.

7.4 Coherent averaging of HRRPs

Consider a sequence of N complex HRRPs which are collected with an ideal noiseless receiver. The received data matrix of size $N \times n$ can be written

$$\begin{array}{c} \text{range bin index} \\ \longrightarrow \\ \left[\begin{array}{ccc} a_{11}e^{j\theta_{11}} & \cdots & a_{1n}e^{j\theta_{1n}} \\ \vdots & a_{lm}e^{j\theta_{lm}} & \vdots \\ a_{N1}e^{j\theta_{N1}} & \cdots & a_{Nn}e^{j\theta_{Nn}} \end{array}\right] \end{array} \begin{array}{l} \\ \\ \downarrow \text{HRRP index} \end{array} \tag{7.44}$$

where a_{lm} is a real number, θ_{lm} is a real number in the range $[0, 2\pi)$, $l = 1 \ldots N$ is a HRRP index and $m = 1 \ldots n$ is a range bin index. HRRP number l is collected at time t_l. Radial motion compensation and adaptive beamforming (see Appendix A) must be applied to the HRRP data before coherent integration can be used. The signal in a single range bin m after radial motion compensation and adaptive beamforming is

$$s_m(t_i) = A_m e^{j\omega_m t_i + j\phi_m} \tag{7.45}$$

where A_m is the amplitude of the dominant scatterer in range bin m, ϕ_m is a real number in the range $[0, 2\pi)$ and ω_m is a frequency which is dependent on the cross-range position of the dominant scatterer in range bin m. Figure 7.3 illustrates the relationship between w_m and the cross-range position of the dominant scatterer in range bin m. The Doppler gradient across the target [33] with respect to cross-range position d_c is

$$\frac{\partial \beta_D}{\partial d_c} = \frac{2\omega \bar{f}}{c} \tag{7.46}$$

where ω is the angular velocity of the target, $\bar{f}$ is the centre frequency of the radar waveform, c is the speed of light and β_D is the target Doppler bandwidth which is defined in Section 7.4.3. The Doppler frequency of the signal in range bin m is

$$\omega_m = \frac{\partial \beta_D}{\partial d_c} \times (d_m - d_b) \tag{7.47}$$

where d_m is the cross-range position of the dominant scatterer in range bin m and d_b is the cross-range position of the scatterer used as a phase synchronising source. After range alignment and adaptive beamforming, the HRRP data can be written as

$$\begin{array}{c} \text{range bin index} \\ \longrightarrow \\ \left[\begin{array}{ccc} A_1 e^{j\omega_1 t_1 + j\phi_1} & \cdots & A_n e^{j\omega_n t_1 + j\phi_n} \\ \vdots & A_m e^{j\omega_m t_1 + j\phi_m} & \vdots \\ A_1 e^{j\omega_1 t_N + j\phi_1} & \cdots & A_n e^{j\omega_n t_N + j\phi_n} \end{array}\right] \downarrow \text{HRRP index} \end{array} \tag{7.48}$$

where A_m is the amplitude of the dominant scatterer in range bin m, ϕ_m is a real number in the range $[0, 2\pi)$ and ω_m is the frequency given in Equation 7.47.

The signal $s_m(t_i)$ in each range bin can be coherently integrated in the same way as the signal defined in Equation 7.1. Three steps are required to form the "coherent average" of a sequence of N complex HRRPs:

1. Perform radial motion compensation and adaptive beamforming on the data from Equation 7.44. This processing transforms the data into the form shown in Equation 7.48;

2. Coherently integrate the signal in each range bin to produce a range-Doppler image;

3. Extract an "averaged" HRRP from the range-Doppler image;

The remainder of this chapter presents the way in which these steps are implemented to produce a coherently averaged HRRP.

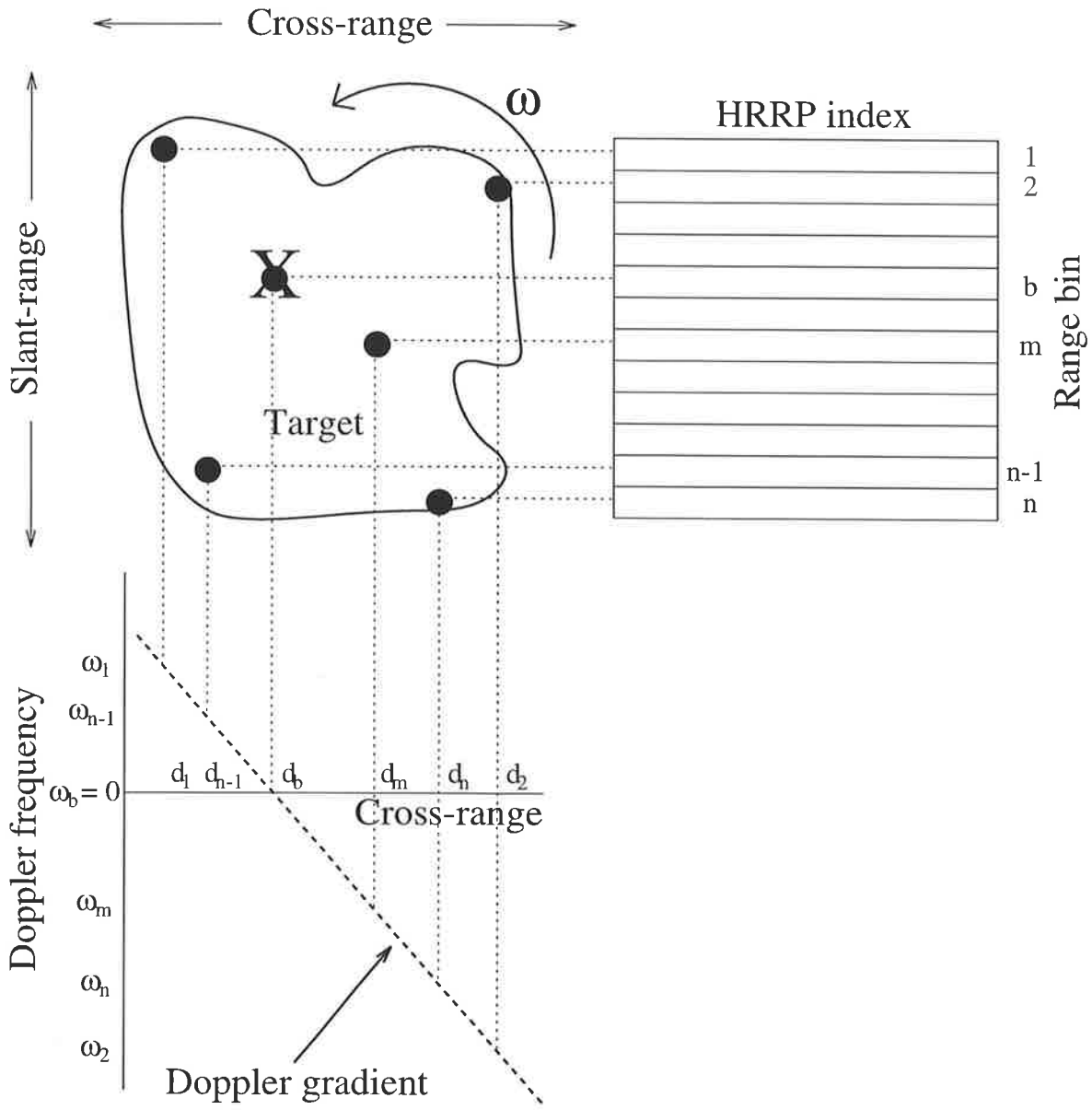

Figure 7.3: The relationship between w_m and the cross-range position of the dominant scatterer in range bin m. Adaptive beamforming has used the dominant scatterer in range bin b (marked with an **X**) as a phase synchronising source to make $\omega_b = 0$. The Doppler gradient across the target is $\frac{\partial \beta_D}{\partial d_c} = \frac{2\omega \bar{f}}{c}$ where ω is the angular velocity of the target and d_c represents cross-range position.

7.4.1 The operational context in which coherent averaging is used

It is appropriate to explain the operational context in which the coherent averaging of HRRPs is used. A radar using a chirp waveform[4] for high resolution in range, transmits and receives N consecutive pulses from a moving aircraft target. The transmitted waveform is known as a *coherent pulse train.* An example of a coherent pulse train is shown in Figure C.2 (Appendix C). Each received pulse is dechirped using a matched filter to produce a complex HRRP. Coherent processing (see Section 3.5 or Appendix A) can be performed on the sequence of HRRPs.

For a synthetic aperture radar, the achievable resolution in the cross-range direction Δr_c depends upon the relative target rotation rate ω seen by the radar over the sequence of HRRPs which are to be integrated. Equation 3.4 describes the relationship between cross-range resolution and the target rotation rate. Poor cross-range resolution is achieved if the aspect change seen by the radar is not large enough. Particular reasons why this aspect change may not be large enough have been mentioned in Section 3.5.4. Coherent averaging is used when the target does not cover, in a suitable time period, the aspect angle required for a suitable (ISAR) cross-range resolution.

7.4.2 An overview of coherent averaging

Coherent averaging has two advantages when it is compared to non-coherent averaging. The first advantage is that coherent averaging produces an averaged HRRP in which the SNR of each range bin is better than that which is achieved with non-coherent averaging. This improvement in SNR was discussed in Section 7.2. The second advantage is that the coherently averaged HRRP can be thresholded in a statistical manner without actually localising the target in range.

The basic principle of coherent averaging is to coherently integrate a number of received HRRPs and then separate the target from the noise according to Doppler frequency. Since the target moves through a number of range bins during the coherent integration time, coherent processing with motion compensation is necessary. The target Doppler bin in the focussed range-Doppler image is extracted to give an averaged HRRP. The fact that the target energy is localised in Doppler is used as a basis for CFAR thresholding. The localisation of target energy in Doppler enables the noise power to be safely estimated from Doppler bins adjacent to the target Doppler bin. If the noise power were estimated from range bins adjacent to the target, then there is a risk that the noise estimate would be contaminated with target energy if an error in target localisation was made. The steps required for coherent averaging and thresholding are listed below:

---

[4] A chirp waveform is used because stepped frequency coherent integration at long-range is not practical due to the low effective PRF of a stepped frequency waveform.

1. The target Doppler bandwidth is estimated from Equation 7.49;
2. The radar parameters are chosen according to Section 7.4.3 to localise the target energy in a single Doppler bin;
3. Coherent processing with motion compensation is performed. The coherent processing used is described in Appendix A;
4. The target Doppler bin is extracted from the range-Doppler image to give a coherently averaged HRRP;
5. The noise level in the averaged HRRP is estimated from non-target region of the range-Doppler image;
6. A statistical test is evaluated to determine whether the coherent processing has been successful. The statistical test used is described in Section 7.4.6;
7. CFAR thresholding is performed on the averaged HRRP. The CFAR thresholding used is described in Section 7.4.7.

The steps for both non-coherent and coherent averaging are shown in Figure 7.4.

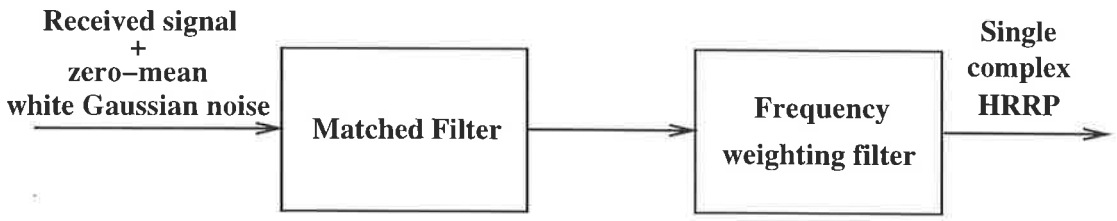

(a) The processing required to produce a single HRRP.

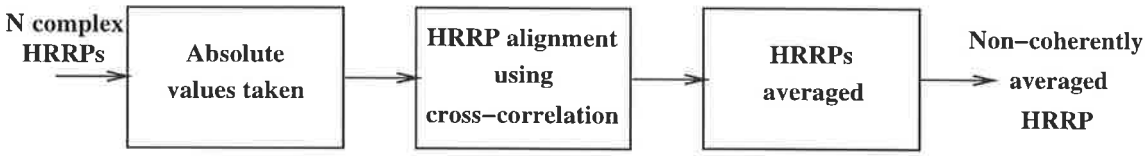

(b) The processing required to produce a non-coherently averaged HRRP from a sequence of complex HRRPs.

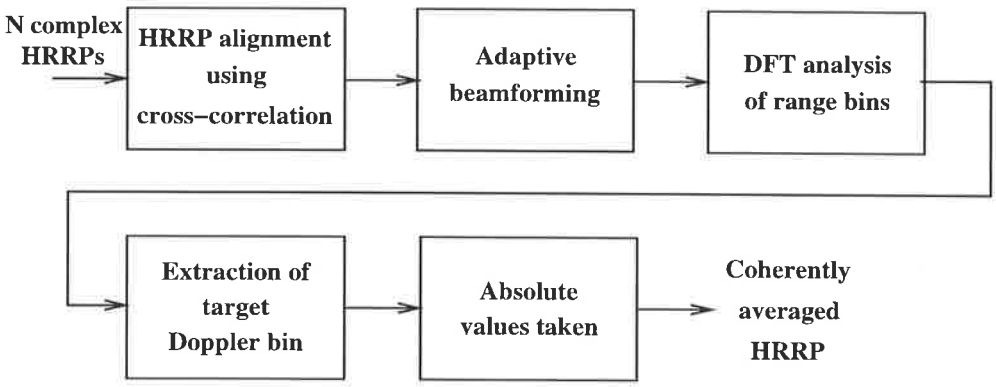

(c) The processing required to produce a coherently averaged HRRP from a sequence of complex HRRPs.

Figure 7.4: The processing required to produce averaged HRRPs using either coherent or non-coherent averaging.

7.4.3 The target Doppler bandwidth

It is reasonable to assume that a target would be under track before any attempt is made to collect information for target classification. The radar tracking system can be expected to provide range, velocity, range-rate and azimuth-rate information. From the tracking information it is possible to calculate the appropriate radar parameters for the coherent averaging of HRRPs. An important parameter that is calculated from the tracking information is the target Doppler bandwidth

$$\beta_D = \frac{2\omega w_c \bar{f}}{c} \tag{7.49}$$

where w_c is the maximum cross-range extent of the target, ω is the effective rotation rate of the target, c is the speed of propagation and $\bar{f}$ is the centre frequency of the radar waveform. Note that Doppler frequency is measured relative to the phase centre of the target which is determined by the adaptive beamforming process [46]. The rate at which the target moves through the field of view determines the minimum radar PRF required to unambiguously sample the target Doppler bandwidth.

$$\mathrm{PRF}_{\min} = \beta_D \tag{7.50}$$

The maximum possible radar PRF is determined by the range ambiguity constraint [33].

$$\mathrm{PRF}_{\max} = \frac{c}{2R} \tag{7.51}$$

where R is the range to the target.

The choice of the radar PRF and the number of pulses N to be integrated determines the Doppler frequency resolution

$$\Delta f_D = \frac{\mathrm{PRF}}{N} \tag{7.52}$$

The choice of the radar parameters (PRF and N) can be seen as a two stage decision process:

1. The choice of the integration time $T = \frac{1}{\Delta f_D}$;
2. The choice of the radar PRF and number of pulses N to satisfy Equation 7.52.

There is an upperbound on the integration time T because of operational constraints on the radar. These operational constraints, which also prevent ISAR imaging of the target, were discussed in Section 3.5.4. If there were no operational constraints on the radar, then the integration time T could be as long as desired. Even if ISAR imaging is not operationally possible, it is possible that T can be long enough such that

$$T > \frac{1}{\beta_D} \tag{7.53}$$

If this is the case, the target energy is spread over more than one Doppler bin in the range-Doppler image. This situation corresponds to a range-Doppler image with a poor cross-range resolution. The fact that the target energy is spread over more than one Doppler bin causes two problems:

1. Since the distribution of the target scatterers in cross-range is unknown, it is difficult to determine, from the range-Doppler image, whether the coherent processing has succeeded or not;

2. Since the distribution of the target scatterers in cross-range is unknown, it is difficult to specify an optimal procedure for combining the spread target Doppler returns into an averaged HRRP.

If there is no hope of resolving the individual target scatterers in cross-range and since there are disadvantages in spreading the target energy over more than one Doppler bin, the integration time is chosen so that the target energy is concentrated into a single Doppler bin

$$T \leq \frac{1}{\beta_D} \tag{7.54}$$

By concentrating the target energy in a single Doppler bin, it is easy to:

1. Determine whether the coherent processing has succeeded;

2. Extract a coherently averaged HRRP from the range-Doppler image.

The statistical test, to determine whether the coherent processing has succeeded, is presented in Section 7.4.6. The way in which an averaged HRRP is extracted from the range-Doppler image is presented in Section 7.4.4.

If T must be chosen according to Equation 7.54 then it is essential to have

$$\frac{1}{T} = \Delta f_D \approx \beta_D \tag{7.55}$$

The choice of T according to Equation 7.55 is optimal according to two criteria:

1. The choice of T is as large as possible while still satisfying Equation 7.54. The choice of T ensures that the maximum possible integration time is available to interrogate the target;

2. The choice of T means that the Doppler frequency resolution Δf_D is *matched* to the target Doppler bandwidth β_D. This matched condition means that the noise in the target Doppler bin is minimised and the SNR is maximised.

If T is chosen according to Equation 7.55 then the radar PRF and N must still be chosen according to Equation 7.52. For a fixed integration time T, both the radar PRF and number of pulses N must be chosen as large as possible to ensure that the maximum

amount of energy is received from the target. The signal processing gain from coherent averaging increases in proportion to the number of pulses N received from the target. Unfortunately there is an upper limit on the radar PRF that can be chosen. This upper limit on the radar PRF was given by Equation 7.51. Hence the radar PRF is chosen to be as large as possible while still satisfying Equation 7.51. The number of pulses N is calculated from Equation 7.52.

The result of successful range-Doppler processing is shown in Figure 7.5. Note that the noise energy is evenly spread over the range-Doppler image whereas the target energy is *localised* in Doppler. The localisation of target energy is used in two ways. Firstly, a coherently averaged HRRP is extracted from the target Doppler bin. The other Doppler bins do not contribute to the coherently averaged HRRP. Secondly, the noise power is estimated from the range-Doppler region which does not contain any target energy. The noise power estimate is used to CFAR threshold the coherently averaged HRRP. The steps required for choosing the coherent averaging parameters are illustrated in Figure 7.6 and are summarised below:

1. A conservative[5] estimate of the Doppler bandwidth across the target is calculated from Equation 7.49;

2. The minimum possible PRF is given by Equation 7.50 and the maximum possible PRF is given by Equation 7.51;

3. A PRF, which is as large as possible, is chosen to maximise the energy on the target for a given dwell time T;

4. The number of pulses N is calculated from Equation 7.52 with Δf_D chosen to satisfy Equation 7.55.

[5] The estimate of the target Doppler bandwidth is made to ensure that $(\beta_D)_{\text{estimate}} \geq (\beta_D)_{\text{actual}}$.

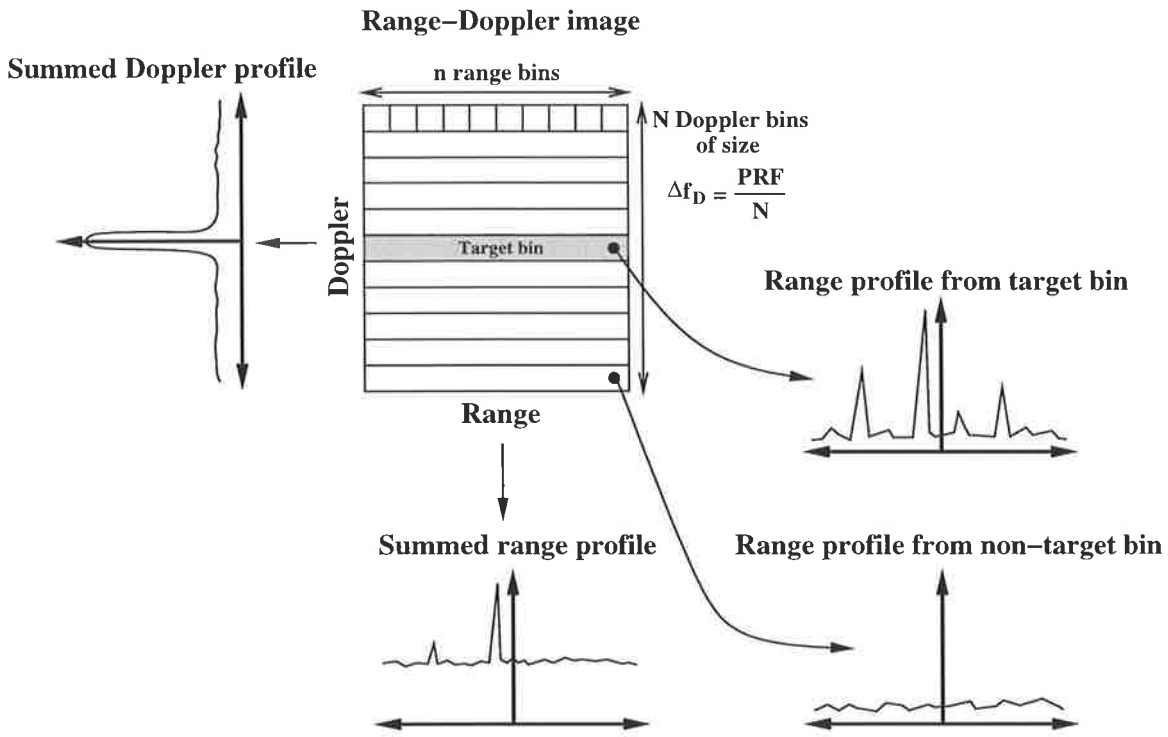

Figure 7.5: The result of Doppler processing on a sequence of range-aligned HRRPs. Since there is not enough aspect change to get a reasonable cross-range resolution, the target energy is localised in a single Doppler bin. The summed Doppler profile illustrates the way in which the target energy is localised in Doppler. The summed Doppler profile is formed by summing, over slant-range, the amplitudes in each Doppler bin. The summed range profile is formed by summing, over Doppler, the Doppler amplitudes in each range bin. Two range profile cross-sections of the range-Doppler image are shown. The range profile from the target Doppler bin has sharp peaks corresponding to target energy, whereas the range profile from the non-target Doppler bin contains only noise energy.

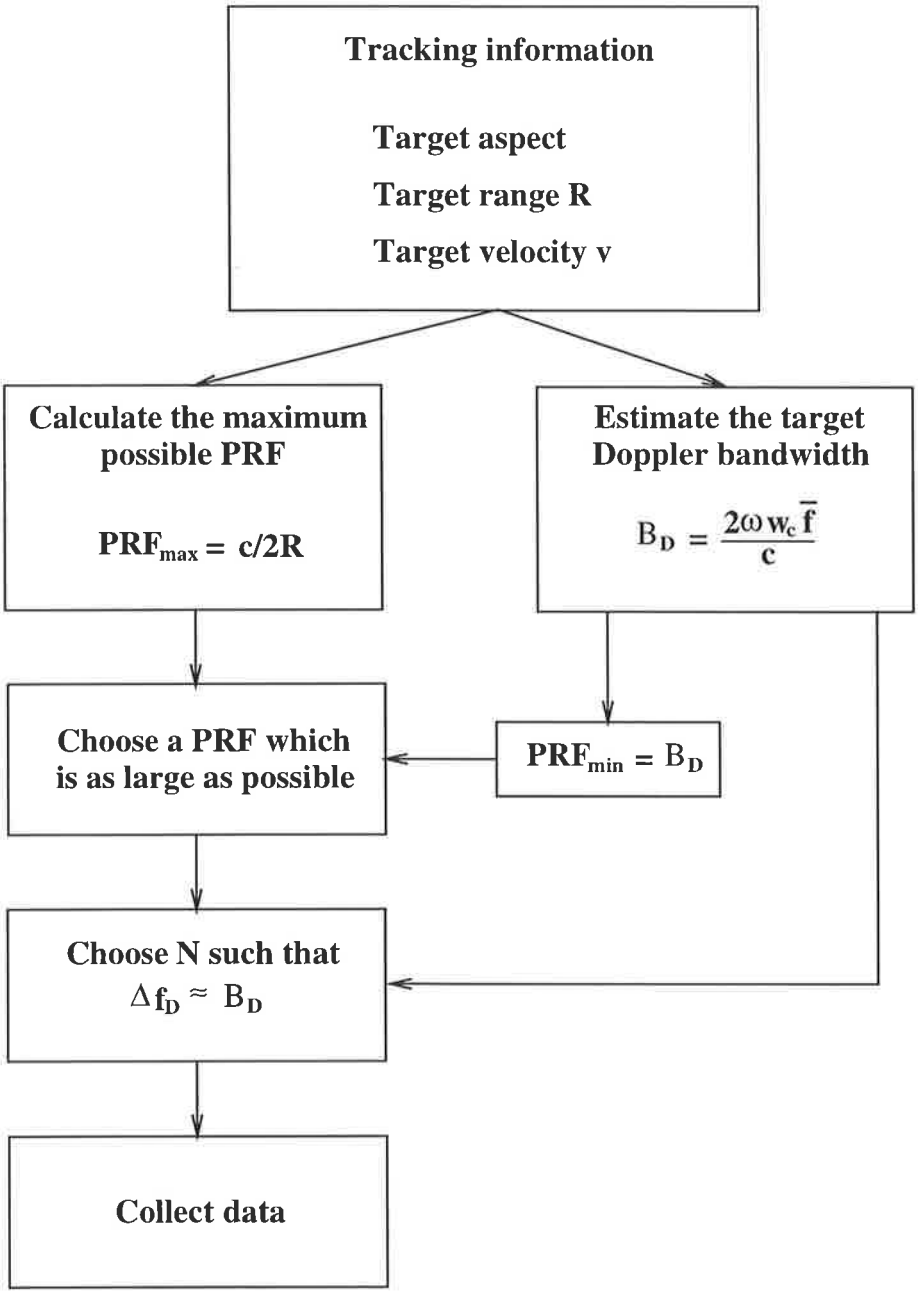

Figure 7.6: The steps required to choose the radar parameters for the coherent averaging of HRRPs.

7.4.4 *Extraction of the averaged HRRP*

Let the signal plus noise in each range bin m prior to Doppler processing be

$$z_m(t_i) = s_m(t_i) + n_i \tag{7.56}$$

where the signal $s_m(t_i)$ was defined in Equation 7.45 and the noise n_i was defined in Equation 7.4. The result of successful Doppler processing is shown in Figure 7.5 and the range-Doppler image can be represented as

$$\begin{bmatrix} v_{11}e^{j\nu_{11}} & \dots & v_{1m}e^{j\nu_{1m}} & \dots & v_{1n}e^{j\nu_{1n}} \\ \vdots & & \vdots & & \vdots \\ v_{l_01}e^{j\nu_{l_01}} & \dots & v_{l_0m}e^{j\nu_{l_0m}} & \dots & v_{l_0n}e^{j\nu_{l_0n}} \\ \vdots & & \vdots & & \vdots \\ v_{l1}e^{j\nu_{l1}} & \dots & v_{lm}e^{j\nu_{lm}} & \dots & v_{ln}e^{j\nu_{ln}} \\ \vdots & & \vdots & & \vdots \\ v_{N1}e^{j\nu_{N1}} & \dots & v_{Nm}e^{j\nu_{Nm}} & \dots & v_{Nn}e^{j\nu_{Nn}} \end{bmatrix} \begin{array}{l} \longrightarrow \text{range bin index} \\ \\ \\ \\ \\ \downarrow \text{Doppler bin index} \end{array} \tag{7.57}$$

where

$$\begin{bmatrix} v_{1m}e^{j\nu_{1m}} \\ \vdots \\ v_{lm}e^{j\nu_{lm}} \\ \vdots \\ v_{Nm}e^{j\nu_{Nm}} \end{bmatrix} = \text{DFT} \begin{bmatrix} z_m(t_1) \\ \vdots \\ z_m(t_l) \\ \vdots \\ z_m(t_N) \end{bmatrix} \qquad \forall\, m = 1 \dots n \tag{7.58}$$

DFT is the discrete Fourier transform operator, v_{lm} is a real number, ν_{lm} is a real number in the range $[0, 2\pi)$, $m = 1 \dots n$ is the range bin index, $l = 1 \dots N$ is the Doppler bin index and l_0 is the Doppler bin index corresponding to zero Doppler frequency. Since the radar parameters are chosen to give $\Delta f_D \approx \beta_D$, all of the target energy falls into a single Doppler bin located at zero Doppler frequency. Hence the coherently averaged HRRP is

$$[v_{l_01} \dots v_{l_0n}] \tag{7.59}$$

The PDF of the noise in a single range bin (containing no target energy) of the averaged HRRP is given by Equation 7.22. The PDF is Rayleigh and its mean and variance are given by Equations 7.23 and 7.24 respectively.

7.4.5 *Estimating the HRRP noise level from the range-Doppler image*

There are two reasons why it is necessary to estimate the noise variance in the range-Doppler image:

1. The estimate of the noise variance in the range-Doppler image is used to determine whether the coherent processing has been successful. The procedure used to test whether the coherent processing has been successful is described in Section 7.4.6.

2. The estimate of the noise variance in the range-Doppler image is used to calculate the noise variance in the coherently averaged HRRP. The noise variance in the averaged HRRP is then used to calculate a threshold level for the averaged HRRP. The procedure for thresholding the averaged HRRP is described in Section 7.4.7.

Let the noise variance in a single range bin, prior to Doppler processing, be σ_0^2. The noise variance after Doppler processing is $N\sigma_0^2$ where N is the number of HRRPs averaged. In practice σ_0^2 is unknown and it must be estimated from the range-Doppler image. If the noise level is estimated from the range-Doppler image of Figure 7.5 there is a danger that the estimate of the noise variance would be contaminated by the target sidelobe energy.

In the same way that range sidelobes occur due to the frequency envelope of the chirp waveform, Doppler sidelobes occur due to the time envelope of the coherent pulse train. On transmission, a pulse train envelope is rectangular so that the maximum amount of energy is transmitted. A rectangular envelope in the time domain causes Doppler sidelobes in the frequency domain. Doppler sidelobes are undesirable because their presence makes the estimation of the noise level in the range-Doppler image difficult and inaccurate. If the target Doppler sidelobes are reduced, then a reliable estimate of the noise level in the range-Doppler image can be made confidently. To reduce the Doppler sidelobes, a window must be applied to the received pulse train. The window is applied across the HRRP sequence before Doppler processing. Different Doppler windows spread the target energy to different extents. For example, if a particular window spreads the mainlobe target energy over 5 adjacent Doppler bins and if 11 consecutive HRRPS are coherently averaged, then there will be 5 Doppler bins containing target energy and 6 Doppler bins from which the noise statistics can be estimated. The range-Doppler image resulting from successful windowing and coherent processing is shown in Figure 7.7. Note how the range-Doppler image can be divided into distinct target and non-target regions.

Let the window that is used prior to Doppler processing be

$$\boldsymbol{w} = \begin{bmatrix} w_1 \\ \vdots \\ w_N \end{bmatrix} \tag{7.60}$$

where $w_1 \ldots w_N$ are real. The signal plus noise in range bin m becomes

$$z'_m(t_i) = (s_m(t_i) + n_i)w_i \tag{7.61}$$

The range-Doppler image is calculated, as before, by applying a DFT to each range bin.

$$\begin{bmatrix} v'_{1m}e^{j\nu'_{1m}} \\ \vdots \\ v'_{lm}e^{j\nu'_{lm}} \\ \vdots \\ v'_{Nm}e^{j\nu'_{Nm}} \end{bmatrix} = \text{DFT} \begin{bmatrix} z'_m(t_1) \\ \vdots \\ z'_m(t_l) \\ \vdots \\ z'_m(t_N) \end{bmatrix} \qquad \forall\, m = 1 \ldots n \tag{7.62}$$

The noise variance after windowing and Doppler processing is

$$\sigma_w^2 = N\left(\frac{\left(\sum_{i=1}^{N} w_i^2\right)\sigma_0^2}{N}\right) = \left(\sum_{i=1}^{N} w_i^2\right)\sigma_0^2 \tag{7.63}$$

The quantity σ_w^2 can be safely estimated from the non-target region[6] of the range-Doppler image shown in Figure 7.7. The variance of the noise in the coherently averaged HRRP is given by Equation 7.24 where σ_0^2 is calculated from Equation 7.63.

7.4.6 *Checking that the coherent processing worked*

The coherent processing used in this chapter is equivalent to ISAR processing. However, the coherent processing required for coherent averaging does not depend on any specific ISAR processing or motion compensation algorithm. A variety of algorithms can be used to produce a focussed range-Doppler image of the target. The coherent processing used in this chapter was developed by Haywood [44].

It is important to recognise that coherent processing is not always successful. The conditions under which coherent processing could fail were discussed in Section 3.5.3. Successful coherent processing means that the motion compensation and Doppler processing have been correctly performed and that the energy in each range bin has been correctly separated according to Doppler frequency. Successful coherent processing results in a focussed image which may have a good or a poor cross-range resolution. If the cross-range resolution is good then the image may be suitable for target classification. If the cross-range resolution is poor then the target energy must be recombined to produce an averaged HRRP.

It is important to *know* whether the coherent processing has been successful or not. If the coherent processing is unsuccessful then there is no point in proceeding with coherent

[6] The level at which the peak target Doppler sidelobes appear can be used as a guide for the selection of Doppler bins which "do not" contain target energy. The level of the target Doppler sidelobes also determines the minimum noise level that can be estimated with a target of a particular amplitude present.

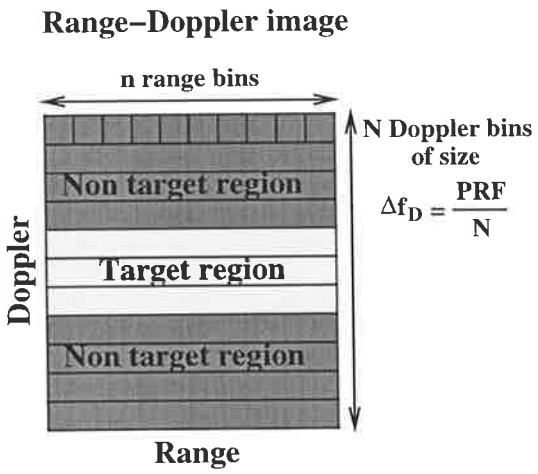

Figure 7.7: The way in which the target energy is localised in the range-Doppler image when a window is used prior to coherent processing. Note that with successful coherent processing there are distinct target and non-target regions of the range-Doppler image. The noise level is estimated from the non-target region where the target Doppler sidelobes have been reduced to an acceptable level.

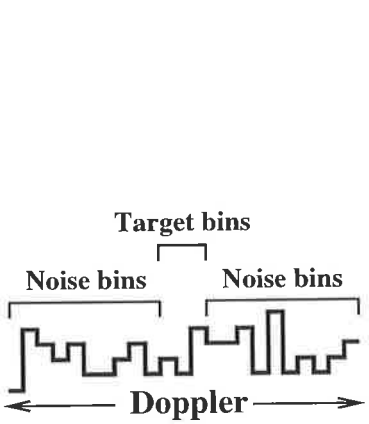

(a) The summed Doppler profile if the coherent processing has failed.

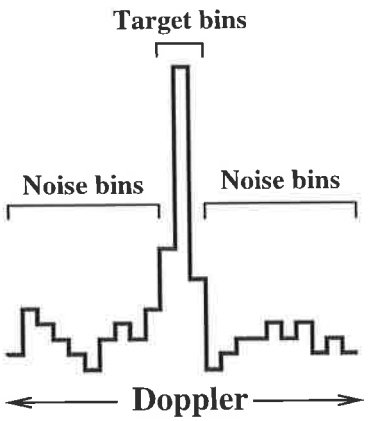

(b) The summed Doppler profile if the coherent processing has succeeded.

Figure 7.8: The possible results of coherent processing. If the coherent processing has succeeded, the summed Doppler profile is as shown in (b). If the coherent processing has failed, the Doppler energy is uniformly spread in Doppler as shown in (a).

averaging and non-coherent averaging must be used instead. If the coherent processing has been successful then the result is as depicted in Figure 7.5. One way of determining whether the coherent processing has been successful, is by examining the summed Doppler profile of the range-Doppler image. The summed Doppler profile is formed by summing the absolute values of each Doppler profile in the range-Doppler image. The summed Doppler profiles for both unsuccessful and successful coherent processing are shown in Figure 7.8. Another way to determine whether the coherent processing has been successful is to examine the statistics of the range-Doppler image. The statistics of the region in which target energy is expected can be compared to the statistics of the region where only noise energy is expected. To ensure that the estimate of the noise statistics is not contaminated by target sidelobe energy, a window must be used prior to Doppler processing. The use of a window ensures that the peak target sidelobes are kept below a desired level. The range-Doppler image obtained when a window is used prior to Doppler processing is shown in Figure 7.7.

To determine whether the coherent processing has been successful, a statistical test is performed on the range-Doppler image of Figure 7.7. Let the region where the target energy should be localised be denoted region 1. Region 1 is centred on zero Doppler. Let the rest of the range-Doppler image be denoted region 2. The sample means $\bar{x}_1$, $\bar{x}_2$ and variances s_1^2, s_2^2 are calculated for the target and non-target regions of the image. If the target energy is localised then the mean of the target region should be significantly higher, in a statistical sense, than the mean of the non-target region. The statistical null hypothesis for an appropriate test is

$$H_0 : \mu_1 = \mu_2 \tag{7.64}$$

This hypothesis says that the means of the two regions are equal and implies that the energy is evenly spread over the range-Doppler image. The alternative hypothesis is

$$H_a : \mu_1 > \mu_2 \tag{7.65}$$

This hypothesis says that the mean of region 1 is significantly higher than the mean of region 2 and this implies that the target energy is localised in Doppler.

The sampling distributions of $\bar{x}_1$ and $\bar{x}_2$ must be estimated to determine whether $\bar{x}_1$ and $\bar{x}_2$ are statistically different. The Central Limit Theorem [92] implies that the sampling distribution for $\bar{x}$, where $\bar{x} = \frac{1}{n}\sum_{i=1}^{n} x_i$ and x_i are taken from any population, is approximately Gaussian if the number of samples n is greater than 30. In the case of range-Doppler imaging, there are likely to be at least 30 range-Doppler bins in both the target and non-target regions of the range-Doppler image. Consequently, the sampling distributions of $\bar{x}_1$ and $\bar{x}_2$ can be assumed to be Gaussian because of the Central Limit Theorem. Hence the Gaussian test statistic

$$z = \frac{(\bar{x}_1 - \bar{x}_2)}{\sqrt{(s_1^2/n_1) + (s_2^2/n_2)}} \tag{7.66}$$

is used to statistically compare $\bar{x}_1$ and $\bar{x}_2$. n_1 and n_2 are the number of range-Doppler bins in regions 1 and 2 respectively.

Two types of errors are possible with the statistical test. The errors are normally referred to as Type I and Type II errors. A Type I error refers to rejecting the null hypothesis when it is actually true and a Type II error refers to accepting the null hypothesis when it is actually false. In the context of this application, a Type I error means that the test has indicated that the coherent processing has succeeded when in fact it has not. A Type I error is a severe error because it means that erroneous data are passed onto the next stage of processing. A Type II error means that the test has indicated that the coherent processing has failed when it fact it has succeeded. This error is not as severe as a Type I error because no data are passed onto the next stage of processing. A Type II error is most likely to occur when the SNR of the averaged HRRP is extremely low. If the SNR is extremely low, the quality of the HRRP is correspondingly low and hence it is not a major problem if the low quality HRRP is not passed onto the next stage of processing.

The probability of a Type I error is given by the *level of significance* α of the statistical test. The Type I error probability can be made as small as desired. The probability of a Type II error β depends on the SNR of the range-Doppler image and α. β is inversely proportional to the SNR. Since a Type II error is not a major concern for this particular application, α is chosen to keep Type I errors below a specified level. A summary of the hypothesis testing procedure is given below:

1. The null and alternative hypotheses are stated and the significance level α for the test is chosen;

2. The critical value z_c of the test statistic z is calculated from a desired α and a Gaussian distribution curve;

3. The sample means $\bar{x}_1$, $\bar{x}_2$ and variances s_1^2, s_2^2 for the target and non-target regions of the range-Doppler image are calculated;

4. The test statistic z is calculated from Equation 7.66;

5. If $z > z_c$ the null hypothesis is rejected in favour of the alternative hypothesis; otherwise the null hypothesis is accepted.

7.4.7 *CFAR processing for thresholding the averaged HRRP*

CFAR processing [36] is used in the detection of radar targets. The detected targets are passed to a tracking processor which initiates and maintains target tracks according to the incoming detections. The objective of CFAR processing is to provide a high target detection probability whilst maintaining a low *constant* false alarm rate. A low false alarm rate is desired so that the tracking processor does not become saturated with false detections. A constant false alarm rate is desired so that the data rate to the tracking processor is approximately constant. In this section CFAR processing is used to threshold the coherently averaged HRRP. It is desirable to minimise the amount of noise passed onto the next stage of processing but still detect as many target scatterers as possible.

The basic principle of CFAR processing is to obtain an estimate of the noise present and then use this noise estimate to set the target detection threshold. The main difficulty of CFAR is obtaining a true estimate of the noise in the bin in which detection (thresholding) is taking place. Normally the noise estimate is made from adjacent bins in range, Doppler, azimuth angle, or some other combination of radar coordinates.

For the CFAR algorithm described in this section, the noise in each range bin (prior to Doppler processing) is assumed to be additive, zero-mean, white, Gaussian noise with variance σ_0^2. If there is clutter or a jamming signal present, the type of noise and its distribution over the range-Doppler image will be affected. In this case an alternate CFAR algorithm, which is beyond the scope of this thesis, will have to be used. It was shown in Section 7.4.5 that the noise PDF in the averaged HRRP is Rayleigh with a PDF, mean and variance given by Equations 7.22, 7.23 and 7.24 respectively. Section 7.4.5 described how to estimate the noise PDF parameters in the averaged HRRP.

By setting a low false alarm rate, the number of spurious peaks in the averaged and thresholded HRRP are minimised. If one spurious peak is tolerated in every p averaged HRRPs, then the desired false alarm rate is given by

$$P_{\text{fa}} = \frac{1}{pn} \tag{7.67}$$

where n is the number of range bins in the averaged HRRP. For the noise probability distribution given in Equation 7.22 the required threshold $\mathcal{X}_t$ is given by

$$P_{\text{fa}} = \int_{\mathcal{X}_t}^{\infty} p(v^c)\mathrm{d}v^c \tag{7.68}$$

The steps for CFAR processing of the averaged HRRP are summarised below:

1. The desired false alarm rate is chosen in terms of the rate at which noise peaks, exceeding the threshold level $\mathcal{X}_t$, can be tolerated in the averaged HRRPs;

2. The required false alarm rate is calculated from Equation 7.67;

3. The parameters for the Rayleigh noise distribution in the averaged HRRP are estimated according to Section 7.4.5;

4. The required threshold $\mathcal{X}_t$ is calculated from Equation 7.68 and the range bins in the averaged HRRP are thresholded.

7.5 An example

7.5.1 The scenario

The data with which the HRRP averaging algorithms were exercised were generated with ISARLAB [58]. ISARLAB is a simulation tool that is used for the generation of high resolution radar data. ISARLAB was described in Chapter 5. Real data corresponding to the operational situation described in Section 7.4.1 were unavailable and the sampling rate of the real data presented in earlier chapters was not fast enough relative to the target rotation rate for the application of coherent averaging.

In the series of simulations which are presented in this chapter, the target consisted of 5 collinear point scatterers, equally spaced at 20 m intervals. The point scatterers which defined the target model had relative amplitude levels of 0 dB, -15 dB, -20 dB, -25 dB and -10 dB. The target model is illustrated in Figure 7.9. A simple target model, rather than a complete aircraft model, was used so that the performance differences between coherent averaging and non-coherent averaging were highlighted.

The same target classification scenario was used for a series of five simulations. The target classification scenario consisted of a radar stationary at the origin and a target moving towards the radar at an azimuth bearing of 20° from the radar line of sight (RLOS). The target was at a range of 150 km and it was moving with a speed of 1000 kmhr^{-1}. The target classification scenario is depicted in Figure 7.10. To achieve an appropriate cross-range resolution, say 2 m, in this scenario, an imaging time of approximately 13 s is required. This length of time is unacceptably long in an operational context and hence an averaged HRRP was necessary for target classification.

Radar data were simulated for five combinations of radar PRF and N the number of HRRPs averaged. The radar parameters which were common to each simulation are detailed in Table 7.2. The radar parameters which varied between each of the five HRRP averaging simulations are detailed in Table 7.3. The radar waveform was a coherent pulse train consisting of N chirp pulses of length 50 μs and bandwidth 75 MHz. The centre frequency of the radar waveform was 9 GHz. The returned pulses were sampled at a rate of 150 MHz and the noise present on the raw received data (I and Q channels) was zero-mean white Gaussian noise. The simulated data were generated so that the SNR in the range bin containing the largest scatterer was 20 dB at the output of the chirp matched filter. The SNRs in the range bins containing the other scatterers were 5 dB, 0 dB, -5 dB and 10 dB respectively.

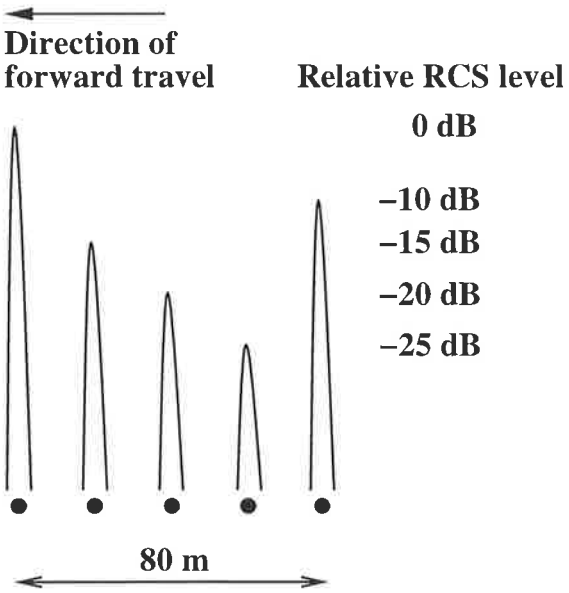

Figure 7.9: The simple target model that was used for exercising both the coherent averaging and non-coherent averaging algorithms. The target model consisted of 5 collinear point scatterers equally spaced at 20 m intervals. The target "forward" direction is indicated. The "height" of each scatterer represents its relative amplitude level.

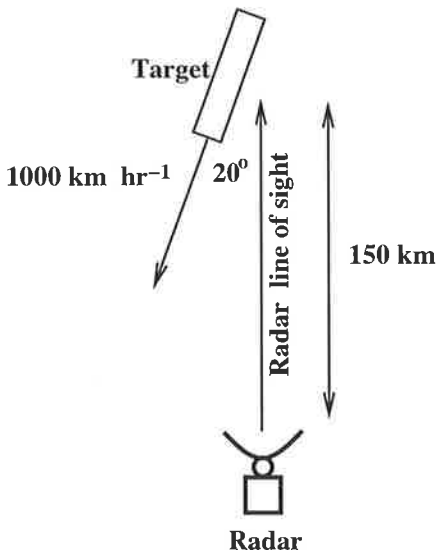

Figure 7.10: The target classification scenario that was used in the series of five HRRP averaging simulations. ISAR imaging, within a reasonable time, is not possible for this scenario.

Radar parameter	Value
Centre frequency	9 GHz
Waveform type	Linear FM
Bandwidth	75 MHz
Pulse width	50 μs
Sampling rate	150 MHz
Samples per pulse	8192
Range window	256 range bins

Table 7.2: The common radar parameters that were used for the series of five HRRP averaging simulations. The radar PRF and the number of HRRPs averaged were varied in the five simulations according to Table 7.3.

Simulation number	Radar parameters			
	PRF (Hz)	Number of HRRPs N	Δf_D (Hz)	Integration time T (seconds)
1	100	32	3.125	0.32
2	200	64	3.125	0.32
3	400	128	3.125	0.32
4	100	64	1.573	0.64
5	400	64	6.25	0.16

Table 7.3: The radar parameters which were varied for the series of five HRRP averaging simulations. The radar parameters which were common to each simulation are listed in Table 7.2.

7.5.2 Calculations for the simulation

The radar parameters

From the scenario information given in Section 7.5.1, the target Doppler bandwidth β_D was estimated using Equation 7.49

$$\omega = \frac{v_T}{R} = \frac{\sin 20 \times 1000 \times 10^3}{3600 \times 150 \times 10^3} = 6.33 \times 10^{-4} \text{ rad s}^{-1}$$

$$\beta_D = \frac{2\omega w_c \bar{f}}{c} = \frac{2 \times 6.33 \times 10^{-4} \times 80 \times 9 \times 10^9}{3 \times 10^8} = 3.0 \text{ Hz}$$

where a cross-range ambiguity window of $w_c = 80$ m was used. The minimum possible radar PRF that could be used was $\text{PRF}_{\text{min}} = 3.0$ Hz and the maximum PRF that could be used was $\text{PRF}_{\text{max}} = \frac{c}{2R} = \frac{3\times10^8}{2\times150\times10^3} = 1000$ Hz.

Radar data were simulated for the five combinations of radar parameters which are listed in Table 7.3. The first three simulations were designed with $\Delta f_D = 3.125 \text{ Hz} \approx \beta_D$ which conservatively ensured that all of the target energy fell into a single Doppler bin. The reasons for choosing $\Delta f_D \approx \beta_D$ were discussed in Section 7.4.3. The remaining two simulations were designed to show what happens when $\Delta f_D < \beta_D$ ($\Delta f_D = 1.573$ Hz) and $\Delta f_D > \beta_D$ ($\Delta f_D = 6.25$ Hz) respectively.

Chirp processing

The intrinsic resolution capability of a chirp is determined by its bandwidth. In this series of simulations, the chirp bandwidth was 75 MHz and this bandwidth corresponds to a range resolution of 2 m. The received chirp was oversampled at a rate of 150 MHz, which means that each range bin has a width of 1 m. The received pulse length was approximately 50 μs which corresponds to 7500 samples at a sampling rate of 150 MHz.

It is essential that the entire received chirp is sampled and convolved[7] with the transmitted chirp. When the transmitted and received chirps are convolved, the result is approximately 15000 samples long. 15000 samples corresponds to a range extent of approximately 15 km! To make the subsequent coherent processing computationally affordable, the target return was *range-gated*. Range-gating is the extraction of the immediate region surrounding the target in the 15 km range extent. A coarse target location is initially obtained from the track information and a target "window" is formed by locating the maximum target response and forming a window around it. The range window must be larger than the expected target length which means that a large conservative range window is usually chosen. In this series of simulations, a range window of length 256 m (256 samples) was used for the 80 m target.

[7] For an efficient FFT based convolution, the number of received chirp samples is made a power of two. In this series of simulations, 8192 samples of the received chirp were used.

Range sidelobe reduction

Amplitude weighting was used on the spectrum of the dechirping matched filter to reduce the range sidelobes caused by transmitting a chirp with a rectangular window. The weighting function used was a Blackman window [39]. The Blackman window reduced the range sidelobes to approximately 58 dB below the peak target response and the range resolution was degraded to approximately 3.4 m. There were two penalties incurred in achieving this sidelobe reduction. Firstly, the mainlobe response was broadened (loss of resolution), and secondly a small reduction in SNR (processing loss) occured due to the mismatched filter. The worst case processing loss for the Blackman weighting used is 3.47 dB [39].

Range-Doppler image noise estimation

To reliably estimate the noise level in the range-Doppler image a window was used prior to Doppler processing. A Blackman window [39] was used to reduce the Doppler sidelobes. The Blackman window reduced the Doppler sidelobes to 58 dB and it spread the target energy over 7 Doppler bins[8] in the range-Doppler image.

The statistical parameters

The only parameter that needed to be chosen for the statistical test was the level of significance α. Since it is important that erroneous data are not passed to the next processing stage, a high level of significance was chosen. In the series of simulations presented in this chapter, $\alpha = 0.001$ was used and this gave a critical value of $z_c = 3.09$. The test statistic z was calculated from Equation 7.66 and it was compared to this critical value.

The CFAR parameters

In the series of simulations presented in this chapter, the desired false alarm rate was chosen to be one spurious peak per 10 averaged HRRPs. The number of range bins in an averaged HRRP is $n = 256$. Hence the required false alarm probability is

$$P_{\text{fa}} = \frac{1}{10 \times 256} = 3.9 \times 10^{-4}$$

The parameters of the noise distribution in the range-Doppler image were estimated from the range-Doppler image according to Section 7.4.5. The 7 Doppler bins centred on zero Doppler frequency (the target region) were excluded when the noise estimate was made.

[8] At three Doppler bins from the central target Doppler bin, the target energy is reduced to 60 dB below the peak target mainlobe response.

7.5.3 *Comparing the results of coherent and non-coherent averaging*

The following method, which is illustrated in Figure 7.11, was used to compare the averaged HRRPs produced from both coherent and non-coherent averaging:

1. Both the coherently averaged HRRP and the non-coherently averaged HRRP were thresholded with the same false alarm rate. The coherently averaged HRRP was thresholded according to Section 7.4.7.

   The noise distribution in the non-coherently averaged HRRP was Gaussian. The PDF of the noise distribution is given by Equation 7.21 and the mean and variance of the PDF are given by Equations 7.19 and 7.20 respectively. The mean and variance of the noise were estimated from the non-coherently averaged HRRP using a priori knowledge[9] of the target's position in range.

2. The threshold level was subtracted from each averaged and thresholded HRRP. The amplitude of the target scatterers from coherent and non-coherent averaging could now be directly compared. The integration loss for a scatterer in range bin m is

   $$L_i = 20 \log_{10} \left(\frac{A_m^{\mathrm{c}}}{A_m^{\mathrm{nc}}} \right)$$

   where A_m^{c} is the amplitude of the scatterer in the coherently averaged HRRP and A_m^{nc} is the amplitude of the scatterer in the non-coherently averaged HRRP.

[9] The noise level was estimated from the range bins in the averaged HRRP, which were known a priori not to contain any target energy.

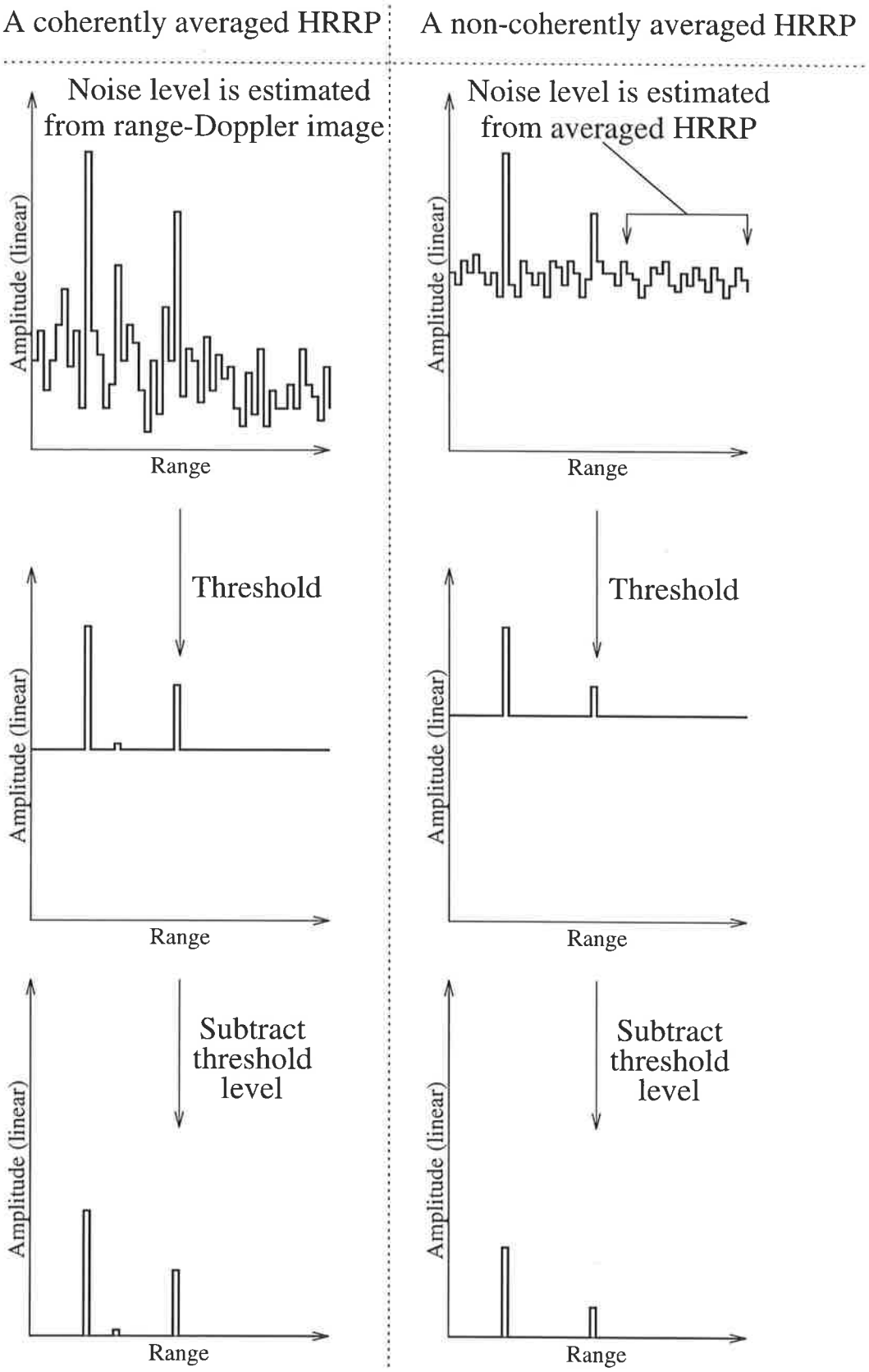

Figure 7.11: The comparison of a coherently averaged HRRP with a non-coherently averaged HRRP. Note that for the coherently averaged HRRP, the noise level was estimated from the range-Doppler image. For the non-coherently averaged HRRP, the noise level was estimated from the averaged HRRP using a priori target location information.

7.5.4 *Results and discussion*

The results from the five HRRP averaging simulations are shown in Figures 7.12 to 7.21. Figure 7.12 shows the results of the radar simulation when the radar PRF was 100 Hz and the number of averaged HRRPs was 32. Figure 7.12(a) shows the envelope of a single chirp pulse received by the radar. Figure 7.12(b) shows the HRRP which would be obtained if there was no noise on the received chirp. A HRRP which was obtained by processing a single received chirp pulse, with an SNR in the range bin containing the largest target scatterer of 20 dB, is shown in Figure 7.12(c). Thresholding the HRRP shown in Figure 7.12(c) with a reasonable false alarm rate would only detect two of the five target scatterers.

The summed Doppler profile of 32 consecutive HRRPs which have been coherently processed is shown in Figure 7.12(d). Note how the target energy has been localised in Doppler. Figure 7.13 shows the results of both non-coherently and coherently averaging 32 consecutive HRRPs. Figure 7.13(a) shows the averaged HRRP resulting from non-coherent averaging and Figure 7.13(c) shows the averaged HRRP resulting from coherent averaging. Both averaged HRRPs have been normalised with respect to the amplitude of the largest target scatterer. Figures 7.13(b) and 7.13(d) show the averaged HRRPs which have been thresholded according to Sections 7.4.7 and 7.5.3. Both averaged HRRPs have been thresholded with a false alarm rate of one spurious peak in every 10 averaged HRRPs. For each plot, the calculated scatterer relative amplitudes are shown. The scatterer amplitudes are measured relative to the amplitude of the largest target scatterer. The correct relative amplitudes are 0, -15, -20, -25, -10 (dB). Figure 7.13(b) shows the non-coherent integration losses for each scatterer in the non-coherently averaged HRRP.

It can be seen by comparing Figures 7.13(b) and 7.13(d) that coherent averaging outperforms non-coherent averaging in terms of target scatterer detectability. Coherent averaging provides a higher scatterer amplitude relative to the HRRP threshold level. The non-coherent integration loss is a measure of how much coherent averaging outperforms non-coherent averaging in terms of target scatterer detectability. Note that the performance gap (integration loss) becomes greater as the SNR becomes smaller. Section 7.2 foreshadowed that coherent integration would markedly outperform non-coherent integration as the SNR dropped below 20 dB. For a large SNR of 20 dB (leftmost scatterer), coherent averaging outperforms non-coherent averaging by 1 dB. For a SNR of 15 dB (rightmost scatterer) the integration loss increases to 2 dB. The performance gap between coherent and non-coherent averaging is largest for the smallest two detected scatterers which have SNR's of 5 dB and 0 dB. In these two cases the integration losses are 6.9 dB and 14.6 dB respectively. Coherent averaging provides a better estimate of the scatterer relative amplitudes than non-coherent averaging. Once again the difference between coherent and non-coherent averaging becomes larger as the SNR becomes smaller.

Figures 7.15 and 7.17 show the results for non-coherent and coherent averaging when 64 (simulation 2) and 128 HRRPs (simulation 3) are averaged. The integration losses and scatterer relative amplitudes for non-coherent averaging are similar to the results seen in Figure 7.13 (simulation 1). The increase in averaging gain between simulations 1 and 2 should be approximately 3 dB (a factor of 2)[10] and the increase in averaging gain between simulations 2 and 3 should also be approximately 3 dB. This increase in averaging gain can be seen in the summed Doppler profiles for each simulation and the absolute scatterer amplitudes seen in each averaged HRRP. A comparison of Figures 7.12(d), 7.14(d) and 7.16(d) reveals that the increase in averaging gain between these simulations is indeed 3 dB as expected.

In simulations 1, 2 and 3 non-coherent averaging has failed to detect the fifth and smallest target scatterer. Coherent averaging has failed to detect the fifth target scatterer in simulation 1 but has succeeded in detecting the fifth target scatterer in simulations 2 and 3. In all three simulations, coherent averaging has made a better estimate of the scatterer relative amplitudes than non-coherent averaging. Coherent averaging has provided better estimates of the scatterer relative amplitudes as the number of HRRPs averaged has been increased.

Simulations 4 and 5 were intended to show the performance degradation in coherent averaging when Δf_D was chosen such that it was not matched to β_D. The results for both non-coherent and coherent averaging of 64 HRRPs at a radar PRF of 100 Hz (simulation 4) are shown in Figure 7.19. The results shown in this figure should be compared to the results shown in Figure 7.15. The Doppler frequency resolution in simulation 4 is 1.563 Hz. This Doppler frequency resolution implies that the target energy is spread over more than one Doppler bin. The difficulty of combining target Doppler energy spread over more than one Doppler bin was mentioned in Section 7.4.3. The point was made that since the distribution of the target Doppler energy is unknown, an optimal weighting scheme for recombining the target Doppler energy cannot be established. Hence Section 7.4.3 recommended that the target Doppler energy be localised in a single Doppler bin.

In simulation 4 the coherently averaged HRRP was extracted from a single Doppler bin. Unfortunately this Doppler bin did not contain all of the target energy since $\beta_D \approx 2\Delta f_D$. Hence the performance of coherent averaging shown in Figure 7.19(d) should be worse than that shown in Figure 7.15(d). A comparison of these two figures shows that this is indeed the case because the fifth target scatterer has not been detected in Figure 7.19(d) (simulation 4) whereas it has been detected in Figure 7.15(d) (simulation 2). The scatterer relative amplitudes for coherent averaging are also worse for simulation 4 when compared to simulation 2.

---

[10] Since twice as many HRRPs are averaged.

Simulation number 5 was designed with a Doppler frequency resolution of 6.25 Hz. This choice of Δf_D implies that the target Doppler energy falls into a single Doppler bin and hence the coherently averaged HRRP of Figure 7.21(d) (simulation 5) contains the same amount of target energy as Figure 7.15(d) (simulation 2). Simulation 5 differs from simulation 2 in the amount of noise which is present in the coherently averaged HRRP.

In simulation 5 the target energy in a single Doppler bin has to compete with noise from a Doppler bin of width 6.25 Hz. In simulation 2 the target energy in a single Doppler bin has only to compete with noise from a Doppler bin of width 3.125 Hz. Consequently the coherently averaged HRRP of simulation 2 should provide a better target scatterer detectability than the coherently averaged HRRP of simulation 5. The improved target scatterer detectability of simulation 2 can be seen by comparing Figure 7.15(d) and Figure 7.21(d). In Figure 7.15(d) the fifth target scatterer has been detected whereas in Figure 7.21(d) the fifth target scatterer has not been detected. The scatterer relative amplitudes are similar for simulation 2 and simulation 5.

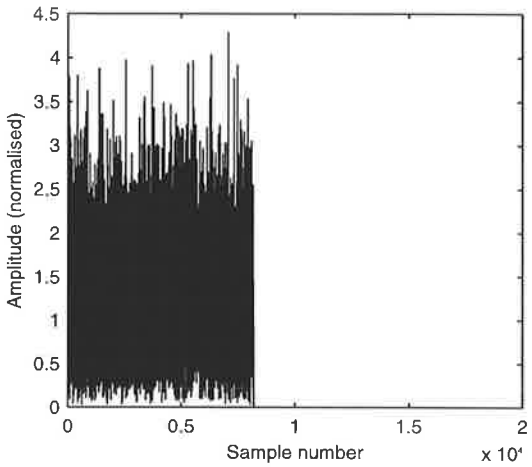

(a) The envelope of the chirp received by the radar.

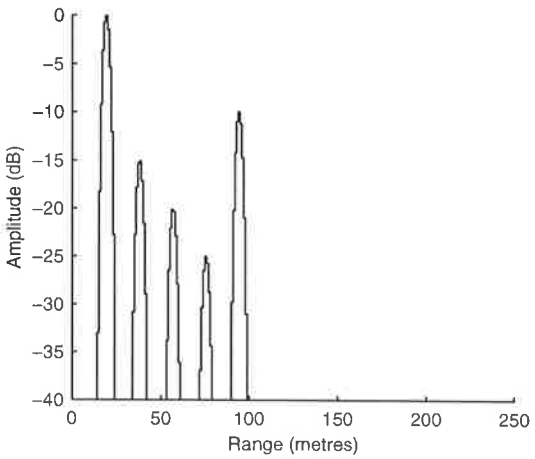

(b) The HRRP obtained when there was no noise on the received signal.

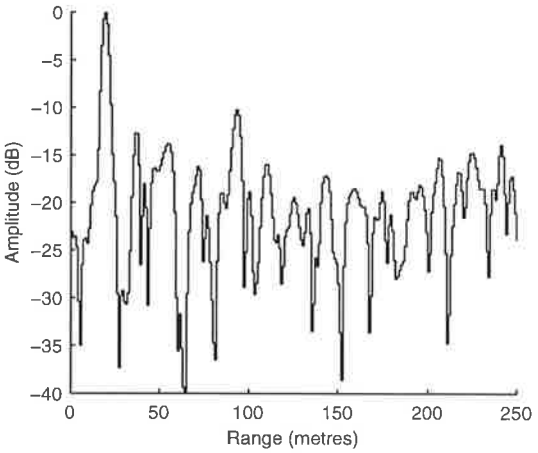

(c) A single HRRP after matched filter processing. The SNR in the range bin containing the largest target scatterer is approximately 20 dB.

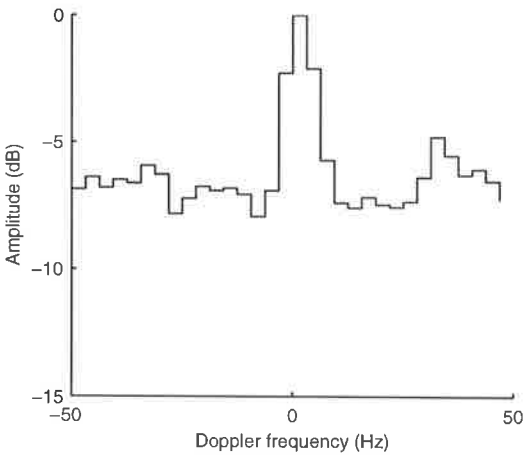

(d) The Doppler profile of 32 consecutive HRRPs. Note that the target energy is spread over 5 of the 32 Doppler bins since a window was used prior to Doppler processing.

Figure 7.12: The results of the radar simulation for a radar PRF of 100 Hz and the averaging of 32 HRRPs.

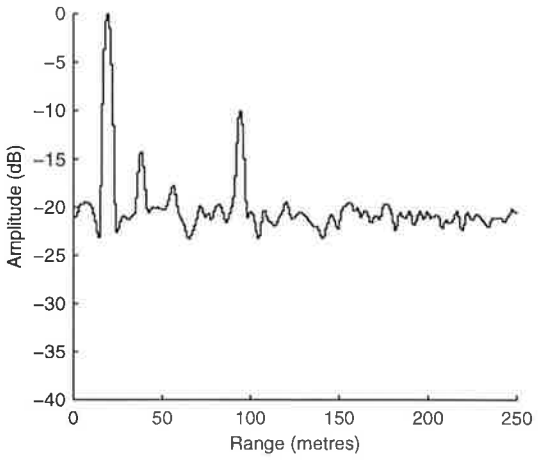

(a) A non-coherent average of 32 consecutive HRRPs.

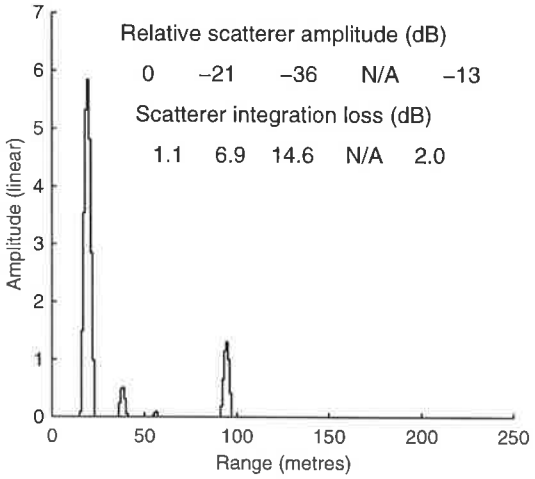

(b) A non-coherent average of 32 consecutive HRRPs which has been thresholded using CFAR processing with a false alarm rate of one spurious peak per 10 averaged HRRPs. The integration loss for each scatterer is shown. The correct relative amplitude levels are 0, -15, -20, -25, -10 (dB).

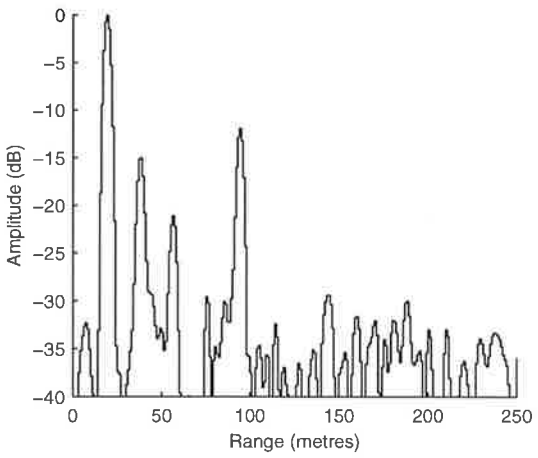

(c) A coherent average of 32 consecutive HRRPs.

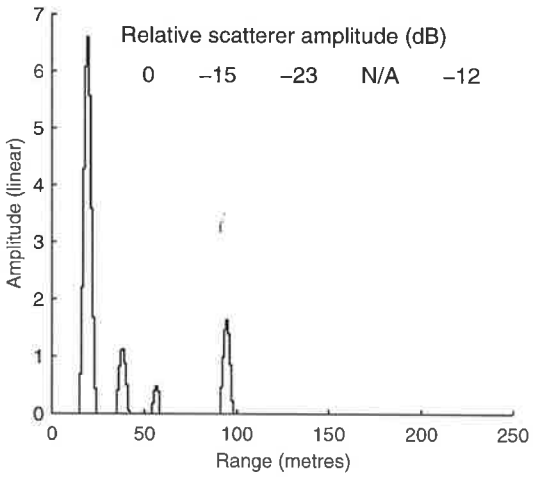

(d) A coherent average of 32 consecutive HRRPs which has been thresholded using CFAR processing with a false alarm rate of one spurious peak per 10 averaged HRRPs. The correct relative amplitude levels
are 0, -15, -20, -25, -10 (dB).

Figure 7.13: The results of both non-coherent and coherent averaging for a radar PRF of 100 Hz and the averaging of 32 HRRPs.

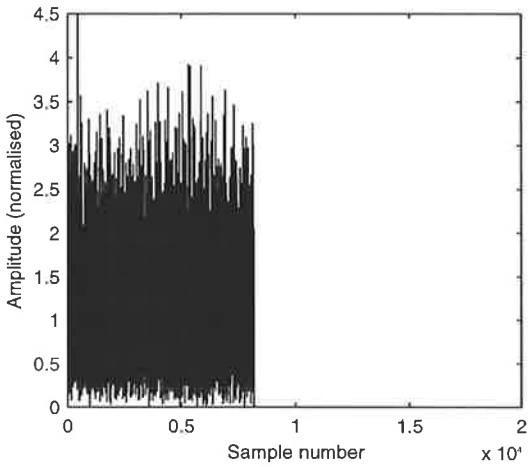

(a) The envelope of the chirp received by the radar.

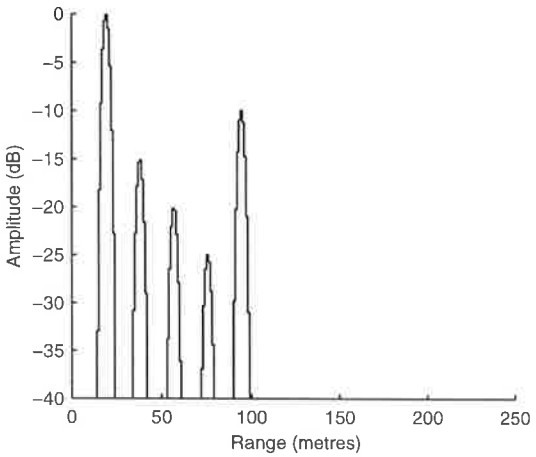

(b) The HRRP obtained when there was no noise on the received signal.

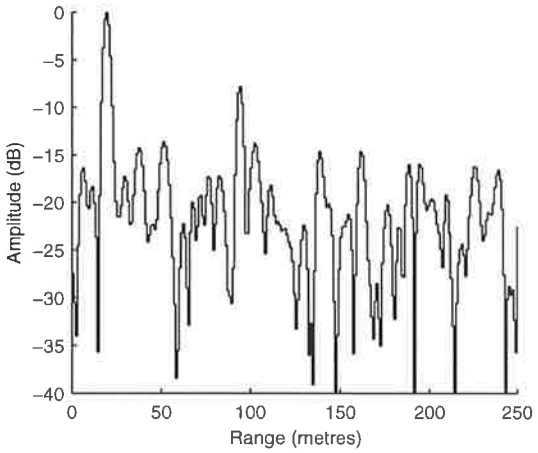

(c) A single HRRP after matched filter processing. The SNR in the range bin containing the largest target scatterer is approximately 20 dB.

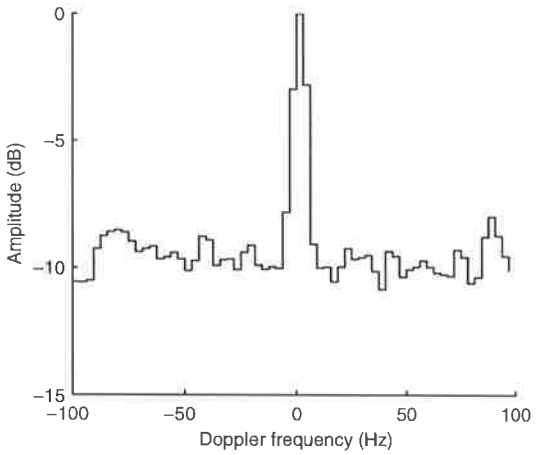

(d) The Doppler profile of 64 consecutive HRRPs. Note that the target energy is spread over 5 of the 64 Doppler bins since a window was used prior to Doppler processing.

Figure 7.14: The results of the radar simulation for a radar PRF of 200 Hz and the averaging of 64 HRRPs.

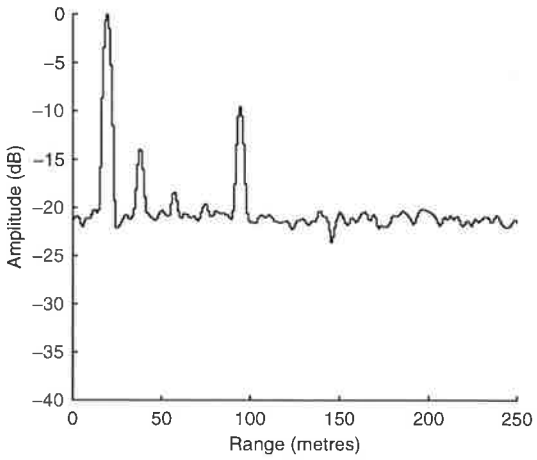

(a) A non-coherent average of 64 consecutive HRRPs.

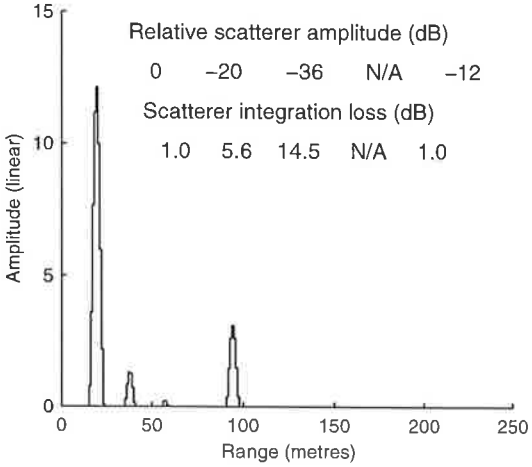

(b) A non-coherent average of 64 consecutive HRRPs which has been thresholded using CFAR processing with a false alarm rate of one spurious peak per 10 averaged HRRPs. The integration loss for each scatterer is shown. The correct relative amplitude levels are 0, -15, -20, -25, -10 (dB).

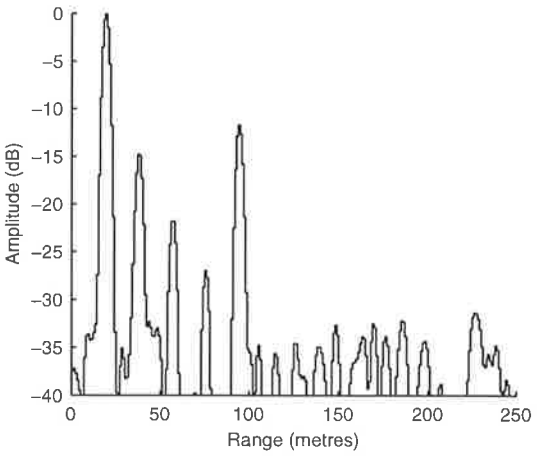

(c) A coherent average of 64 consecutive HRRPs.

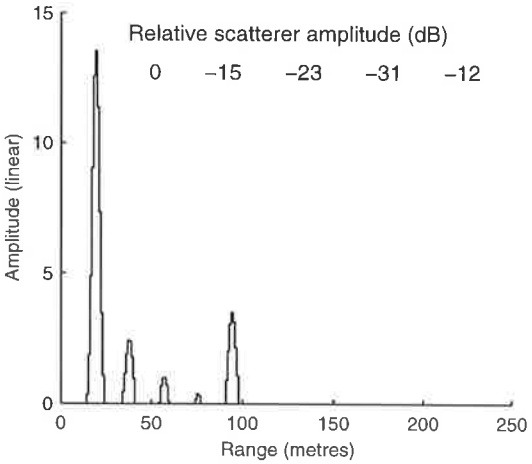

(d) A coherent average of 64 consecutive HRRPs which has been thresholded using CFAR processing with a false alarm rate of one spurious peak per 10 averaged HRRPs. The correct relative amplitude levels
are 0, -15, -20, -25, -10 (dB).

Figure 7.15: The results of both non-coherent and coherent averaging for a radar PRF of 200 Hz and the averaging of 64 HRRPs.

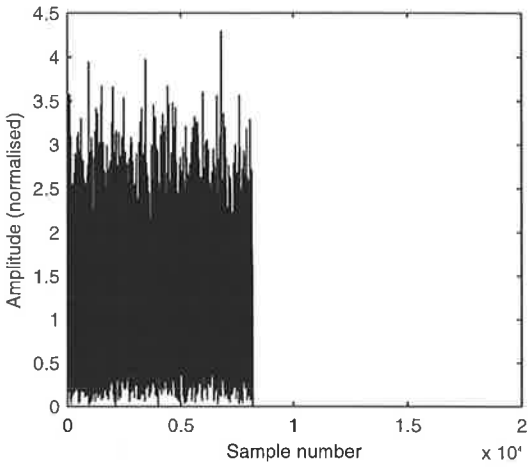

(a) The envelope of the chirp received by the radar.

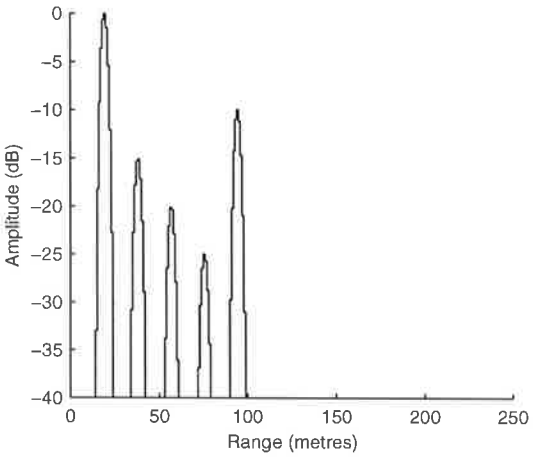

(b) The HRRP obtained when there was no noise on the received signal.

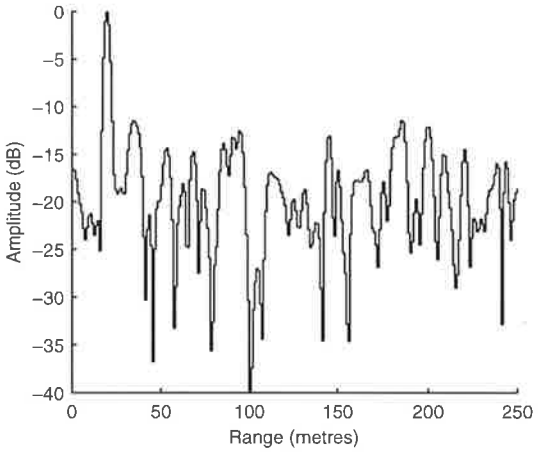

(c) A single HRRP after matched filter processing. The SNR in the range bin containing the largest target scatterer is approximately 20 dB.

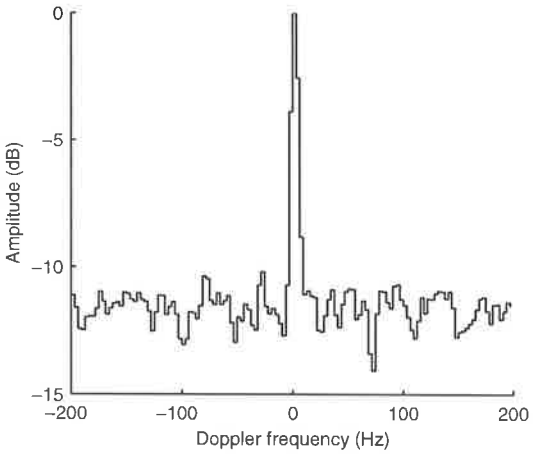

(d) The Doppler profile of 128 consecutive HRRPs. Note that the target energy is spread over 5 of the 128 Doppler bins since a window was used prior to Doppler processing.

Figure 7.16: The results of the radar simulation for a radar PRF of 400 Hz and the averaging of 128 HRRPs.

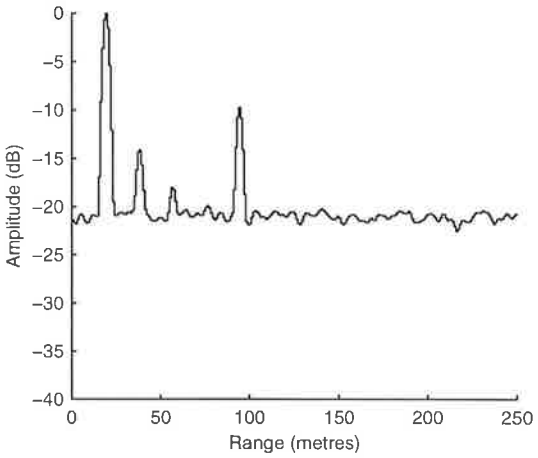

(a) A non-coherent average of 128 consecutive HRRPs.

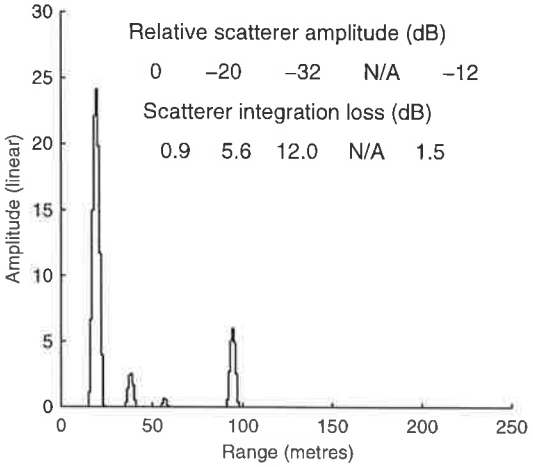

(b) A non-coherent average of 128 consecutive HRRPs which has been thresholded using CFAR processing with a false alarm rate of one spurious peak per 10 averaged HRRPs. The integration loss for each scatterer is shown. The correct relative amplitude levels are 0, -15, -20, -25, -10 (dB).

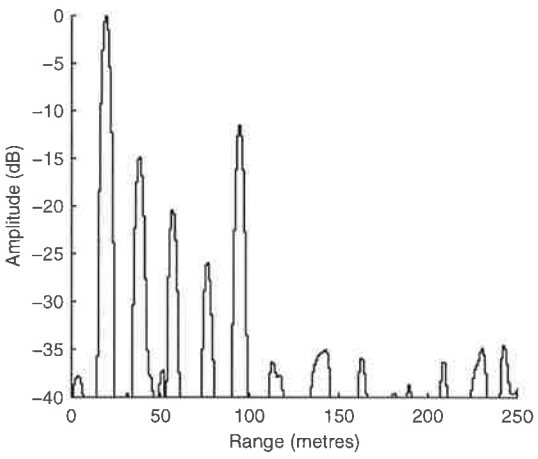

(c) A coherent average of 128 consecutive HRRPs.

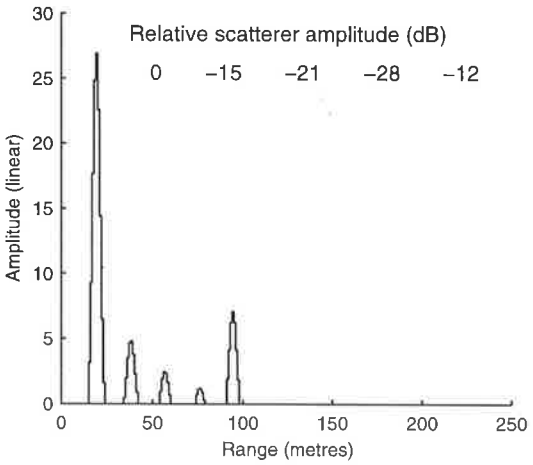

(d) A coherent average of 128 consecutive HRRPs which has been thresholded using CFAR processing with a false alarm rate of one spurious peak per 10 averaged HRRPs. The correct relative amplitude levels
are 0, -15, -20, -25, -10 (dB).

Figure 7.17: The results of both non-coherent and coherent averaging for a radar PRF of 400 Hz and the averaging of 128 HRRPs.

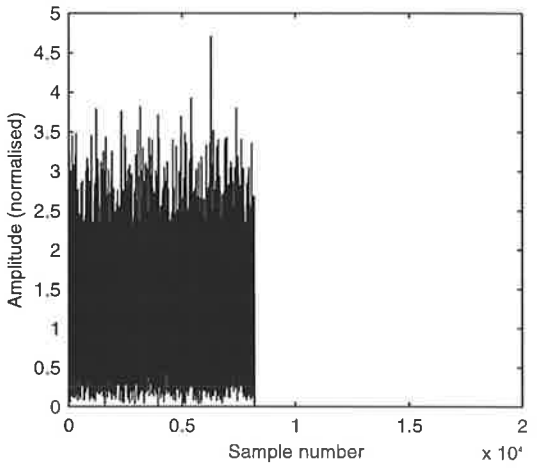

(a) The envelope of the chirp received by the radar.

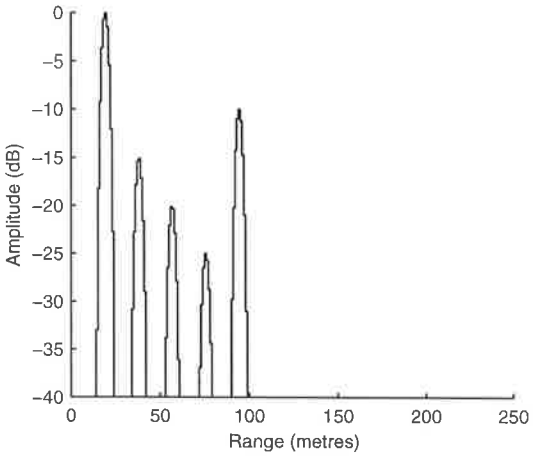

(b) The HRRP obtained when there was no noise on the received signal.

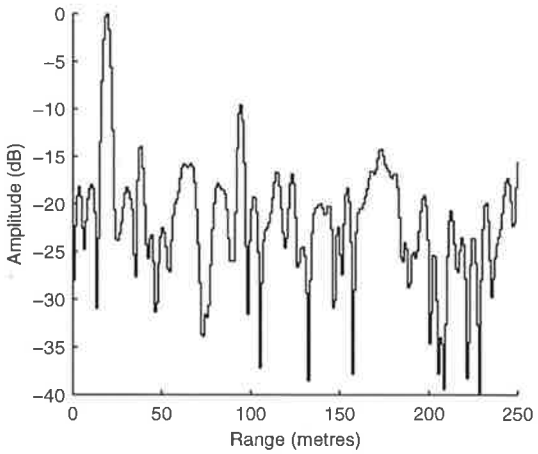

(c) A single HRRP after matched filter processing. The SNR in the range bin containing the largest target scatterer is approximately 20 dB.

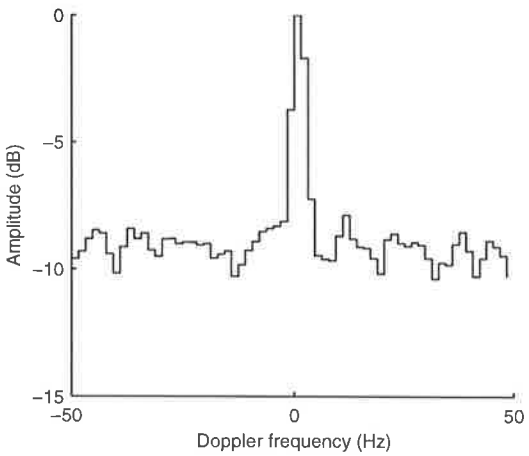

(d) The Doppler profile of 64 consecutive HRRPs. Note that the target energy is spread over 5 of the 64 Doppler bins since a window was used prior to Doppler processing.

Figure 7.18: The results of the radar simulation for a radar PRF of 100 Hz and the averaging of 64 HRRPs.

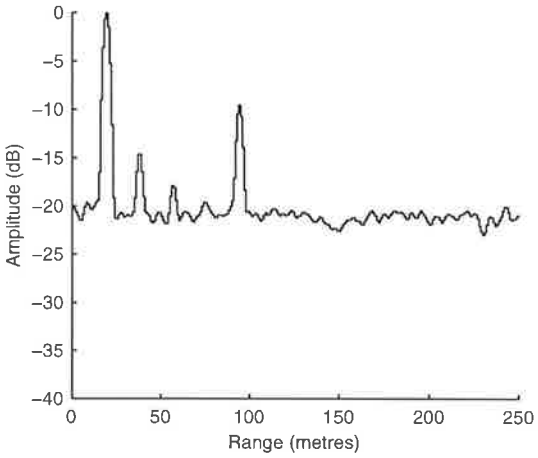

(a) A non-coherent average of 64 consecutive HRRPs.

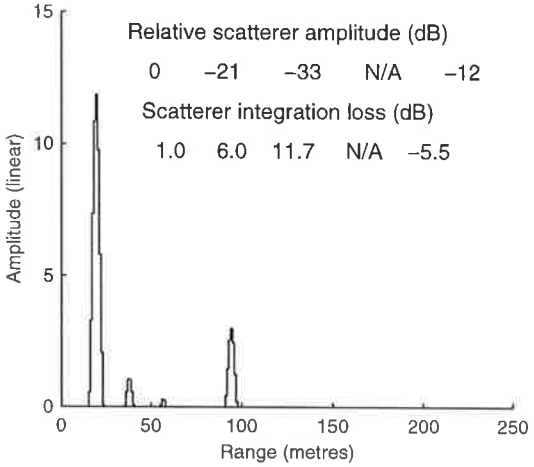

(b) A non-coherent average of 64 consecutive HRRPs which has been thresholded using CFAR processing with a false alarm rate of one spurious peak per 10 averaged HRRPs. The integration loss for each scatterer is shown. The correct relative amplitude levels are 0, -15, -20, -25, -10 (dB).

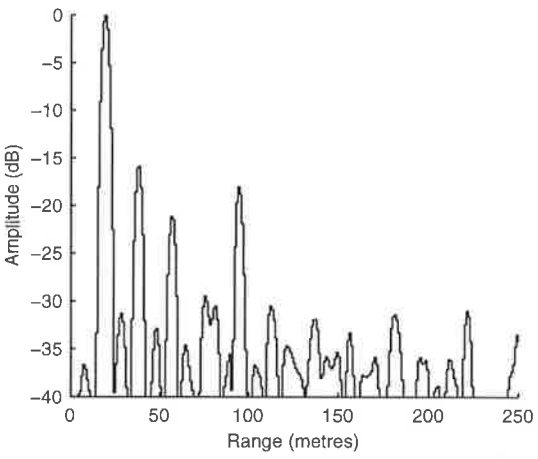

(c) A coherent average of 64 consecutive HRRPs.

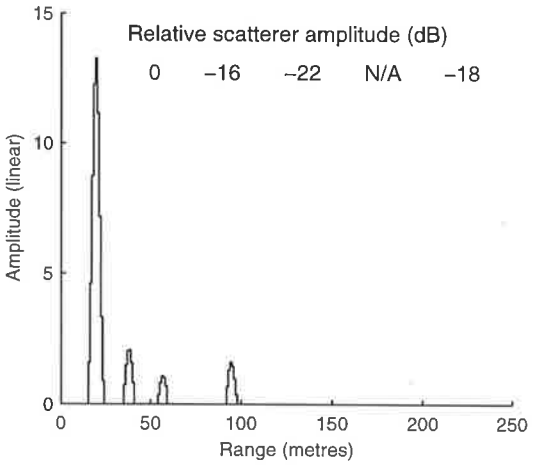

(d) A coherent average of 64 consecutive HRRPs which has been thresholded using CFAR processing with a false alarm rate of one spurious peak per 10 averaged HRRPs. The correct relative amplitude levels
are 0, -15, -20, -25, -10 (dB).

Figure 7.19: The results of both non-coherent and coherent averaging for a radar PRF of 100 Hz and the averaging of 64 HRRPs.

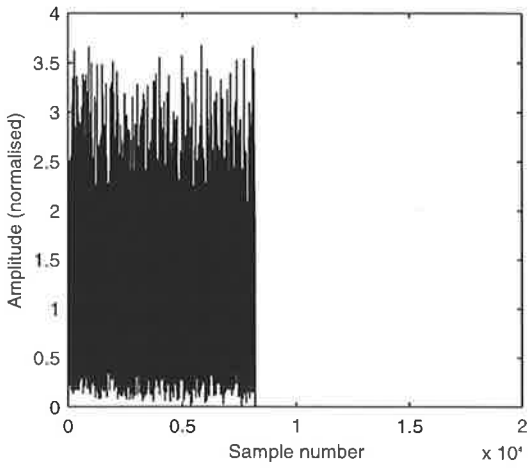

(a) The envelope of the chirp received by the radar.

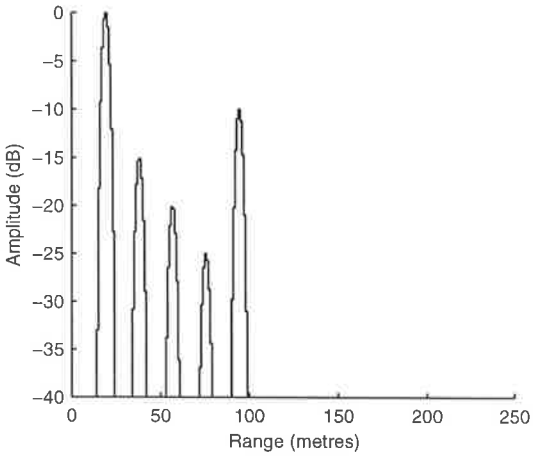

(b) The HRRP obtained when there was no noise on the received signal.

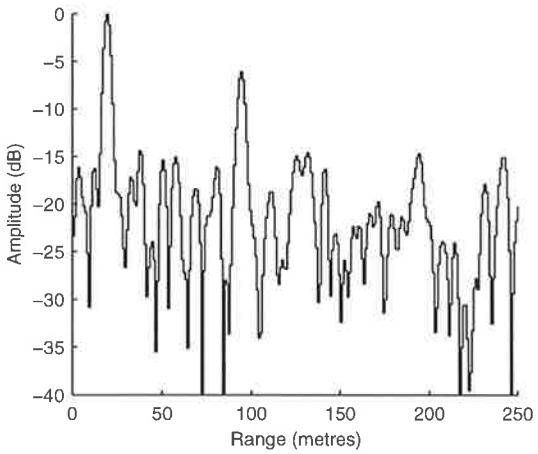

(c) A single HRRP after matched filter processing. The SNR in the range bin containing the largest target scatterer is approximately 20 dB.

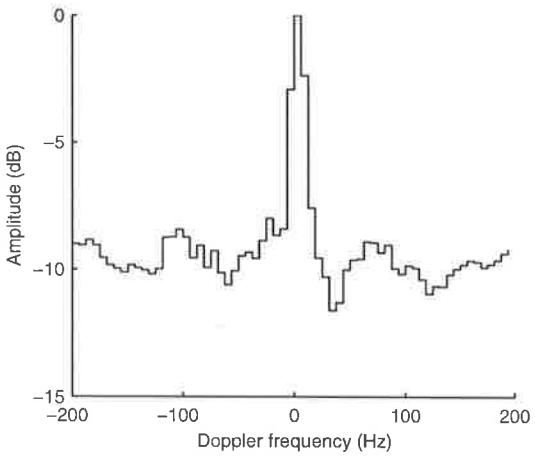

(d) The Doppler profile of 64 consecutive HRRPs. Note that the target energy is spread over 5 of the 64 Doppler bins since a window was used prior to Doppler processing.

Figure 7.20: The results of the radar simulation for a radar PRF of 400 Hz and the averaging of 64 HRRPs.

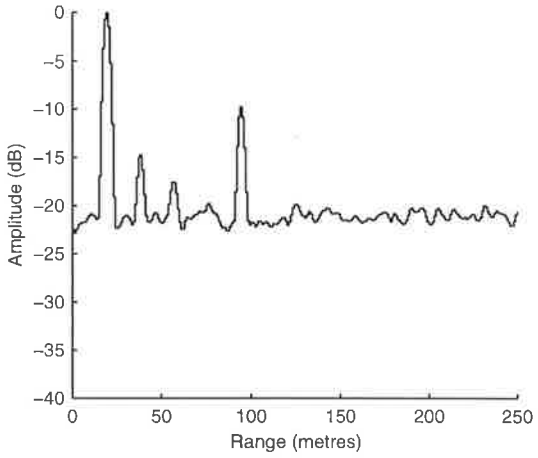

(a) A non-coherent average of 64 consecutive HRRPs.

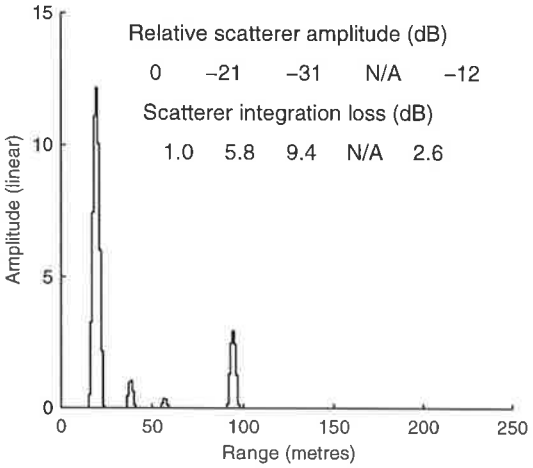

(b) A non-coherent average of 64 consecutive HRRPs which has been thresholded using CFAR processing with a false alarm rate of one spurious peak per 10 averaged HRRPs. The integration loss for each scatterer is shown. The correct relative amplitude levels are 0, -15, -20, -25, -10 (dB).

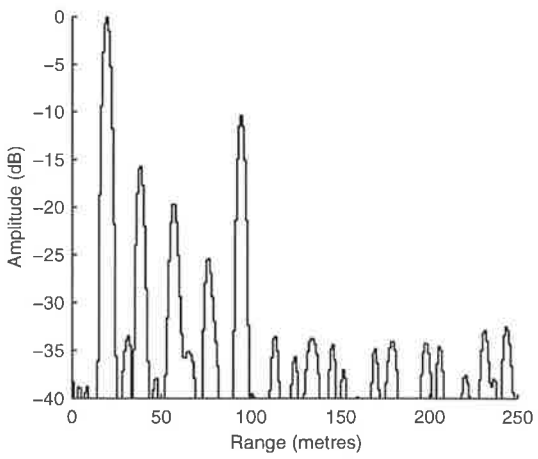

(c) A coherent average of 64 consecutive HRRPs.

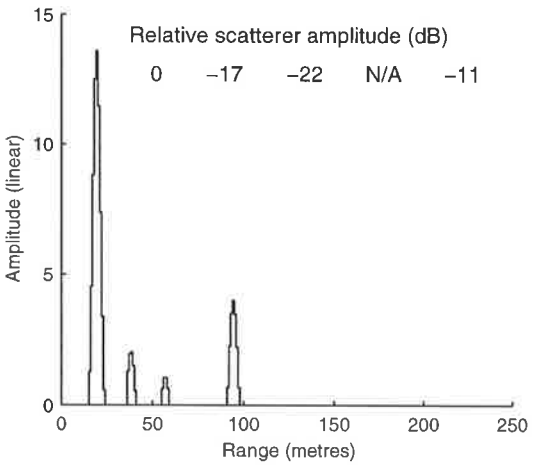

(d) A coherent average of 64 consecutive HRRPs which has been thresholded using CFAR processing with a false alarm rate of one spurious peak per 10 averaged HRRPs. The correct relative amplitude levels
are 0, -15, -20, -25, -10 (dB).

Figure 7.21: The results of both non-coherent and coherent averaging for a radar PRF of 400 Hz and the averaging of 64 HRRPs.

7.6 Summary

This chapter began by reviewing the principles of both coherent and non-coherent integration. It was seen that coherent integration provides a SNR gain of N for N samples integrated whereas non-coherent integration provides a SNR gain between $\sqrt{N}$ and N. It was foreshadowed that as the SNR becomes smaller, the difference between coherent and non-coherent integration should become larger.

Section 7.3 discussed the non-coherent averaging of HRRPs. The concept of coherently averaging HRRPs was introduced in Section 7.4. The operational context in which the coherent averaging of HRRPs would be used was described in Section 7.4.1 and an overview of the coherent averaging of HRRPs was presented in Section 7.4.2. The basic principle of coherent averaging is to oversample the target returns in Doppler and then separate the target from the noise according to Doppler. The radar parameters are chosen according to an estimate of the target Doppler bandwidth. The way in which the radar parameters are chosen was described in Section 7.4.3. Section 7.4.4 described how a coherently averaged HRRP can be extracted from the range-Doppler image and Section 7.4.5 presented a method for reliably estimating the noise level in the coherently averaged HRRP. In Section 7.4.6 a statistical test was proposed to determine whether the coherent processing was successful or not. A technique to CFAR threshold the coherently averaged HRRP was presented in Section 7.4.7.

A series of five HRRP averaging simulations was presented in Section 7.5. The first three simulations showed how the improvement in target scatterer detectability depends upon the number of HRRPs averaged. The results from the simulations confirmed that coherent averaging produces better averaged HRRPs, in terms of target scatterer detectability, than non-coherent averaging. The performance gap (integration loss) between non-coherent averaging and coherent averaging was seen to increase as the SNR became smaller. Simulations 4 and 5 showed the degraded performance of coherent averaging when the Doppler resolution Δf_D was set to values other than the ideal value of $\Delta f_D \approx \beta_D$. The reasons for the degraded performance when $\Delta f_D \neq \beta_D$ were detailed.

Chapter VIII

THESIS SUMMARY

Chapter 2 reviewed the previous work in the area of radar target classification. It was found that the majority of the previously proposed target classification techniques are only of academic interest. The techniques of HRRP, ISAR and JEM were identified as having practical potential and their advantages and disadvantages were discussed in Section 2.5. It was found that ISAR and JEM provide good information for target classification but this information is not available for all operational scenarios. In contrast, HRRPs are more difficult to classify but they are obtainable in all operational scenarios. It was decided that HRRPs should receive particular emphasis in this thesis.

Chapter 3 reviewed some basic high resolution radar concepts such as slant-range resolution, cross-range resolution, coherency and synthetic aperture processing. The commonly used high resolution radar waveforms were discussed in Section 3.3. Sections 3.4 and 3.5 introduced HRRP and ISAR processing respectively.

Chapter 4 began by summarising some of the theoretical aspects of radar backscatter from complex targets. Sections 4.3 and 4.4 described two experiments in which real radar data of full-scale aircraft targets were collected. High resolution radar imagery of real aircraft in flight and of a Mirage aircraft on a turntable was collected. The experiments were carefully chosen to highlight the important characteristics of radar backscatter and provide a background to radar backscatter phenomenology. In Section 4.5, the results of the experimental investigation into radar backscatter phenomenology were discussed in the context of radar target classification and several important backscatter characteristics such as engine cavity backscatter and JEM were discussed.

Chapter 5 discussed the development of a high resolution radar data simulator called ISARLAB. ISARLAB was based upon well established radar backscatter theory and the observations of radar backscatter from full-scale aircraft made in Chapter 4. ISARLAB was designed to model only the essential target attributes which are required to produce realistic high resolution radar imagery. ISARLAB was validated by comparing the imagery produced from its simulated data to imagery produced from corresponding real data.

Chapter 6 discussed radar target classification from HRRPs. The chapter began in Section 6.2 by discussing HRRP preprocessing issues. In particular, the issues of: aspect independent classification; target localisation; HRRP averaging and HRRP thresholding were discussed. Specific solutions for each preprocessing issue were discussed. The

remainder of Chapter 6 presented an experiment where real HRRPs were preprocessed and classified. Real data were collected from a local airport and the objective was to differentiate Boeing 727 aircraft from Boeing 737 aircraft over a limited range of aspects. The SNR of the HRRPs was increased by non-coherently averaging consecutive HRRPs. The target localisation problem was avoided by using the magnitude of the FFT as a shift-invariant transform. Dimensionality reduction based upon a generalised linear discriminant was used prior to final target classification. Final classification was achieved using a Bayes classifier. The results of the target classification experiment were discussed in Section 6.8. The correct classification rates achieved were very good and the results of the experiment auger well for aircraft target classification from HRRPs.

Chapter 7 began by reviewing the principles of coherent and non-coherent integration. An algorithm for the coherent averaging of HRRPs was proposed and the operational context in which the algorithm would be used was discussed. The algorithm produced the best possible averaged HRRP, in terms of target scatterer detectability, for a given number of HRRPs averaged and the algorithm was applicable when the target was at medium to long range or when the target rotation rate was small. The basic principle of coherent averaging was to oversample the target returns in Doppler and then separate the target from the noise according to Doppler. The radar parameters were chosen according to an estimate of the target Doppler bandwidth. A sequence of HRRPs was collected and it was coherently processed to produce a range-Doppler image. A coherently averaged HRRP was extracted from the range-Doppler image. A statistical test was proposed to determine whether the coherent processing was successful or not. The coherently averaged HRRP was thresholded using a CFAR technique.

A series of five HRRP averaging simulations was presented. The first three simulations showed how the improvement in target scatterer detectability depended upon the number N of HRRPs averaged. The results from these simulations confirmed that coherent averaging produces better averaged HRRPs, in terms of target scatterer detectability, than non-coherent averaging. It was seen that the performance gap (integration loss) between coherent and non-coherent averaging increased as the SNR became smaller. Simulations 4 and 5 showed the degraded performance of coherent averaging when the Doppler resolution Δf_D was set to values other than the ideal value of $\Delta f_D \approx \beta_D$. The reasons for the degraded performance when $\Delta f_D \neq \beta_D$ were detailed.

8.1 Future work needed

This thesis has addressed the subject of target classification using high resolution radar imagery. The emphasis of the thesis has been on preprocessing issues and little has been said on a complete system for target classification. A complete target classification system for HRRPs will need to address:

- The level of HRRP SNR which is required for reliable target classification;
- The type of feature extraction scheme which is used on the averaged and thresholded HRRPs;
- The storage requirements and retrieval method for HRRPs of multiple targets from multiple aspects;
- The way in which unknown or novel HRRP inputs are identified;
- The way in which a confidence level is assigned to each particular target classification decision.

Appendix A

HAYWOOD'S ALGORITHM FOR ISAR PROCESSING

Haywood's ISAR motion compensation algorithm [44] is used in this thesis to produce ISAR imagery. It is also used to produce a focussed range-Doppler image for the coherent averaging algorithm described in Chapter 7. There are a number of algorithms [33] which produce focussed range-Doppler imagery and the content of this thesis is not dependent in any particular way on the use of Haywood's algorithm. Haywood's algorithm is reproduced in this appendix for convenient reference.

Haywood's algorithm is a three stage algorithm consisting of:

1. Radial motion compensation;
2. Adaptive beamforming;
3. Doppler processing.

Assume there are N complex HRRPs $\boldsymbol{r}_1 \ldots \boldsymbol{r}_N$ each with n range bins. This gives a HRRP data matrix of size $N \times n$

$$\begin{bmatrix} \boldsymbol{r}_1 \\ \vdots \\ \boldsymbol{r}_N \end{bmatrix} = \begin{bmatrix} A_{11}e^{j\phi_{11}} & \overset{\text{range bin index}}{\longrightarrow} \ldots & A_{1n}e^{j\phi_{1n}} \\ \vdots & A_{lm}e^{j\phi_{lm}} & \vdots \\ A_{N1}e^{j\phi_{N1}} & \ldots & A_{Nn}e^{j\phi_{Nn}} \end{bmatrix} \downarrow \text{HRRP index} \tag{A.1}$$

where A_{lm} is a real number, ϕ_{lm} is a real number in the range $[0, 2\pi)$, $l = 1 \ldots N$ is a HRRP index and $m = 1 \ldots n$ is a range bin index. Radial motion compensation is achieved with cross-correlation. A reference HRRP

$$\boldsymbol{r}_p = [A_{p1}e^{j\phi_{p1}} \ldots A_{pn}e^{j\phi_{pn}}] \tag{A.2}$$

is arbitrarily chosen and each HRRP (magnitude only) is cross-correlated with the reference HRRP

$$\boldsymbol{c}_l = |\text{IDFT}\,(\,\text{DFT}(|\boldsymbol{r}_p|)\;\;\text{DFT}(|\boldsymbol{r}_l|)^*\,)| \qquad \forall\; l = 1 \ldots N \tag{A.3}$$

where DFT and IDFT represent the discrete Fourier operators. The location of the peak of $\boldsymbol{c}_l$ indicates the range shift (time delay) necessary for alignment with the reference HRRP

$$d_l = \text{location}[\max(\boldsymbol{c}_l)] \qquad \forall\; l = 1 \ldots N \tag{A.4}$$

The sequence of discrete range delays $d_1 \ldots d_N$ is smoothed by fitting a low order polynomial to the sequence of delays. The smoothed delay corrections $s_1 \ldots s_N$ are applied to the original HRRPs by element-wise multiplication in the frequency domain with a phase shift vector $\boldsymbol{\Phi}$

$$\boldsymbol{r}'_l = \text{IDFT}\left(\boldsymbol{\Phi}\ \text{DFT}\left([A_{l1}e^{j\phi_{l1}} \ldots A_{lm}e^{j\phi_{lm}} \ldots A_{ln}e^{j\phi_{ln}}]\right)\right) \quad \forall\ l = 1 \ldots N \tag{A.5}$$

where

$$\boldsymbol{\Phi} = e^{j\frac{2\pi}{\beta}} \times [e^{-js_l(f_s+\Delta f)} \ldots e^{-js_l(f_s+m\Delta f)} \ldots e^{-js_l(f_s+n\Delta f)}] \tag{A.6}$$

and $\beta = N\Delta f$ is the waveform bandwidth, f_s is the waveform start frequency, Δf is the frequency increment and DFT, IDFT represent the discrete Fourier operators. After range alignment the HRRP data can be represented as

$$\begin{bmatrix} \boldsymbol{r}'_1 \\ \vdots \\ \boldsymbol{r}'_N \end{bmatrix} = \begin{bmatrix} A'_{11}e^{j\phi'_{11}} & \ldots & A'_{1n}e^{j\phi'_{1n}} \\ \vdots & A'_{lm}e^{j\phi'_{lm}} & \vdots \\ A'_{N1}e^{j\phi'_{N1}} & \ldots & A'_{Nn}e^{j\phi'_{Nn}} \end{bmatrix} \tag{A.7}$$

where A'_{lm} is a real number, ϕ'_{lm} is a real number in the range $[0, 2\pi)$, $l = 1 \ldots N$ is a HRRP index and $m = 1 \ldots n$ is a range bin index.

The second step in the algorithm is adaptive beamforming. This is necessary to compensate for phase changes caused by range shifts which are only fractions of a wavelength. The adaptive beamforming technique used is based upon the DSA [46]. The basic principle of the DSA is to find a dominant scatterer and use that scatterer as a phase synchronising source. The scatterer is considered dominant if it provides a majority contribution to the phasor sum of backscatter in a particular range bin. Since a range bin with a small amplitude variance is likely to be dominated by a single scatterer, the amplitude variance for each range bin is calculated over the N HRRPs

$$\sigma_m^2 = \frac{1}{(N-1)}\sum_{l=1}^{N}\left(A'_{lm} - \frac{1}{N}\sum_{l=1}^{N}A'_{lm}\right)^2 \qquad \forall\ m = 1 \ldots n \tag{A.8}$$

The range bin with the minimum amplitude variance (range bin q), is chosen as the phase synchronising source as long as it satisfies the "dominant" scatterer criteria

$$\sigma_q^2 < \sigma_m^2 \qquad \forall\, m \neq q \tag{A.9}$$

and

$$\sum_{l=1}^{N}\left(A'_{lq}\right)^2 > \frac{1}{n}\sum_{m=1}^{n}\left(\sum_{l=1}^{N}(A'_{lm})^2\right) \tag{A.10}$$

The phase differences between the reference bin in the reference HRRP and the reference bin in every other HRRP are now calculated

$$\psi_l = \phi'_{lq} - \phi'_{pq} \qquad \forall\ l = 1 \ldots N \tag{A.11}$$

These phase differences are applied to every HRRP

$$\boldsymbol{r}''_l = e^{-j\psi_l}\boldsymbol{r}'_l \qquad \forall\ l = 1\ldots N \tag{A.12}$$

After adaptive beamforming the HRRP data can be represented as

$$\begin{bmatrix} \boldsymbol{r}''_1 \\ \vdots \\ \boldsymbol{r}''_N \end{bmatrix} = \begin{bmatrix} A''_{11}e^{j\phi''_{11}} & \ldots & A''_{1n}e^{j\phi''_{1n}} \\ \vdots & A''_{lm}e^{j\phi''_{lm}} & \vdots \\ A''_{N1}e^{j\phi''_{N1}} & \ldots & A''_{Nn}e^{j\phi''_{Nn}} \end{bmatrix} \tag{A.13}$$

where $A''_{lm} = A'_{lm}$ is a real number, ϕ''_{lm} is a real number in the range $[0, 2\pi)$, $l = 1\ldots N$ is a HRRP index and $m = 1\ldots n$ is a range bin index.

The third and final step of the algorithm is Doppler spectral analysis. This is done by performing a one–dimensional DFT on each range aligned and phase compensated range bin

$$\begin{bmatrix} D_{1m}e^{j\theta_{1m}} \\ \vdots \\ D_{Nm}e^{j\theta_{Nm}} \end{bmatrix} = \mathrm{DFT}\begin{bmatrix} A''_{1m}e^{j\phi''_{1m}} \\ \vdots \\ A''_{Nm}e^{j\phi''_{Nm}} \end{bmatrix} \tag{A.14}$$

to give a range-Doppler image

$$\begin{bmatrix} D_{11}e^{j\theta_{11}} & \ldots & D_{1n}e^{j\theta_{1n}} \\ \vdots & D_{lm}e^{j\theta_{lm}} & \vdots \\ D_{N1}e^{j\theta_{N1}} & \ldots & D_{Nn}e^{j\theta_{Nn}} \end{bmatrix} \begin{matrix} \xrightarrow{\text{range bin index}} \\ \\ \downarrow \text{Doppler bin index} \end{matrix} \tag{A.15}$$

where D_{lm} is a real number, θ_{lm} is a real number in the range $[0, 2\pi)$, $l = 1\ldots N$ is a Doppler bin index and $m = 1\ldots n$ is a range bin index.

Appendix B

CALCULATIONS FOR ISAR IMAGING AT ADELAIDE AIRPORT

This appendix contains the radar parameter calculations for the non-cooperative aircraft imaging experiment described in Section 4.4. The geometry for the data collection is shown in Figure 4.10 and the various equations used for the calculations are found in [33]. The following parameters were either given or required:

- The radar centre frequency was $\bar{f} = 8.96$ GHz;
- A slant-range resolution[1] of $\Delta r_s = 0.6$ m was required;
- A cross-range resolution[1] of $\Delta r_c = 0.6$ m was required;
- An aircraft speed of approximately 70 ms^{-1} was assumed;
- The maximum aircraft length (Boeing 747) was 71 m.

The required bandwidth for a range resolution of $\Delta r_s = 0.6$ m was calculated from Equation 3.1

$$\begin{aligned} \beta &= \frac{c}{2\Delta r_s} \\ &= \frac{3 \times 10^8}{2 \times 0.6} \\ &= 250 \text{ MHz} \end{aligned}$$

$n = 128$ was chosen to give a slant-range ambiguity window of

$$\begin{aligned} w_s &= n\Delta r_s \\ &= 128 \times 0.6 \\ &\approx 75 \text{ m} \end{aligned}$$

This slant-range ambiguity window was large enough to contain the full extent of all aircraft targets appearing at Adelaide airport. The cross-range ambiguity window w_c

[1] The actual resolution became 1.0 m when a Hann window was used before the IDFT.

was also chosen to be 75 m. To meet the required bandwidth of approximately 250 MHz with $n = 128$ frequency steps, a frequency step size of $\Delta f = 2.0$ MHz was required.

If the aircraft was travelling at 70 ms^{-1} at a range of 1700 m and with a geometry as indicated in Figure 4.10, the effective perpendicular velocity v_T seen by the radar was

$$\begin{aligned} v_T &= v\cos\theta \\ &= 70\cos 39^\circ \\ &= 54.4 \text{ ms}^{-1} \end{aligned}$$

The angular rotation speed ω was given by

$$\begin{aligned} \omega &= \frac{v_T}{R} \\ &= \frac{54.4}{1700} \\ &= 0.032 \text{ rads}^{-1} \end{aligned}$$

The minimum required Doppler bandwidth $\beta_D^{\min}$ was given by

$$\begin{aligned} \beta_D^{\min} &= \frac{2\omega w_c \bar{f}}{c} \\ &= \frac{2 \times 0.032 \times 75 \times 8.96 \times 10^9}{3 \times 10^8} \\ &= 143 \text{ Hz} \end{aligned}$$

This gave a maximum PRI $T_{\text{pri}}^{\max}$ of

$$\begin{aligned} T_{\text{pri}}^{\max} &= \frac{1}{\beta_D^{\min}} \\ &= \frac{1}{143} \\ &= 6.97 \text{ ms} \end{aligned}$$

The slant-range ambiguity window w_s was 75 m and this corresponded to a minimum pulse length of $T_p^{\min} = \frac{w_s}{c} = 0.25$ μs. $T_p = 2.5$ μs was chosen since it is difficult to generate and sample very narrow pulses. Choosing a pulse length larger than the minimum required pulse length has limited[2] the maximum effective PRF that can be achieved with the stepped frequency waveform. The return travel time for a pulse was $\frac{2\times R}{c} = 11$ μs.

[2] This limitation is not significant in the imaging scenario discussed in this appendix.

To avoid range ambiguity a minimum PRI of $T_{\text{pri}}^{\text{min}} = 11$ μs was needed. A delay of 50 μs was inserted between the start of one pulse and the start of the next pulse to give

$$\begin{aligned} T_{\text{pri}} &= n\,(50\ \mu\text{s}) \\ &= 128 \times 50 \times 10^{-6} \\ &= 6.4\ \text{ms} \end{aligned}$$

This choice of PRI was in the range dictated by $T_{\text{pri}}^{\text{min}}$ and $T_{\text{pri}}^{\text{max}}$. In summary, the following stepped frequency radar parameters were used to collect data of aircraft at Adelaide airport:

- Centre frequency $\bar{f} = 8.96$ GHz;
- Number of frequency steps $n = 128$;
- Frequency step size $\Delta f = 2.0$ MHz;
- Pulse length $T_p = 2.5$ μs;
- Pulse repetition interval $T_{\text{pri}} = 6.4$ ms;
- Number of sweeps to form an image $N = 128$.

which gave:

- Slant-range and cross-range[3] resolution of 1.0 m when a Hann window was used;
- Slant-range and cross-range ambiguity windows of 75 m.

The stepped frequency waveform used to collect data at Adelaide airport is illustrated in Figure 4.9.

[3] The cross-range resolution is only approximate for a range of 1700 m. The cross-range resolution decreases as the aircraft moves away from the radar.

Appendix C

AN EXAMPLE WHERE ISAR IMAGING IS NOT POSSIBLE

In many encounter scenarios it is not possible to obtain an ISAR image. The example detailed in this appendix should help to illustrate why this is so. Consider a scenario with a stationary radar and an aircraft target, at a range of 150 km, moving perpendicular to the RLOS with a speed of 1000 kmhr^{-1}. This scenario is depicted in Figure C.1. Assume that a slant-range resolution Δr_s and a cross-range resolution Δr_c of 1 m are needed for ISAR target classification. For a target of length 50 m, it is prudent to have a range window w_s and cross-range window w_c each of approximately 75 m. An operational radar would use a chirp waveform to achieve the bandwidth required for the desired slant-range resolution. Let the centre frequency of this chirp waveform be $\bar{f}$ = 9 GHz. The coherent pulse train used by the radar for imaging is shown in Figure C.2.

First it is necessary to calculate the range of PRFs that are suitable for ISAR imaging. The necessary coherent integration (imaging) time is determined solely by the geometry of the encounter scenario. The maximum possible PRF is determined by the range to the target (range ambiguity criterion). The minimum possible PRF is determined by the Doppler ambiguity criterion. In this example, the distance to the target is 150 km which means a two way pulse travel time of $\frac{c}{2R}$ = 1 ms. This makes PRF_{max} = 1000 Hz or $T_{\text{pri}}^{\text{min}}$ = 1 ms.

The target's perpendicular velocity of 1000 kmhr^{-1} corresponds to 278 ms^{-1}. This gives an angular velocity of $\omega = \frac{v_T}{R} = 1.85 \times 10^{-3}$ rads^{-1}. The minimum possible PRF (PRF_{min}) is determined by the target Doppler bandwidth (see Equation 7.49)

$$\begin{aligned} \beta_D &= \frac{2\omega w_c \bar{f}}{c} \\ &= \frac{2 \times 0.00185 \times 75 \times 9 \times 10^9}{3 \times 10^8} \\ &= 8 \text{ Hz} \end{aligned}$$

From the values of PRF_{min} (8 Hz) and PRF_{max} (1000 Hz) it can be seen that choosing a PRF suitable for ISAR imaging is not a problem.

The change in aspect angle required to achieve a resolution of Δr_c = 1 m over the

coherent integration interval is calculated from Equation 3.4

$$\begin{aligned}\Delta\theta &= \frac{\lambda}{2\Delta r_c} \\ &= \frac{0.033}{2 \times 1} \\ &= 0.0165 \text{ rad}\end{aligned}$$

The time taken for the target to traverse this distance (coherent integration time) is

$$\begin{aligned}\Delta t &\approx \frac{R\Delta\theta}{v_T} \\ &= \frac{150 \times 10^3 \times 0.0165}{278} \\ &= 8.9 \text{ s}\end{aligned}$$

It is possible to exclusively dedicate 9 seconds of (radar) time for imaging but this is not a desirable action in an operational context because the radar is unavailable to perform other functions during this time period. Note that in this example, the target is travelling at the most favourable aspect with respect to the RLOS. If the target velocity is not perpendicular to the RLOS then the imaging time increases significantly and hence ISAR imaging becomes even more undesirable.

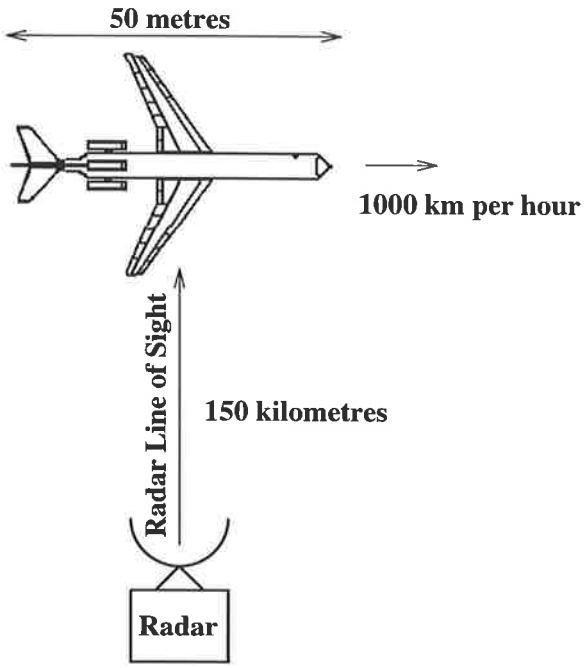

Figure C.1: A typical encounter scenario. In this scenario it is unlikely that ISAR imaging will be possible. Note that in this case the target is moving at the most favourable aspect with respect to the RLOS. If the target were viewed from a different aspect the required imaging time would be substantially longer.

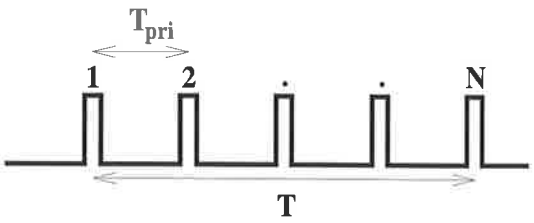

Figure C.2: A coherent pulse train transmitted by the radar. The PRI is T_{pri} and the coherent integration time for N pulses is T.

Appendix D

RADAR IMAGERY OF THE MIRAGE AIRCRAFT

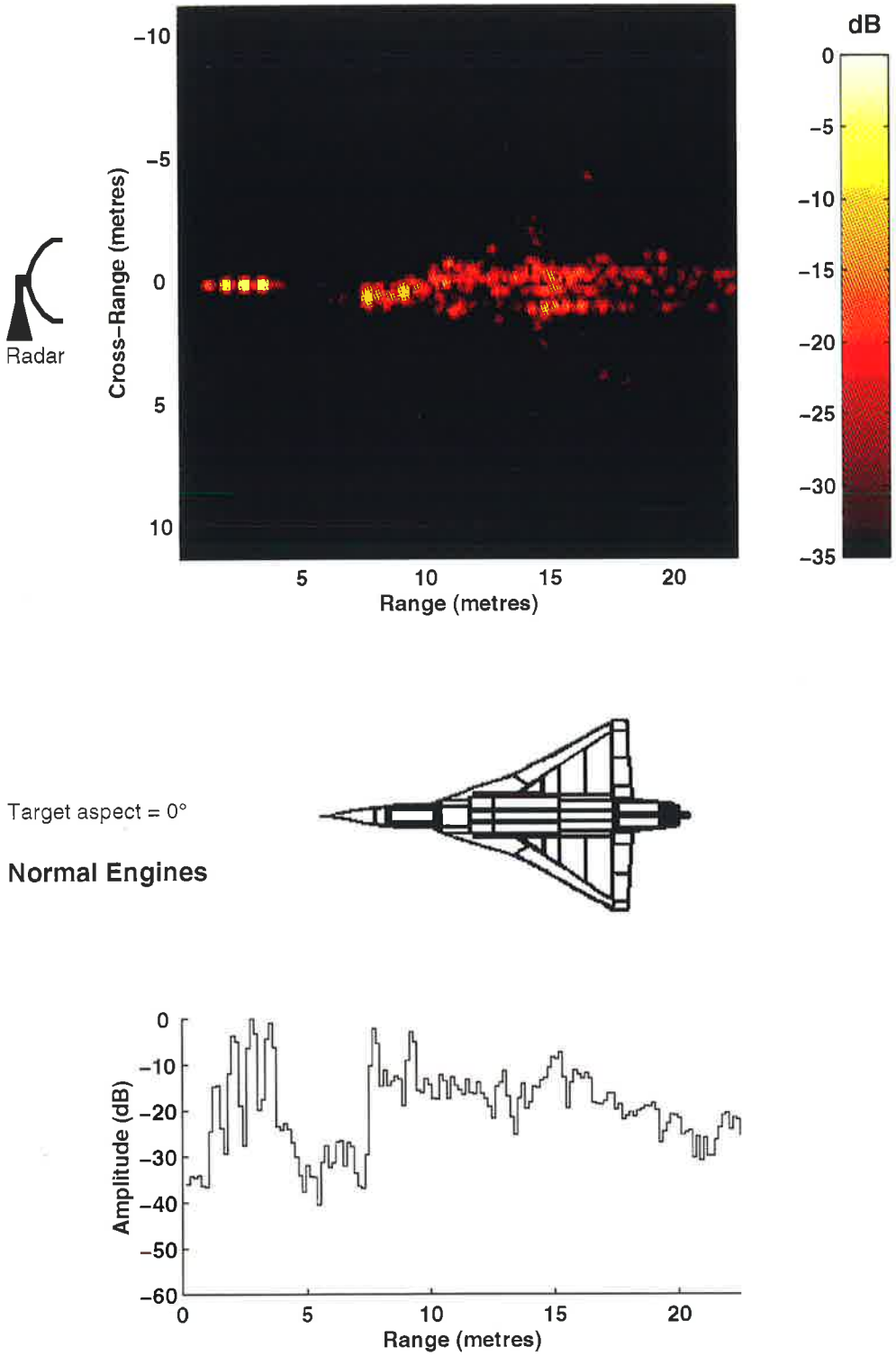

Figure D.1: An ISAR image and a HRRP of the Mirage aircraft viewed from an aspect of 0°. The polarisation is H–H and the engines are in the normal state.

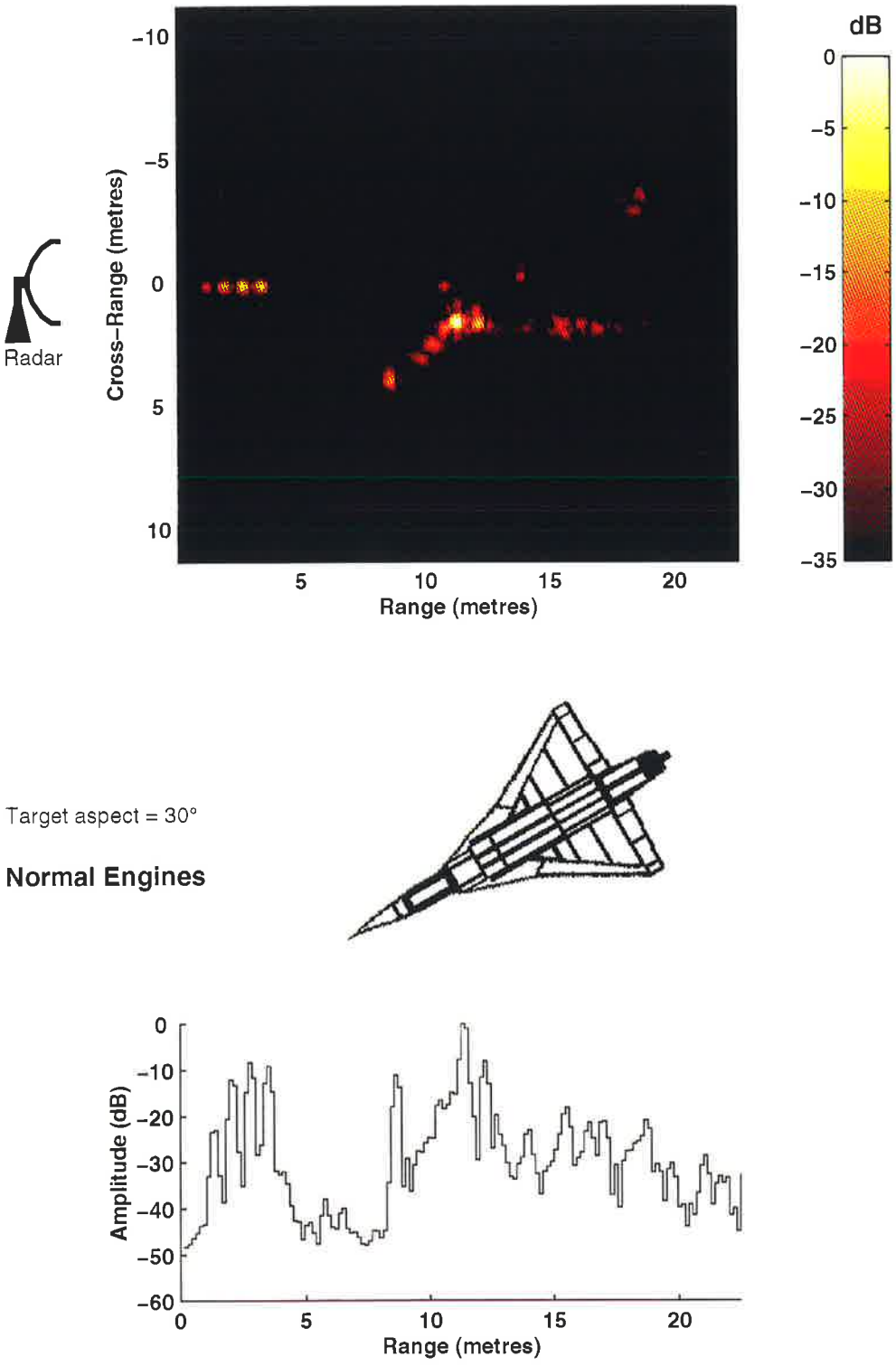

Figure D.2: An ISAR image and a HRRP of the Mirage aircraft viewed from an aspect of 30°. The polarisation is H–H and the engines are in the normal state.

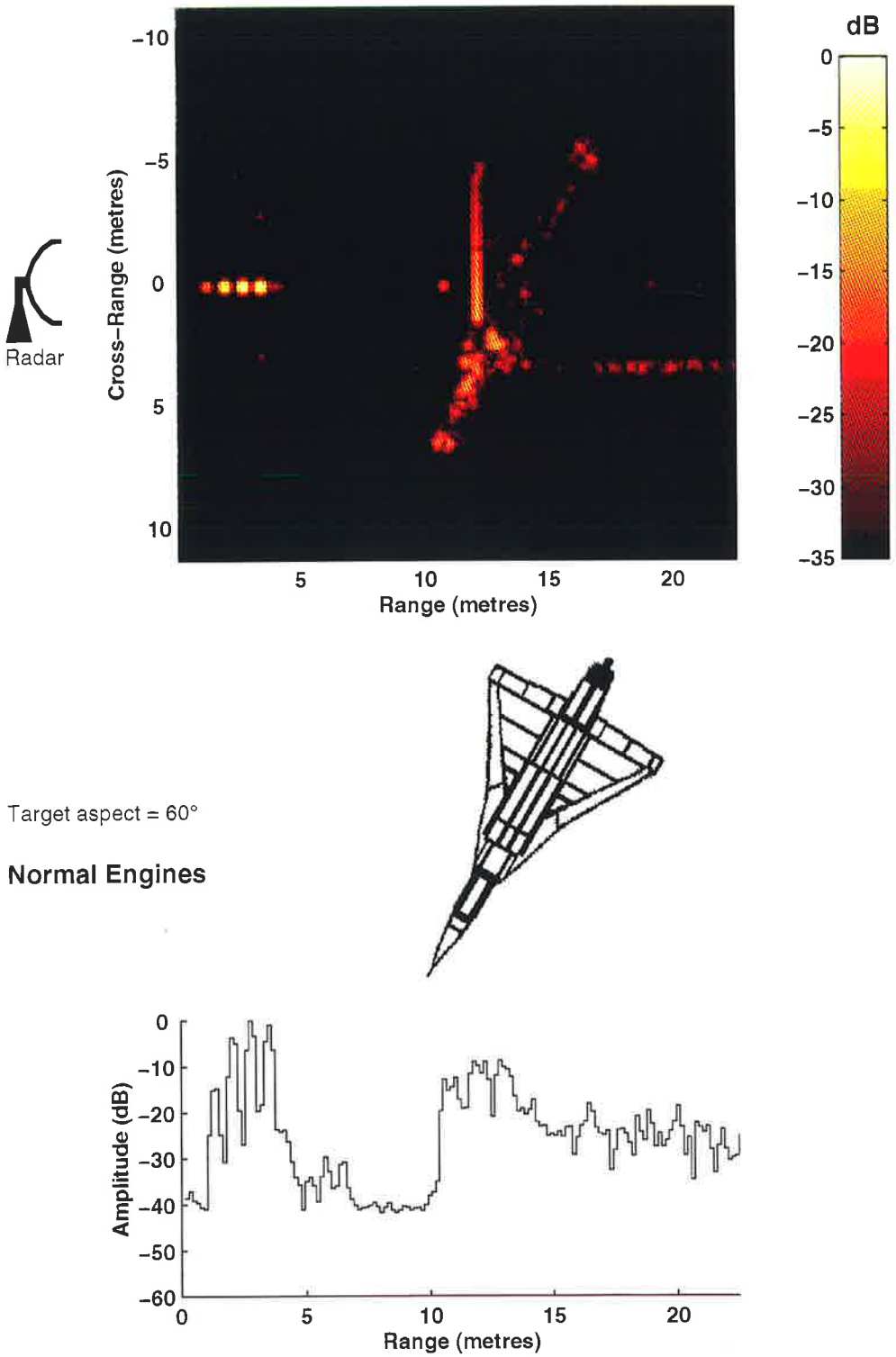

Figure D.3: An ISAR image and a HRRP of the Mirage aircraft viewed from an aspect of 60°. The polarisation is H–H and the engines are in the normal state.

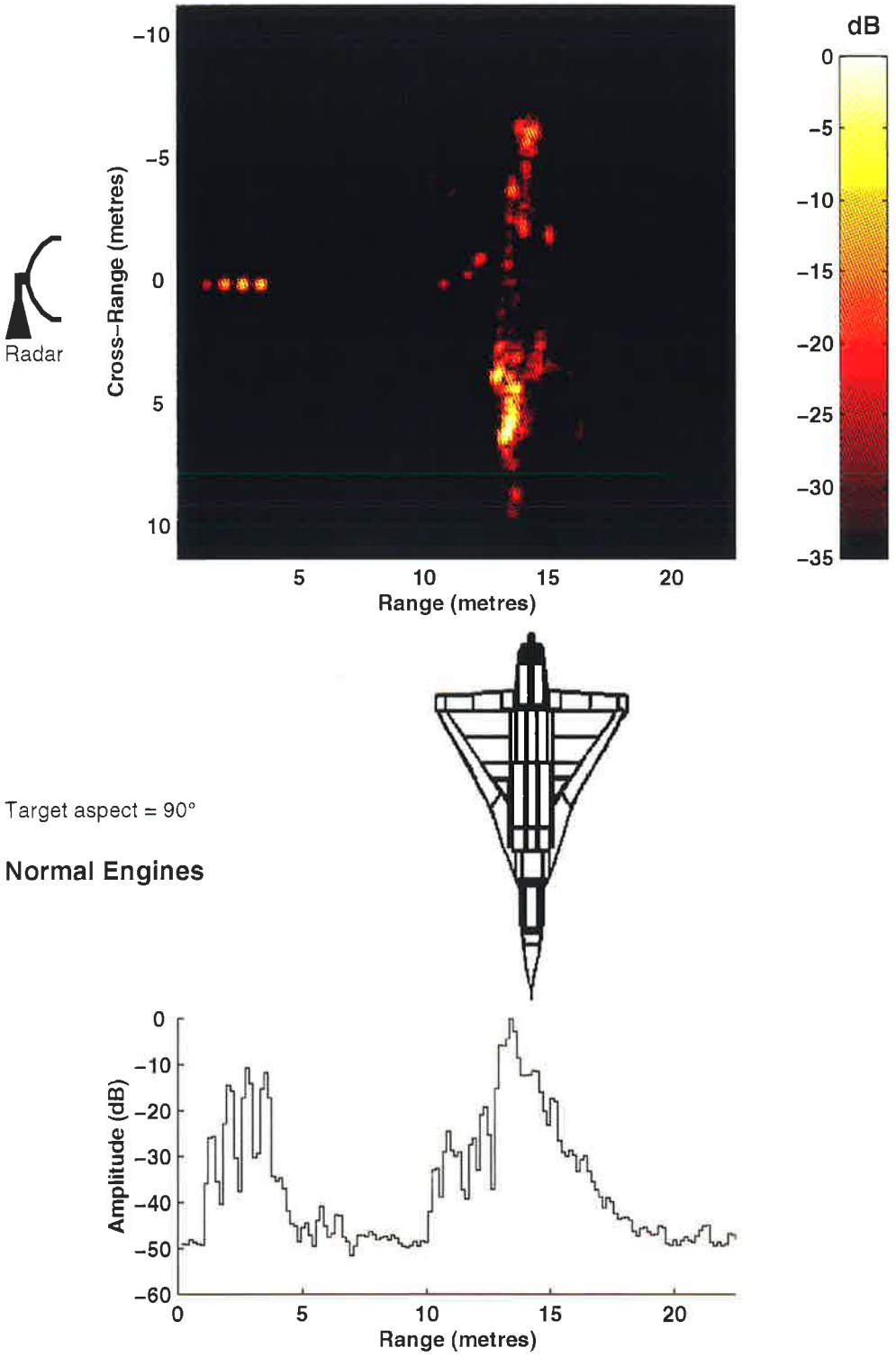

Figure D.4: An ISAR image and a HRRP of the Mirage aircraft viewed from an aspect of 90°. The polarisation is H–H and the engines are in the normal state.

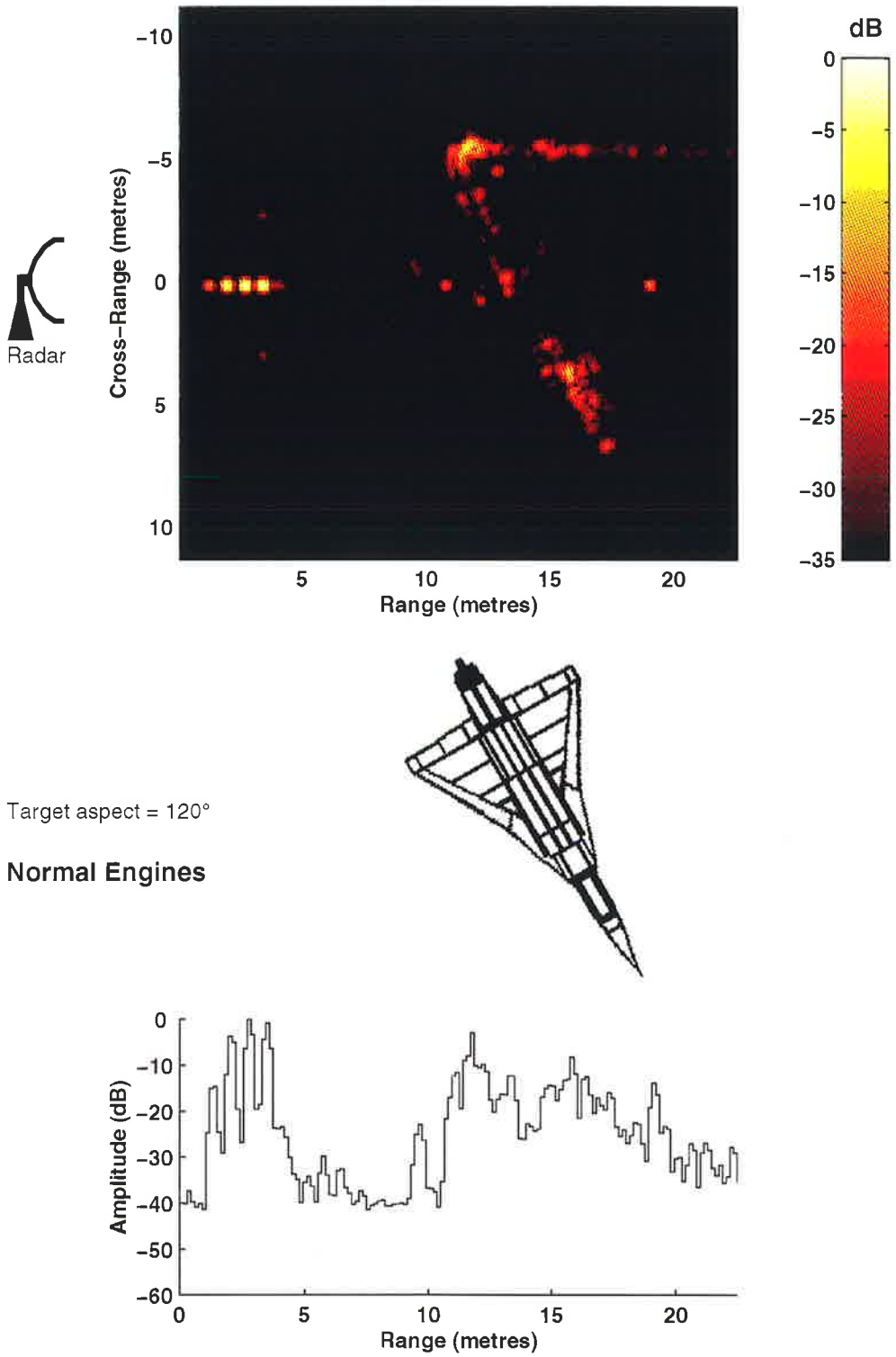

Figure D.5: An ISAR image and a HRRP of the Mirage aircraft viewed from an aspect of 120°. The polarisation is H–H and the engines are in the normal state.

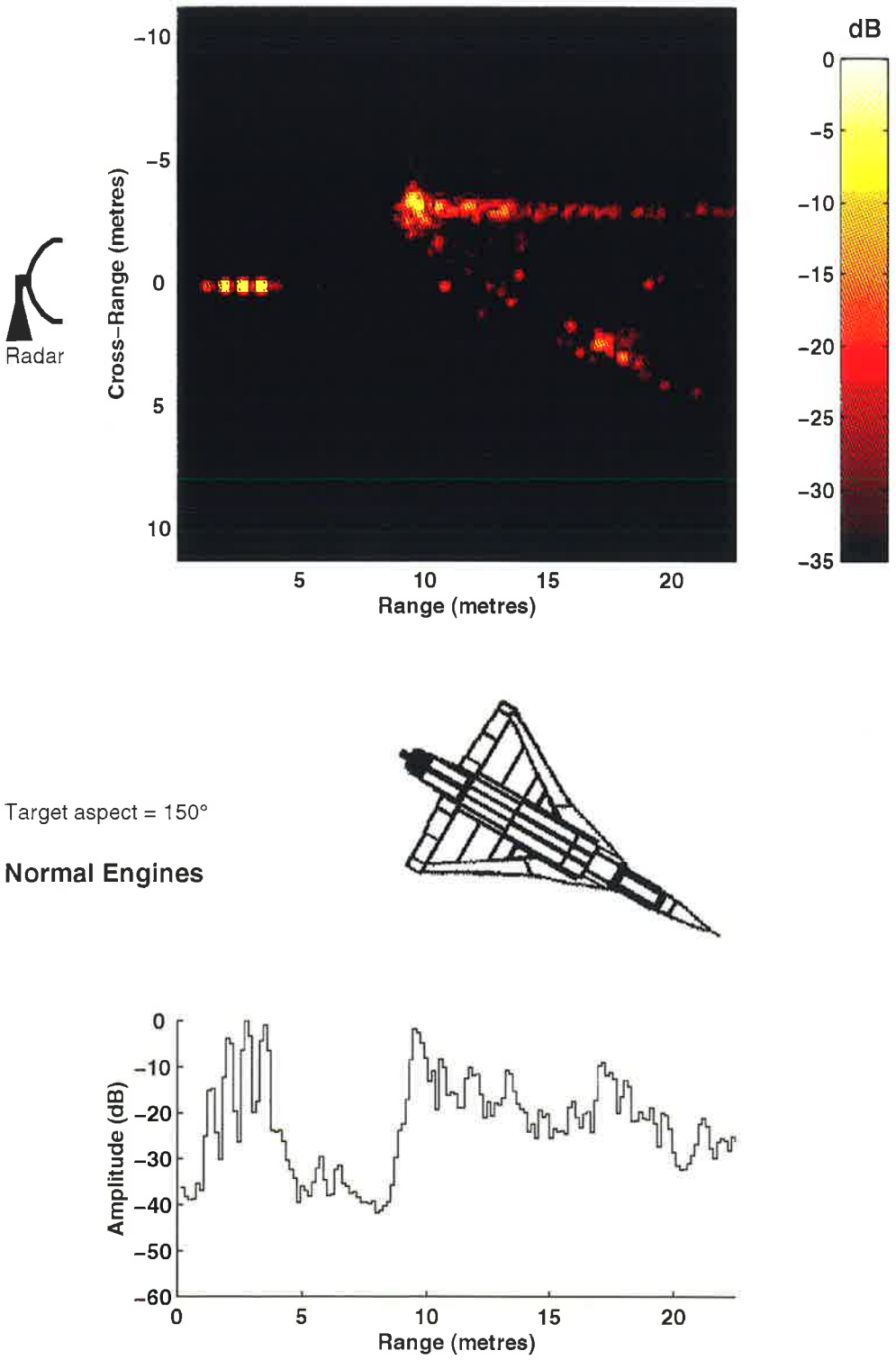

Figure D.6: An ISAR image and a HRRP of the Mirage aircraft viewed from an aspect of 150°. The polarisation is H–H and the engines are in the normal state.

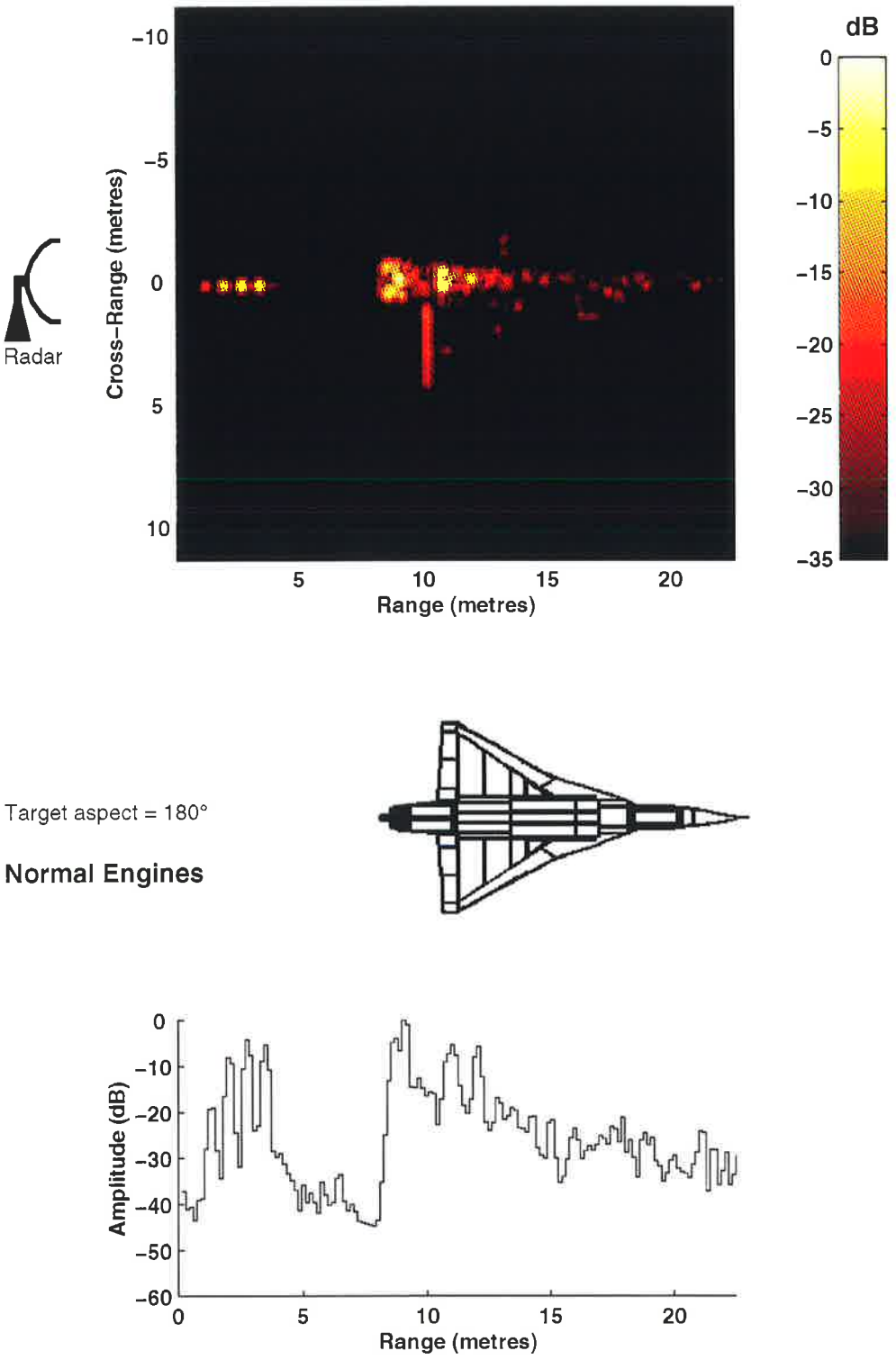

Figure D.7: An ISAR image and a HRRP of the Mirage aircraft viewed from an aspect of 180°. The polarisation is H–H and the engines are in the normal state.

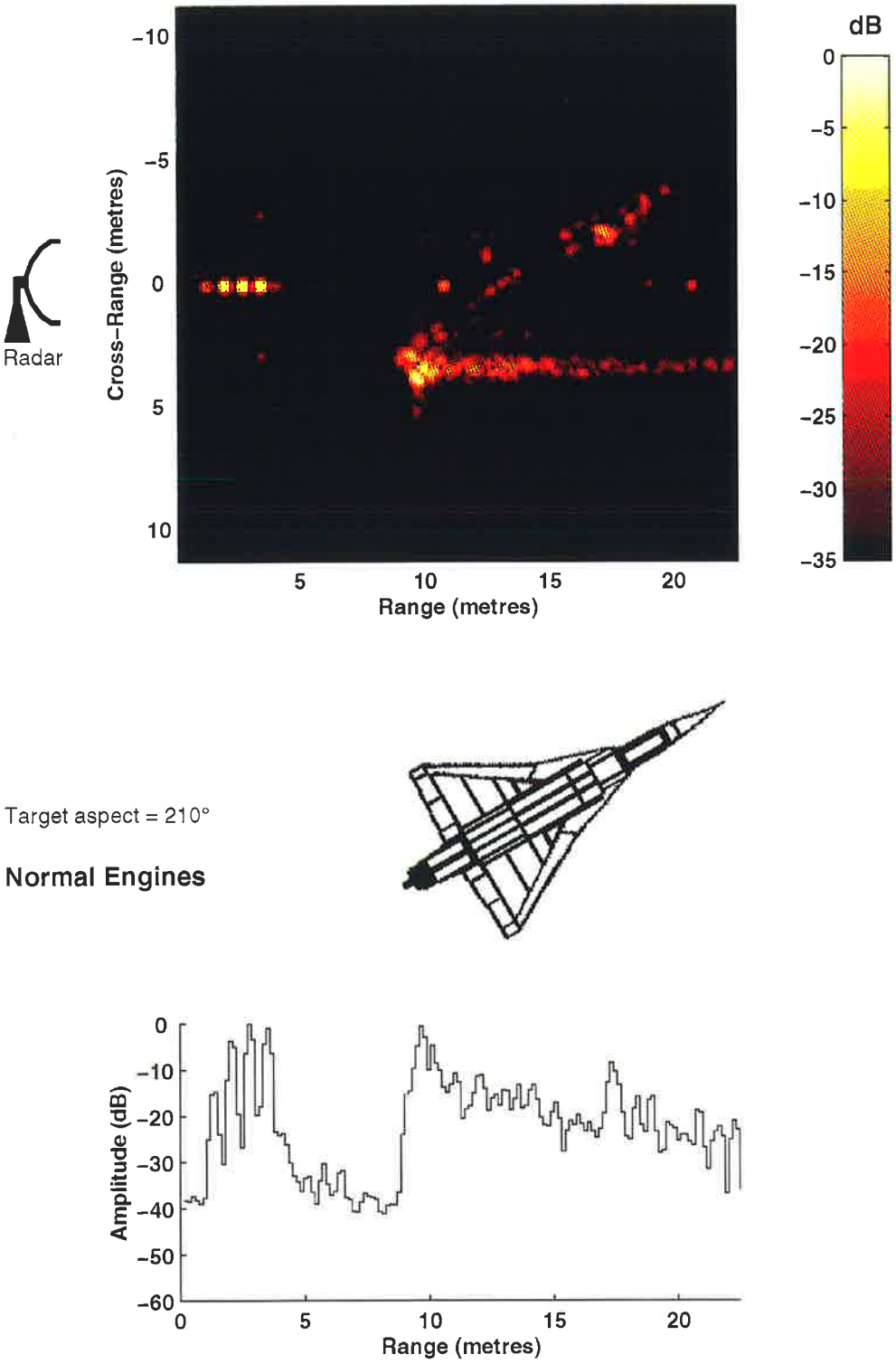

Figure D.8: An ISAR image and a HRRP of the Mirage aircraft viewed from an aspect of 210°. The polarisation is H–H and the engines are in the normal state.

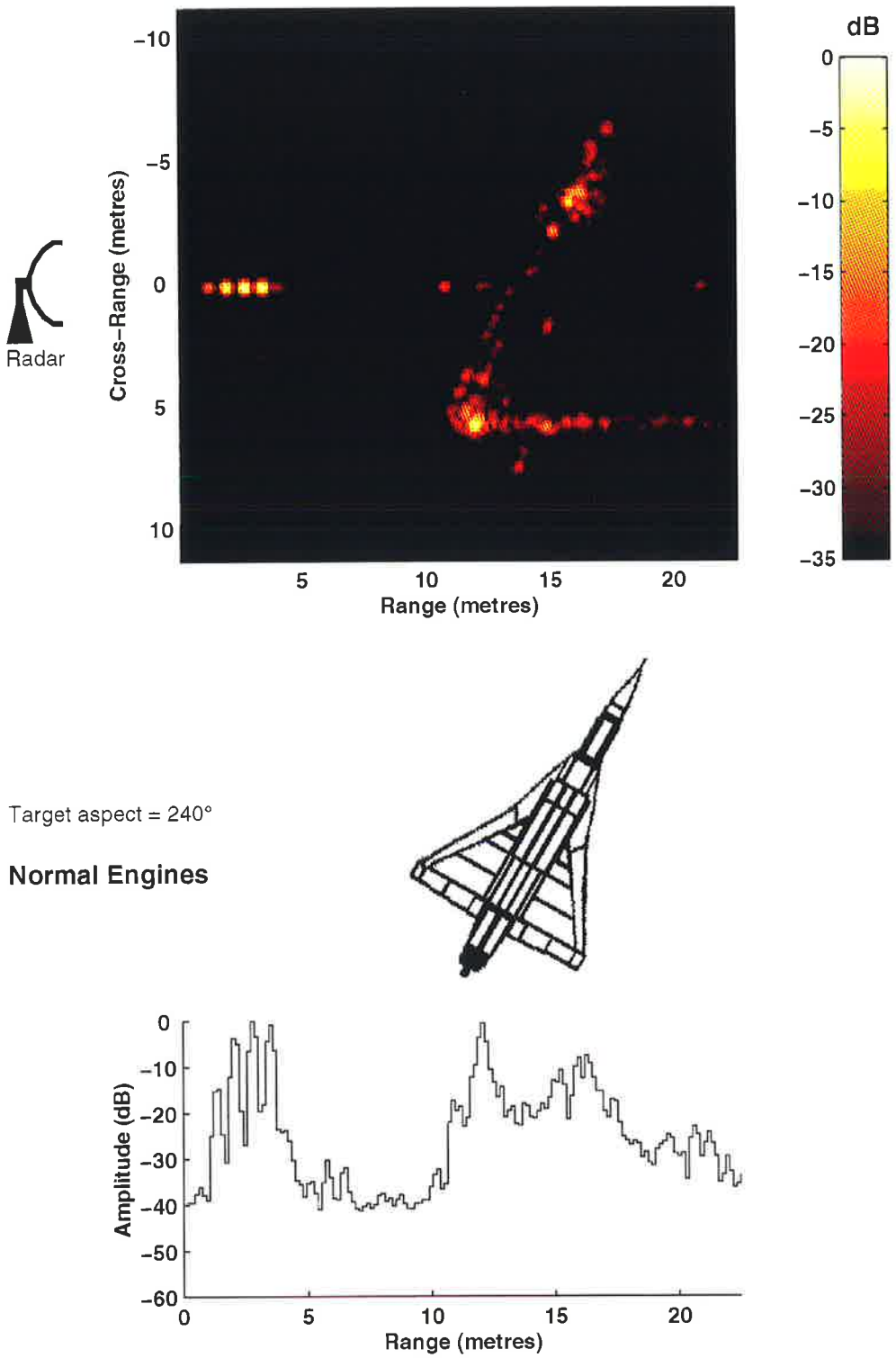

Figure D.9: An ISAR image and a HRRP of the Mirage aircraft viewed from an aspect of 240°. The polarisation is H–H and the engines are in the normal state.

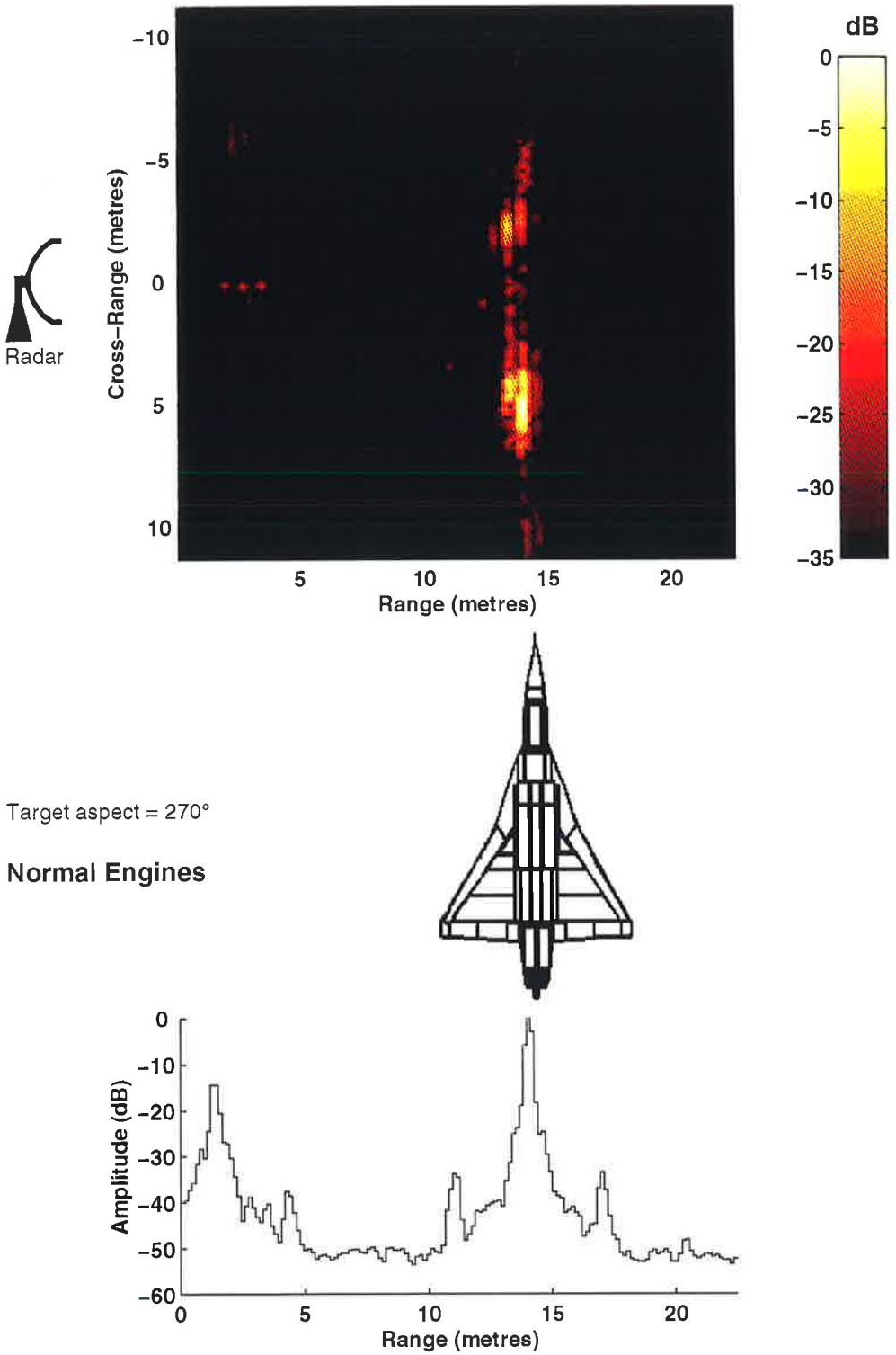

Figure D.10: An ISAR image and a HRRP of the Mirage aircraft viewed from an aspect of 270°. The polarisation is H–H and the engines are in the normal state.

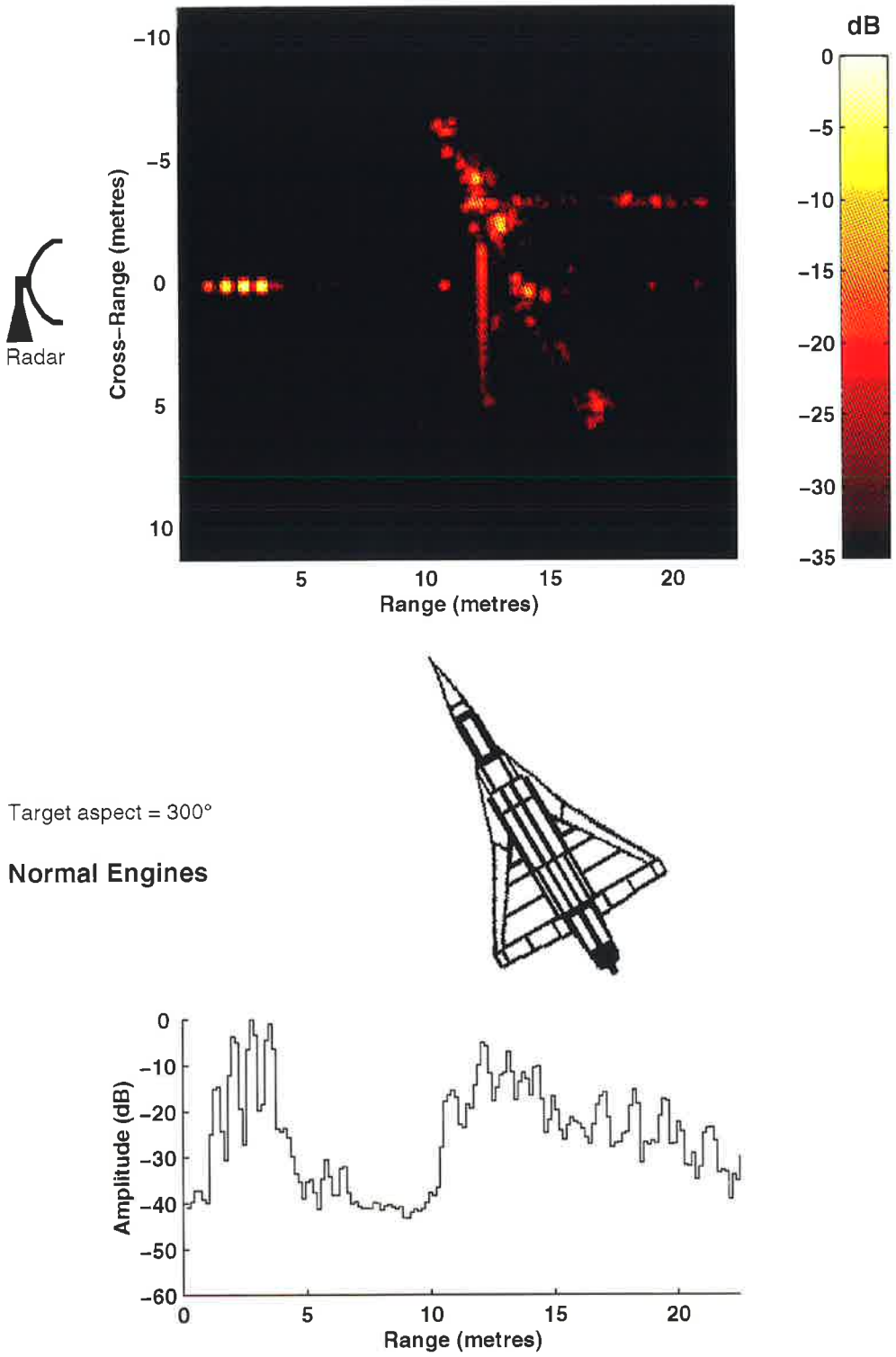

Figure D.11: An ISAR image and a HRRP of the Mirage aircraft viewed from an aspect of 300°. The polarisation is H–H and the engines are in the normal state.

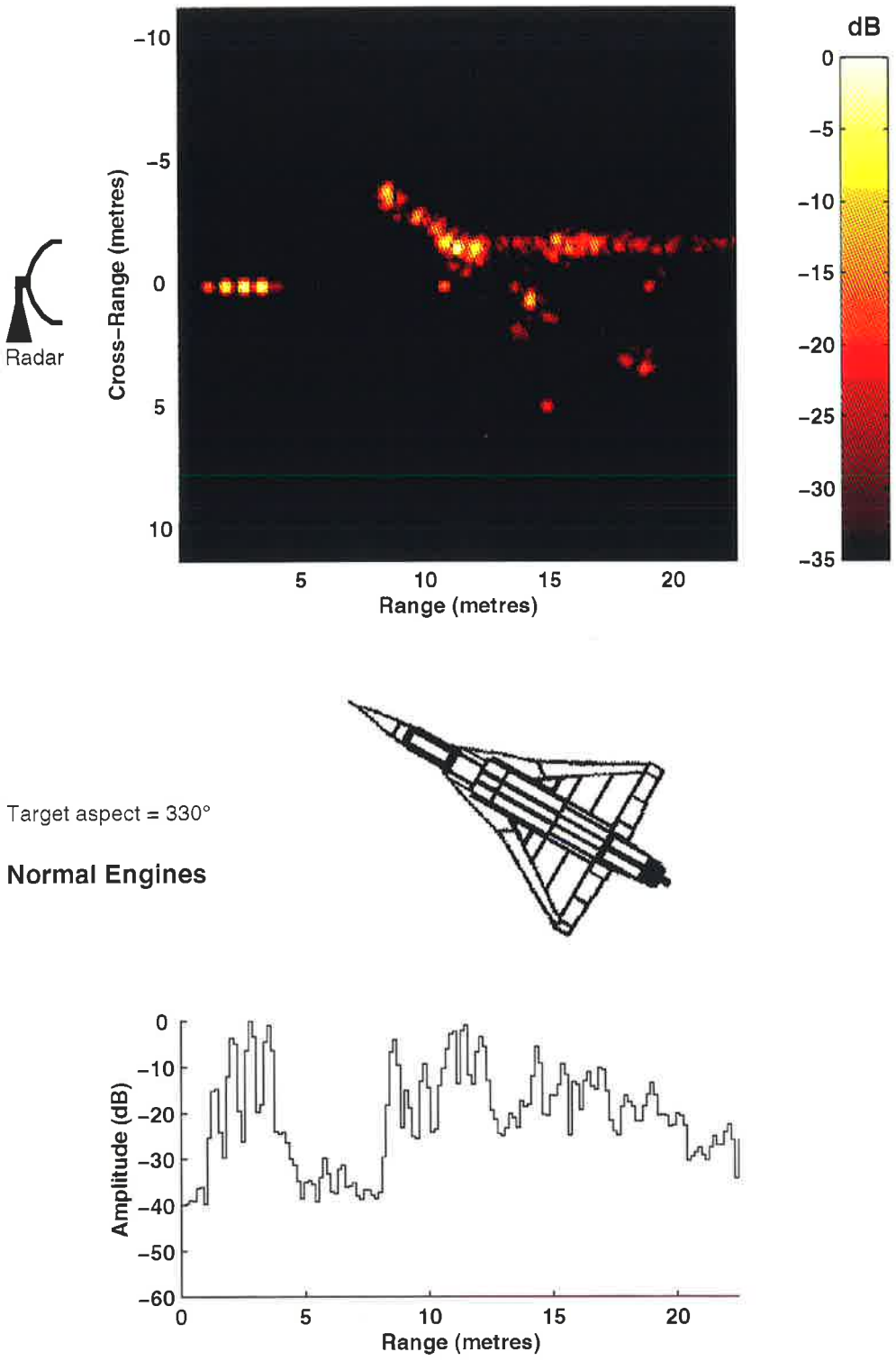

Figure D.12: An ISAR image and a HRRP of the Mirage aircraft viewed from an aspect of 330°. The polarisation is H–H and the engines are in the normal state.

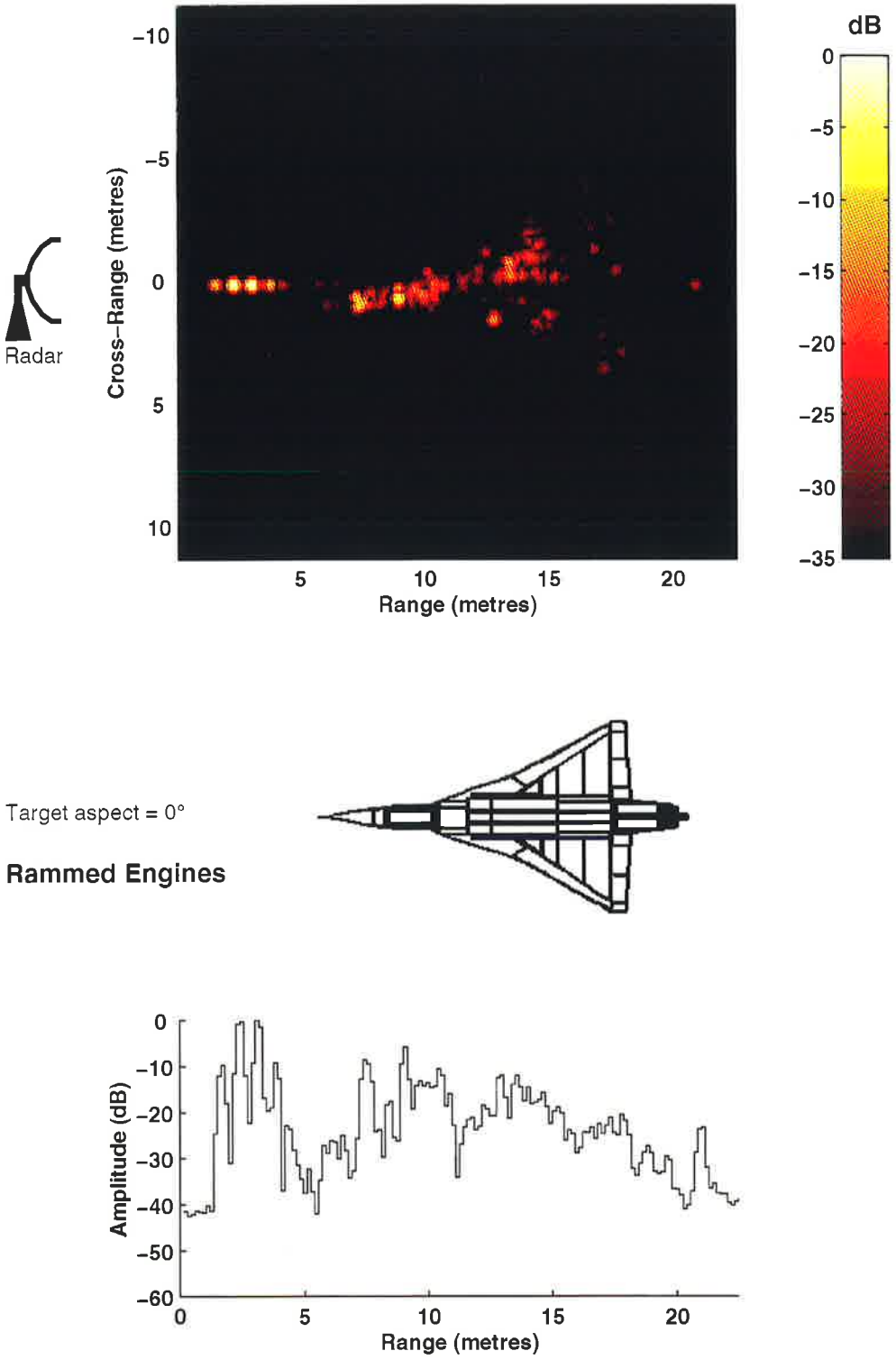

Figure D.13: An ISAR image and a HRRP of the Mirage aircraft viewed from an aspect of 0°. The polarisation is V–V and the engines are in the rammed state.

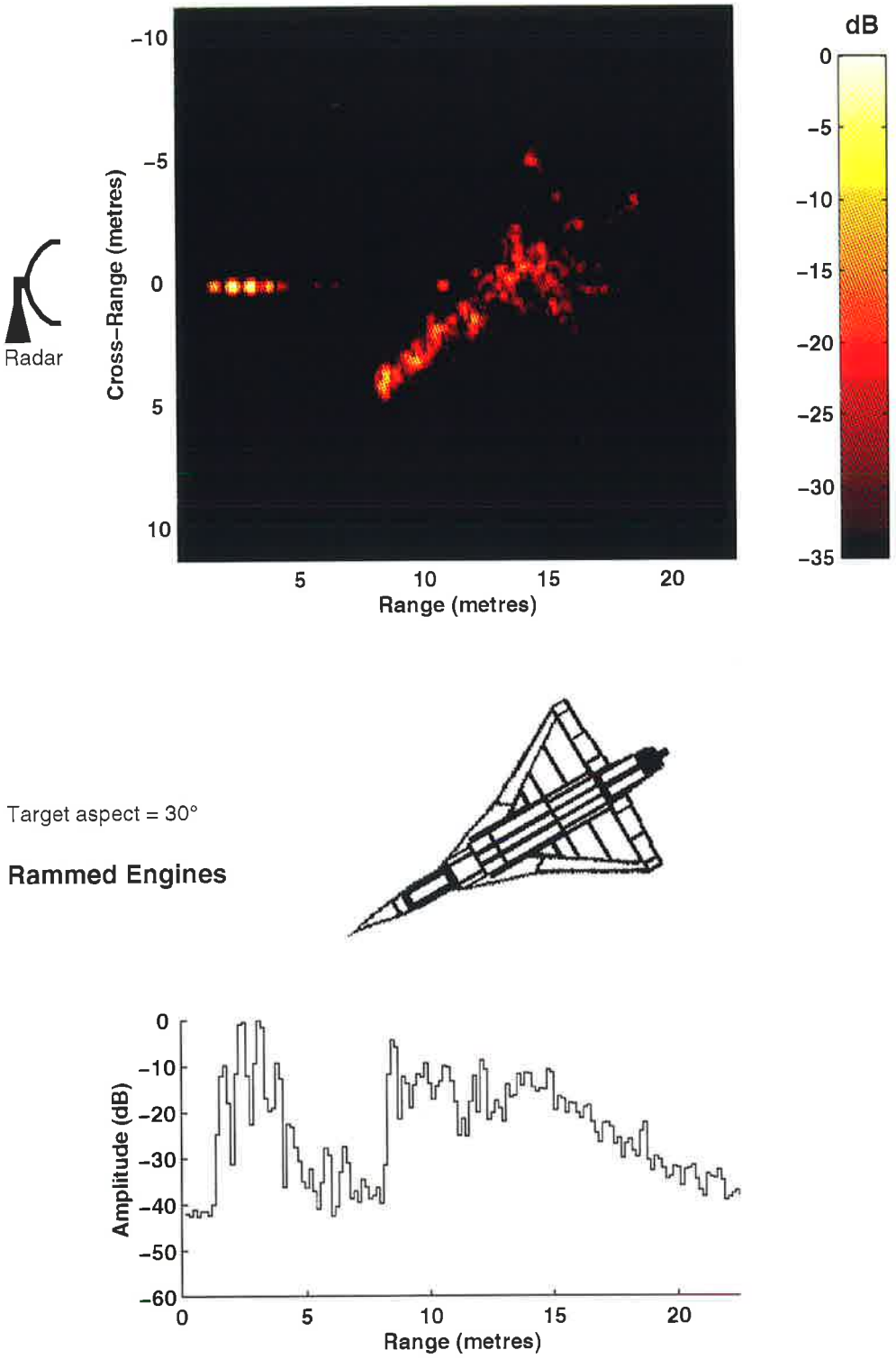

Figure D.14: An ISAR image and a HRRP of the Mirage aircraft viewed from an aspect of 30°. The polarisation is V–V and the engines are in the rammed state.

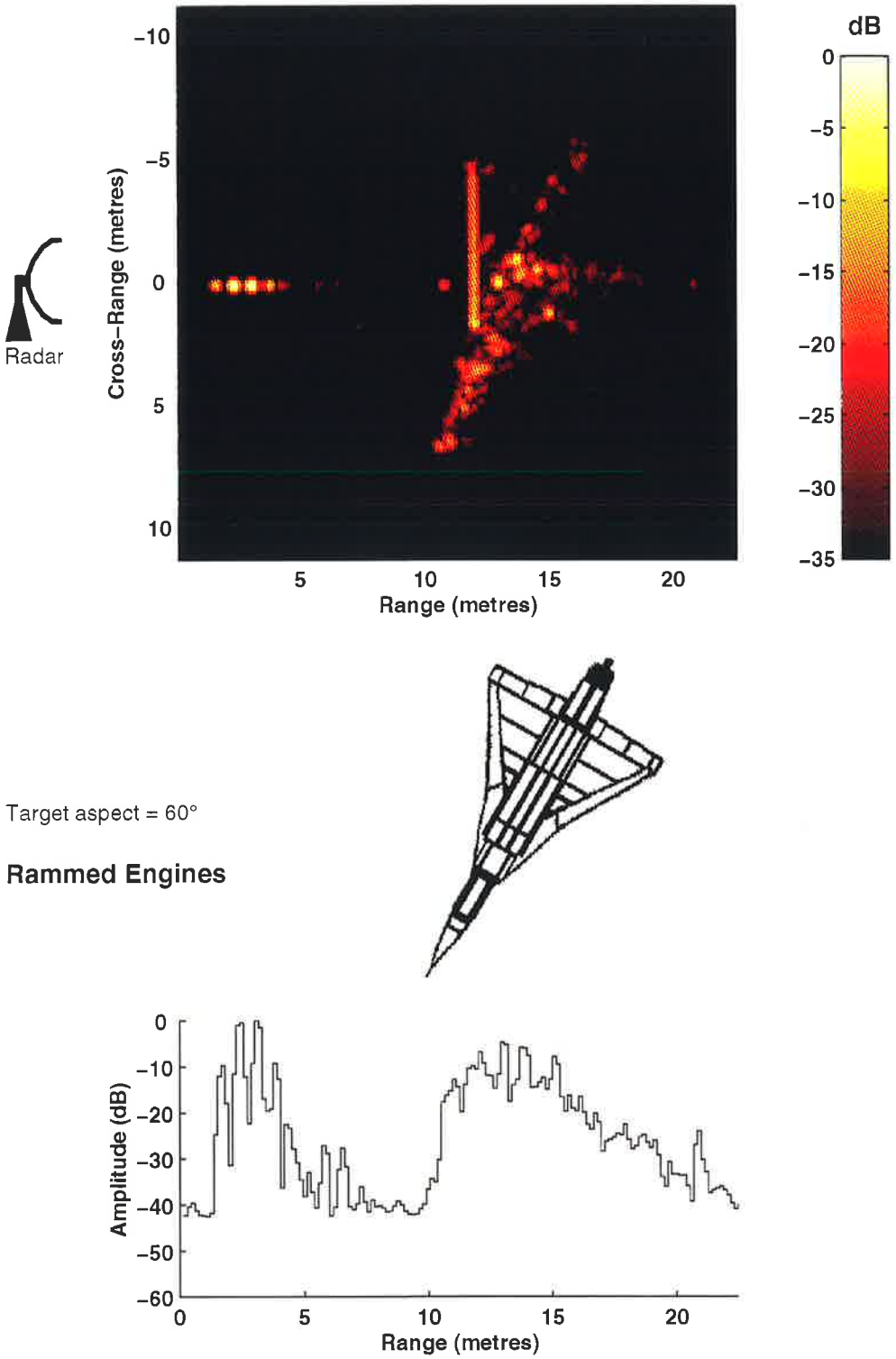

Figure D.15: An ISAR image and a HRRP of the Mirage aircraft viewed from an aspect of 60°. The polarisation is V–V and the engines are in the rammed state.

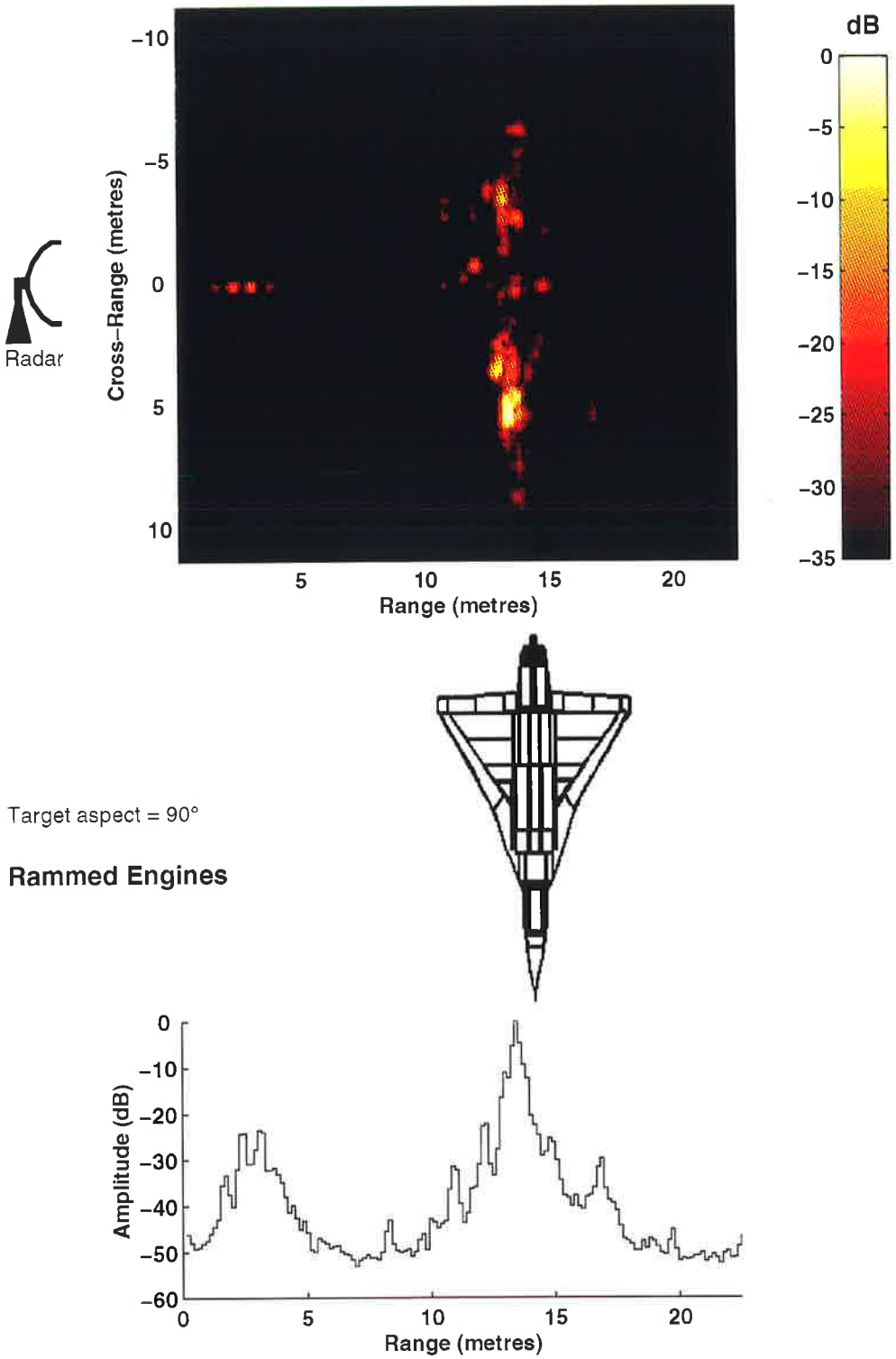

Figure D.16: An ISAR image and a HRRP of the Mirage aircraft viewed from an aspect of 90°. The polarisation is V–V and the engines are in the rammed state.

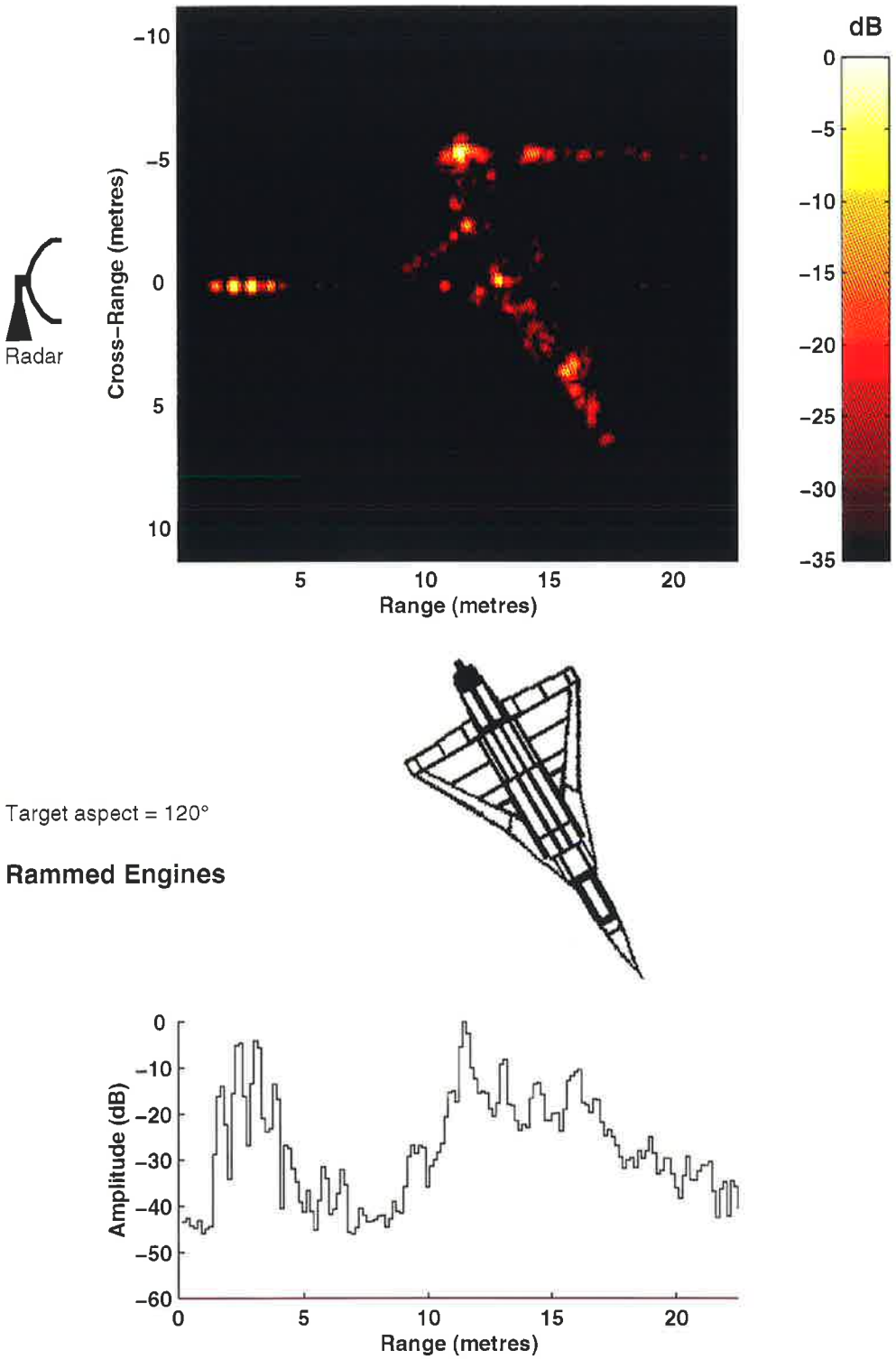

Figure D.17: An ISAR image and a HRRP of the Mirage aircraft viewed from an aspect of 120°. The polarisation is V–V and the engines are in the rammed state.

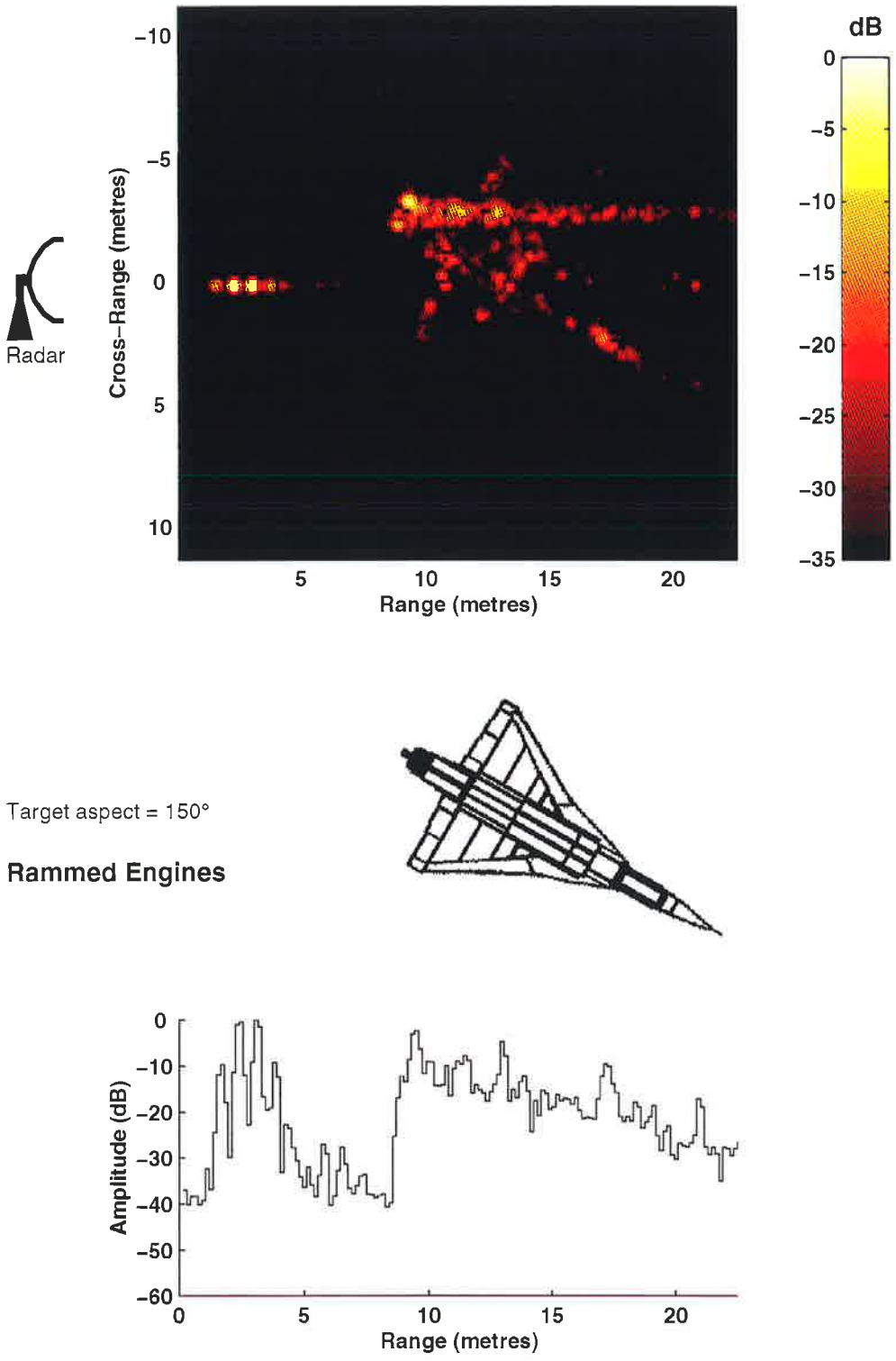

Figure D.18: An ISAR image and a HRRP of the Mirage aircraft viewed from an aspect of 150°. The polarisation is V–V and the engines are in the rammed state.

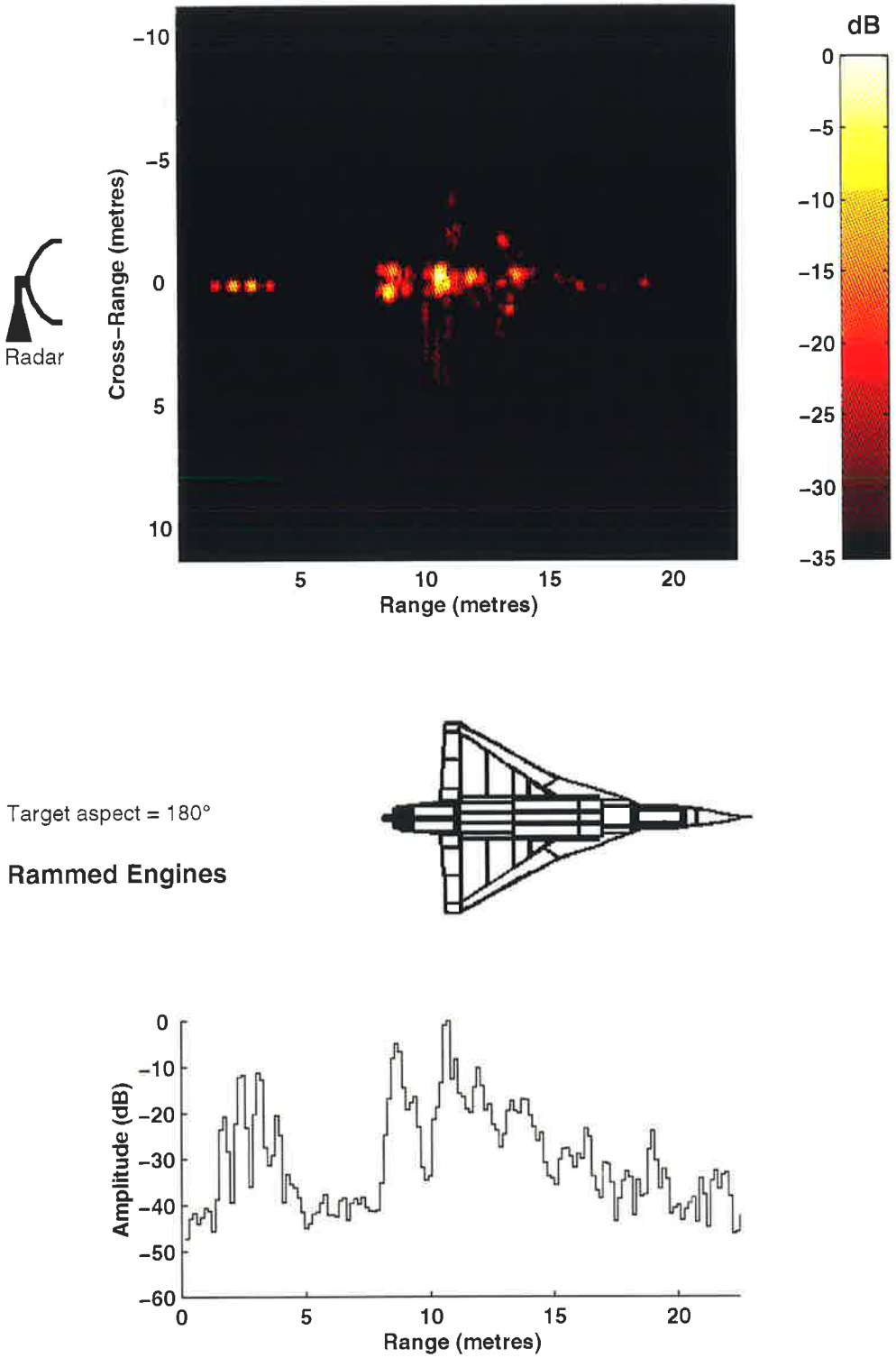

Figure D.19: An ISAR image and a HRRP of the Mirage aircraft viewed from an aspect of 180°. The polarisation is V–V and the engines are in the rammed state.

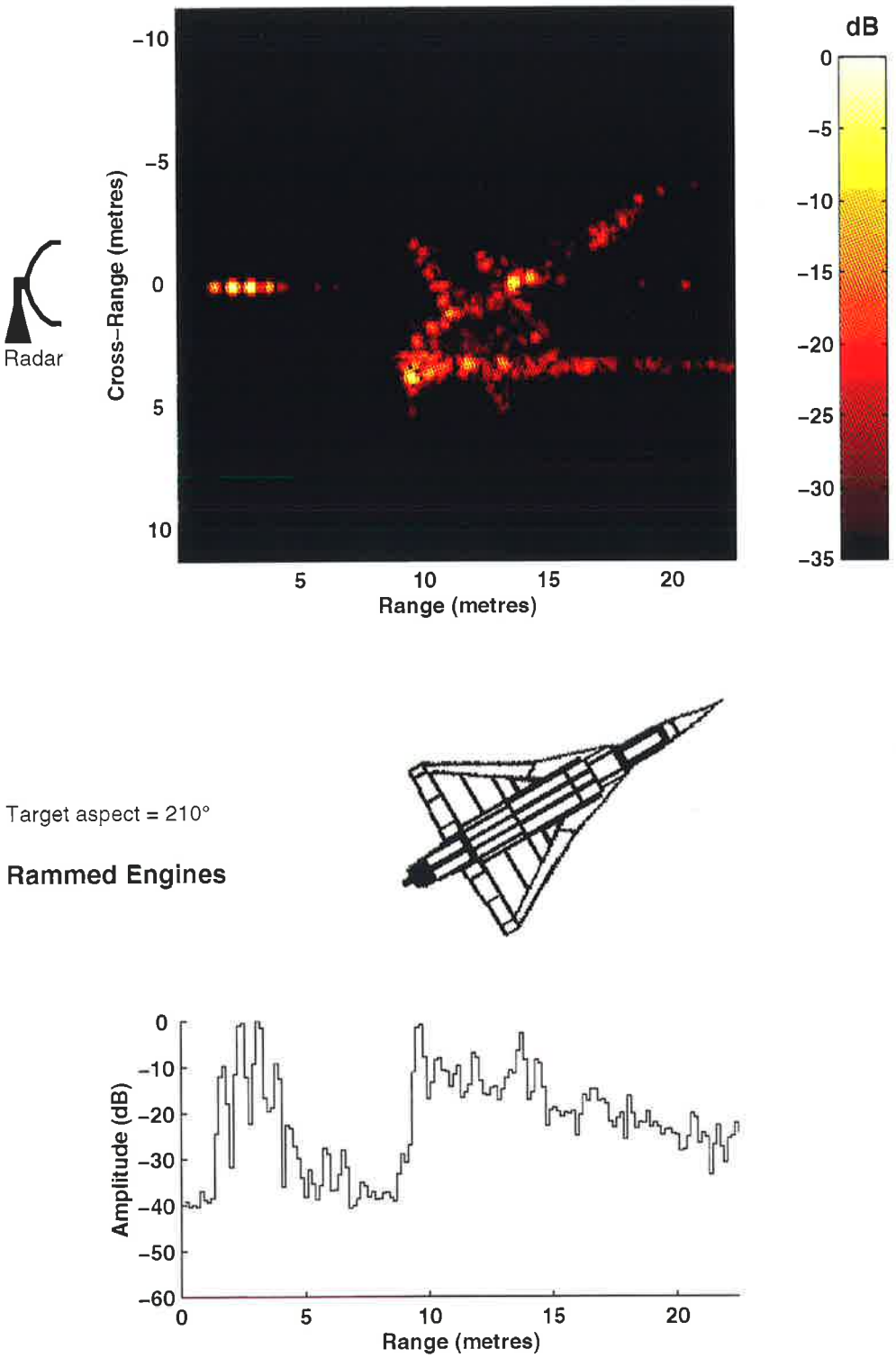

Figure D.20: An ISAR image and a HRRP of the Mirage aircraft viewed from an aspect of 210°. The polarisation is V–V and the engines are in the rammed state.

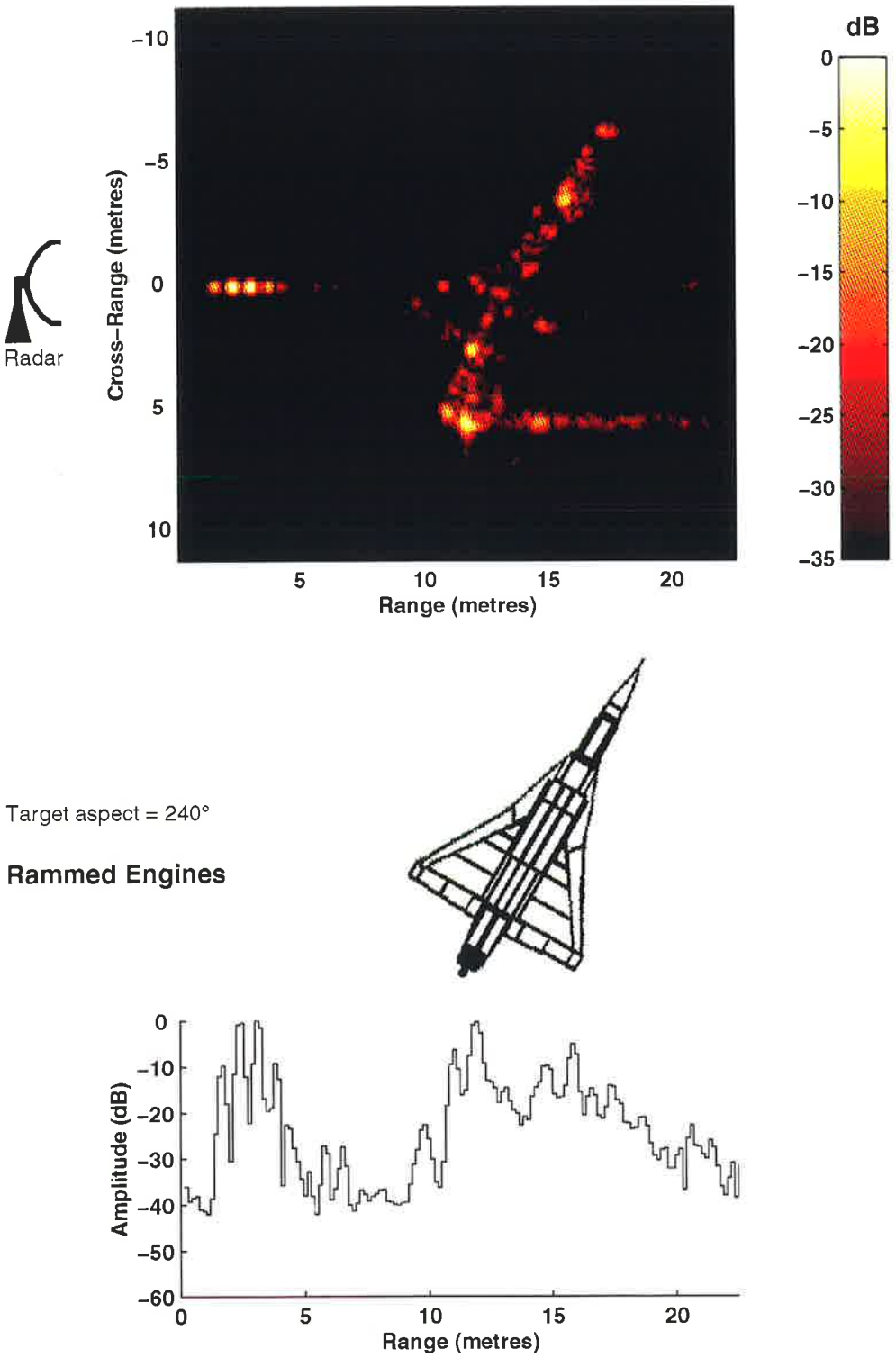

Figure D.21: An ISAR image and a HRRP of the Mirage aircraft viewed from an aspect of 240°. The polarisation is V–V and the engines are in the rammed state.

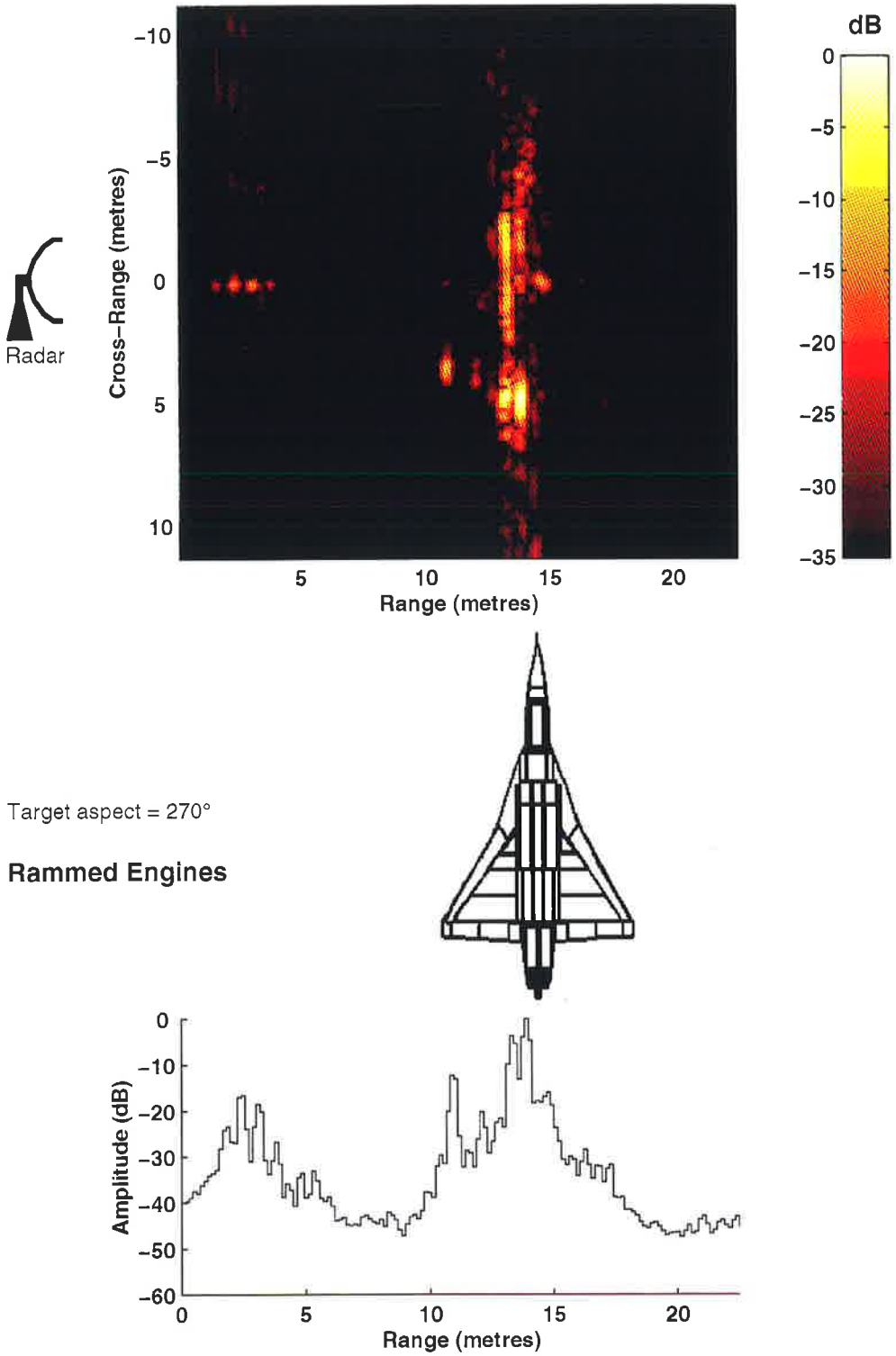

Figure D.22: An ISAR image and a HRRP of the Mirage aircraft viewed from an aspect of 270°. The polarisation is V–V and the engines are in the rammed state.

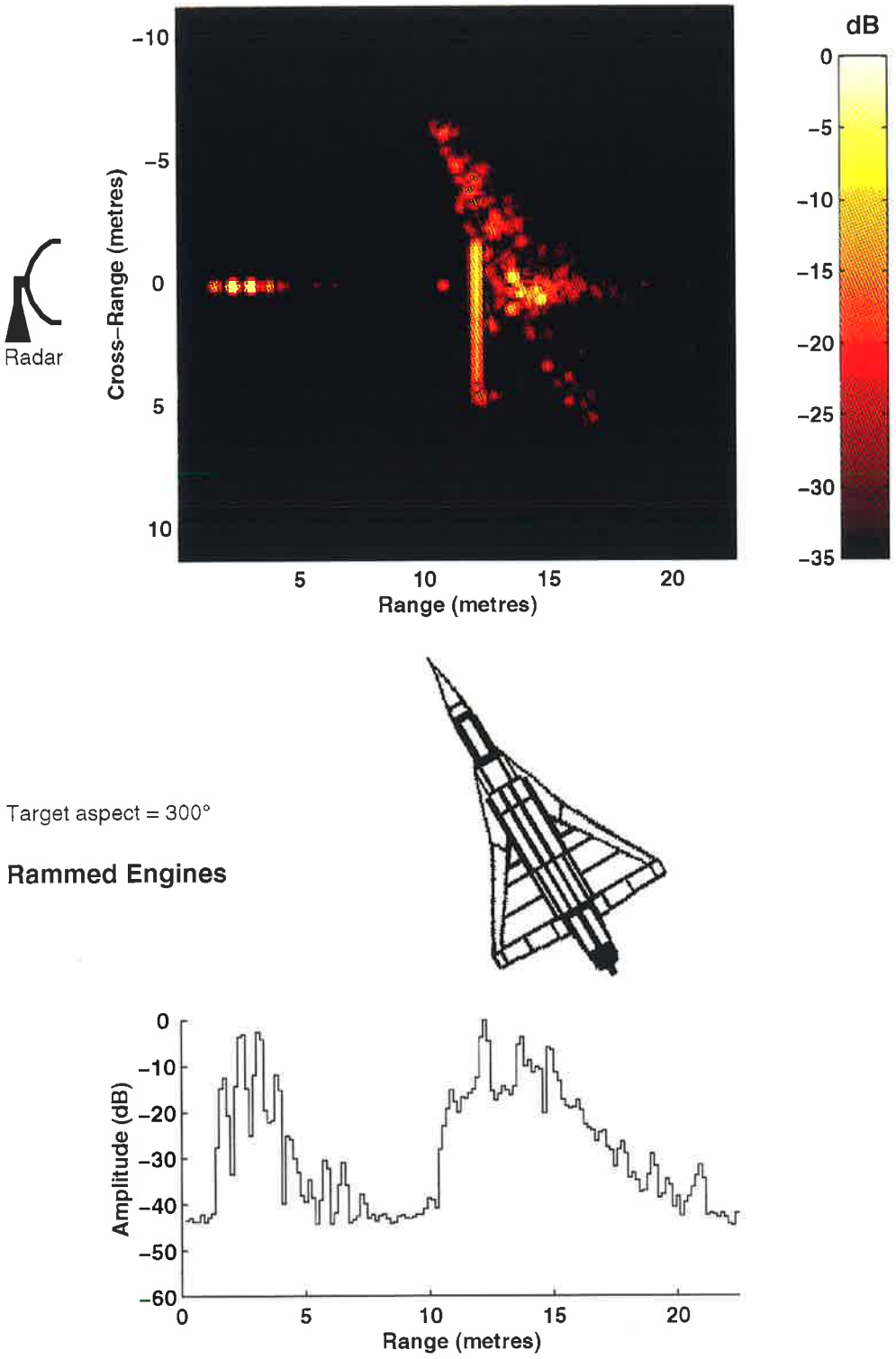

Figure D.23: An ISAR image and a HRRP of the Mirage aircraft viewed from an aspect of 300°. The polarisation is V–V and the engines are in the rammed state.

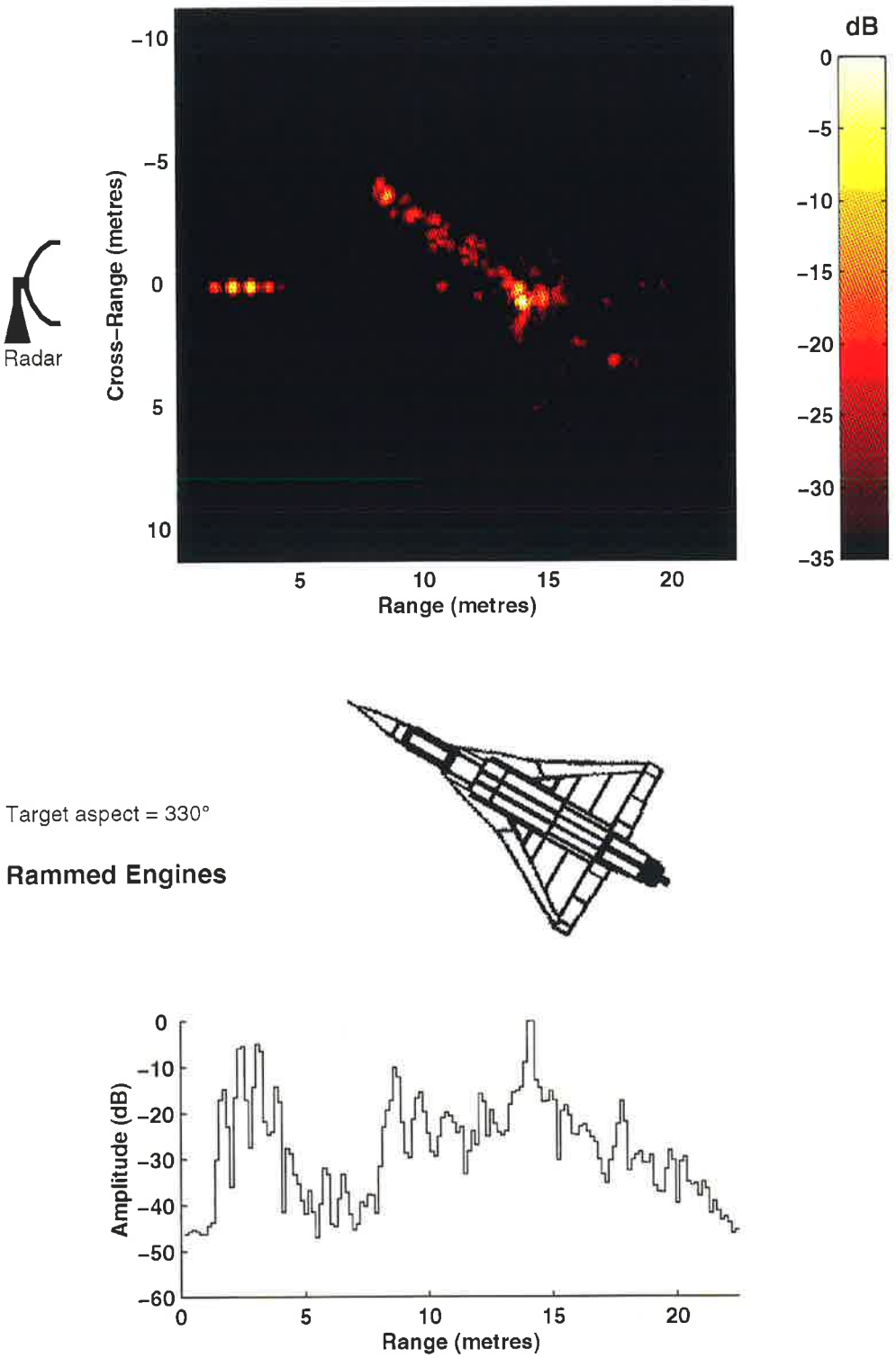

Figure D.24: An ISAR image and a HRRP of the Mirage aircraft viewed from an aspect of 330°. The polarisation is V–V and the engines are in the rammed state.

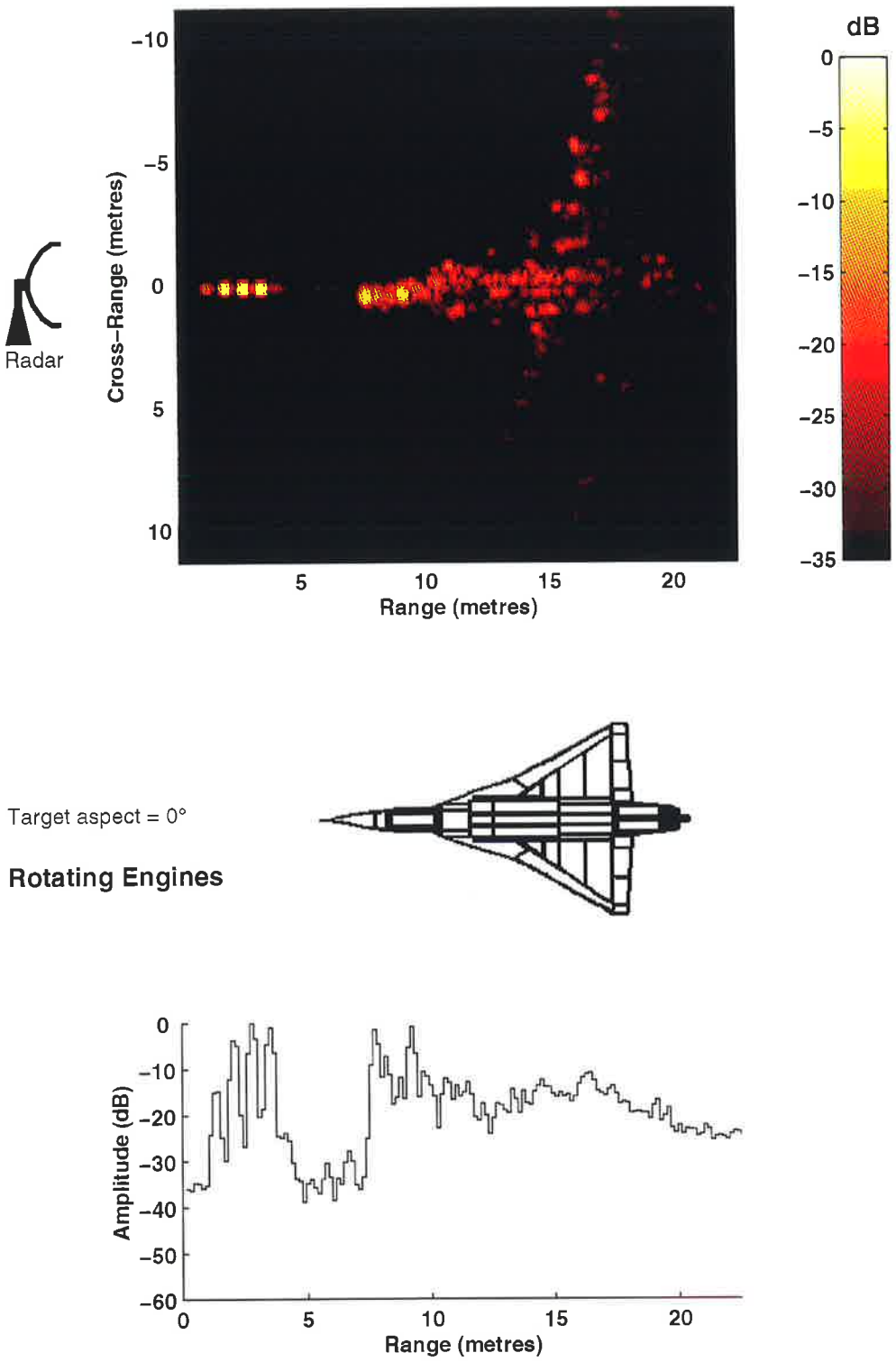

Figure D.25: An ISAR image and a HRRP of the Mirage aircraft viewed from an aspect of 0°. The polarisation is H–H and the engines are in the rotating state.

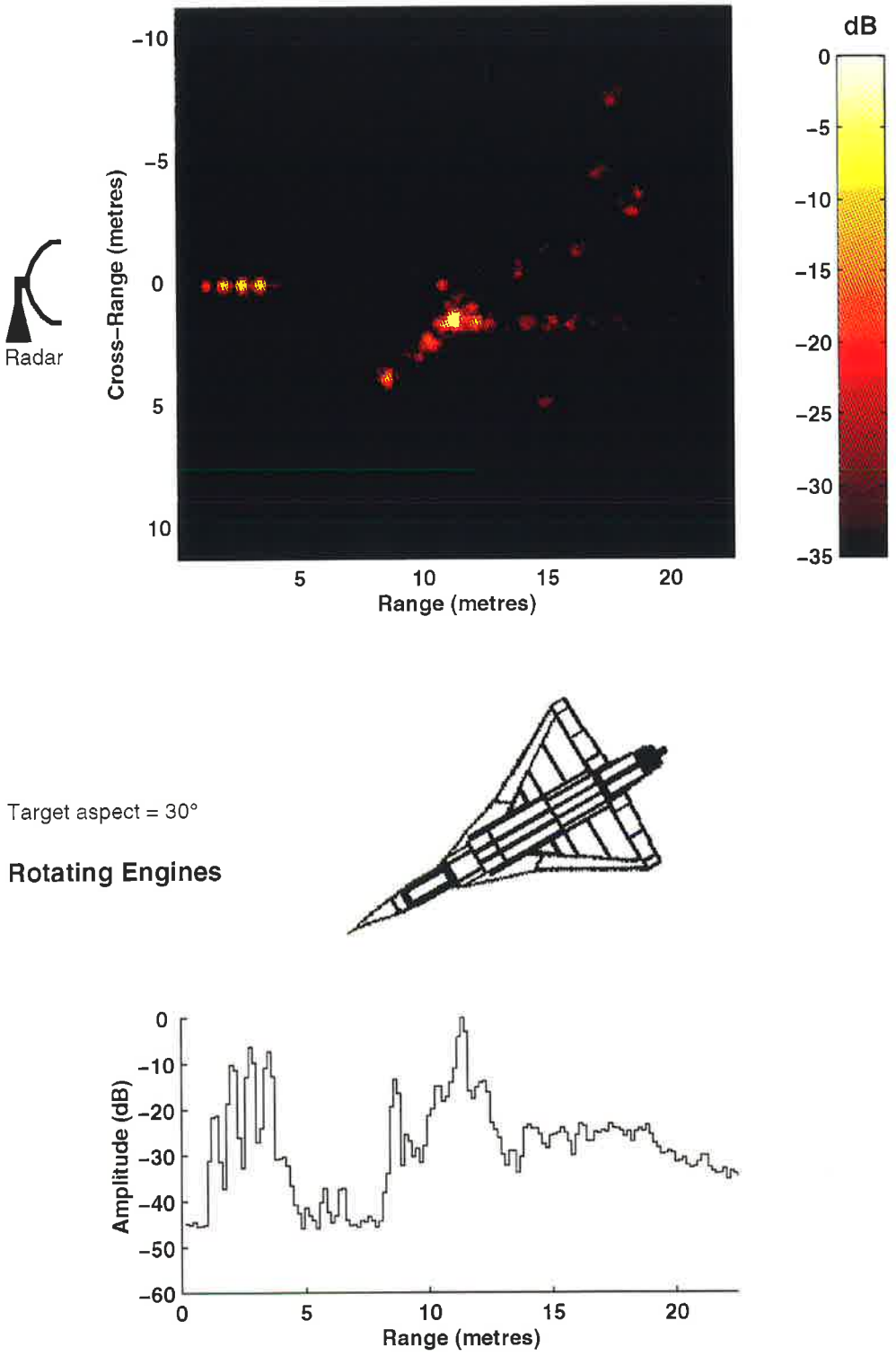

Figure D.26: An ISAR image and a HRRP of the Mirage aircraft viewed from an aspect of 30°. The polarisation is H–H and the engines are in the rotating state.

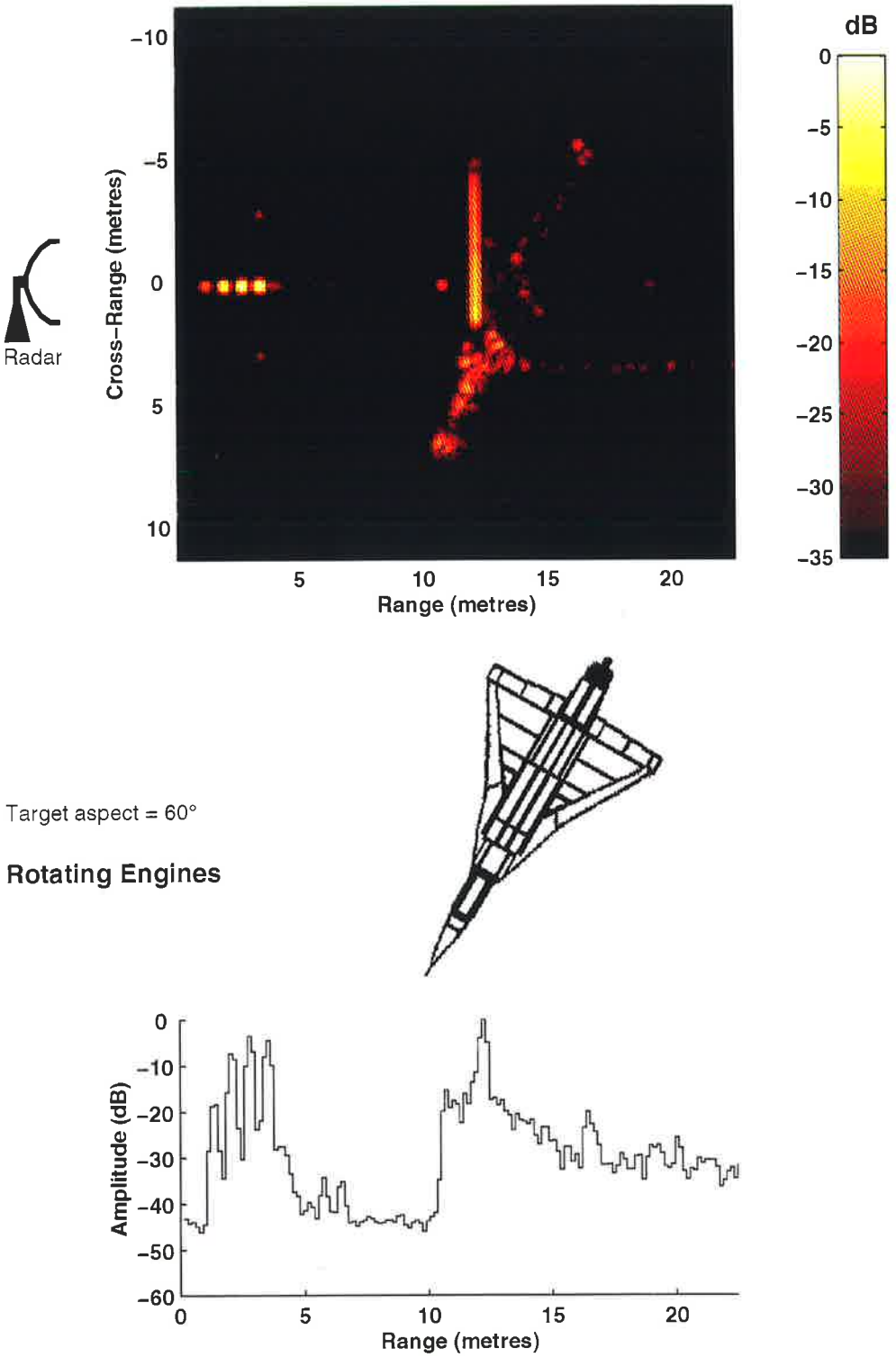

Figure D.27: An ISAR image and a HRRP of the Mirage aircraft viewed from an aspect of 60°. The polarisation is H–H and the engines are in the rotating state.

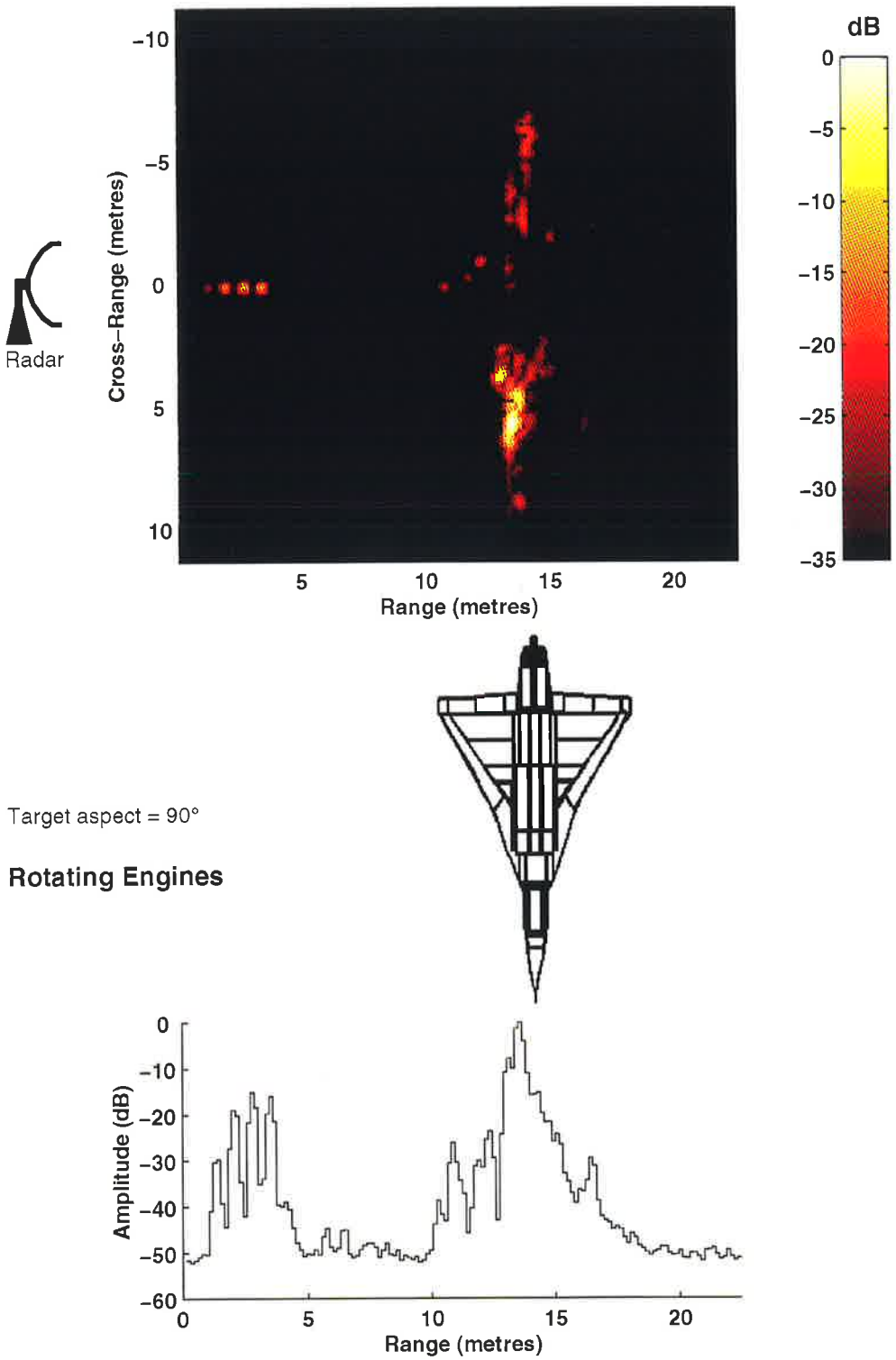

Figure D.28: An ISAR image and a HRRP of the Mirage aircraft viewed from an aspect of 90°. The polarisation is H–H and the engines are in the rotating state.

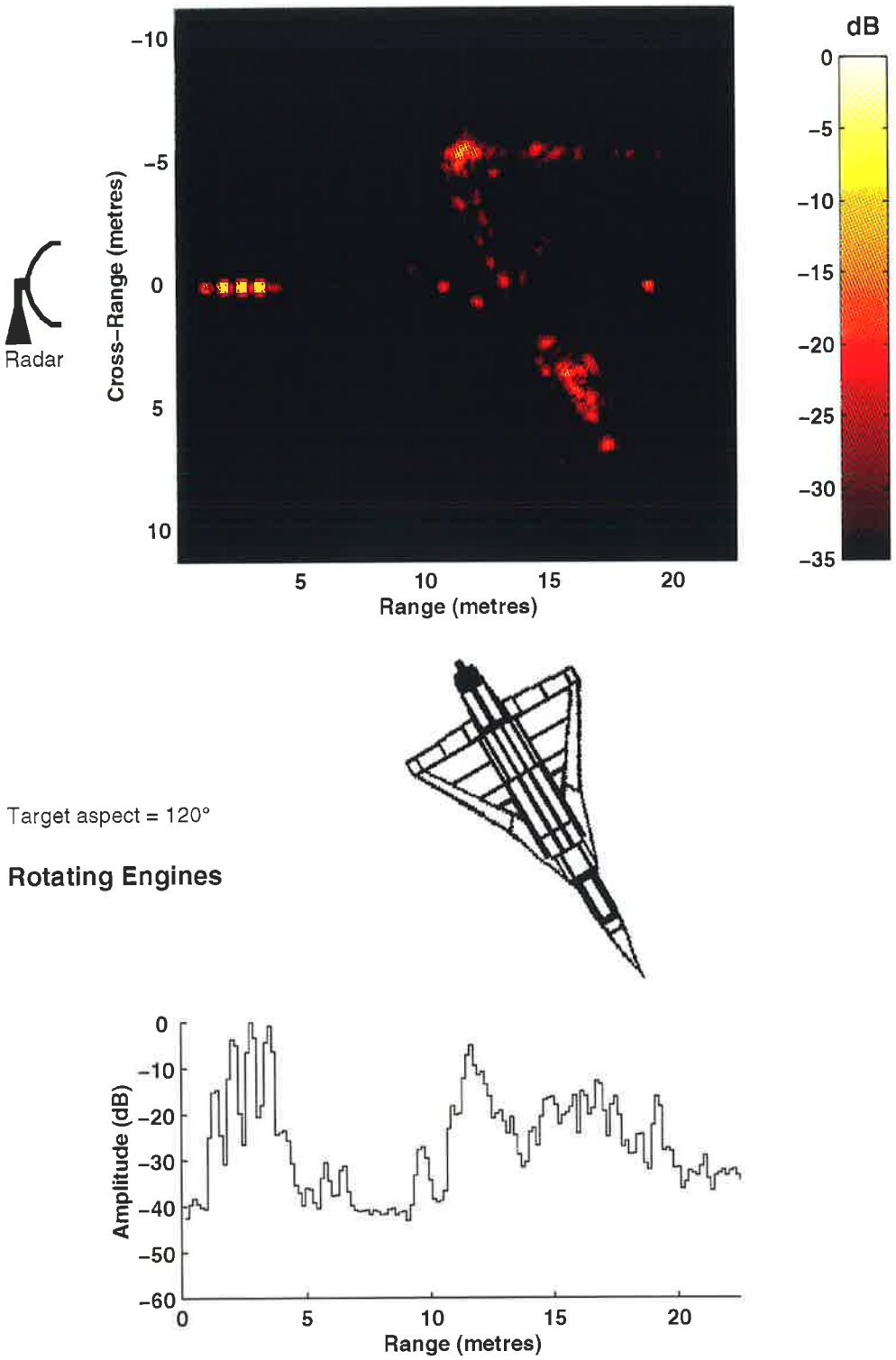

Figure D.29: An ISAR image and a HRRP of the Mirage aircraft viewed from an aspect of 120°. The polarisation is H–H and the engines are in the rotating state.

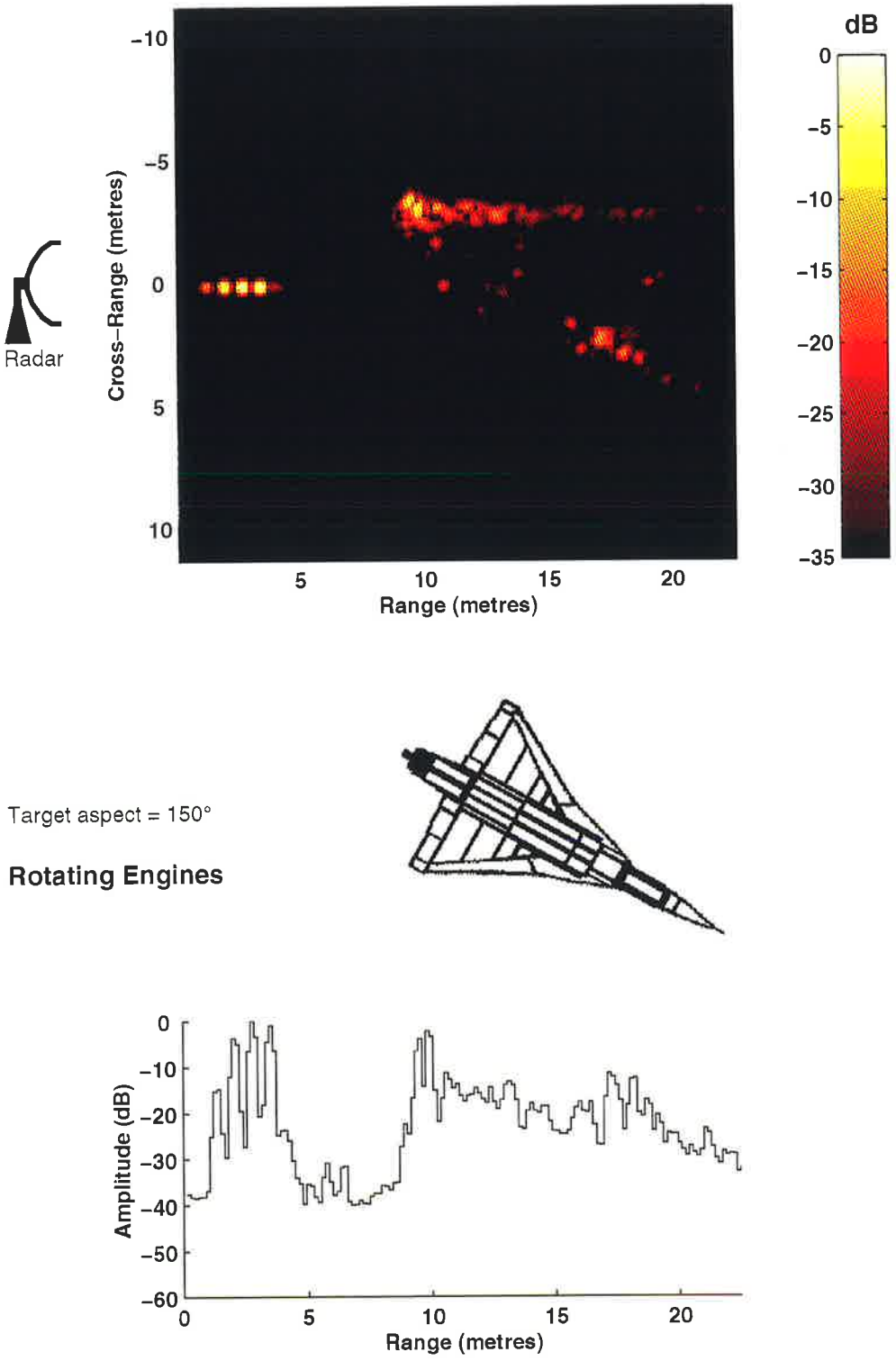

Figure D.30: An ISAR image and a HRRP of the Mirage aircraft viewed from an aspect of 150°. The polarisation is H–H and the engines are in the rotating state.

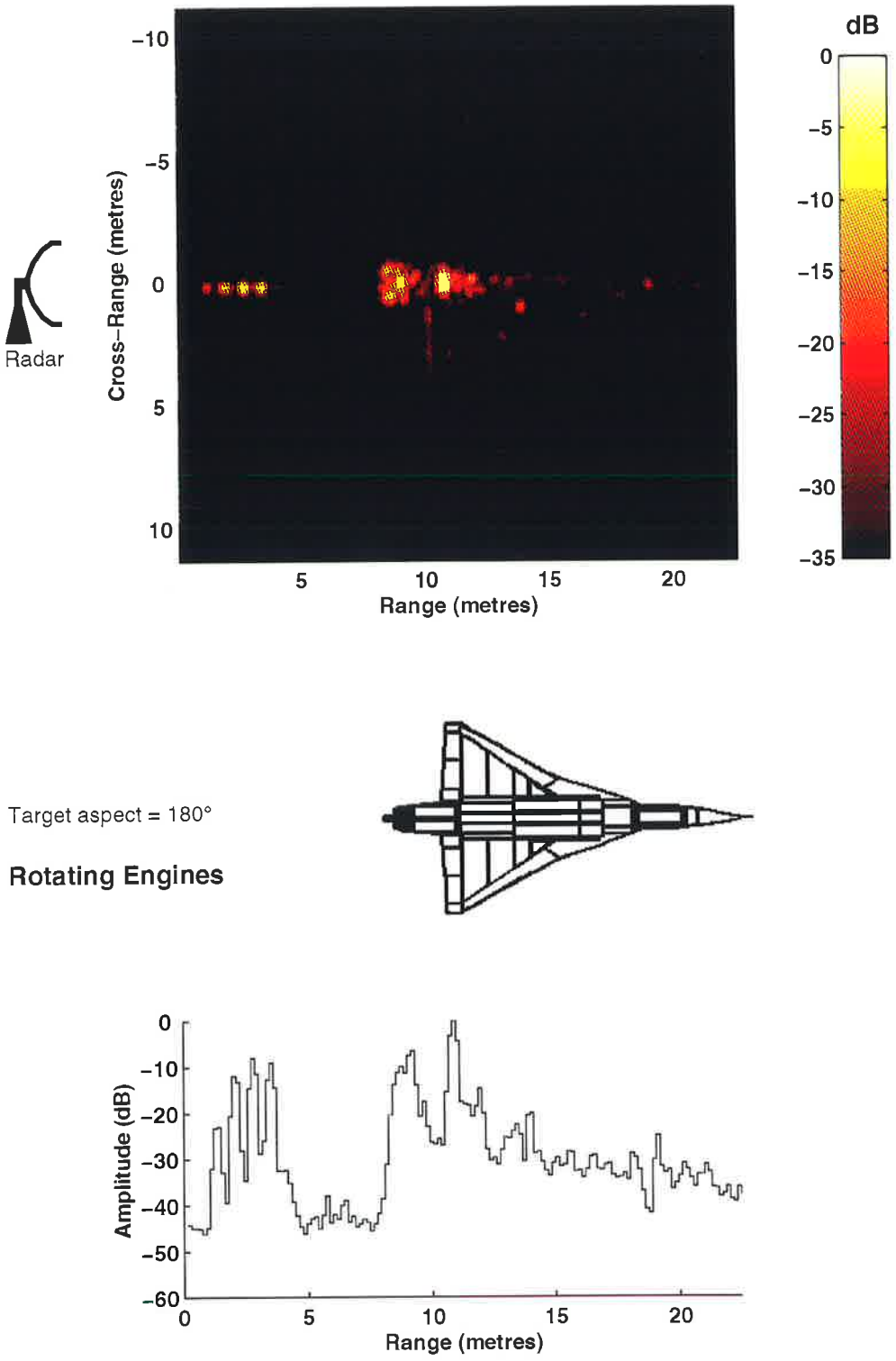

Figure D.31: An ISAR image and a HRRP of the Mirage aircraft viewed from an aspect of 180°. The polarisation is H–H and the engines are in the rotating state.

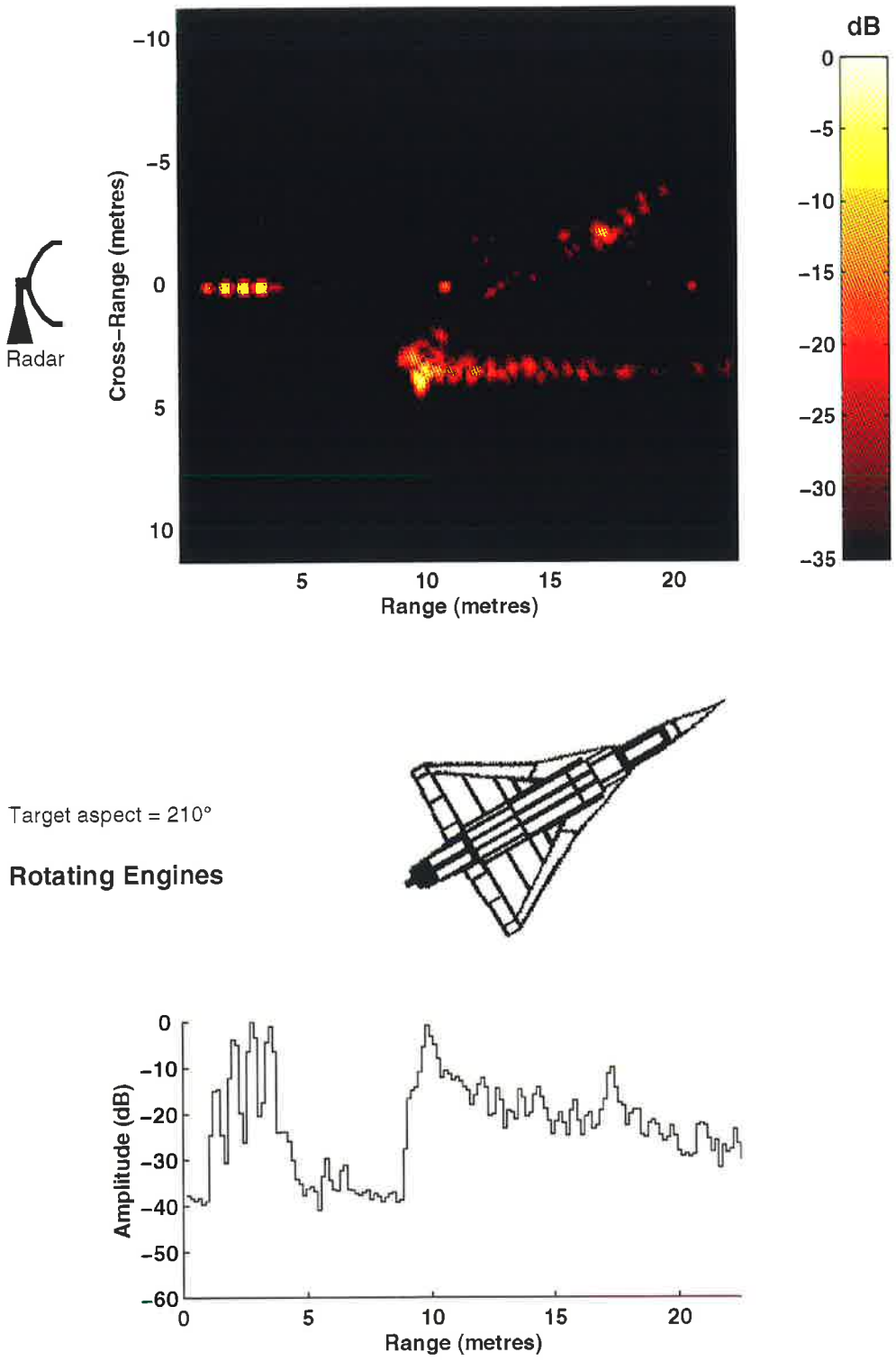

Figure D.32: An ISAR image and a HRRP of the Mirage aircraft viewed from an aspect of 210°. The polarisation is H–H and the engines are in the rotating state.

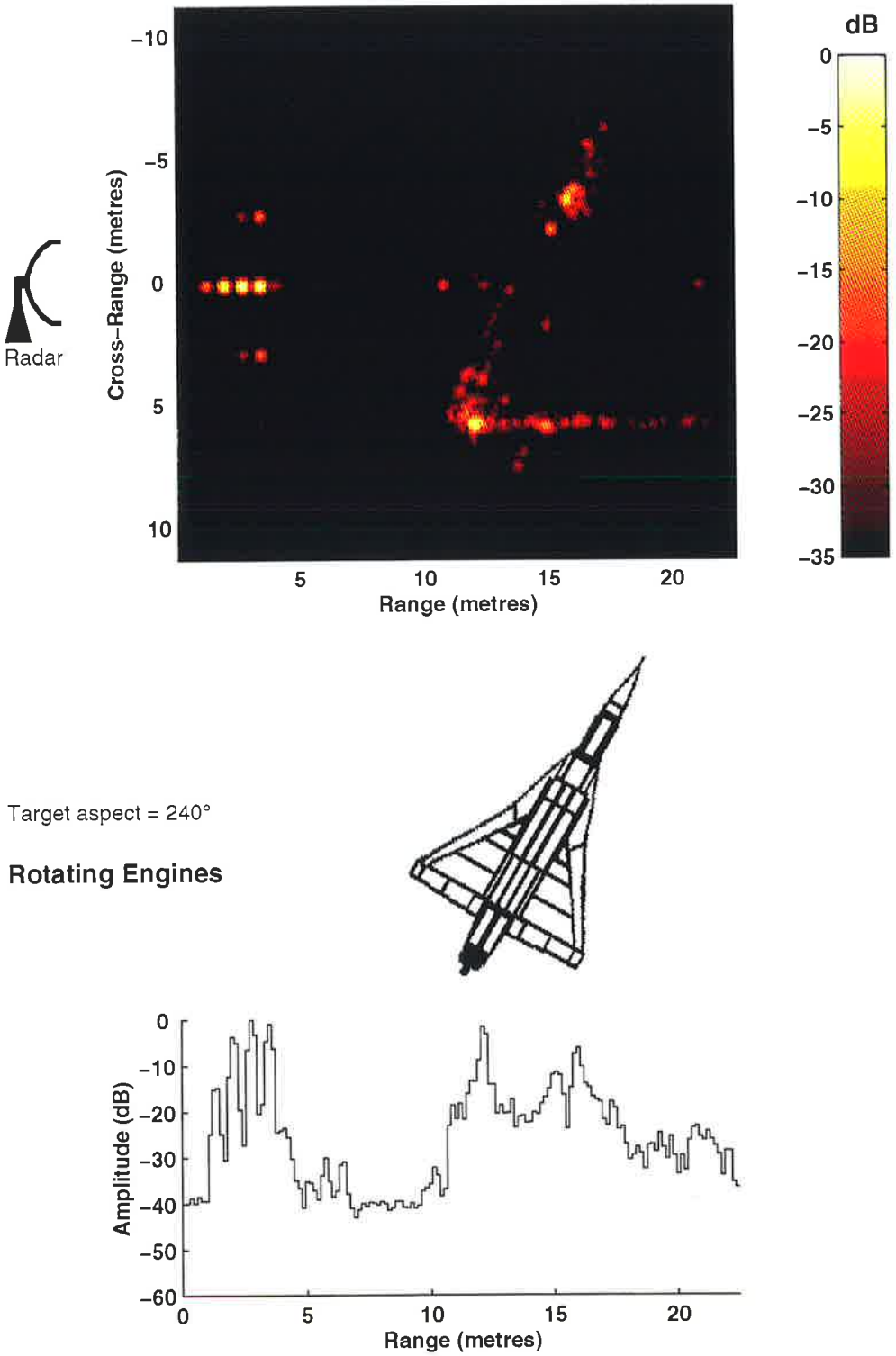

Figure D.33: An ISAR image and a HRRP of the Mirage aircraft viewed from an aspect of 240°. The polarisation is H–H and the engines are in the rotating state.

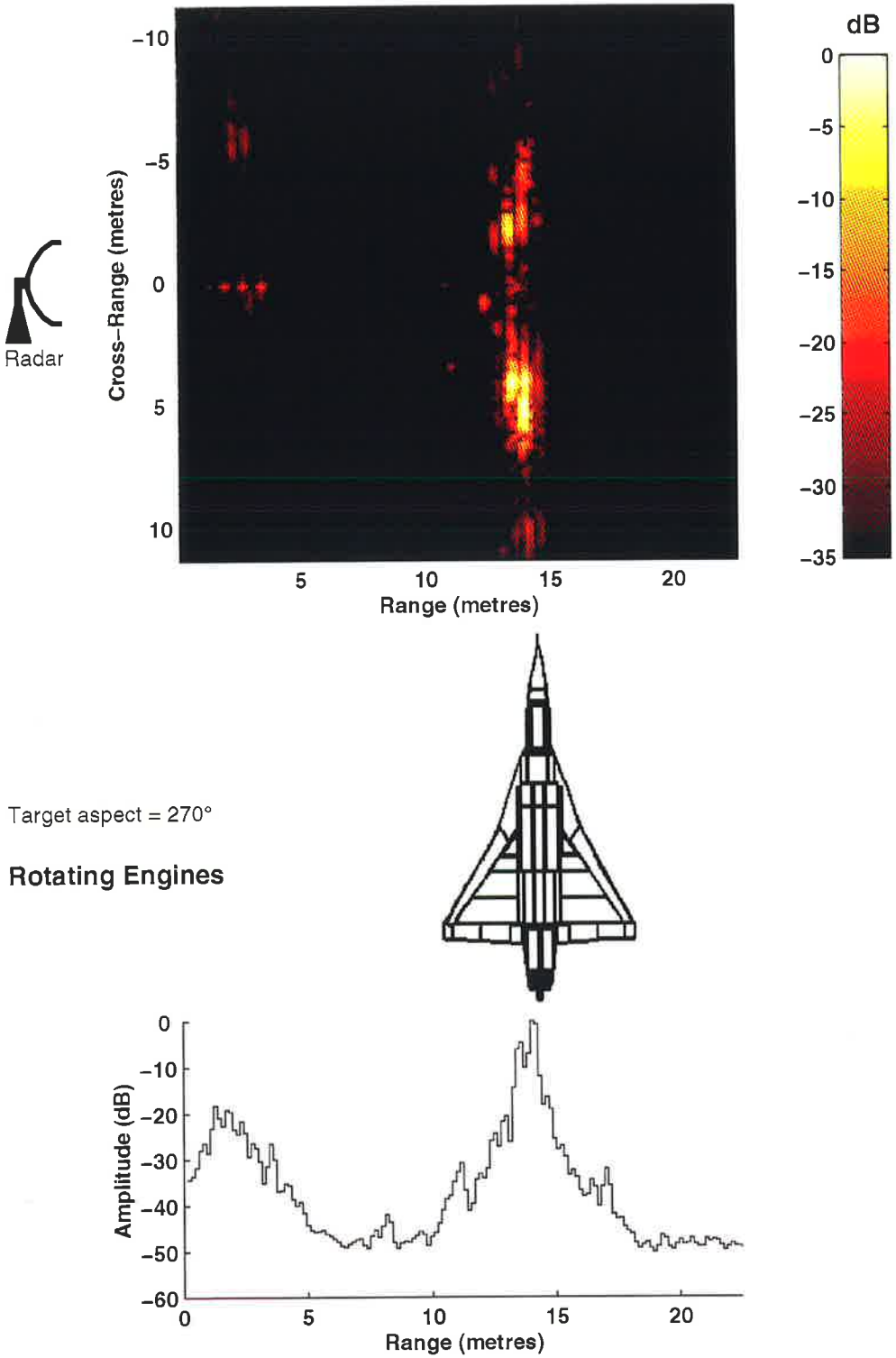

Figure D.34: An ISAR image and a HRRP of the Mirage aircraft viewed from an aspect of 270°. The polarisation is H–H and the engines are in the rotating state.

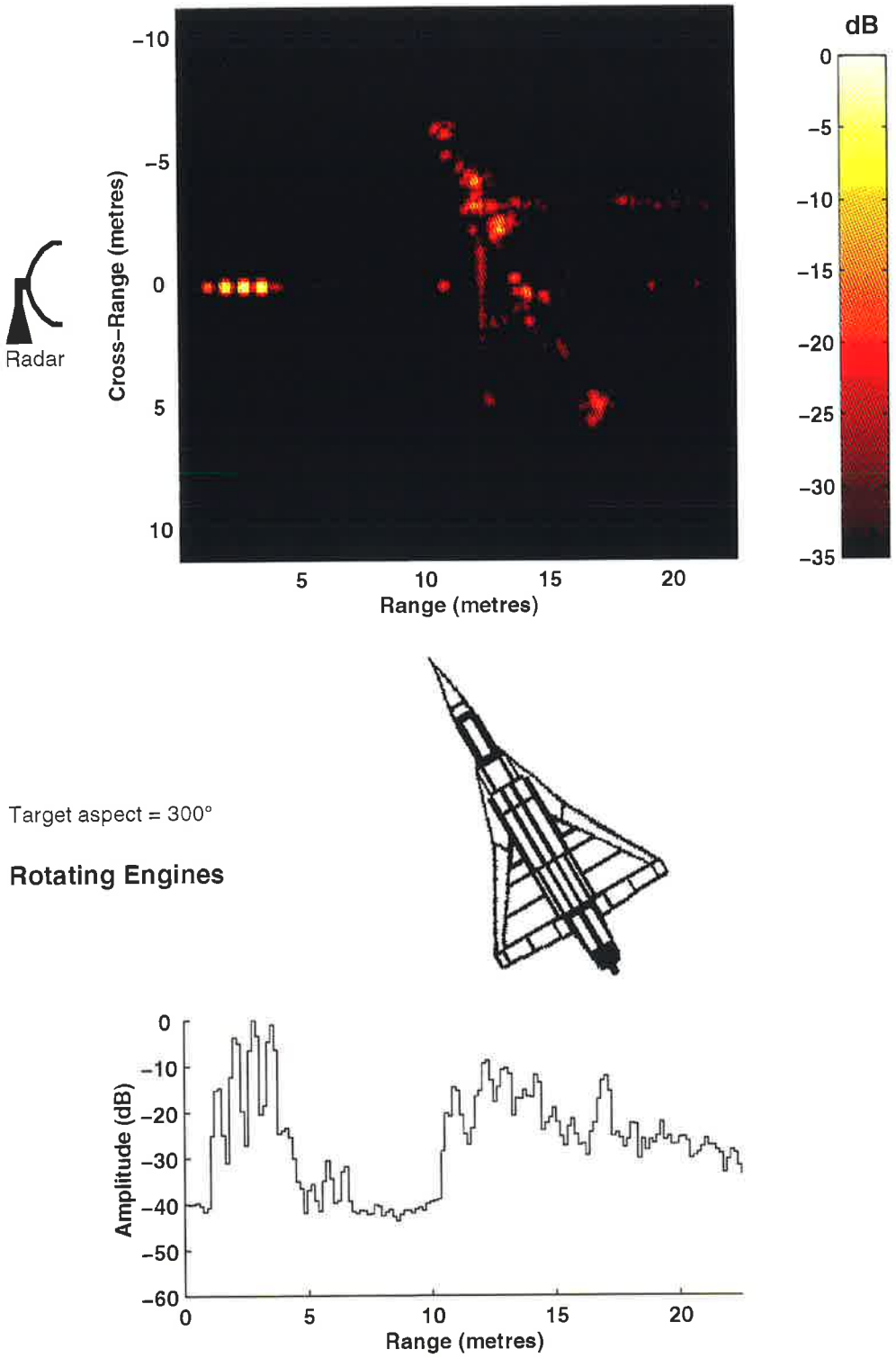

Figure D.35: An ISAR image and a HRRP of the Mirage aircraft viewed from an aspect of 300°. The polarisation is H–H and the engines are in the rotating state.

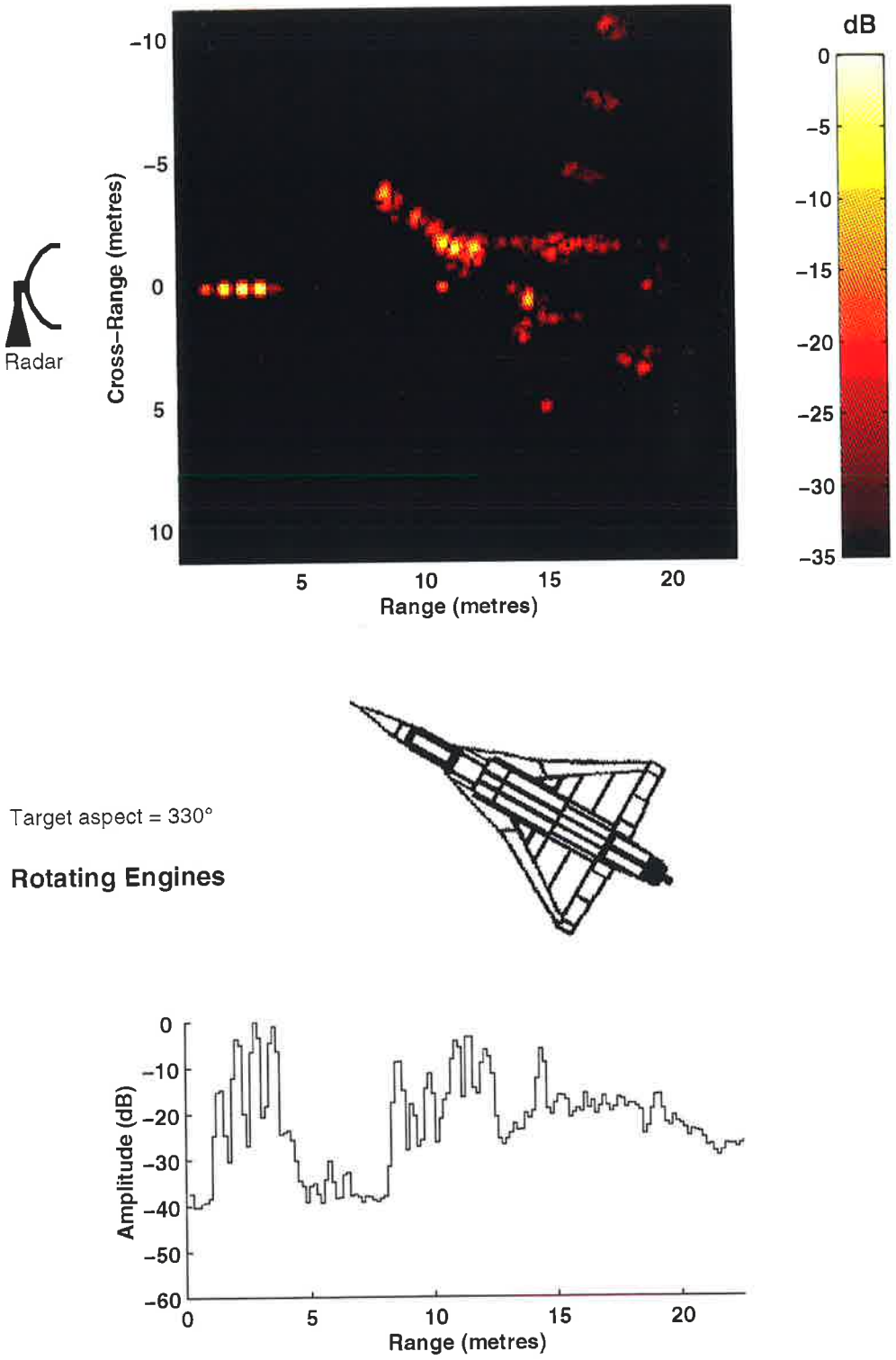

Figure D.36: An ISAR image and a HRRP of the Mirage aircraft viewed from an aspect of 330°. The polarisation is H–H and the engines are in the rotating state.

Appendix E

PUBLICATIONS

October 1993

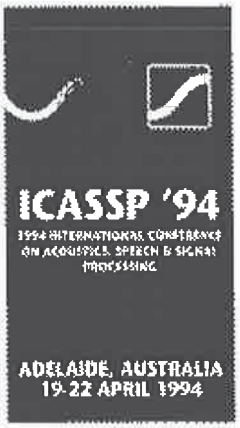

Dr Anthony Zyweck
The Cooperative Research Centre for Sensor Signal and Information Processing
Technology Park
THE LEVELS SA 5095
AUSTRALIA

Dear Author,
470/2.5 - Radar Target Recognition using Range Profiles

I am happy to inform you that your paper, detailed above has been accepted for presentation at ICASSP 94, which will be held in Adelaide, South Australia, 19-22 April 1994. Your Author's Kit will be mailed to you within the next couple of weeks. This will include the date and time of your presentation and type of presentation ie poster or lecture, as well as registration and accommodation information.

Please note you must register and pay the registration fee by the closing date for the receipt of camera ready papers, 17 December 1993, as a commitment to attend, or your paper may not be included in the published proceedings.

I would like to stress that the 17 December deadline is not flexible. Late December is a traditional holiday period in Australia, with most businesses closing down between 25 December to 3 January, as this is our summer vacation.

Please be aware that any correspondence, including courier deliveries will need to be dispatched well in advance of the 17 December deadline.

An advance technical program and regular updates will be available by anonymous ftp on ftp.qut.edu.au in the file papers/sprc/icassp/program. Please check the latest program ahead of your travelling, as changes in the program may affect you. Please note that security at this ftp site limits access to correctly configured Internet machines.

We look forward to seeing you at ICASSP 94.

Yours sincerely,

Prof Boualem Boashash
TECHNICAL PROGRAM CHAIRMAN
ICASSP 94.
ICASSPAU.LET

Zyweck, A., and Boger, R.E., (1994) Radar target recognition using range profiles. *ICASSP '94., 1994 IEEE International Conference on Acoustics, Speech, and Signal Processing, v. ii, pp. 373-376.*

October 1993

Dr Anthony Zyweck
Defence Science and Technology Organisation
CSSIP,SRI Building
Technology Park
THE LEVELS SA 5095
AUSTRALIA

Dear Author,

459/6.3 - ISARLAB: A Radar Signal Processing Tool

I am happy to inform you that your paper, detailed above has been accepted for presentation at ICASSP 94, which will be held in Adelaide, South Australia, 19-22 April 1994. Your Author's Kit will be mailed to you within the next couple of weeks. This will include the date and time of your presentation and type of presentation ie poster or lecture, as well as registration and accommodation information.

Please note you must register and pay the registration fee by the closing date for the receipt of camera ready papers, 17 December 1993, as a commitment to attend, or your paper may not be included in the published proceedings.

I would like to stress that the 17 December deadline is not flexible. Late December is a traditional holiday period in Australia, with most businesses closing down between 25 December to 3 January, as this is our summer vacation.

Please be aware that any correspondence, including courier deliveries will need to be dispatched well in advance of the 17 December deadline.

An advance technical program and regular updates will be available by anonymous ftp on ftp.qut.edu.au in the file papers/sprc/icassp/program. Please check the latest program ahead of your travelling, as changes in the program may affect you. Please note that security at this ftp site limits access to correctly configured Internet machines.

We look forward to seeing you at ICASSP 94.

Yours sincerely,

Prof Boualem Boashash
TECHNICAL PROGRAM CHAIRMAN
ICASSP 94.

ICASSPAUL.E1

Haywood, B., Zyweck, A., and Kyprianou, R., (1994) ISARLAB: a radar signal processing tool.
ICASSP '94., 1994 IEEE International Conference on Acoustics, Speech, and Signal Processing, v. v, pp. 177-180.

IEEE

TRANSACTIONS ON ANTENNAS AND PROPAGATION

Dr. Ronald J. Marhefka
Editor

April 20, 1994

PLEASE REPLY TO:
The Ohio State University
ElectroScience Laboratory
1320 Kinnear Road
Columbus, OH 43212-1191 USA
Tel: (614) 292-5049
Fax: (614) 292-7297
E-mail: apstrans@tiger.eng.ohio-state.edu

Mr. Anthony Zyweck
The Centre for Sensor Signal and Information Processing
SPRI Building
Technology Park
The Levels, Pooraka 5095
AUSTRALIA

Paper No.: C-12-3-434

Title: High Resolution Radar Signatures of the Mirage III Aircraft.

Dear Mr. Zyweck:

It is my pleasure to inform you that the editorial board has recommended that your contribution be published in the IEEE *Transactions on Antennas and Propagation*.
Before your manuscript can be published, however, we must receive the following items:

- ✓ Original Figures
- ✓ List of Figures
- ____ Biographical Sketch(es) and Photo(s)
- ____ Copyright Form
- ____ Page Charge Form
- ✓ Electronic Version

Please forward these items as soon as possible.

If you can provide your manuscript in an electronic format on a computer disk please do so. The IEEE may be able to use the disk to increase the speed and accuracy with which your paper is typeset. It should be accompanied with complete identification of what word processor or other program was used to produce it. And, of course, the electronic version of the manuscript must contain all updates and other information that the final hardcopy manuscript contains.

Thank you.

Sincerely,

Ronald J. Marhefka
Editor, IEEE *Transactions on Antennas and Propagation*

Zyweck, A., and Bogner, R.E., (1994) High-resolution radar imagery of the Mirage III aircraft.
IEEE Transactions on Antennas and Propagation, v. 42 (9), pp. 1356-1360.

IEEE INTERNATIONAL RADAR CONFERENCE

May 1995

ORGANIZING COMMITTEE

October 18, 1994

Anthony Zyweck
Microwave Radar Division
Defence Science and Technology
Organization
P. O. Box 1500
Salisbury 5108, AUSTRALIA

Dear Mr. Zyweck:

I am pleased to inform you that your paper submitted to the 1995 International Radar Conference, RADAR-95, has been selected for presentation and publication in the conference proceedings. You will shortly receive an Author's Kit from the Publication Chairman with instructions for the publication and presentation format.

I congratulate you on your acceptance and look forward to seeing you at the conference.

Sincerely,

RADAR-95 INTERNATIONAL CONFERENCE

Russell J. Lefevre
Technical Program Chairman

RJL:csm

RADAR - 95
1000 Wilson Blvd.
30th floor
Arlington, VA 22209-3905
(703) 247-2988

A. Zyweck and R.E. Bogner (1995) Coherent averaging of range profiles. *Radar Conference, 1995., Record of the IEEE 1995 International held Alexandria, VA, 8-11 May 1995*

IEEE TRANSACTIONS ON AEROSPACE AND ELECTRONIC SYSTEMS

G. R. Krumpholz
Editor for Radar

June 20, 1994

PLEASE REPLY TO:
MIT Lincoln Laboratory
P.O. Box 73
Lexington, MA 02173 USA
Tel: (617) 981-5651
Fax: (617) 981-4591

Manuscript No.: 93069R

Mr. Anthony Zyweck
The Centre for Sensor Signal and Information Processing
SPRI Building, Technology Park, The Levels
Pooraka 5095
AUSTRALIA

Dear Mr. Zyweck:

Thank you for submitting a revised version of the manuscript "Radar Target Classification of Commercial Aircraft." The revision has satisfied the criticisms of the reviewers and myself. I particularly appreciate the effort that you expended in documenting your revision efforts. The manuscript is now acceptable for publication as a full paper in the *IEEE Transactions on Aerospace and Electronic Systems*.

Accordingly, I have forwarded your manuscript to Mr. David B. Dobson, Administrative Editor for the *AES Transactions*. Mr. Dobson will inform you of any additional items that may be needed and of the procedures that are involved in publishing your manuscript.

Sincerely yours,

Gary R. Krumpholz
Editor for Radar

Zyweck, A., and Bogner, R.E., (1996) Radar target classification of commercial aircraft.
IEEE Transactions on Aerospace and Electronic Systems, v. 32 (2), pp. 598-606.

BIBLIOGRAPHY

[1] M. Cohen, "A survey of radar-based target recognition techniques," in *Data Structures and Target Classification: SPIE Vol. 1470*, pp. 233–42, April 1991.

[2] E. F. Knott, J. F. Schaeffer, and M. T. Tuley, *Radar Cross Section.* Artech House, 1993.

[3] E. F. Knott, "A progression of high-frequency RCS prediction techniques," *Proceedings of the IEEE*, vol. 73, pp. 252–264, February 1985.

[4] B. Bhanu, "Automatic target recognition: State of the art survey," *IEEE Transactions on Aerospace and Electronic Systems*, vol. 22, pp. 364–379, July 1986.

[5] C. Castro, "Automatic target recognition shows promise," *Defense Electronics*, vol. 22, pp. 49–53, August 1990.

[6] M. W. Roth, "Neural networks for automatic target recognition," *Johns Hopkins APL Technical Digest*, vol. 11, pp. 117–120, January 1990.

[7] C. R. Smith and P. M. Goggans, "Radar target identification," *IEEE Antennas and Propagation Magazine*, vol. 35, pp. 27–38, April 1993.

[8] G. Corsini, E. Dalle Mese, M. Mancianti, L. Verrazzani, and A. Cantoni, "Classification of radar targets: An overview," in *Proceedings of the 1984 International Symposium on Noise and Clutter Rejection in Radars and Imaging Sensors*, pp. 65–70, October 1984.

[9] E. J. Rothwell, D. P. Nyquist, K.-M. Chen, and B. Drachman, "Radar target discrimination using the extinction-pulse technique," *IEEE Transactions on Antennas and Propagation*, vol. 33, pp. 929–936, September 1985.

[10] E. J. Rothwell, D. P. Nyquist, K.-M. Chen, and W. Sun, "New progress on E/S pulse techniques for noncooperative target recognition," *IEEE Transactions on Antennas and Propagation*, vol. 40, pp. 829–833, July 1993.

[11] E. J. Rothwell, D. P. Nyquist, K.-M. Chen, P. Ilavarasan, and J. Ross, "Performance of an automated radar target discimination scheme using E pulses and S pulses," *IEEE Transactions on Antennas and Propagation*, vol. 41, pp. 582–588, May 1993.

[12] E. Walton and J. Young, "The Ohio State University compact radar cross-section measurement range," *IEEE Transactions on Antennas and Propagation*, vol. 32, pp. 1218–1223, November 1984.

[13] F. D. Garber, "Recent advances in automatic radar target identification," in *Proceedings of the IEEE National Aerospace and Electronics Conference NAECON 1991*, pp. 353–359, IEEE New York, NY, USA, May 1991.

[14] O. S. Sands and F. D. Garber, "Pattern representations and syntactic classification of radar measurements of commercial aircraft," *IEEE Transactions on Pattern Analysis and Machine Intelligence*, vol. 12, pp. 204–211, February 1990.

[15] J. Chen and E. Walton, "Comparison of two target classification techniques," *IEEE Transactions on Aerospace and Electronic Systems*, vol. 22, pp. 15–22, January 1986.

[16] E. K. Walton and I. Jouny, "Bispectrum of radar signatures and application to target classification," *Radio Science*, vol. 25, pp. 101–113, March 1990.

[17] P. B. Silverstein, O. S. Sands, and F. D. Garber, "Radar target classification and interpretation by means of structural descriptions of backscatter signals," *IEEE Aerospace and Electronics Systems Magazine*, vol. 6, pp. 3–7, May 1991.

[18] N. E. Chamberlain, E. K. Walton, and F. D. Garber, "Radar target identification of aircraft using polarization-diverse features," *IEEE Transactions on Aerospace and Electronic Systems*, vol. 27, pp. 58–67, January 1991.

[19] N. F. Chamberlain, "Syntactic classification of radar targets using polarimetric signatures," in *IEEE International Conference on Systems Engineering*, pp. 490–494, IEEE New York, NY, USA, August 1990.

[20] R. Carriere and R. L. Moses, "High resolution radar target modeling using a modified prony estimator," *IEEE Transactions on Antennas and Propagation*, vol. 40, pp. 13–18, January 1992.

[21] F. D. Garber, N. F. Chamberlain, and Ó. Snorrason, "Time domain and frequency domain feature selection for reliable radar target identification," in *Proceedings of the IEEE 1988 National Radar Conference*, pp. 79–84, IEEE, IEEE Press, April 1988.

[22] A. G. Repjar, A. A. Ksienski, and L. J. White, "Object identification from multi-frequency radar returns," *The Radio and Electronic Engineer*, vol. 45, pp. 161–175, April 1975.

[23] A. A. Ksienski, Y.-T. Lin, and L. J. White, "Low-frequency approach to target identification," *Proceedings of the IEEE*, vol. 63, pp. 1651–1659, December 1975.

[24] Y.-T. Lin and A. A. Ksienski, "Identification of complex geometrical shapes by means of low-frequency radar returns," *The Radio and Electronic Engineer*, vol. 46, pp. 472–486, October 1976.

[25] C. L. Bennett and J. P. Toomey, "Target classification with multiple frequency illumination," *IEEE Transactions on Antennas and Propagation*, vol. 29, pp. 352–358, March 1981.

[26] M. Menon, E. Boudreau, and P. Kolodzy, "An automatic ship classification system for ISAR imagery," *Lincoln Laboratory Journal*, vol. 6, no. 2, pp. 289–308, 1993.

[27] R. J. Drazovich, F. X. Lanzinger, and T. O. Binford, "Radar target classification," in *IEEE Conference on Pattern Recognition and Image Processing*, pp. 496–501, IEEE, IEEE Press, August 1981.

[28] B. D. Bullard and P. C. Dowdy, "Pulse doppler signature of a rotary-wing aircraft," *IEEE Aerospace and Electronics Systems Magazine*, vol. 6, pp. 28–30, May 1991.

[29] G. Collot, "Fixed/rotary wings classification/recognition," in *Proceedings of CIE 1991 International Conference on Radar*, pp. 610–612, International Academic Publishers, Beijing, China, October 1991.

[30] M. R. Bell and R. A. Grubbs, "JEM modelling and measurement for radar target identification," *IEEE Transactions on Aerospace and Electronic Systems*, vol. 29, pp. 73–87, January 1993.

[31] A. Robinson, "Radar signature analysis in the UK," *International Defense Review*, vol. 23, pp. 1011–1014, September 1990.

[32] P. Pellegrini, S. Cuomo, and S. Pardini, "Radar signals analysis oriented to target characterization applied to civilian ATC radar," in *RADAR92*, pp. 438–445, 1992.

[33] D. R. Wehner, *High resolution radar.* Artech House, Norwood, MA, 1987.

[34] D. L. Mensa, *High resolution radar cross-section imaging.* Artech House, Norwood, MA, 1991.

[35] A. Rihaczek, *Principles of High-Resolution Radar.* McGraw-Hill, New York, NY, 1969.

[36] M. I. Skolnik, *Introduction to radar systems.* McGraw Hill, 1980.

[37] C. E. Cook and M. Bernfeld, *Radar Signals: An introduction to theory and application.* Artech House, Norwood, MA, 1993.

[38] J. Klauder, A. Price, S. Darlington, and W. Albersheim, "The theory and design of chirp radars," *The Bell System Technical Journal*, vol. 39, pp. 745–808, July 1960.

[39] fred harris, "On the use of windows for harmonic analysis with the discrete Fourier transform," *Proceedings of the IEEE*, vol. 66, pp. 51–81, January 1978.

[40] C. Chen and H. C. Andrews, "Multifrequency imaging of radar turntable data," *IEEE Transactions on Aerospace and Electronic Systems*, vol. 16, pp. 15–22, January 1980.

[41] C. Chen and H. C. Andrews, "Target motion induced radar imaging," *IEEE Transactions on Aerospace and Electronic Systems*, vol. 16, pp. 2–14, January 1980.

[42] fred harris, "Overview of radar imaging (SAR and ISAR)," in *Proceedings of Radarcon '90. First Australian Radar Conference*, pp. 155–163, Defence Science Technology Organisation, Salisbury, SA, Australia, April 1990.

[43] S. Halevy, "Tomographic radar imaging techniques," in *Twenty-Second Asilomar Conference on Signals, Systems and Computers*, pp. 668–672, Maple Press San Jose, CA, USA, October 1989.

[44] B. Haywood and R. J. Evans, "Motion compensation for ISAR imaging," in *Proceedings of ASSPA'89, Adelaide, Australia*, pp. 113–117, April 1989.

[45] R. P. Bocker, T. B. Henderson, S. A. Jones, and B. R. Frieden, "A new inverse synthetic aperture radar algorithm for translational motion compensation," in *Stochastic and Neural Methods in Signal Processing, Image Processing, and Computer Vision*, vol. SPIE 1569, pp. 298–310, 1991.

[46] B. D. Steinberg, "Microwave imaging of aircraft," *Proceedings of the IEEE*, vol. 76, pp. 1578–1592, December 1988.

[47] B. Kang, H. M. Subbaram, and B. D. Steinberg, "Improved adaptive-beamforming target for self-calibrating a distorted phased array," *IEEE Transactions on Antennas and Propagation*, vol. 38, pp. 186–194, February 1990.

[48] R. P. Bocker and S. A. Jones, "ISAR motion compensation using the burst derivative measure as a focal quality indicator," *International Journal of Imaging Systems and Technology (IJIST)*, vol. 4, pp. 285–297, 1992.

[49] K. R. Shillington, P. A. Jahans, E. H. Buller, and J. K. E. Tunaley, "An ISAR simulator for ships," in *Antennas and Propagation Society Symposium 1991 Digest*, pp. 1032–5, June 1991.

[50] A. Zyweck and R. E. Bogner, "High-resolution radar imagery of the Mirage III aircraft," *IEEE Transactions on Antennas and Propagation*, vol. 42, pp. 1356–1360, September 1994.

[51] T. E. Tice, "An overview of radar cross section measurement techniques," *IEEE Transactions on Instrumentation and Measurement*, vol. 39, pp. 205–207, February 1990.

[52] W. Anderson, P. Dansie, R. Hawkes, and A. Mahoney, "The MRD high resolution radar facility and its application to target signature analysis," in *Proceedings of Radarcon '90, First Australian Radar Conference*, pp. 485–491, Defence Science Technology Organization, Salisbury 5108, Australia, April 1990.

[53] B. D. Bullard and P. C. Dowdy, "Pulse doppler signature of a rotary-wing aircraft," in *1991 IEEE National Radar Conference*, pp. 160–163, IEEE, March 1991.

[54] M. J. Muuss, P. Dykstra, K. Applin, G. Moss, E. Davisson, P. Stay, and C. Kennedy, "Ballistic Research Laboratory CAD Package, Release 1.21," BRL internal publication, Ballistic Research Laboratory, USA, June 1987.

[55] J. L. Gustafson, R. E. Benner, M. P. Sears, and T. D. Sullivan, "A radar simulation program for a 1024-processor hypercube," in *Proceedings of Supercomputing '89*, pp. 96–105, November 1989.

[56] M. L. Harman and S. H. W. Simpson, "EPSILON — a radar cross-section modelling package," in *Proceedings of the 1990 UKSC Conference on Computer Simulation*, pp. 236–43, September 1990.

[57] M. B. Murch and M. S. McFarlin, "N-point scatterer model development of a fighter aircraft using radar cross section prediction codes," in *Proceedings of the 1992 Summer Computer Simulation Conference*, pp. 821–5, July 1992.

[58] A. Zyweck, B. Haywood, and R. Kyprianou, "ISARLAB: A radar signal processing tool," in *Proceedings of ICASSP 94, Adelaide, Australia*, pp. V–177–180, April 1994.

[59] R. Bhattacharyya, *Dynamics of Marine Vehicles*. John Wiley and Sons, 1978.

[60] A. Zyweck and R. E. Bogner, "Radar target recognition using range profiles," in *Proceedings of ICASSP 94, Adelaide, Australia*, pp. II–373–376, April 1994.

[61] A. Zyweck and R. E. Bogner, "Radar target classification of commercial aircraft," to appear in *IEEE Transactions on Aerospace and Electronic Systems*, vol. 31, October 1995.

[62] H. J. Li and S. H. Yang, "Using range profiles as feature vectors to identify aerospace objects," *IEEE Transactions on Antennas and Propagation*, vol. 41, pp. 261–268, March 1993.

[63] S. Hudson and D. Psaltis, "Correlation filters for aircraft identification from radar range profiles," *IEEE Transactions on Aerospace and Electronic Systems*, vol. 29, pp. 741–748, July 1993.

[64] H. Songhua, Z. Wei, and G. Guirong, "Target discrimination and recognition using high resolution range features," in *Proceedings of the IEEE 1992 National Aerospace and Electronics Conference, NAECON 1992*, pp. 280–283, May 1992.

[65] D. R. Wehner, "On the resolution required for HRRP target recognition." private communication, February 1993.

[66] M. W. Long, ed., *Airborne early warning system concepts*, ch. 12, pp. 457–495. Artech House: Boston, 1992.

[67] S. Mori, C. Suen, and K. Yamamoto, "Historical review of ocr research and development," *Proceedings of the IEEE*, vol. 80, pp. 1029–1058, July 1992.

[68] S. Mori, C. Suen, and M. Berthod, "Automatic recognition of hand-printed characters— the state of the art," *Proceedings of the IEEE*, vol. 68, pp. 469–487, April 1980.

[69] M. N. Cohen, "Variability of ultrahigh-range-resolution radar profiles and some implications for target recognition," in *Signal Processing, Sensor Fusion, and Target Recognition: Proceedings of the SPIE*, vol. 1699, pp. 256–266, April 1992.

[70] A. Williams, "Feature extraction considerations for high resolution radar signals," in *20th Asilomar Conference on Circuits, Systems and Computers, Pacific Grove, CA*, pp. 619–625, IEEE Press, November 1987.

[71] H. J. Li and V. Chiou, "Aerospace target identification — comparision between the matching score approach and the neural network approach," *Journal of Electromagnetic Waves and Applications*, vol. 7, no. 6, pp. 873–893, 1993.

[72] P. E. Zwicke and I. Kiss, Jr., "A new implementation of the Mellin transform and its application to radar classification of ships," *IEEE Transactions on Pattern Analysis and Machine Intelligence*, vol. 5, pp. 191–199, Mar. 1983.

[73] T. Einstein, "Generation of high resolution radar range profiles and range profile auto-correlation functions using stepped-frequency pulse trains," Tech. Rep. Project report TT-54, MIT Lincoln Laboratory, October 1984.

[74] A. V. Oppenheim and J. S. Lim, "The importance of phase in signals," *Proceedings of the IEEE*, vol. 69, pp. 529–541, May 1981.

[75] V. A. Ditkin, *Integral transforms and operational calculus.* Pergamon: New York, 1965.

[76] G. Guirong, G. Xiuhuang, Y. Wenxian, and H. Songhua, "An effective method for ship target recognition," in *Proceedings of CIE 1991 International Conference on Radar*, pp. 606–9, Int. Acad. Publishers, Beijing, China, October 1991.

[77] L. Min, S. Zhongkang, and L. Juchang, "The second-order neural network for radar ship target recognition," in *Proceedings of the IEEE 1992 National Aerospace and Electronics Conference, NAECON 1992*, pp. 270–274, May 1992.

[78] N. Mohamed, "Target signature using nonsinusoidal radar signals," *IEEE Transactions on Electromagnetic Compatibility*, vol. 35, pp. 457–65, November 1993.

[79] N. H. Farhat, "Microwave diversity imaging and automated target identification based on models of neural networks," *Proceedings of the IEEE*, vol. 77, pp. 670–681, May 1989.

[80] N. H. Farhat and B. Bai, "Echo inversion and target shape estimation by neuromorphic processing," *Neural Networks*, vol. 2, no. 2, pp. 117–125, 1989.

[81] N. Farhat and H. Babri, "Phase space engineering for neurodynamic target identification," in *AP-S International Symposium 1989*, pp. 768–771, June 1989.

[82] G. T. Herman, *Image reconstruction from projections.* Springer-Verlag: New York, 1979.

[83] D. Casasent and E. Barnard, "Invariance and neural networks," *IEEE Transactions on Neural Networks*, vol. 2, pp. 498–508, September 1991.

[84] R. Duda and P. Hart, *Pattern classification and scene analysis.* John Wiley and Sons, New York, NY, 1973.

[85] A. Zyweck and R. E. Bogner, "Coherent averaging of range profiles," in *IEEE International Radar Conference, Washington D.C. USA*, May 1995.

[86] S. O. Rice, "The mathematical analysis of random noise," *Bell System Technical Journal*, vol. 23, pp. 282–332, July 1944.

[87] S. O. Rice, "The mathematical analysis of random noise," *Bell System Technical Journal*, vol. 24, pp. 46–156, January 1945.

[88] S. O. Rice, "Statistical properties of a sine wave plus random noise," *Bell System Technical Journal*, vol. 27, pp. 109–157, January 1948.

[89] J. I. Marcum, "A statistical theory of target detection by pulsed radar," *IRE Transactions*, vol. IT-6, pp. 59–144, July 1963.

[90] J. I. Marcum, "Mathematical appendix," *IRE Transactions*, vol. IT-6, pp. 145–269, July 1963.

[91] L. Blake, *Radar range-performance analysis.* Artech House, 1986.

[92] N. A. Weiss and M. J. Hasset, *Introductory Statistics.* Addison-Wesley, 1987.

[93] M. Schwartz, W. Bennett, and S. Stein, *Communication systems and techniques.* McGraw-Hill, 1966.